Doctoral theses at NTNU, 2023:215

Henrik Erring Hansen

Sonochemical Synthesis of Nanoparticles for Fuel Cells and Electrolyzers

Doctoral thesis

NTNU
Norwegian University of Science and Technology
Thesis for the Degree of
Philosophiae Doctor
Faculty of Natural Sciences
Department of Materials Science and Engineering

NTNU
Norwegian University of
Science and Technology

Henrik Erring Hansen

Sonochemical Synthesis of Nanoparticles for Fuel Cells and Electrolyzers

Thesis for the Degree of Philosophiae Doctor

Trondheim, June 2023

Norwegian University of Science and Technology
Faculty of Natural Sciences
Department of Materials Science and Engineering

NTNU
Norwegian University of
Science and Technology

NTNU
Norwegian University of Science and Technology

Thesis for the Degree of Philosophiae Doctor

Faculty of Natural Sciences
Department of Materials Science and Engineering

ISBN 978-82-326-7132-8 (printed ver.)
ISBN 978-82-326-7131-1 (electronic ver.)
ISSN 1503-8181 (printed ver.)
ISSN 2703-8084 (online ver.)

Doctoral theses at NTNU, 2023:215

Printed by NTNU Grafisk senter

Preface

This thesis is a product of my work as a PhD candidate at the Department of Materials Science and Engineering at the Norwegian University of Science and Technology (NTNU) from 2019 to 2023. My work was funded by ENERSENSE (grant 68024013) in a joint cooperation between the Department of Materials Science and Engineering, and the Department of Energy and Process Technology both at NTNU.

The thesis is built around our published works which are presented in chronological order after date of publication in Chapter 4-7. Relevant theory and methodology are provided in Chapter 2 and 3, respectively. Findings from our publications are also discussed in conjunction with each other in Chapter 8, and the main conclusions are presented in Chapter 9. My contributions to the research articles presented in this thesis are summarized below:

Two Routes for Sonochemical Synthesis of Pt-nanoparticles with a Narrow Size Distribution: After having performed countless dosimetry experiments under different ultrasound parameters I wondered whether two completely different ultrasound setups could be tuned to exhibit the same radical generation. This sparked the idea of finding out if the same nanoparticle properties could be achieved as long as the radical generation rate was controlled. A 20 kHz probe sonicator and a 408 kHz plate sonicator system were therefore chosen as they represent two completely different ultrasound setups. Following the initial idea, I conducted all experiments, performed the necessary analysis, and wrote the article. My supervisors provided insight into the interpretation of the results on a weekly basis and contributed to the editing of the manuscript.

Frequency Controlled Agglomeration of Pt-Nanoparticles in Sonochemical Synhtesis: Inspired by the frequency work on gold nanoparticles by Okitsu et al.

[1], I wanted to investigate the proposed ideal frequency range for sonochemical synthesis of Pt-nanoparticles. I conducted all experiments myself, except for the TEM-imaging which was performed by Inger-Emma Nylund. I analyzed and wrote the manuscript myself. My supervisors provided insight into the interpretation of the results on a weekly basis and contributed to the editing of the manuscript.

Sonochemical Synthesis of Cu@Pt Bimetallic Nanoparticles: Following the similar electrochemical performance displayed by the Pt-nanoparticles in our previous article, I wanted to explore whether a core-shell structure could increase the mass activity. I therefore put out an advertisement for a master student project to figure out if a core-shell structure was achievable using the sonochemical method. All experiments were therefore performed by my master student, Daniel Ø. Fakhri. In close collaboration with Daniel, I analyzed and interpreted the results. I also wrote the manuscript. My supervisors provided insight into the interpretation of the results on a weekly basis and contributed to the editing of the manuscript.

Optimum Scavenger Concentrations for Sonochemical Nanoparticle Synthesis: Suspected formation of H_2O_2 in our previous work led me to believe that for a certain scavenger concentration, all primary radicals will be scavenged and no H_2O_2 will be formed. Upon discovering this, I suspected that we could correlate the concentration at which complete scavenging occurs to the reduction rate of Ag(I) to Ag-nanoparticles which is what this work demonstrates in detail for several different alcohols. I conducted all experiments myself, and also analyzed all data and wrote the manuscript myself. My supervisors provided insight into the interpretation of the results on a weekly basis and contributed to the editing of the manuscript. I regard this as my best work so far.

Acknowledgements

First and foremost, I would like to thank my supervisors, Professor Frode Seland, Professor Bruno Pollet, Professor Odne Burheim, and Professor Svein Sunde for their invaluable guidance throughout my PhD. I have really appreciated you taking the time out of your busy schedules to have weekly meetings with me consistently over the past four years. Having the opportunity to discuss my work with you for an entire hour every week has been one of the highlights of my PhD.

My five master students, Nicolas, Ingeborg, Daniel, Kristina, and Thea also deserve a special recognition. Not only has it been a pleasure assisting you in your respective projects, but your ideas, experiments, and results have been a tremendous help for my project as well. Our little sonochemistry group has been able to cover so much more ground thanks to your work.

I would also like to thank all members of the electrochemistry group at the Department of Materials Science and Engineering (IMA) and all members of Enersense for their willingness to help with both practical solutions in the lab, as well as fruitful discussions of results and general theoretical questions. A special thanks to my office mates over the years who have contributed to a fun and engaging work environment.

The technical staff at IMA also deserves a special gratitude. Their work in keeping the labs up and running in a safe and secure manner has made working in the lab a pleasure. Their quick and precise response to my countless requests for equipment, chemicals or general assistance has been a key factor in keeping my productivity up.

I would also like to thank Professor Byron Gates and the members of his group at Simon Fraser University for allowing me to join their group from May to August

2022. I learned a lot from this experience, and it was a pleasure getting to know you all.

Last, but not least I would like to thank my family and friends for their support through these past four years. Most of all, perhaps, I would like to thank Marion for her everlasting confidence and support. Having to listen to my theories, look at my results, and endure hours of explanations on sonochemical theory is admirable to say the least.

Henrik Erring Hansen
Gløshaugen, 13th April 2023

Summary

Green hydrogen represents an environmentally friendly alternative to fossil fuels as an energy carrier in many different energy-demanding industries. However, commercialized electrochemical conversion devices utilizing hydrogen are expensive mostly due to the use of noble metals such as platinum and iridium in the catalyst layer. To make these devices a viable alternative to fossil fuels, the catalyst performance needs to be increased while also reducing the amount of noble metals. Large scale production with a high degree of reproducibility is also desired when trying to reduce the cost. In order to achieve this, new nanoparticle synthesis methods must be developed. The current synthesis routes are typically based on batch processes which are difficult to control. They also utilize harmful chemicals which can be a hazard to the chemist and the environment alike. Replacing these with a continuous synthesis process where every parameter is easily controlled could therefore contribute to making hydrogen a viable energy carrier.

The main objective of this thesis work was to develop the sonochemical synthesis method for the production of electrocatalysts in water electrolyzers and fuel cells. The focus has been on improving the slow rate of catalyst production through systematic investigations of different ultrasound parameters like the ultrasonic frequency and radical scavenger composition. Different material systems including platinum-, copper-, and silver-nanoparticles have also been synthesized with the sonochemical method to evaluate how versatile this method is.

The rate of catalyst production has been monitored through UV-visible spectroscopy with various colorimetric techniques. Direct UV-vis measurements of the nanoparticle colloidal solution were performed to assess the development of the nanoparticle colloidal solutions. This was more relevant when monitoring silver and copper due to their pronounced localized surface plasmon resonance peaks.

For platinum, the development of Pt(IV) and Pt(II) were used as a measure of the catalyst formation rate. This was achieved through colorimetric enhancements of the Pt(IV) and Pt(II) peaks through the addition of potassium iodide. Rate of radical formation is closely related to the catalyst production rate which was also monitored colorimetrically through detection of H_2O_2 and I_3^-.

The performance of the resulting catalysts has mainly been measured by their hydrogen evolution reaction activity in acidic solution. This was used to assess the activity of both Pt-nanoparticles synthesized at different ultrasonic frequencies, and sonochemically synthesized Cu@Pt-nanoparticles. Corresponding particle size measurements through electron microscopy and X-ray diffraction have also been recurring methods for evaluating the effect of changing sonochemical parameters. Our measurements revealed that the sonochemical method allows for very reproducible Pt-nanoparticle sizes and hydrogen evolution performance over a broad frequency range (20 kHz - 488 kHz), and using a wide selection of acoustic powers 11.8 W - 70.0 W.

The choice of radical scavenger and its concentration was found to be one of the most important parameters in the sonochemical method towards achieving higher reduction rates. A scavenger concentration equivalent to complete bubble coverage leads to the highest reduction rates for reactions driven by secondary radicals. These include the reduction of Pt(II) and Ag(I) to their respective metal nanoparticles. However, with appropriate choice of scavenger (ethylene glycol), pyrolytic decomposition is also able to drive the reduction of Ag(I) to Ag-nanoparticles. For reactions where pyrolytic decomposition products are also contributing (Pt(IV), Pd(II) and Au(III)), the optimal scavenger concentration is increased by an order of magnitude towards higher concentrations.

From this work we have found that the sonochemical synthesis method is very well suited for producing Pt-nanoparticles for electrocatalytic purposes. The reproducibility is good, the size range and size distribution attainable by the sonochemical method are within the optimal range for Pt-electrocatalysts, and there is a significant potential for scaling up the sonochemical synthesis method. There is some concern related to the versatility of this method as the first row transition metals are either impossible to synthesize or impractically slow. Continued pursuit of the electron transfer behaviour between secondary radicals and transition metal ions are therefore necessary in order to explain why some transition metals are reduced more easily than others with the sonochemical method. Perhaps identifying these mechanisms also allows for new ways of bypassing them. Developing larger scale reactors to study the scale-up potential of the sonochemical method is also a highly important area of research if the sonochemical method is to be applicable on an industrial scale.

Contents

Preface **iii**

Acknowledgements **v**

Abstract **vii**

1 Introduction **1**

1.1 Background and Motivation 1

1.2 Aim of Thesis 4

1.3 Outline of the Thesis 5

2 Theory **7**

2.1 Acoustics 7

2.1.1 Frequency of Acoustic Waves 9

2.1.2 Propagation of Acoustic Waves 10

2.1.3 Reflection of Acoustic Waves 12

2.1.4 Standing Waves 12

2.2 Ultrasound 15

2.2.1 Ultrasonic Transducers 15

2.2.2 Impedance Matching 17
2.2.3 Direct and Indirect Sonication 19
2.2.4 Cavitation 21
2.3 Sonochemistry and Current Development 28
2.3.1 Historical Perspective of Sonochemistry 29
2.3.2 Sonochemical Synthesis 30
2.3.3 Ultrasound Parameters 39
2.3.4 Scale Up 55
2.4 Electrocatalysis 57
2.4.1 Introduction to Catalysis 57
2.4.2 Electrochemical Energy Conversion Devices 58

3 Methodology 65
3.1 Physical Characterization 65
3.1.1 UV-Visible Spectroscopy 65
3.1.2 X-ray Diffraction 72
3.1.3 Electron Microscopy 76
3.1.4 Dynamic Light Scattering 79
3.2 Electrochemical Characterization 81
3.2.1 Linear Sweep Voltammetry 84
3.2.2 Cyclic Voltammetry 85
3.3 Ultrasound Characterization 87
3.3.1 Calorimetry 87
3.3.2 Dosimetry 89

4 Two Routes for Sonochemical Synthesis of Platinum Nanoparticles with Narrow Size Distribution 93

5 Frequency Controlled Agglomeration of Pt-nanoparticles in Sonochemical Synthesis 119

6 Sonochemical Synthesis of Cu@Pt Bimetallic Nanoparticles 151

7 Optimum Scavenger Concentrations for Sonochemical Nanoparticle Synthesis 169

8 Discussion 209

8.1 Effect of Radical Scavengers 209

8.2 Impedance Mismatch 212

8.3 Direct Sonication and Indirect Sonication 213

8.4 Sonochemistry in Electrocatalyst Preparation 214

9 Conclusions and Outlook 219

Bibliography 234

Nomenclature 235

Chapter 1

Introduction

1.1 Background and Motivation

Following the signing of the Paris agreement in 2015, 196 countries agreed to limit global warming to less than $2\,^{\circ}\mathrm{C}$ above pre-industrial levels [2]. This is a binding contract for the signatories so they are obliged to limit the emission of green house gases in an effort to achieve a climate neutral world by 2050. Even though water vapour is the most abundant green house gas in our atmosphere [3], the increases in green house gases observed in the past century has primarily come from the burning of fossil fuel sources such as oil and gas: One of the most prominent by-products being carbon dioxide (CO_2) [4].

Replacing fossil fuels with more sustainable alternatives is a key solution to fulfilling the terms of the Paris agreement. Electric power generated without the consumption of fossil fuels appears to be the desired alternative. This is reflected in the ever increasing number of electric vehicles, transition to electric furnaces in heavy industry, and electricity-based heating solutions for homes and office buildings. The new demand for electric energy from sustainable energy sources requires massive investments into expanding this type of infrastructure. Solar power plants, wind turbine parks, and hydroelectric power plants are some examples of renewable energy solutions which could lead the way in such a carbon neutral energy market. However, geographical constraints might limit several of these solutions. For example, there is limited benefit in building a hydroelectric power plant in a country without significant elevation like Denmark or the Benelux-countries. Additionally, wind- and solar-energy can be harnessed all over the world, though, some places are more ideal than others. One problem with wind- and solar-energy is that its energy output is variable over time. It does not necessarily align with the

energy demand. This means that the energy needs to be stored so it can be used at a time when the demand is higher.

Multiple existing energy storage solutions mostly revolve around storing the energy as chemical energy. Electrolyzers and batteries are two examples of such energy storage devices. In an electrolyzer, electric energy is used to produce hydrogen gas which can later be used as fuel in a fuel cell to regenerate some of the electric energy. The energy in this case is stored as hydrogen. Of these two energy storage solutions, hydrogen most closely resembles the existing solutions in which a fuel (hydrogen) is added to an energy conversion device (fuel cell). Hydrogen could therefore fill the role that fossil fuels have today by adopting fuel cells instead of combustion engines, furnaces, and ovens. Likewise, oil refineries that produce the fossil fuels today could be replaced by electrolysis plants where hydrogen is produced instead.

The transition from fossil fuels to hydrogen, although seemingly analogous, requires a lot of modifications to existing infrastructure [5]. Where fossil fuels draw from the massive oil and gas rigs, hydrogen must be connected to a grid, preferably supplied by renewable energy sources. To satisfy the energy demand currently fulfilled by fossil fuels, renewables must be massively upscaled. Where oil can be stored as a liquid under fairly standard conditions, hydrogen must be stored in carefully designed tanks either as a liquid at cryogenic temperatures or as a gas in a high pressure tank [6]. The explosive nature of hydrogen also requires extra safety precautions. The final obstacle in relation to hydrogen technology is the conversion process from electricity to hydrogen and from hydrogen to electricity. In order for this process to proceed at a reasonable rate and with as little loss as possible, a catalyst is needed. The current top-performing catalysts for electrochemical conversion of hydrogen are based on noble metals such as platinum and iridium [7]. The limited availability of these precious metals and their requirement in many technologies has caused their prices to skyrocket. As such, fuel cells and electrolyzers are by extension also expensive, which is a barrier towards mass commercialization.

Much work on developing catalysts of other more abundant materials like nickel or iron has been undertaken [8–10], however, the noble metals still persist in state-of-the-art fuel cells and electrolyzers [7, 10]. Another strategy to minimize fuel cell cost is therefore to limit the amount of the noble metals while maintaining, or even improving the performance. Various solutions such as core-shell structures, bimetallics, and alloys have been developed in response to this challenge [11–14]. What these solutions have in common is that they try to maximize the number of active sites on the catalyst surface, which is achievable only when the catalyst size is reduced to the nano scale. The increased surface to volume ratio displayed by

nanoparticles allows for more of the atoms to contribute to the activity, since they are present at the catalyst surface.

Developing methods of large scale nanoparticle production has therefore been of the utmost importance to produce affordable catalysts for fuel cells and electrolyzers. However, most of the current synthesis methods are batch processes as they rely on chemical reduction methods [8, 15–17]. Scaling up batch processes is not very efficient as there will inevitably be considerable down-time while product is extracted. It also relies on the addition of chemicals that might be environmentally harmful or pose a danger to the operator by nature of their biproducts. Chemical reduction also suffers from difficulties in controlling particle sizes as the solution volume, precursor concentration, and surfactant concentration must be carefully controlled to achieve the desired particle properties [16]. Variability between syntheses is therefore inevitable and leads to differences in performance of the fuel cells and electrolyzers [18].

An alternative to chemical reduction methods is the sonochemical synthesis method. It utilizes ultrasonic sound waves to generate reducing agents in situ, which therefore allows for continuous production of catalysts [19, 20]. There is also no need for the addition of harmful chemicals as it is solely driven by electric energy. This is also an upside since electric energy is the predicted successor to fossil fuels. The highly tunable ultrasound parameters also provide a high degree of control over the nucleation and growth processes, which in turn result in monodisperse nanoparticles [21–23]. An additional effect of the ultrasonic waves is the intense shock waves generated upon collapse of cavitation bubbles [24, 25]. These ensure thorough mixing and dispersion of the catalyst and can impact the degree of agglomeration of the nanoparticles [23].

The primary challenge with sonochemical synthesis is that it is inherently slow. The reducing agents are generated at a rate of 10-20 $\mu\mathrm{mol}\,\mathrm{dm}^{-3}\,\mathrm{min}^{-1}$ [26–30]. It therefore remains unclear whether the sonochemical synthesis method is feasible for large scale processes. Some promising initial works do suggest that increasing the reactor height increases the number of radicals being produced, and that the continuous operation of a sonochemical reactor makes it well suited for continuous catalyst production [31, 32]. One of the drawbacks for chemical reduction methods is that it can be difficult to predict how changes in one experimental parameter may affect the resulting particle properties [16]. This means that scaling up the synthesis becomes unpredictable. If the sonochemical method allows for reproducible particle properties when experimental parameters are changed, it may therefore also retain its particle properties when the method is scaled up as well.

There is also uncertainty connected to exactly how the sonochemical reactions un-

fold. Specifically, how radical scavengers interact with cavitation bubbles and how the resulting secondary radical is transferred to the target species. These knowledge gaps become apparent when comparing the sonochemical synthesis of gold and rhodium nanoparticles in the work of Okitsu et al. [26]. They observed that Au-nanoparticles are readily formed with almost any radical scavenger, while Rh-nanoparticles are only formed when sodium formate is used as the scavenger. The choice of scavenger is further complicated with the scavenger efficiency being related to how hydrophobic the scavenger is [33, 34]. Also, not all secondary radicals formed from scavenging are able to donate electrons to the target species which puts additional restrictions on the choice of scavenger [35]. In order to optimize the transfer of primary radicals to the target species it is therefore paramount to choose the right scavenger. But what about the scavenger concentration? Is there an optimum scavenger concentration for nanoparticle synthesis? Can it be used in excess? Answering these questions will provide much needed information as to how the sonochemical reduction process unfolds.

The choice of scavenger is not the only ultrasound parameter which affects the sonochemical synthesis method; the ultrasonic frequency [1], saturating gas [36], acoustic power [32], and bulk temperature [37] all contribute to the number of radicals formed during bubble collapse. The ultrasonic frequency is one of the most studied ultrasound parameters, and much of the focus has been on identifying the optimum frequency for radical formation [1, 38–40]. The ultrasonic frequency not only affects the radical formation, but also the acoustic streaming and mechanical effects of ultrasound. All these effects are relevant in nanoparticle synthesis as they directly influence the nucleation and growth as well as any agglomeration behaviour during synthesis. The mechanical effects are expected to diminish in strength for higher ultrasonic frequencies, while the sonochemical radical formation is expected to reach a maximum at higher ultrasonic frequencies. A suitable ultrasonic frequency range for achieving reproducible nanoparticles therefore needs to take into account the mechanical effects and sonochemical effects.

1.2 Aim of Thesis

In this thesis the sonochemical method has been explored as an alternative method for metal nanoparticle synthesis, relevant for fuel cells and electrolyzers. The aforementioned challenges with the sonochemical synthesis method related to use of radical scavengers, scale up potential and versatility has been studied in the context of the sonochemical synthesis of platinum nanoparticles. Alternative catalyst materials, Ni, Fe, Au, Ir, Ag, Cu and Cu@Pt has also been investigated to some extent. UV-visible spectroscopy plays a central role in this thesis work. It has been used to monitor radical formation rates and reduction rates. Physical char-

acterization of the resulting nanoparticles by X-ray diffraction as well as electron microscopy are also heavily utilized to determine the physical properties of the catalysts. Catalytic activity of the catalysts towards hydrogen evolution was used to evaluate the electrocatalytic performance of some of the catalysts.

1.3 Outline of the Thesis

The thesis is built around a series of research articles which have already been published. A comprehensive literature and methodology section has been included to provide some background information for the research articles. Some information may therefore be presented multiple times. I believe this results in a better reading experience of the thesis as the alternative would be that key information is "saved" until it is presented in the relevant research articles. For the inexperienced sonochemist it would also provide for a much easier introduction to the field of sonochemistry than having the information presented in an otherwise unorganized manner.

Chapter 1 provides a brief introduction of the thesis and how sonochemistry can be used to synthesize electrocatalysts for electrochemical energy conversion devices. It also provides a motivation of the work as well as some of the main objectives that have been addressed through this research.

Chapter 2 describes the underlying theory related to acoustics before diving deeper into ultrasound and sonochemistry. It provides all the information necessary to understand the interactions between acoustic waves and aqueous media and how the sonochemical effects arise, how they can be controlled, and its application as a synthesis route. Current development in the field of sonochemistry is also discussed. Lastly, relevant information on electrocatalysis is presented.

Chapter 3 deals with the methodology that has been used in this work. The chapter is divided into three sections: physical characterization, electrochemical characterization, and ultrasound characterization. All sections present the characterization techniques used in this work, their working principle, any relevant theoretical background, how measurements are conducted in practice, and how the results are interpreted. Specific configurations and experimental parameters are presented in the experimental section in each separate article.

Chapters 4-7 consist of a collection of research articles presented in chronological order after date of publication. The first article in Chapter 4 is entitled "Two Routes for Sonochemical Synthesis of Pt-Nanoparticles with a Narrow Size Distribution" and was published in Materials Advances [21]. It demonstrates how two completely different ultrasound configurations can be adjusted to exhibit a similar radical generation rate, which in turn results in similar particle sizes for

Pt-nanoparticles. It also shows how heterogeneous nucleation affects the rate of reaction in a sonochemical environment, and why low frequency ultrasound should not be used to disperse particle solutions directly.

The second article in Chapter 5 is concerned with the frequency effects of ultrasound on Pt-nanoparticles and is entitled "Frequency Controlled Agglomeration of Pt-Nanoparticles in Sonochemical Synthesis". This work was published in Ultrasonics Sonochemistry [23]. It demonstrates how the choice of ultrasonic frequency can affect the agglomeration behaviour of Pt-nanoparticles.

The third article in Chapter 6 is entitled "Sonochemical Synthesis of Cu@Pt Bimetallic Nanoparticles" and was published in Molecules [13]. It describes that core-shell or bimetallic systems are indeed achievable through the sonochemical method, and that the resulting catalysts have a substantial increase in mass activity compared to Pt on its own.

The fourth article presented in Chapter 7 is concerned with how the scavenger concentration can be optimized for sonochemical nanoparticle synthesis. Choice of scavenger and the underlying mechanisms related to the scavenger process is also explained in detail. The article is entitled "Optimum Scavenger Concentration for Sonochemical Nanoparticle Synthesis" and was published in Scientific Reports [41].

Chapter 8 provides a discussion of the aforementioned articles where the findings are related to each other. Details on how findings in the most recent articles fits with the earlier work will also be discussed. A discussion regarding the contributions to the field and its possible implications for other sonochemist is also briefly touched upon. The suitability of the sonochemical method as a synthesis method for electrocatalysts is also discussed.

Chapter 9 summarizes the main conclusions from the thesis and the published works. It also provides details regarding ideas for further work in the field of sonochemistry as well as some reflections on which ultrasound parameters will be important for large scale applications.

Chapter 2

Theory

2.1 Acoustics

From the low frequency acoustic waves displayed by singing whales to the ultrasonic waves used by bats to navigate, nature spans quite a broad range when it comes to the utilization of acoustics. Predators and prey alike rely on excellent perception of sound to stay alive. This is reflected in the way some species have evolved to perceive sounds that give them an advantage. This is also true for humans, which perhaps have gone further with acoustics than any other species. Our need for communication has resulted in the development of long distance communication infrastructure (Figure 2.1) starting with the development of the telegraph in late 1700s [42]. This evolved into the telephone in 1876 [42], before expanding into the hitherto unexplored territory of radio waves. Soon other frequencies beyond our audible range were utilized for more than communication. Radar and sonar technology were developed to map the skies and the oceans. Not even celestial bodies were beyond the reach of radio waves with the invention of radio telescopes. Acoustics have therefore been a tremendous driving force for our technological development and will certainly still be important going forward as well.

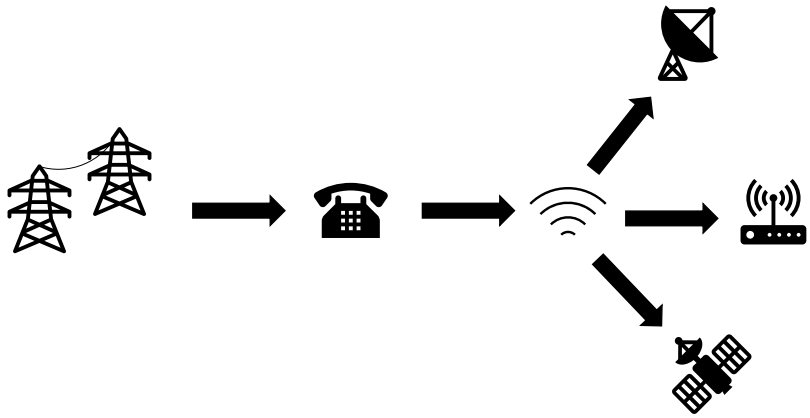

Figure 2.1: Development of communication infrastructure from wired transmission to utilization of radio waves.

Acoustic waves are generated through vibrations. Humans speak through vibrations of their vocal cords. A loudspeaker generates sound by way of making a magnet vibrate. And musical instruments like a guitar generates sound with harmonic oscillations in the instrument [43]. In short, an acoustic wave can be described as a periodic oscillation in a given medium. A wave (u) at a specific point in space (x) and time (t) is therefore given as

$$u(x,t) = A\sin\left(\frac{2\pi x}{\lambda} - 2\pi f t + \varphi\right) \tag{2.1}$$

where A is the amplitude, λ is the wavelength, f is the frequency, and φ is the phase. An example of a sinusoidal wave is provided in Figure 2.2 to illustrate the physical interpretation of the different variables. The frequency is related to the wavelength by the dispersion relation

$$v = \lambda f \tag{2.2}$$

where v is the velocity of the wave [44, p. 29].

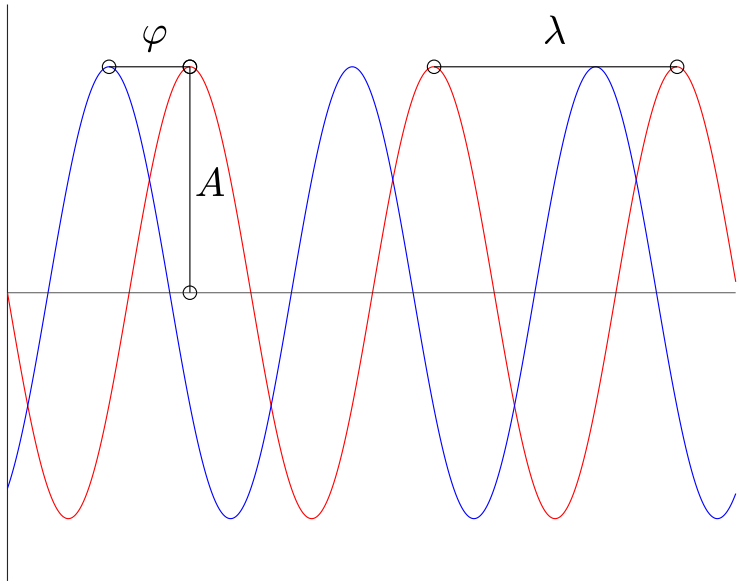

Figure 2.2: Two sinusoidal waves where the amplitude (A), wavelength (λ), and phase shift (φ) have been marked.

2.1.1 Frequency of Acoustic Waves

The frequency of an acoustic wave is determined by the frequency of the vibrations. In a loud speaker, the magnet moves back and forth with a frequency determined by the electrical signal. For a musical instrument, however, there is a set of fixed frequencies determined by the resonance frequencies of the instrument [43]. The resonance frequency is the frequency that will produce the greatest amplitude when the system is driven by an external force [45]. The system will also continue to oscillate at this frequency when the external force is not acting on it anymore. The resonance frequency (ω_r) is determined by the mass (m) and stiffness (k) of the oscillating system [46, p. 463].

$$\omega_\mathrm{r} = \sqrt{\frac{k}{m}} \tag{2.3}$$

As such, a heavier system will display a lower resonance frequency than a lighter system. The guitar is an excellent example of how both mass and stiffness affect

the resonance frequency. The strings which produce the highest frequencies are both the thinnest (lightest), and are more tightly strung (more stiff). The strings producing a lower frequency are thicker (heavier) and are more loosely strung (less stiff) [43].

2.1.2 Propagation of Acoustic Waves

All acoustic waves in gases and liquids move longitudinally contrary to electromagnetic waves which are transversal [44, p. 25]. The waves move through compression and rarefaction of the medium. During the compression phase a maximum inward pressure is exerted on the medium. For the rarefaction phase, a maximum outward pressure is exerted on the medium. These phases are illustrated as alternating dark and light parts in Figure 2.3.

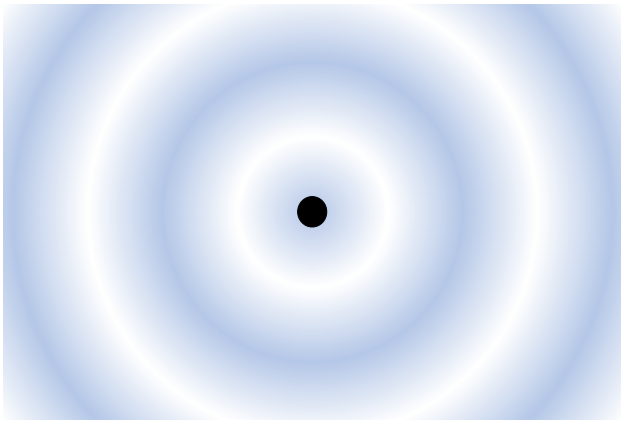

Figure 2.3: Longitudinal wave emitted from a point source in the center. The white areas illustrate the rarefaction process where there is a low pressure and therefore a lower density of the propagation medium. The darker blue areas illustrate the compression process where the pressure and density of the propagation medium is higher.

The stiffness and density of the medium itself is crucial to the propagation of acoustic waves. In fact, the speed of sound (v) in a gas or liquid can be expressed as

$$v = \sqrt{\frac{K_\mathrm{s}}{\rho}} \tag{2.4}$$

where K_s is the stiffness coefficient of the medium, and ρ is the density of the medium [44, p. 32]. A dense, non-viscous medium will therefore reduce the speed of sound. In deionized water the speed of sound is $1482\,\mathrm{m\,s^{-1}}$ at $20\,^\circ\mathrm{C}$ [47]. The speed of sound in most alcohols typically ranges from 1100-$1300\,\mathrm{m\,s^{-1}}$[47]. For ethylene glycol it is $1660\,\mathrm{m\,s^{-1}}$ [47].

Most real world sources of sound create a multidirectional wave, which means that it moves equally in all directions as illustrated in Figure 2.3. As a result, the sound intensity drops off following the inverse square of the distance between the sound source and receiver [44, p. 45]. A plane wave, on the other hand, will not be attenuated in the same way and will propagate with undiminished intensity apart from the sound absorption from the medium itself [44, p. 594]. However, it is not possible to create a perfect plane wave as it would require an infinitely large planar sound source. Approximations of plane waves, on the other hand, can be made if the sound source is a large planar surface and the distance from the sound source is short.

Sound absorption is entirely dependent on the absorption coefficient of the medium and can be described in the same way as light absorption. However, sound intensity is usually measured in decibel (dB) while light absorption is measured in absorbance [44, p. 594].

$$\mathrm{dB} = 10\log\left(\frac{A}{A_0}\right) = \alpha x \tag{2.5}$$

In this expression A is the amplitude of the sound wave, A_0 is the initial amplitude, x is the distance from the sound source, and α is the attenuation coefficient. The attenuation coefficient can be determined from the viscosity (μ), density (ρ), speed of sound (v) in the medium, and the frequency (f) of the acoustic wave [48].

$$\alpha = \frac{2\mu(2\pi f)^2}{3\rho v^3} \tag{2.6}$$

Considering the viscosity (μ = $10^{-3}\,\mathrm{Pa\,s}$) [49], density (ρ = $997\,\mathrm{kg\,m^{-3}}$ [50], and speed of sound (v = $1482\,\mathrm{m\,s^{-1}}$) in water [47], the attenuation coefficient is estimated to be $8 \times 10^{-5}\,\mathrm{cm^{-1}\,MHz^{-2}}$. Frequencies in the sub MHz range propagating on the centimeter scale through aqueous solutions can therefore be assumed to be undiminished in intensity for all practical purposes.

2.1.3 Reflection of Acoustic Waves

Another important aspect to consider for acoustic waves is reflection phenomena. Reflection of sound waves follows the same reflection rules as electromagnetic waves [51]. The wave is reflected with the same angle as the incident wave [44, pp. 120–121]. In addition to reflection, some portion of the sound wave may be transmitted upon interacting with the reflective boundary. The ratio of the reflected wave (R) to the transmitted wave is determined by how similar the media are in terms of their density (ρ) and speed of sound (v) [51][44, pp. 124, 152]. This is referred to as the impedance mismatch.

$$R = \left(\frac{\rho_2 v_2 - \rho_1 v_1}{\rho_1 v_1 + \rho_2 v_2} \right)^2 \tag{2.7}$$

The speed of sound in a medium is determined by its density and stiffness following equation 2.4. Two mediums with similar density and stiffness would therefore give favourable transmission of the acoustic wave. For two mediums with very different density and stiffness, there will be very little transmission, and most of the wave will be reflected. In the specific example where an acoustic wave is reflected off a water-air interface, the impedance mismatch would be substantial [44, pp. 153–154]. The density of air is $1.204\,\mathrm{kg\,m^{-3}}$ [52] whereas the density of water is $997\,\mathrm{kg\,m^{-3}}$ [50]. As for the speed of sound, it is $1482\,\mathrm{m\,s^{-1}}$ for water and $343\,\mathrm{m\,s^{-1}}$ for air [47]. This gives a value of R=0.9988. Most of the acoustic wave would therefore be reflected at the air-water interface. This means that you would not be able to eavesdrop on a conversation taking place on dry land if you are submerged under water yourself. As for the transmission of acoustic waves from water into pyrex glass (v = $5640\,\mathrm{m\,s^{-1}}$ [53], $\rho \approx 2210\,\mathrm{kg\,m^{-3}}$ [54]), the value of R = 0.62. A majority of the acoustic wave is therefore also reflected off the glass, but some will be transmitted as well.

2.1.4 Standing Waves

When both ends of a wave are fixed, a phenomenon referred to as a standing wave can occur [55]. This happens when a wave is generated from a fixed source, and is reflected off a fixed perpendicular interface as illustrated in Figure 2.4.

As such, the forward wave and the reflected wave will interfere with each other generating a stationary or standing wave [55]. This can be described by adding two waves with opposite propagation direction and equal amplitude.

$$u(x,t) = 2A \sin\left(\frac{2\pi x}{\lambda}\right) \cos\left(2\pi f t\right) \tag{2.8}$$

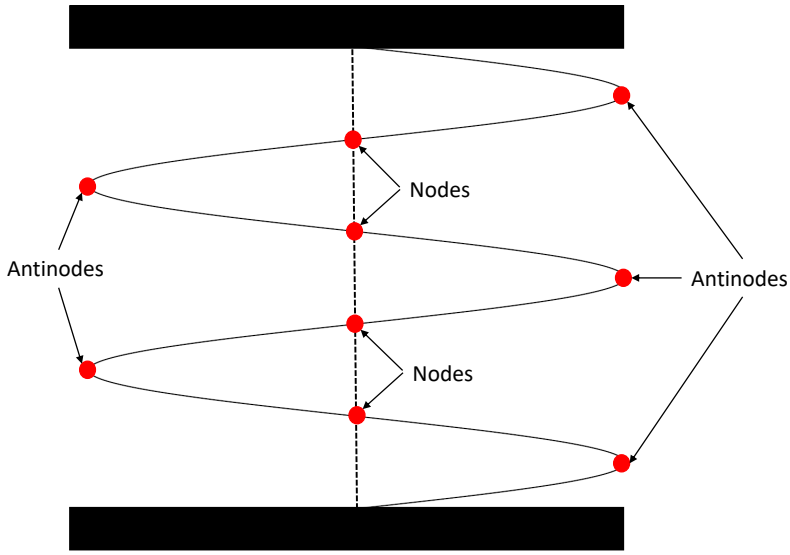

Figure 2.4: Standing wave between two fixed boundaries. Nodes and antinodes are highlighted with red filled circles.

From this equation several observations can be made. At positions equal to $\frac{1}{2}n\lambda$ the amplitude of the wave is zero at all times. These positions are referred to as nodes [55]. For positions equal to $\frac{1}{4}(2n-1)\lambda$, the sine term is alternating between 1 and -1. These positions are referred to as antinodes, and their amplitude will oscillate with time following the cosine term in equation 2.8 [55]. For times equal to $\frac{1}{2}n\frac{1}{f}$ the cosine term is either 1 or -1. At these times the antinodes will have an amplitude equal to 2A or -2A which are the maximum amplitudes. The antinodes therefore alternate between 2A and -2A, while the nodes remain constant at zero.

If significant attenuation of the standing wave occurs between its two boundaries, the standing wave field is broken close to the source of the wave. If the amplitude of two opposing waves differ the higher amplitude wave will start to dominate and a travelling wave field in the forward direction will be the result of the superposition of the two waves. This effect is greater near the source as this is where the loss in amplitude between the forward wave and the reflected wave is the highest [31]. Closer to the reflective boundary the forward wave and the reflected wave are much more similar which means that the conditions for a standing wave are more

easily achieved [31]. This is illustrated in Figure 2.5. The result of significant attenuation in the wave amplitude is therefore a travelling wave field close to the source, and a standing wave field close to the reflective boundary.

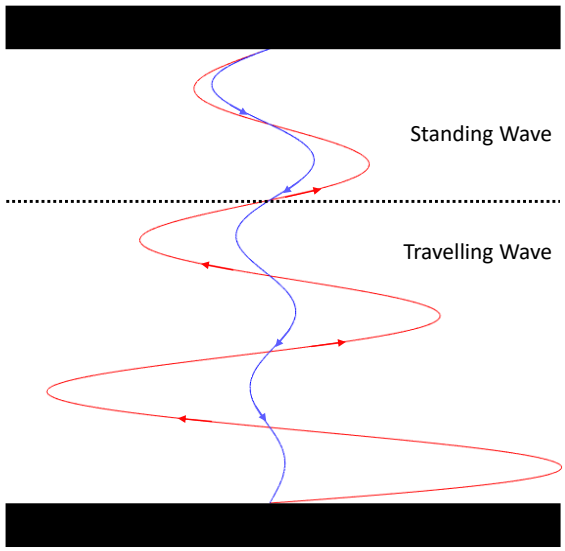

Figure 2.5: Standing wave between two fixed boundaries under constant wave attenuation. The forward wave (red) and the reflected wave (blue) have similar amplitudes near the reflector which produces a standing wave field. Closer to the source, the forward wave dominates and as such a travelling wave is formed.

An example of a standing wave field is found when acoustic waves propagating in water are reflected off the water-air-interface. The large difference in impedance between water and air as discussed in the previous section provides excellent reflection off this interface, and the low attenuation coefficient of water also prevents significant decrease in the amplitude of the acoustic wave. However, other loss mechanisms connected to cavitation phenomena may lead to a diminished intensity [31].

2.2 Ultrasound

Another class of acoustic waves which emerged in the 20. century was ultrasonic waves. These acoustic waves are characterized by frequencies above $20\,\mathrm{kHz}$ and are therefore beyond human hearing [56, p. 21]. Animals such as bats and dolphins, however, have long utilized ultrasound for navigation purposes. It was first utilized by humans with the invention of sonar technology and is based on the same working principles as these animals take advantage of [57]. Ultrasonic waves have also been utilized for medical purposes as a diagnostic tool to examine internal parts of the body. The small scales on which the ultrasonic waves travel inside the body along with the need for high resolution imaging makes high frequencies ideal for these medical applications. That is also why the frequency range above $5\,\mathrm{MHz}$ is often referred to as diagnostic ultrasound [56, p. 21].

Ultrasound has also found its way to numerous engineering applications. This includes nanomaterial synthesis, chemical processing, waste removal, welding, and cleaning to name a few [56, p. 23]. These applications typically make use of the high powers generated by ultrasonic waves in the frequency range between $20\,\mathrm{kHz}$ and $2\,\mathrm{MHz}$ [56, p. 21]. It is therefore referred to as power ultrasound. In addition to its many applications, ultrasound has also proven to be an unwanted side effect in certain applications. The most well known example is that of rotating propellers in naval vessels. If the rotation of the propellers reaches a frequency between $20\,\mathrm{kHz}$ and $100\,\mathrm{kHz}$, the resulting ultrasonic wave will lead to cavitation at the propeller surface causing damage to the propeller itself [58]. The same type of damage is also observed in low frequency ultrasonic horns which frequently need to be replaced [21].

2.2.1 Ultrasonic Transducers

Ultrasound is generated the same way as any other acoustic wave; through vibrations which induce alternating compression and rarefaction of a specific medium. However, the generation of ultrasonic waves requires these oscillations to occur with a frequency above $20\,\mathrm{kHz}$ [56, p. 21]. Such fast oscillations can be difficult to generate mechanically, and would require a lot of energy. Electrical signals are therefore used to generate the ultrasonic wave as its frequency and amplitude can be generated easily by a signal generator [59, 60]. The signal is then passed through a piezoelectric material which converts the electrical signal into a mechanical wave with the same frequency [59–61]. This is called an ultrasonic transducer [59, 60].

Different types of ultrasonic transducers exist and are used for different purposes. Horn-type ultrasonic transducers are typically used when low frequencies and high

powers are needed [56, pp. 23–24]. Homogenization of solutions, ultrasonic cleaning or welding are some applications where these conditions are needed, and as such the horn-type is usually the transducer of choice [59, 60, 62, 63][56, p. 23]. An ultrasonic horn typically consists of a cylinder containing the piezoelectric transducer connected to a longer piece of corrosion resistant material called the sonotrode [59]. Examples of such designs are shown in Figure 2.6(a). The transducer transfers the ultrasonic vibrations to the sonotrode which serves to amplify the amplitude of the ultrasonic wave [59, 62]. Several designs exist for the sonotrode to increase the amplitude; tapered, exponential, and stepped. All designs are based on a decrease in sonotrode cross section which leads to an amplification of the amplitude [59, 63]. As previously mentioned, horn-type transducers are prone to erosion from high powers and low frequencies. Sonotrodes consisting of titanium, vanadium and aluminium alloys or stainless steels are therefore common due to their excellent mechanical and chemical properties [48, 59, 62, 63]. However, probe erosion will still happen if the power is sufficiently high [21]. This can be recognized as small pits on the sonotrode tip. This is shown in Figure 2.6(b).

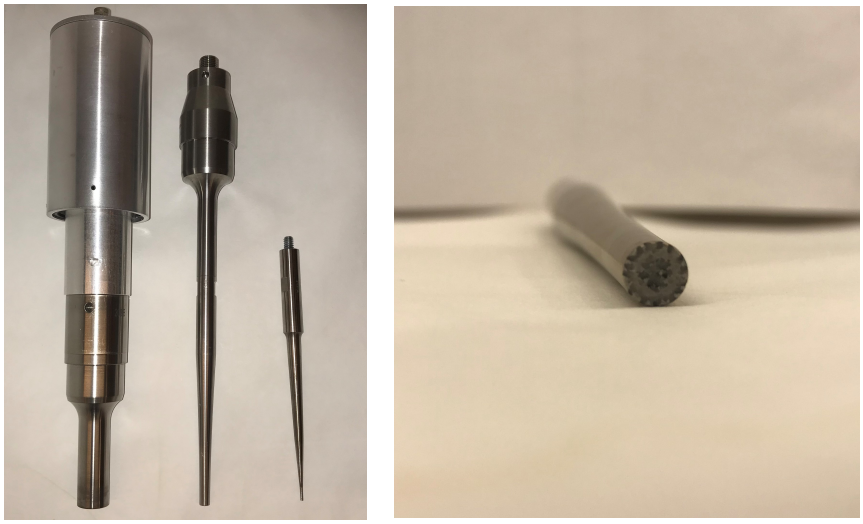

(a) **(b)**

Figure 2.6: Example of horn type sonotrodes with different cross sectional area (a), and how a sonotrode which is damaged by cavitation looks like (b).

For low power ultrasonic cleaning, an ultrasonic cleaning bath is typically used. These consist of a metal tank where an array of transducers have been mounted beneath the bottom of the tank [56, p. 35]. Each transducer transfers its vibrations to the metal plate making up the bottom of the tank which in turn transfers the ultra-

sonic waves to the solution [60]. As such there will be zones located directly above each transducer which have more ultrasonic activity than other parts [60]. This can often be visualized by using a variety of simple tests including the aluminium foil test or the ceramic ring test [60]. Such inhomogenities in the ultrasonic field make ultrasonic baths inherently unreliable for quantitative applications. However, they are very well suited for simple and rapid routine cleaning processes.

When higher frequencies than $100\,\mathrm{kHz}$ are needed, plate transducers are typically used [48, 60]. Nanomaterial synthesis or other chemical ultrasound processes are some of the most common applications for these types of transducers [20]. A plate transducer consists of a single wide transducer connected to an even wider metal plate [48]. The transducer material is typically a ceramic piezoelectric like lead zirconate titanate (PZT) [63, 64]. The transducer transfers its vibrations to the plate which in turn transfers it to the solution [48]. The plate is typically made out of a highly corrosion resistant stainless steel [48, 59, 62, 63]. An example of a plate transducer is shown in Figure 2.7(a). It does not have to be as mechanically stable as a sonotrode due to the higher frequencies and lower powers [60]. Pitting from erosion rarely happens, but it can occur when operated incorrectly. Examples of such operation is exceeding the power limit of the transducer or sonication of incompatible materials. Figure 2.7(b) shows how a damaged plate transducer might look like. This was used above the recommended power limit (50 W) in a chloride rich solution, both of which were discouraged by the manufacturer (Honda Electronics).

2.2.2 Impedance Matching

To limit the losses when electrical signals are converted into mechanical waves, it is important that there is no phase shift in the signal across this boundary [64, 65]. A phase shift in the signal occurs if the impedance of the generator and the transducer is different [64]. The result of such an impedance mismatch is that some part of the forward wave from the signal generator is reflected instead of being transmitted to the transducer [64]. The reflected wave is therefore wasted energy, and can even contribute to damages in the transducer and the signal generator [64].

A signal generator typically operates at $50\,\Omega$, while the impedance of the transducer is frequency dependent and can range from $10\,\Omega$ to $400\,\Omega$ [65, 66]. The lowest impedance of the transducer is achieved at its resonance frequency [61, 64–66]. An ultrasonic transducer should therefore always be operated at or close to its resonance frequency [61, 65, 66]. From equation 2.3 we can see that the resonance frequency of a material is determined by its stiffness and mass. A heavier transducer would therefore have a lower resonance frequency. The impedance at the resonance frequency typically increases with the thickness of the transducer.

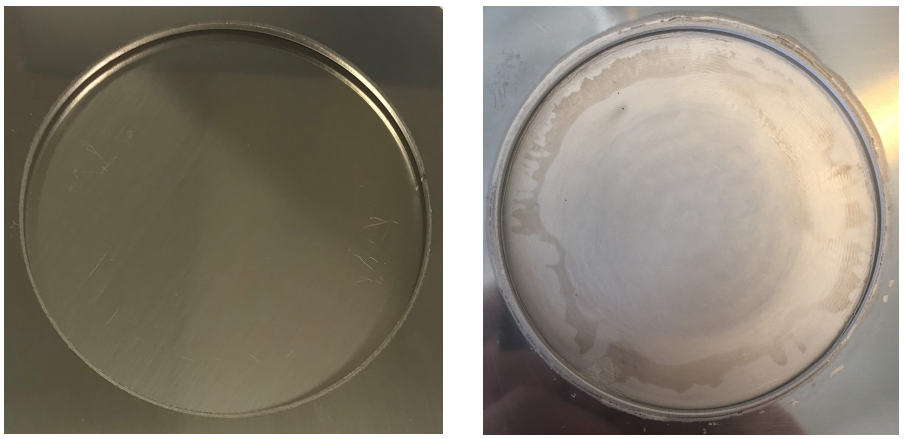

(a) **(b)**

Figure 2.7: Image of a plate transducer (a) and a plate transducer exhibiting signs of pitting and erosion (b). The damages are clear from the circular holes in the plate and the folds in the surface. This particular plate was ruined by sonication of an acidic solution with a high chloride concentration. The material is not compatible with high chloride concentrations.

Switching between transducers with different resonance frequencies will therefore also change the degree of impedance mismatch. The ultrasonic amplitude of the resulting ultrasonic wave will therefore not necessarily be the same for two different transducers. This is a major problem when comparing transducers and could easily result in incorrect conclusions if one is not aware of the impedance mismatch.

To make sure there is no mismatch between the signal generator and the transducer, an impedance matching circuit can be introduced between the signal generator and the transducer [64–66]. A schematic circuit diagram of an impedance matching unit is provided in Figure 2.8. This piece of circuitry serves to change the impedance of the electrical signal (Z_{S}) to match that of the transducer (Z_{L}). This allows for maximum transfer of electrical signals to ultrasonic waves no matter what resonance frequency the transducer is operated at [61, 65]. Some signal generators, like the AG 1012 RF signal generator from T&C Power Conversion, can also measure how much of its signal that is being reflected by the transducer. Minimizing the reflected wave by choosing appropriate impedance matching will therefore ensure maximum transfer of the electrical signal into a mechanical ultrasonic wave.

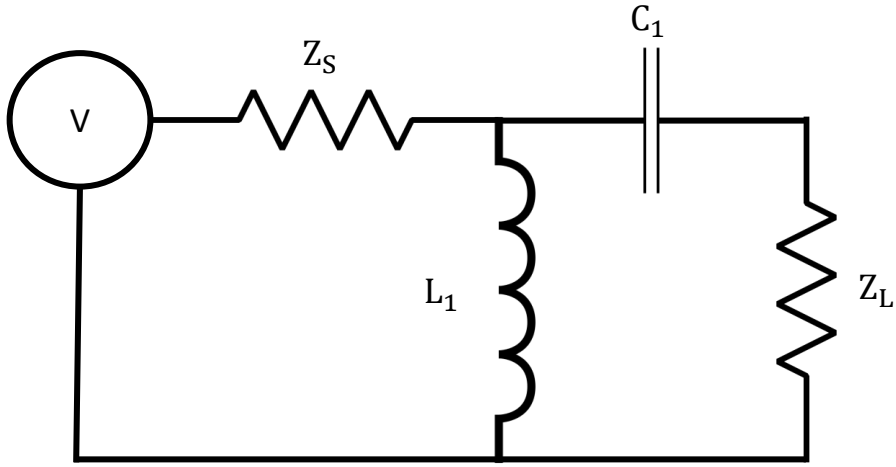

Figure 2.8: Impedance matching circuit diagram showing the signal generator (V) and signal generator impedance (Z_S) connected to the matching circuit. The matching circuit contains an inductor (L_1) in parallel with a capacitor (C_1). The impedance of the transducer (Z_L) is then connected to the matching circuit [65].

2.2.3 Direct and Indirect Sonication

Even though the ultrasonic signal transfer from generator to transducer can occur with minimal losses, it will still be subject to attenuation throughout the reactor volume by various loss mechanisms [48]. The most apparent impact comes when comparing direct and indirect sonication. For direct sonication the target solution is in direct contact with the ultrasonic transducer plate/sonotrode. As such, the ultrasonic wave may travel practically unhindered by the aqueous solution over the entire solution height. This follows from the small value of the attenuation coefficient for aqueous solutions presented in Section 2.1.2.

Indirect sonication is when the target solution is separated from the ultrasonic transducer plate/sonotrode by a partition in which no exchange of contents can occur [48]. This is usually done to protect either the transducer plate/sonotrode from the target solution or vice versa. For the ultrasonic wave to interact with the target solution, it has to be transmitted through the partition. The degree of re-

flection (and transmission) from one medium to another is determined by equation 2.7. However, seeing as the partition is simply a separation between two aqueous media, the expression must be modified to include the thickness (l) of the partition and the wavelength (λ) of the acoustic wave in the partition [48].

$$R = \frac{(\rho_1 v_1 - \rho_2 v_2)^2}{4\cot^2\left(\frac{2\pi l}{\lambda}\right) + (\rho_1 v_1 + \rho_2 v_2)^2} \tag{2.9}$$

If the transmission of the ultrasonic wave through the partition is to be optimized (R = 0), the thickness of the partition must be equal to $l = \frac{n\lambda}{2}$ [48, 64]. To minimize transmission, the thickness of the partition must be equal to $l = \frac{(2n-1)\lambda}{4}$ [48]. The expression is then reduced to that of equation 2.7.

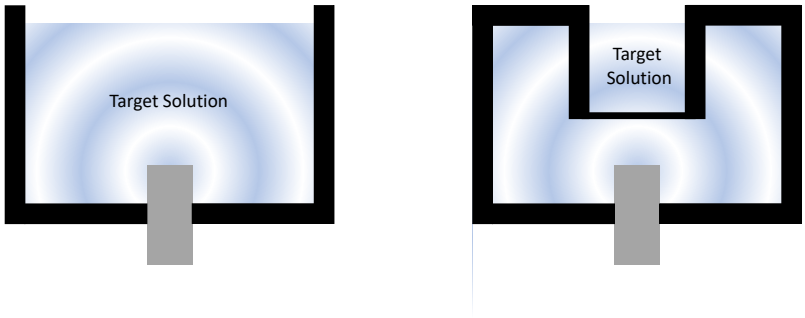

Figure 2.9: Illustration of direct (a) and indirect (b) sonication. The utrasonic waves are unhindered for sonication and can reach the target solution with limited attenuation. For indirect sonication, the partion between the sonotrode and the target solution may cause severe attenuation of the wave.

For a partition made of pyrex glass, we recall from Section 2.1.3 that the reflection ratio from water to pyrex glass was found to be 0.62. This means that the intensity of the ultrasonic wave transmitted to the target solution inside a pyrex beaker can vary from $100\,\%$-$38\,\%$ of its initial intensity. It is all dependent on the thickness of the bottom of the beaker and the frequency of the ultrasonic wave. For a simple ultrasonic bath with a frequency of $42\,\mathrm{kHz}$ maximum transmission would therefore occur at a partition thickness of $6.7\,\mathrm{cm}$. Minimum transmission would occur at $3.35\,\mathrm{cm}$. However, even though the difference between the maximum and minimum is rather large, the cotangens function rapidly decreases from infinity moving away from π.

If the frequency was increased to $346\,\mathrm{kHz}$, the situation would change. The thicknesses required for maximum and minimum transmission is now $2\,\mathrm{mm}$ and $1\,\mathrm{mm}$, respectively. A single millimeter difference in the partition thickness can reduce the wave intensity from $100\,\%$ to $38\,\%$. Indirect sonication at higher ultrasonic frequencies therefore becomes exceedingly more difficult to control. Imperfections in the partition emerging over continued use, exposure to chemicals or other types of wear and tear would inevitably alter its thickness. Achieving reproducibility from one experiment to the next would therefore be impossible due to a change in the transmission properties. The issue becomes even more complicated when considering experiments where different frequencies are compared. In those cases the partition thickness of the reactor would have to be custom made for each frequency with such accuracy that the transmission would be the same for all.

2.2.4 Cavitation

When low intensity acoustic plane waves pass through water, there is practically no attenuation of the intensity as described by equation 2.6 in Section 2.1.2. However, for high intensity ultrasonic waves, new interactions between the sound wave and the medium will begin to take effect. These interactions arise as a result of non-linearity in the ultrasonic waves [67]. One of these interactions is referred to as cavitation, and it leads to a loss of wave intensity (energy) along the ultrasonic wave [20]. As a consequence of the non-linearity of the ultrasonic waves, both acoustic streaming and heat transfer phenomena are both interacting with the cavitation event [67, 68]. However, to provide estimates of the trends caused by cavitation, the non-linear interactions will be disregarded going forward.

When preparing an aqueous solution, the solution may look homogeneous to the naked eye. In reality, however, the solution contains dissolved gas nuclei [19]. When a high intensity ultrasonic wave passes through the aqueous solution, these gas bubbles will be affected by the compression and rarefaction imposed by the ultrasonic waves on the propagation medium [19, 20]. In the rarefaction cycle, the bubble expands due to the low local pressure. As a result, a pressure gradient between the bubble interior and aqueous solution will arise which leads to diffusion of gas into the bubble to equalize the pressure [19]. In the compression cycle, the bubble is compressed due to the high local pressure. Consequently, gas will diffuse out to counter the new pressure gradient. However, for each ultrasonic cycle, there is a net growth of the gas bubble due to a phenomenon known as rectified diffusion [19]. Upon expansion of the gas bubble, the surface area also increases which promotes diffusion of gases into the bubble. This area effect is therefore one of the reasons why more gas enters the bubble compared to what leaves the bubble. Another reason is referred to as the shell effect [19]. As the bubble expands the water shell around the bubble decreases in thickness which

also promotes diffusion. The combined effect of the area effect and the shell effect therefore leads to rectified diffusion and results in a gradual growth of the gas bubbles for every ultrasound cycle [19].

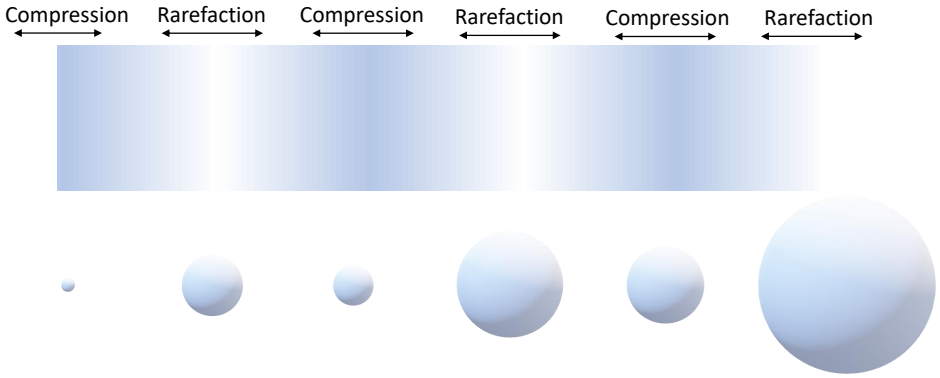

Figure 2.10: Growth of a cavitation bubble over several compression and rarefaction cycles. For every cycle there is a net growth in size due to rectified diffusion caused by the area- and shell-effect.

The bubble will continue to grow until it reaches its resonance size at which point it continues to expand during the rarefaction cycle before collapsing violently during the compression cycle [36, 69]. The process of bubble growth and collapse by ultrasonic waves consumes energy and the process is called cavitation. Such bubbles are therefore referred to as cavitation bubbles. The resonance size, as well as the maximum bubble size, is determined by the frequency of the ultrasonic wave with lower frequencies producing larger resonance- and maximum bubble sizes [69, 70]. The lower the ultrasonic frequency the more time the bubble has to expand during the final rarefaction phase. More comprehensive descriptions of the resonance size of cavitation bubbles exists, but for the purposes of this thesis, only the general trends are examined [68].

Pressure

The abrupt change in the bubble volume upon collapse happens on the scale of micro seconds [70]. The process can therefore be considered adiabatic, meaning no heat is lost to the surroundings upon collapse [36]. As no heat is lost during the compression, the final pressure (P) can be calculated from the change in volume

before (V_0) and after (V) the compression and the pressure in the bubble before collapse (P_0)

$$P = P_0 \left(\frac{V_0}{V}\right)^{\gamma} = P_0 \left(\frac{r_0}{r}\right)^{3\gamma} \tag{2.10}$$

where

$$\gamma = \frac{C_{\mathrm{P}}}{C_{\mathrm{V}}} = \frac{f+2}{f} \tag{2.11}$$

where C_{P} and C_{V} are the specific heats at constant pressure and volume, respectively, and f is the degrees of freedom of the gas molecules. Monoatomic gases have 3 degrees of freedom and diatomic gases have 5.

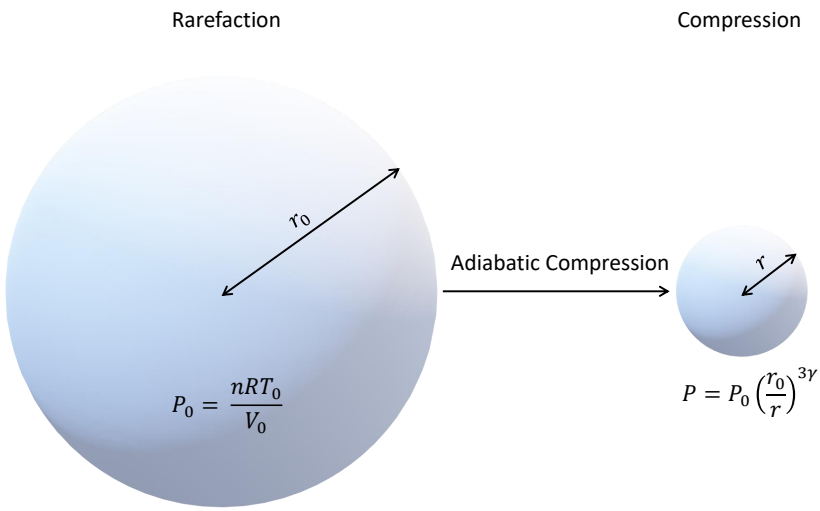

Figure 2.11: Illustration of the final rarefaction cycle and the following collapse during the compression phase. Equations describing the pressure and temperature upon collapse is included.

Merounai et al. [36] have simulated the bubble collapse of cavitation bubbles and

calculated the change in the bubble radius from its maximum to its minimum. They found that the pressure in the bubble can reach over $1000\,\mathrm{atm}$.

Shock Waves

The release of this pressure leads to the formation of a violent shock wave traveling out from the bubble center. The shock wave has been estimated to travel with hundreds of meters per second [36]. However, the wave is rapidly attenuated as it moves spherically outward from the bubble center [56, pp. 30–31].

If cavitation occurs close to a solid surface larger than the cavitation bubble, the cavitation will be asymmetrical [24]. As a result, a microjet forms which is directed towards the surface [56, pp. 30–31]. A concentrated movement of liquid being directed towards a surface with the velocity of the previously mentioned shock waves has the potential to erode the surface. In addition to being the governing mechanism for how ultrasonic cleaning takes place, microjet formation is also the reason for the unwanted erosion mechanisms explained in Section 2.2.3.

The velocity of the microjet (and shock wave) is determined by the final pressure attained during the collapse [36]. A higher pressure means faster microjets. From equation 2.10, a greater pressure arises for greater differences between the maximum and minimum bubble size. As previously explained, the maximum bubble size is achieved during the final rarefaction cycle. This means that larger bubble sizes are achieved when the rarefaction cycle takes longer to complete. Lower ultrasonic frequencies therefore provide longer rarefaction cycles, and will therefore create larger bubbles, which lead to higher pressures and therefore faster microjets. Problems with erosion due to microjets are therefore more pronounced at lower ultrasonic frequencies [21].

Temperature

The temperature inside the bubble during cavitation increases in a process known as adiabatic heating [36]. In a simplified approach, the temperature can be estimated considering that the gases follow the ideal gas law, and as such the temperature can be calculated from that.

$$T = \frac{PV}{nR} = \frac{P_0 V \left(\frac{V_0}{V}\right)^{\gamma}}{nR} \tag{2.12}$$

The initial pressure of the bubble is also given by the ideal gas law, and if we assume spherical bubbles with radius r_0 at the maximum bubble radius we can express equation 2.12 as

$$T = T_0 \left(\frac{r_0}{r}\right)^{3(\gamma-1)} \tag{2.13}$$

Merounai et al. [70] have simulated the bubble collapse of cavitation bubbles and calculated the change in the bubble radius from its maximum to its minimum. Using equation 2.13 for a monoatomic gas and assuming a bulk temperature of $298\,\mathrm{K}$, the resulting temperature within the bubble was found to be $5300\,\mathrm{K}$. This is comparable to the temperature of the sun.

The cooling rate of these extreme temperatures has been estimated to be $10^{10}\,\mathrm{K\,s^{-1}}$ due to the bulk solution still being kept at ambient temperatures [56, p. 25]. However, during the cooling, there will be a temperature gradient extending out of the collapsed core into the solution over a distance of about $200\,\mathrm{nm}$ as illustrated in Figure 2.12 [71]. This region is referred to as the hot-shell region and will be heated to temperatures of around $1900\,\mathrm{K}$ [71].

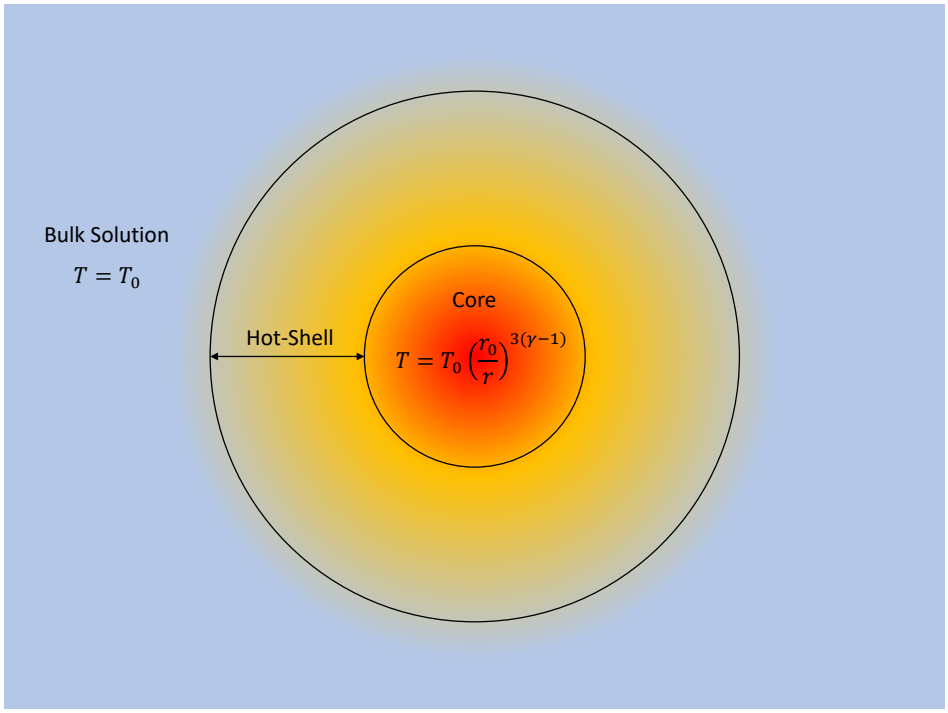

Figure 2.12: Illustration of the temperature profile from the core of the collapsing bubble, through the surrounding hot-shell region, and finally in the bulk solution.

Bjerknes Forces

Cavitation bubbles are subject to several forces including gravity, buoyancy and drag. When an ultrasonic standing wave field is applied to an aqueous solution, additional forces are introduced which all affect the gas bubbles. If the wavelength of the resulting standing wave is much greater than the gas bubble, the pressure difference between the inside of the bubble and the antinodes will drive the bubbles towards the antinodes as illustrated in Figure 2.13 [72]. This force is called the primary Bjerknes force (F_p) and it is dependent on the ultrasonic frequency (f) and acoustic power (P_a) [72].

$$F_p = V P_\mathrm{a} A \frac{2\pi f}{v} \sin \frac{4\pi f x}{v} \tag{2.14}$$

V is the bubble volume, v is the speed of sound in the aqueous solution ($1482\,\mathrm{m\,s^{-1}}$ in deionized water), and x is the position along the ultrasonic wave. A is an acoustic factor, which is negative for bubbles and positive for solid particles. This means that the primary Bjerknes force will direct bubbles towards the antinodes [72]. The primary Bjerknes forces therefore help to position the gas bubbles at the antinodes where they can be subject to compression and rarefaction until they reach their critical size and collapse.

From the expression in Equation 2.14, the primary Bjerknes force increases with increasing ultrasonic power. The increased Bjerknes force therefore makes sure that more bubbles reach the antinode where they can cavitate which is in line with what is observed experimentally in that increased ultrasonic power tends to increase the radical formation rate [32, 69, 73]. The two other factors which affect the magnitude of the primary Bjerknes force is the bubble volume and the ultrasonic frequency. A bubble will only be able to cavitate if it is smaller than the critical bubble size [69]. The critical bubble size is inversely proportional to the applied frequency which means that the maximum bubble size is limited by the frequency [32]. The primary Bjerknes force close to cavitation will therefore be proportional to the ultrasonic power, and inversely proportional to the frequency squared [32].

$$F_p \propto \frac{P}{f^2} \tag{2.15}$$

As a result, the primary Bjerknes force is stronger at lower frequencies and higher ultrasonic powers.

When two bubbles are oscillating in phase as they do under ultrasonic cavitation

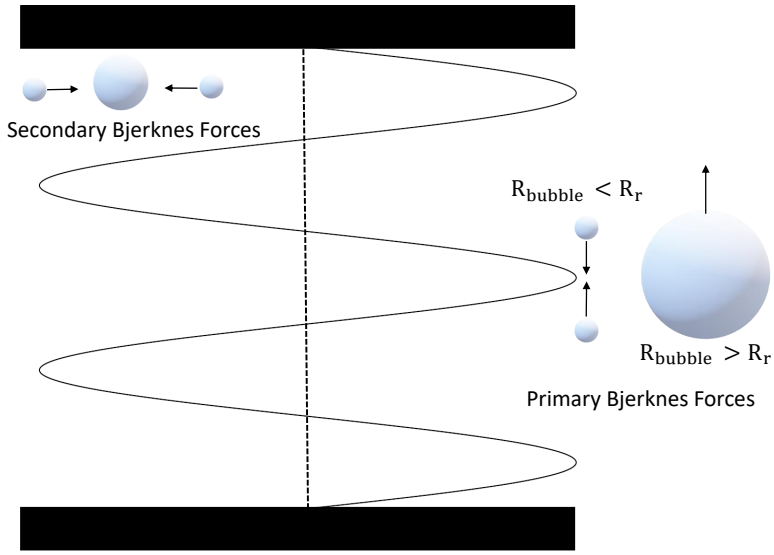

Figure 2.13: Schematic illustration of primary and secondary Bjerknes forces in a standing wave field. Bubbles smaller than the critical bubble size are forced towards the antinodes by primary Bjerknes forces. Cavitating bubbles will also exert an attractive force on each other as a result of secondary Bjerknes forces. This may lead to bubble coalescence if the distance between bubbles is short. Bubbles larger than the critical bubble size are also expelled from the antinodes by primary Bjerknes forces.

there is an attractive force acting between the two bubbles which is called the secondary Bjerknes force [32, 72, 73]. The secondary Bjerknes force (F_s) is also dependent on the ultrasonic power (P), bubble volume (V) and ultrasonic frequency (f), but it is also dependent on the separation between the bubbles (d) [72].

$$F_s \propto (fP)^2 \frac{V_1 V_2}{d^2} \tag{2.16}$$

For two bubbles close to the resonance frequency we can once again use the assumption that the bubble size is inversely proportional to the ultrasonic frequency which results in a simplified expression for the secondary Bjerknes force.

$$F_s \propto \left(\frac{P}{f^2}\right)^2 \frac{1}{d^2} \tag{2.17}$$

At resonance the secondary Bjerknes force also increases with decreasing frequency and increased ultrasonic power [32]. When the secondary Bjerknes forces increase they will lead to more rapid coalescence of smaller bubbles into a larger bubble as illustrated in Figure 2.13 [32, 73]. This has also been found experimentally [74, 75]. If this larger bubble exceeds the critical size for cavitation the acoustic factor (A) in equation 2.14 changes sign and the bubble is expelled from the antinodes [32, 72, 73]. It is rendered useless as a cavitation bubble and is essentially just degassing of the solution. An increase in the secondary Bjerknes forces is therefore not desired.

2.3 Sonochemistry and Current Development

The extreme temperatures and pressures achieved during cavitation are known to produce intense shock waves, microjets and acoustic streaming [19, 20, 76]. These phenomena are all occurring outside the collapsed bubble, but the high temperatures also have an impact on the contents of the bubble. After all, a bubble is a collection of gas in the liquid, so this gas must also be affected by the high temperatures which are comparable to that of the sun. When discussing rectified diffusion in Section 2.2.4, it was mentioned that the bubble growth happens when gas diffuses into the bubble during the rarefaction cycle. This gas consists of any atmospheric gas trapped in the solution, a saturation gas deliberately added to the system, and water vapour from the aqueous solution itself [19]. The gas mixture trapped in the caviation bubble upon collapse will experience a temperature of about $5000\,\mathrm{K}$ which is sufficient to cleave the bonds of any gas molecule in its vicinity. Monoatomic gases are the only gas species that are unaffected as there are no bonds to break [36, 77]. A large amount of the gas present in the cavitation bubbles is water vapour, and as such, H_2O will be cleaved upon collapse [20]. This process is called sonolysis and the result is a generation of highly reactive ·H radicals and ·OH radicals [20].

$$\mathrm{H_2O}))) \cdot \mathrm{H} + \cdot \mathrm{OH} \tag{2.18}$$

The instability of these radicals can be exploited to drive a range of chemical reactions. Utilizing the chemical effects of ultrasound is therefore referred to as sonochemistry.

2.3.1 Historical Perspective of Sonochemistry

Sonochemistry emerged from the development of the ultrasonic transducer by Langevin in 1917 [78]. His intentions for the transducer was to use it to detect submarines. A decade later Wood and Loomis [78] used the Langevin transducer to investigate the physical and biological effects on oil solutions. They observed increased temperatures, smoke generation, and degradation of biological material. Richards and Loomis [57] further went on to investigate the chemical effects arising from sonication and found that some chemical reactions are accelerated. The chemical effects arising from ultrasound were first attributed to the formation of free radicals by Alexander and Fox [79] in 1954. This was shown through H_2O_2 detection and iodine oxidation in an ultrasonic system.

With the established hypothesis of free radical generation by ultrasound, Weissler [80] investigated acrylamide, formic acid, and allylthiourea as potential radical scavengers a few years later. He found that a radical scavenger can be efficient even though it is not volatile, and that the ·OH must be an intermediate in the sonochemical formation of H_2O_2.

Further characterization of the radical formation through ultrasound by H_2O_2 detection was performed by a number of groups after that [33, 81–87]. Most notably perhaps is the Henglein group, which through their work specialized in detection of scavenger decomposition products formed under ultrasonic irradiation. A range of scavengers including formic acid [84], iodide [87], bromide, azide, methanol [82], ethanol [33], glycol, t-butanol, polyvinyl(pyrrolidone) [88], tetranitromethane, and many more organic species were investigated. Much of the knowledge regarding how scavengers interact with the cavitation bubbles, and where radical reactions occur can be traced back to their work through the 1980s and 1990s. Suslick and Hammerton [89] also showed that sonochemical reactions also takes place in the hot-shell surrounding the collapsing bubbles. They also went on to determine the temperature of the hot-spot as well as the temperature and thickness of the surrounding liquid hot-shell [71].

The increased knowledge regarding the mechanisms of sonochemistry initiated a new wave of research into the use of ultrasound for nanoparticle synthesis. One of the most prominent figures of this type of research is Professor Ashokkumar. From the late 1990s to present day, his group has been investigating how different ultrasound parameters affect nanoparticle nucleation and growth as well as cavitation dynamics [1, 31, 34, 38, 90, 91]. Especially the work of Okitsu et al. [1] demonstrated the benefit of using ultrasound for nanoparticle synthesis. In their work they showed how the ultrasonic frequency can be used to tailor the particle size of gold nanoparticles.

Even though many of the core mechanisms of sonochemistry have been elucidated, there are still open questions regarding radical interactions, how to improve reduction rates, scavenger precursor interactions, and scalability. These issues need to be tackled if sonochemistry is to challenge traditional chemical reduction methods as the go-to method for industrial scale nanoparticle synthesis.

2.3.2 Sonochemical Synthesis

The highly unstable radicals from sonolysis will not remain unaffected in solution too long after their generation [92]. The ·H radical is desperate to lose its newly acquired electron while the ·OH radical is craving an extra electron to become stable. In a solution containing nothing but water, the radicals will simply recombine with each other [80].

$$\cdot \mathrm{OH} + \cdot \mathrm{OH} \rightarrow \mathrm{H_2O_2} \tag{2.19}$$

$$\cdot \mathrm{H} + \cdot \mathrm{H} \rightarrow \mathrm{H_2} \tag{2.20}$$

$$\cdot \mathrm{OH} + \cdot \mathrm{H} \rightarrow \mathrm{H_2O} \tag{2.21}$$

Most of the recombination takes place in the hot-shell region surrounding the collapsed bubble [33, 87]. However, the radicals which escape into the bulk solution will eventually succumb to recombination as well [87]. Aqueous solutions containing additional species other than water, also has a probability of reacting with the radicals. The ·H radical will drive reduction reactions and the ·OH radicals will perform oxidation reactions [93].

However, most of the radicals already recombine in the hot-shell and their potential as redox species is lost when this happens. If the sonochemical reactions are to be optimized, all generated radicals should be utilized. The hot-shell therefore needs to be preferentially occupied by the reacting species. The cavitation bubbles are in a unique position regarding such preferential occupation as they exhibit a water-gas interface. Reacting species which are hydrophobic will therefore readily adsorb to this interface and be inside the hot-shell when the bubble collapses [33]. Not all target species have hydrophobic properties so in order to take advantage of all generated radicals, a radical scavenger must be used.

A radical scavenger serves to convert the highly unstable primary radicals to more stable, less reactive secondary radicals [26]. The scavenger collects the primary radicals typically through hydrogen abstraction by the primary radicals [20, 35].

The primary radical is then fully stabilized, while the scavenger is converted into the secondary radical [20, 26].

$$\cdot \mathrm{OH}(\cdot \mathrm{H}) + \mathrm{RH} \rightarrow \mathrm{H_2O}(\mathrm{H_2}) + \cdot \mathrm{R} \tag{2.22}$$

A secondary radical has a much longer lifetime than a primary radical as it is more stabilized by the other bonds in its molecule, whereas the ·OH radical and the ·H radical does not have access to such stabilization. Therefore, the secondary radicals will have time to diffuse out into the rest of the solution and react with the actual target species (M^n) [20, 26].

$$\cdot \mathrm{R} + \mathrm{M}^n \rightarrow \mathrm{R}' + \mathrm{M}^{n-1} \tag{2.23}$$

Through this reduction reaction, the secondary radical is oxidized to a stable compound (R′), while the target species is reduced to a lower oxidation state (M^{n-1}). The use of scavengers in sonochemical synthesis will be presented in detail in section 2.3.3.

When sonochemistry is being used for synthesis purposes, a scavenger is necessary to ensure sufficient reduction rates. This is because the yield of primary radicals is very low with rates on the order of 10-20 $\mu\mathrm{mol\,dm^{-3}\,min^{-1}}$ [26–30]. The scavenger ensures that fewer radicals are lost to recombination. In order to increase the yield of primary radicals per cavitation bubble, a higher collapse temperature should be achieved [36]. The higher the collapse temperature, the more water bonds are cleaved which results in more primary radicals [36]. From equation 2.13 there are several parameters which controls the collapse temperature, the most important ones being the compression ratio (r_0/r) and the polytropic ratio (γ). Achieving higher primary radical yields is therefore all about maximizing the collapse temperature through careful consideration of the ultrasound parameters. These parameters will be presented systematically in section 2.3.3.

With the basic understanding of how sonochemical synthesis works, we will now explore how it has been used for synthesizing nanomaterials. We will be focusing on which material systems are the most common in the literature, but also why certain transition metals are glaring with their absence.

A common thread when looking through sonochemical literature is that noble metal synthesis is dominating. Sonochemical synthesis of gold [1, 26, 94], platinum [26–28, 34, 95, 96], palladium [29, 96], silver [26, 30], rhodium [26], and ruthenium [38] constitutes the bulk of the literature. However, some papers are

also concerned with the synthesis of other transition metals such as nickel [97–99], iron [71, 97, 99], and cobalt [98, 100, 101].

Gold Nanoparticles

For the sonochemical synthesis of Au-nanoparticles, a wide range of frequencies, powers, and radical scavengers have been used. The work of Okitsu et al. [1] showed that adjustments in the ultrasonic frequency enable the tuning of the size of gold nanoparticles between 15 and 30 nm over the entire ultrasonic range (20 kHz - 1100 kHz). Garcia et al. [94] also demonstrated that increasing the acoustic power leads to smaller gold nanoparticles in a 20 kHz setup. Different morphologies were also observed with more facets appearing for higher powers [94].

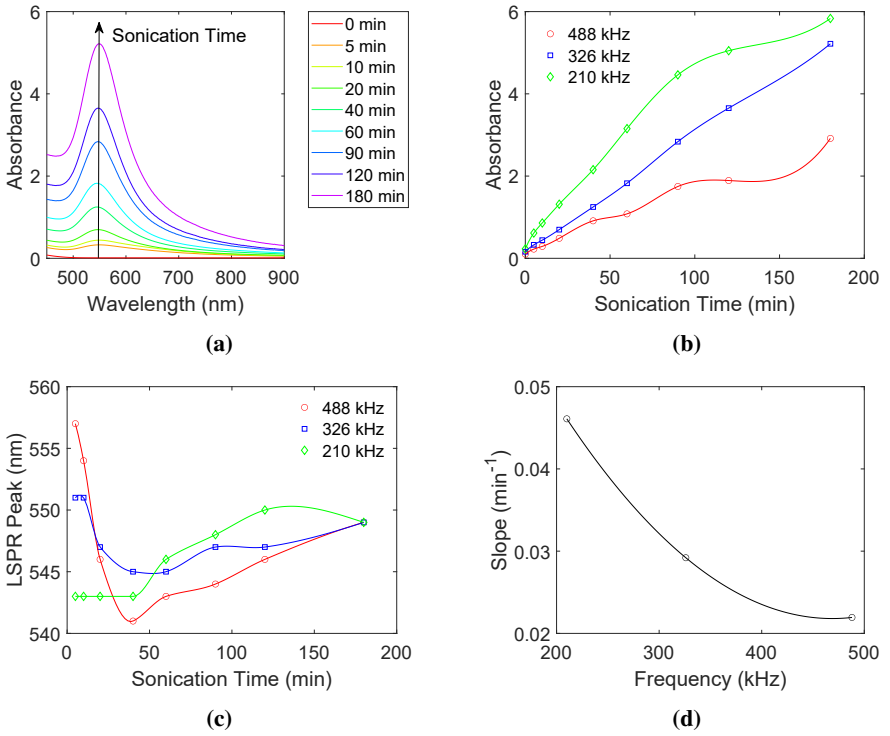

Figure 2.14: Absorbance spectra of sonochemically synthesized Au-nanoparticles at different sonication times with ethanol ($0.8\,\mathrm{mol\,dm^{-3}}$) as the radical scavenger using an ultrasonic frequency of 326 kHz and an acoustic power of 11.8 W (2.14(a)). The absorbance profiles (2.14(b)) and LSPR peak values (2.14(c)) are plotted as a function of sonication time for multiple ultrasonic frequencies. The slope of the resulting absorbance profiles are also plotted as a function of ultrasonic frequency (2.14(d)).

As for the use of radical scavengers, the sonochemical synthesis of Au-nanoparticles is quite versatile. 1-propanol [1], 1-butanol [22], polyvinylpyrrolidone (PVP), sodium dodecylsulfate (SDS), polyoxyethylenesorbitan monolaurate (Tween20), polyethylene glycol monostearate (PEG) [26], and trisodium citrate [94] have all been successfully used to produce gold nanoparticles sonochemically. This is because the reduction of Au(III) to Au-nanoparticles can occur through reactions with pyrolytic decomposition products as explained by Okitsu et al. [22, 26]. Radical scavengers close to the collapsing bubble will decompose into reactive species such as methyl radicals ($\cdot CH_3$) which can react further with metal precursors. Reduction by pyrolytic decomposition products was confirmed by the much higher formation rate of Au-nanoparticles compared to the generation of primary radicals [22, 26]. The sonochemical reduction of Au(III) to metallic nanoparticles occurs via Au(II) and Au(I) through one-electron reactions with reducing radicals (R·) [22]. This can be summarized as

$$\mathrm{Au(III)} + 3\mathrm{R}\cdot \rightarrow \mathrm{Au} + 3\mathrm{R}' \tag{2.24}$$

where R′ is the oxidized version of the scavenger. Our own work on sonochemical synthesis of Au nanoparticles (Figure 2.14) are in agreement with the results obtained by Okitsu et al. [1]. Higher reduction rates were observed at 210 kHz with a decreasing rate observed when going to higher frequencies (Figure 2.14(d)). We also observed an initial decrease in the localized surface plasmon resonance (LSPR) peak similar to Garcia et al. [94] up to about 60 min of sonication (Figure 2.14(b)). However, prolonged sonication after 60 min caused the LSPR-peak to shift to much higher wavelengths either due to enhanced growth or agglomeration.

Platinum Nanoparticles

Sonochemical synthesis of Pt-nanoparticles is probably one of the most explored material systems in sonochemistry [26–28, 34, 95, 96]. The ease of monitoring the development of Pt(IV) and Pt(II) through colorimetric detection with UV-visible spectroscopy also means there is an abundance of information regarding reaction rates [26–28]. The working principle of this colorimetric technique is to form PtI_6^{2-} and PtI_4^{2-} which have a strong absorbance peak at 490 nm (ϵ = $11\,170\,\mathrm{dm^3\,mol^{-1}\,cm^{-1}}$) and 388 nm ($\epsilon$ = $4600\,\mathrm{dm^3\,mol^{-1}\,cm^{-1}}$), respectively [23, 27]. Sodium iodide (NaI) or potassium iodide (KI) added in excess to an aliquot of the Pt-containing solution are typically used as the iodide source [23, 27].

From these colorimetric measurements, the reduction of Pt(IV) to Pt(II) has been identified to be a first order reaction [28]. Similarly to the sonochemical reduction

of Au(III), the reduction of Pt(IV) to Pt(II) is also aided by pyrolytic decomposition products albeit to a slower extent than Au [26]. However, further reduction of Pt(II) to Pt-nanoparticles appears to be unaffected by pyrolytic decomposition products and relies solely on reactions with secondary radicals [26, 28].

$$\mathrm{Pt(IV)} + 2\mathrm{R}\cdot \rightarrow \mathrm{Pt(II)} + 2\mathrm{R}' \tag{2.25}$$

$$\mathrm{Pt(II)} + 2\mathrm{R}\cdot \rightarrow \mathrm{Pt} + 2\mathrm{R}' \tag{2.26}$$

This is apparent from the linear increase in Pt-nanoparticle formation which mimics that of the primary radical formation [27, 28]. The reduction rate is also considerably slower than the reduction of Pt(IV) to Pt(II), and is comparable to the formation rate of primary radicals [28]. Our results are also in good agreement with these observations as can be seen in Figure 2.15.

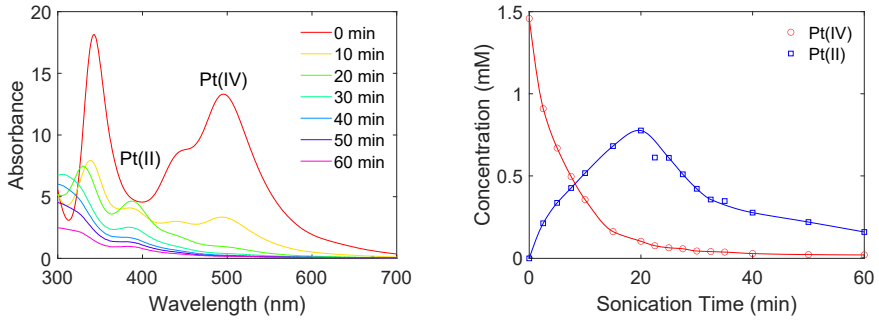

(a) **(b)**

Figure 2.15: Absorbance spectra Pt(IV) and Pt(II) at different sonication times with ethanol ($0.8\,\mathrm{mol\,dm^{-3}}$) as the radical scavenger (2.15(a)) using an ultrasonic frequency of 488 kHz and an acoustic power of 70 W. The resulting concentration profiles of Pt(IV) and Pt(II) are also plotted (2.15(b)).

Silver Nanoparticles

The emerging LSPR peak in the absorbance spectrum of silver nanoparticles makes it easy to monitor changes in the nanoparticle formation during synthesis as can be seen from the absorbance spectra in Figure 2.16(a). UV-Visible spectroscopy measurements have therefore been essential in most of the work on sonochemical synthesis of Ag-nanoparticles in the literature [30, 102]. The LSPR peak is dependent on the size of the Ag-nanoparticles and is located at wavelengths between

400 - 500 nm [103]. This correlation is plotted in Figure 2.16(b). The sonochemical reduction of Ag(I) to Ag-nanoparticles is a simple one electron transfer which readily proceeds through reactions with secondary radicals (·R) [26].

$$\mathrm{Ag(I)} + \cdot\mathrm{R} \rightarrow \mathrm{Ag} + \mathrm{R}' \tag{2.27}$$

The secondary radical is then converted into an oxidized version of the radical scavenger (R′). Similarly to the reduction of Pt(II) to Pt-nanoparticles, the sonochemical reduction of Ag(I) to Ag-nanoparticles also proceeds through secondary radicals and not pyrolytic decomposition products [26]. In the presence of $8\,\mathrm{mmol\,dm^{-3}}$ SDS the rate of Ag-nanoparticle formation was estimated to be $7\,\mu\mathrm{mol\,dm^{-3}\,min^{-1}}$ for an ·OH-radical formation rate of $20\,\mu\mathrm{mol\,dm^{-3}\,min^{-1}}$ [26]. A similar result was obtained by Nagata et al. [30] in which a Ag-nanoparticle formation rate of $7.4\,\mu\mathrm{mol\,dm^{-3}}$ was found using PEG ($0.4\,\mathrm{mmol\,dm^{-3}}$), Tween20 ($3\,\mathrm{mmol\,dm^{-3}}$), and SDS ($8\,\mathrm{mmol\,dm^{-3}}$) as radical scavengers. They also report that monodisperse Ag-nanoparticles are formed with an average size of $(13 \pm 3)\,\mathrm{nm}$ when using SDS as the radical scavenger. The sonochemical synthesis of Ag-nanoparticles also appear to be quite flexible when it comes to tuning the particle size [102]. This was demonstrated by Yang et al. [102] who showed that increasing the molar ratio of benzyl mercaptan to Ag(I) from 2:1 to 15:1 decreased the particle size from $10.4\,\mathrm{nm}$ to $1.4\,\mathrm{nm}$. Changes in Ag-nanoparticle sizes during a synthesis can also be monitored by observing the peak position of the LSPR peak (Figure 2.16). Paramelle et al. [103] correlated the LSPR peak position of Ag-nanoparticles to the particle size and found the relationship shown in Figure 2.16(b).

Palladium Nanoparticles

Sonochemical synthesis of palladium nanoparticles has displayed some of the highest reduction rates among the noble metals [26]. In the presence of surfactants such as PVP, SDS, Tween20, and PEG, the nanoparticle formation rate was found to be 87-$400\,\mu\mathrm{mol\,dm^{-3}\,min^{-1}}$ [29]. This is much higher than the rate of ·OH formation that was measured to $20\,\mu\mathrm{mol\,dm^{-3}\,min^{-1}}$ [29]. It is safe to say that contribution of pyrolytic decomposition products also plays a role in the sonochemical reduction of Pd(II) to Pd-nanoparticles. Particle sizes ranging from 4-110 nm have been reported for the sonochemical synthesis of Pd-nanoparticles with the size depending on the scavenger and the initial concentration of Pd(II) [26, 29, 96]. For instance, increasing the initial concentration of Pd(II) from 0.1 - $1\,\mathrm{mmol\,dm^{-3}}$ using SDS as the scavenger was found to increase the particle size from $8.4\,\mathrm{nm}$ to $110\,\mathrm{nm}$ [29].

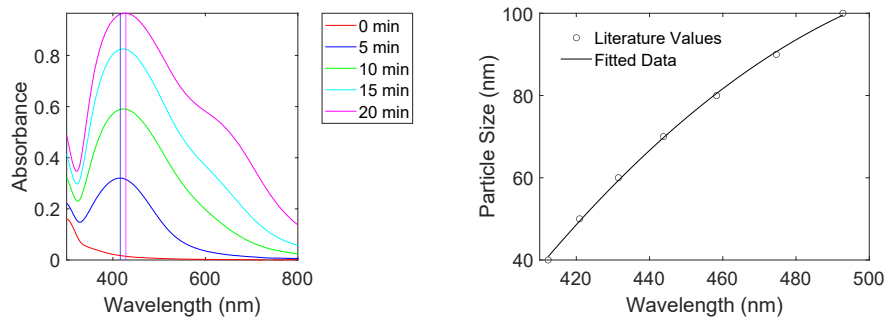

(a) **(b)**

Figure 2.16: Absorbance spectra of sonochemically synthesized Ag-nanoparticles at different sonication times with ethylene glycol ($2\,\mathrm{mol\,dm^{-3}}$) as the radical scavenger (2.16(a)). LSPR peak shifts from 416 to 428 nm for sonication times of 5 and 20 min, respectively, are indicated in the figure. The correlation between the LSPR peak position and the size of the Ag-nanoparticles found by Paramelle et al. [103] is also provided (2.16(b)).

Ruthenium Nanoparticles

Few studies have been performed on the sonochemical synthesis of ruthenium nanoparticles, probably owing to its very slow formation rate [38]. He et al. [38] showed that complete reduction of $1\,\mathrm{mmol\,dm^{-3}}$ Ru(III) to Ru-nanoparticles in the presence of $8\,\mathrm{mmol\,dm^{-3}}$ SDS and $80\,\mathrm{mmol\,dm^{-3}}$ propanol takes around 13 hours, with a reduction rate $< 1\,\mu\mathrm{mol\,dm^{-3}\,min^{-1}}$. They attributed this slow reduction process to sequential one-electron reduction steps. The frequency dependence on the reduction rate was also found to behave similarly to that of Au-nanoparticles with the highest reduction rate observed in the range between 213 and 355 kHz [1].

Other Transition Metals

Much of the work on sonochemical synthesis in the literature has now been presented. However, some noble metals and other transition metals have not yet been mentioned. The reason for this is because studies on the sonochemical synthesis of these transition metals are either quite scarce or absent in the literature.

Sonochemical synthesis of rhodium has been mentioned by Okitsu et al. [26] with the notable observation that the reduction is not possible with SDS, PVP, PEG, Tween20 or any alcohols. Only when sodium formate was used as a scavenger, Rh-nanoparticles was observed. They attributed the reduction to the formation of the highly reducing $\cdot CO_2^-$-radical. The problem with using sodium formate

as a scavenger is that it is not hydrophobic and a very large concentration must therefore be used to avoid the formation of H_2O_2 [104]. In addition, formate itself can act as a reducing agent for certain noble metals like platinum, which defeats the purpose of using ultrasound as the only reducing agent [104].

Another noble metal which has not been reported in the literature is iridium. The reduction of Ir(IV) to Ir(III) proceeds readily, and the peaks belonging to Ir(IV) in the UV-Vis absorbance spectrum almost disappear completely during ultrasonication between 40-60 min as seen in Figure 2.17(a). However, further reduction from Ir(III) to Ir(0) appears to be unfavourable as no change in the absorbance peaks can be detected as seen in Figure 2.17(b). The only change observed in the UV-Vis spectra for Ir(III) belongs to the increasing amount of aldehydes expected through pyrolytic decomposition of ethanol [88].

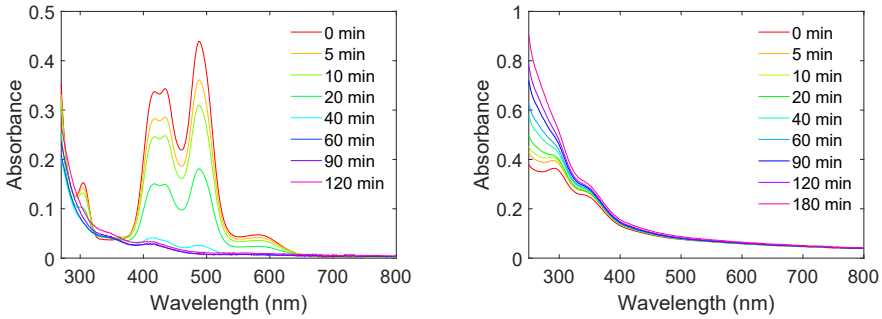

Figure 2.17: Absorbance spectra of Ir(IV) (2.17(a)) and Ir(III) (2.17(b)) for different sonication times using ethanol ($0.8\,\mathrm{mol\,dm^{-3}}$) as the radical scavenger. An ultrasonic frequency of 326 kHz was used with an acoustic power of (38 ± 3) W.

Now that the noble metals have been addressed, we turn our attention to the less expensive common transition metals. The only successful sonochemical synthesis of iron and nickel which exhibits a pure metallic nature was performed with metal carbonyls by Suslick et al. [71]. Use of metal carbonyls in sonochemical synthesis as an alternative to chemical reduction defeats some of the purpose of using a sonochemical route in the first place. First of all, metal carbonyls are extremely toxic following their volatile behaviour, and any HSE department would not touch it with a 10-foot pole. Incidentally, it is the high vapour pressure associated with these metal carbonyls that make them suitable for sonochemical synthesis. The metal carbonyls readily enter the gas phase of the cavitation bubble and the metal carbon bonds are therefore easily cleaved upon cavitation [71]. Secondly, as the metal is already neutral, no reduction is needed, and metal particles readily form.

Kurikka et al. [99] also demonstrated how iron and nickel metal carbonyls can be used to produce $NiFe_2O_4$. To achieve this they employed an O_2-atmosphere during sonication of the carbonyls. NiFe-oxy hydroxides have also been synthesized sonochemically by Lee et al. [97]. They used nickel(II)-acetylacetonate and iron(III)-acetylacetonate as precursors under direct sonication by a 20 kHz horn-type sonicator in an Ar-atmosphere. The resulting product from sonication was found to be metal alkoxides with nickel and iron present as Ni(II) and Fe(III). The sonochemical treatment therefore did not reduce the metal precursors, but instead modified their ligands. That seems to be a trend when attempting to reduce Ni(II) and Fe(II) to their zero-valent state. Similarly to the reduction of Ir(III), these reductions do not appear to be favourable through the sonochemical route. The same can also be said for cobalt which also only appears to be involved in oxide structures [100, 101].

As for the sonochemical synthesis of Cu-nanoparticles, most of the literature also report the formation of oxides such as CuO and Cu_2O [105, 106]. However, metallic Cu can indeed be formed in sonochemical synthesis as we showed in our own work by utilizing sodium formate as the radical scavenger (See paper 3) [13]. The reason why oxides are mostly reported in the literature is probably that metallic Cu readily oxidizes to Cu_2O or CuO upon exposure to air. To solve this we put a protective layer of Pt on the surface of the metallic Cu-nanoparticles through galvanic displacement.

From the present discussion, there appears to be four distinct possibilities for how a sonochemical synthesis proceeds depending on the given transition metal. It can either be fully aided by pyrolytic decomposition and proceed at very high rates exceeding even that of the primary radical formation. It can also proceed at a rate close to the rate of radical formation if only secondary radicals contribute to the reduction. Then there are some elements which are only reduced under the right conditions at a very slow rate. And then there are those elements which do not appear to be suited for sonochemical reduction at all. This has been summarized in a colour coded periodic table for the relevant transition metals in Figure 2.18.

From this figure it becomes apparent that the first-row transition metals are not well suited for sonochemical reduction. One might assume this is because of their low reduction potential, but as iridium (with its high reduction potential) falls into the same category, there must be some other mechanism governing this process. There is also no clear pattern as to which metals can be reduced with the aid of pyrolytic decomposition products. To the best of our knowledge, no explanation to these phenomena have been provided in the literature. Understanding why these differences arise may help improve our understanding of sonochemical mechanisms. As a result, existing sonochemical synthesis routes may be improved, and

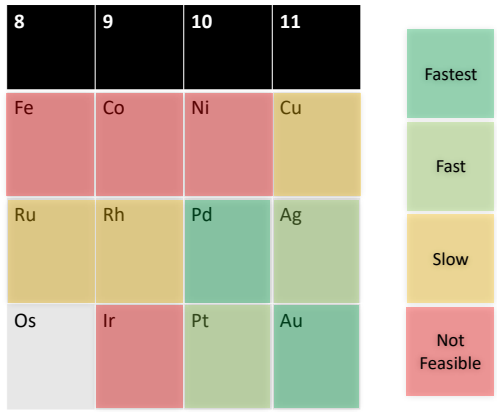

Figure 2.18: Periodic table for a selection of transition metals which are colour coded depending on their behaviour in a sonochemical synthesis. The bright green colour signifies the fastest type of reduction which is aided by pyrolytic decomposition products. The lighter shade of green indicates the elements which are limited by the generation of secondary radicals. The yellow coloured elements belongs to the elements which can be synthesized under the right conditions, but do so very slowly. And finally, the red colour signifies those elements which are not feasible for reduction to metallic nanoparticles through sonochemical synthesis.

new materials can be synthesized.

2.3.3 Ultrasound Parameters

Dissolved Gas

The gas composition of the cavitation bubble is especially important for the bubble collapse. As the collapse occurs adiabatically, the compression at this stage is largely determined by what gas is present inside the bubble. This is reflected by the exponential dependence on the polytropic ratio in the expression for the final cavitation pressure (equation 2.10) and temperature (equation 2.13). The higher the polytropic ratio, the higher the pressure and temperature.

The polytropic ratio is heavily dependent on the degrees of freedom of the gas molecule as shown in equation 2.11. This means that monoatomic gases such as the noble gases have a polytropic ratio of 1.66, while diatomic gases such as O_2 and N_2 have a polytropic ratio of 1.4. If water vapour is the only gas present during

sonication, the polytropic ratio would be even lower as the non-linear triatomic water molecule has 6 degrees of freedom resulting in a polytropic ratio of 1.33. Monoatomic gases can therefore yield higher collapse temperatures and pressures than other gases.

Two of the most common gases in our atmosphere are the diatomic gases nitrogen (N_2) and oxygen (O_2). Solutions exposed to the atmosphere will therefore contain these gases and upon sonication, nitrogen radicals ·N and oxygen radicals ·O will be formed as a result of sonolytic cleaving of their bonds [36]. Both the ·N and the ·O will react with species in the solution and form many different intermediates as described by Merouani et al. [36, 70, 107]. In their work they simulate the effect of dissolved gases on ·OH formation during single-bubble cavitation. The most prominent reaction for the ·O radical is its reaction with water.

$$\cdot\mathrm{O} + \mathrm{H_2O} \rightarrow \ \cdot\mathrm{OH} + \ \cdot\mathrm{OH} \tag{2.28}$$

More ·OH radicals are therefore produced due to the sonolysis of the O_2 itself. From their simulation work, Merouani et al. found that the rate of ·OH radical formation followed the order of Ar > O_2 > air > N_2 > H_2 for frequencies above 515 kHz, and O_2 > air $\sim$ N_2 $\sim$ H_2 > Ar for frequencies below 515 kHz [70]. Our own experimental results for the sonochemical yield from different gases also showed that O_2 gave a higher ·OH formation at 408 kHz compared to Ar (Figure 2.19).

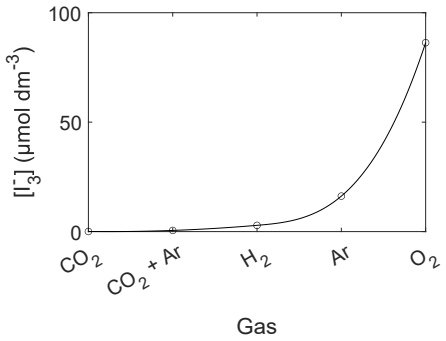

Figure 2.19: Concentration of I_3^- for different saturation gases. Experiments were conducted at 408 kHz with an acoustic power of 53 W. Measurements were taken after 10 min of sonication.

Instead of having polyatomic gases such as N_2 and O_2 in the solution, monoatomic gases such as helium (He), argon (Ar) or xenon (Xe) can be used instead [108,

109]. Not having any bonds to another atom prevents these gases from being cleaved by the extreme conditions inside the cavitation bubbles. Therefore, no radicals are formed from these gases, and we can just consider the sonolysis of water described in Equation 2.18. Another advantage of using monoatomic gases is their higher polytropic ratio (1.66) which results in higher collapse temperatures and therefore a higher generation of primary radicals. Hua et al. [109] demonstrated this by showing that Kr and Ar display a higher ·OH radical and H_2O_2 formation than O_2 in the frequency range between 20 kHz and 513 kHz. They also showed a higher radical yield for Kr > Ar > He. Seeing as the noble gases have the same polytropic ratio, other properties of these gases such as their thermal conductivity and the gas solubility must be evaluated when choosing the most appropriate saturation gas.

A higher thermal conductivity of the gas mixture will result in more dissipation of heat to the surrounding liquid thus reducing the maximum temperature during cavitation [36, 70, 107]. For the gases we have considered so far, Xe ($0.006\,\mathrm{W\,m^{-1}\,K^{-1}}$) < Ar ($0.018\,\mathrm{W\,m^{-1}\,K^{-1}}$) < O_2 ($0.026\,\mathrm{W\,m^{-1}\,K^{-1}}$) $\sim$ N_2 ($0.026\,\mathrm{W\,m^{-1}\,K^{-1}}$) < He ($0.15\,\mathrm{W\,m^{-1}\,K^{-1}}$) [110]. However, Okitsu et al. [108] showed that in real multibubble systems the thermal conductivity does not significantly affect the collapse temperature nor the sonochemical yield at 200 kHz. Instead, the sonochemical yield was found to be directly related to the gas solubility.

Higher gas solubilities result in a higher number of active cavitation bubbles which leads to a higher sonochemical yield, without necessarily affecting the collapse temperature [108]. The solubility order of the aforementioned gases at $20\,^{\circ}\mathrm{C}$ is Xe ($0.58\,\mathrm{g\,dm^{-3}}$) > Ar ($0.059\,\mathrm{g\,dm^{-3}}$) > O_2 ($0.043\,\mathrm{g\,dm^{-3}}$) > N_2 ($0.019\,\mathrm{g\,dm^{-3}}$) > He ($0.0015\,\mathrm{g\,dm^{-3}}$) [110]. It is also important to remember that too many cavitation bubbles may lead to inter-bubble interactions which may reduce the sonochemical activity due to bubble coalescence [111, 112]. CO_2 is an excellent example of a gas with too high gas solubility ($1.69\,\mathrm{g\,dm^{-3}}$) in addition to its low polytropic ratio (1.3) [110]. The very high gas solubility results in bubble coalescence before cavitation can occur [74, 111]. CO_2 is therefore not very effective towards radical generation as is also confirmed experimentally as seen in Figure 2.19.

It is worth noting that the gas solubility is temperature dependent and will decrease with increased temperature. It will therefore decrease the sonochemical yield as well. However, from equation 2.13 higher collapse temperatures results from higher bulk temperatures suggesting that an optimum bulk temperature should exist. Merouani et al. [107] showed that going above $30\,^{\circ}\mathrm{C}$ results in a decrease of sonochemical activity when accounting for these opposing phenomena.

The choice of saturation gas for a sonochemical synthesis should therefore be based on gases with high polytropic ratios to increase the collapse temperature, and a high gas solubility to increase the number of active cavitation bubbles. Self-pyrolysis of the saturation gas as observed for O_2 could also be considered, but this comes at the cost of a lower polytropic ratio. Noble gases has therefore been extensively used in sonochemical synthesis in the literature, with Ar being the preferred choice [1, 26–28, 30, 34, 38, 96]. Ar is cheap and readily available in a common chemistry laboratory, and there is low risk connected to the use of it. Xe would arguably be the better choice due to its much higher gas solubility, but it is also more expensive than Ar.

Other gases have also been employed in sonochemical syntheses [99]. Kurikka et al. [99] successfully synthesized $NiFe_2O_4$-nanoparticles from the respective metal carbonyls using O_2. The reason why oxygen is not widely used in sonochemical synthesis is because of its scavenging properties [80, 85]. In oxygenated solutions, no hydrogen is detected as the oxygen effectively scavenges the ·H radicals which results in the formation of H_2O_2 [85].

$$O_2 + \cdot H \rightarrow \cdot HO_2 \tag{2.29}$$

$$\cdot HO_2 + \cdot HO_2 \rightarrow H_2O_2 + O_2 \tag{2.30}$$

A similar process also appears to occur with secondary radicals under acidic conditions as described by Hart et al. [85].

$$\cdot {CO_2}^- + O_2 \rightarrow CO_2 + \cdot {O_2}^- \tag{2.31}$$

$$\cdot {O_2}^- + \cdot {O_2}^- \rightarrow H_2O_2 + O_2 \tag{2.32}$$

The noble gases do not undergo such scavenging processes which allows the secondary radicals to actually contribute to the reduction of metal ions, whereas O_2 simply results in accumulation of oxidising agents. This can also have its benefits like enhancing the degradation of Bisphenol A as demonstrated by Torres et al. [113]. However, presence of O_2 is generally not desired for sonochemical synthesis of metallic nanoparticles.

Frequency

One of the most significant parameters to control during a sonochemical synthesis is the acoustic frequency. It is directly related to the cavitation events and determines how fast the contraction and rarefaction occur, and by extension also the critical size of the cavitation bubble [69]. It also determines how many antinodes are formed through the cavitation volume as the number of antinodes is determined by the wavelength of the acoustic wave. This was discussed in section 2.1.4. As the ultrasonic range spans three orders of magnitude (20 kHz - 1 MHz), the choice of frequency also allows for a great level of control over the cavitation process.

Slow contraction and rarefaction cycles brought about by low frequency ultrasound allow for a longer expansion time in the final rarefaction cycle leading to a larger bubble size on collapse [69]. Following equation 2.13 and 2.10, a larger collapse size leads to higher collapse pressures and temperatures. The radical yield per bubble is therefore higher at lower frequencies. This has also been shown through single-bubble cavitation simulations by Merouani et al. [36, 70, 107, 114].

Increasing the frequency reduces the duration of the final rarefaction cycle, and therefore results in a smaller bubble size on collapse [69]. However, increasing the frequency also increases the number of active cavitation bubbles which can contribute towards radical formation [1, 69]. An optimum frequency for radical formation should therefore exist. The frequency range between 200-500 kHz has been identified as the optimum range by several groups [1, 38–40].

Okitsu et al. [1] found an optimum frequency of 213 kHz through measurements of the sonochemical reduction rate of Au(III) to gold nanoparticles. He et al. [38] identified the optimum frequency as 355 kHz for the sonochemical reduction of Ru(III) to Ru-nanoparticles. Hua et al. [39] determined the optimum frequency based on sonoluminescence spectra and found 358 kHz to display the highest signal.

A power dependence on the optimum frequency was also found by Asakura et al. [32]. At low acoustic powers (2-5 W), the highest sonochemical efficiency (measured by Weissler dosimetry) was displayed at 209 kHz. Increasing the power (15-25 W) shifted the optimum to 305 kHz. However, in the low acoustic power range (< 10 W), Kanthale et al. [69] demonstrated that the radical yield as measured from H_2O_2 detection, was indistinguishable at 213 kHz, 355 kHz and 647 kHz. From our own measurements we can also see that the rate of H_2O_2 formation is somewhat improved at 210 kHz and 413 kHz compared to the other frequencies when going to higher acoustic powers. This can be seen from the emerging peak at 413 kHz in Figure 2.20. However, the differences between the frequencies in

this range are still very small, and its only at 760 kHz that the rate is consistently lower at all powers.

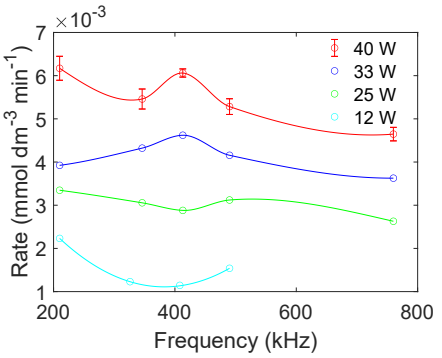

Figure 2.20: Rate of H_2O_2 formation from ultrasound as a function of ultrasonic frequency. The experiments were conducted for acoustic powers between 12 W and 40 W. Lines between datapoints are drawn with spline interpolation to guide the eye.

In the lower frequency range (< 100 kHz), Hua et al. [109] also showed that the radical yield as measured from Weissler dosimetry and terephthalic acid dosimetry increased with increasing frequency (20 kHz - 80 kHz). Moving to higher frequencies (300 kHz - 800 kHz), Torres et al. [113] found that the radical formation measured by H_2O_2 detection was highest at 300 kHz with lower values detected at 500 kHz, 600 kHz, and 800 kHz. They also demonstrated that the degradation of Bisphenol A followed the same trend.

Most of these studies have been concerned with a rather limited frequency range in order to make general conclusion regarding the effect of frequency. Koda et al. [40], however, performed a systematic investigation of the radical yield for nine different frequencies spread out over the entire ultrasonic spectrum (19.5 kHz - 1.2 MHz). They also utilized different setups from four different laboratories, and reported the result as a sonochemical efficiency. Weissler dosimetry and Fricke dosimetry were used to measure the radical formation. They found that the highest sonochemical efficiency is reached between 200 kHz and 500 kHz, and that differences in this frequency range are insignificant. Mark et al. [37] also did a similar investigation in an air-saturated solution at 85 W. They observed a peak at 321 kHz, but looking at their standard deviation, there is no significant difference between 200 kHz and 500 kHz. In our own work we found that the differences in radical formation in this range were also quite small as can be seen from Figure 2.20.

In addition to the chemical effects associated with radical formation, the ultrasonic frequency also affects shock wave pressure and the resulting mechanical effects

during cavitation. Closer examination of equation 2.10 shows that a higher bubble pressure is reached when the critical bubble size is larger. This was confirmed experimentally by McNamara et al. [115] where the shock wave pressure was measured from sonoluminescence spectra. Analogous to the temperature dependence, lower frequencies therefore produce higher pressures as well. The release of this pressure manifests itself as a shock wave emerging from the cavitation bubble [24, 25]. Lower frequencies clearly result in more violent bubble collapses with both higher temperatures and more powerful shock waves. In contrast to the chemical effects of radical formation, however, the shock wave pressure is not dependent on the number of cavitation bubbles, and is monotonically decreasing with increased frequency following equation 2.10. Mechanical effects of ultrasound such as micro jets are therefore more pronounced at lower frequencies [116]. This is the reason why ultrasonic cleaning baths utilize low frequency ultrasound (20 kHz, 42 kHz, 80 kHz), as ultrasonic cleaning takes advantage of the mechanical effects of ultrasound.

In the sonochemical community the main focus on frequency has been concerned with its chemical effects rather than the mechanical ones. This is understandable as sonochemists are interested in optimizing the radical yield. However, in sonochemical synthesis of nanoparticles, the dispersion capabilities of ultrasound may also be of interest as it may affect agglomeration or other growth mechanisms [117]. This is because the mechanical effects induce movement in the sonoreactor [116]. However, only particles which are sufficiently small to not cause asymmetrical collapse of the cavitation bubble will be subject to such acoustic streaming [24, 116]. For microjet formation to occur, particles equal to or larger than the collapsing bubble must be present near the collapsing bubble [24].

Suslick et al. [25] have investigated the shock wave effects of low frequency ultrasound (20 kHz) on the agglomeration of solid zinc particles in a sonoreactor. They found that interparticle collisions caused by the ultrasound shock wave may lead to the fusing of two particles at the point of collision. This assumes that the collision velocity exceeds the threshold (v_c) determined by the melting point (T_m) of the solid particles.

$$v_\mathrm{c} = \sqrt{2}\sqrt{C(T_\mathrm{m} - T_\mathrm{b}) + L} \tag{2.33}$$

C is the specific heat capacity of the solid, T_b is the bulk temperature in the sonoreactor, and L is the heat of fusion of the material. For zinc, this lower threshold was identified to be $728.5\,\mathrm{m\,s^{-1}}$ [25]. The actual velocity (v) reached by the solid particles as a result of the shock wave was found to be dependent on the particle radius (r) [25].

$$v \approx \frac{Pr}{6\eta}\left[1 - \exp\left(-\frac{9\eta\Delta t}{2\rho r^2}\right)\right] \tag{2.34}$$

P is the shock wave pressure, η is the viscosity of the medium, Δt is the duration of the shock wave, and ρ is the density of the particle. Particles smaller than $2.2\,\mu\mathrm{m}$ and larger than $38\,\mu\mathrm{m}$ were not able to reach the critical velocity, and no agglomeration could therefore occur [25].

In our work, we also observed a similar fusing of sonochemically synthesized Au-nanoparticles as seen in Figure 2.21. However, the critical velocity required to fuse these particles together upon impact can not be reached. Gold displaying a higher melting point than Zn results in a higher critical velocity. In addition the higher frequency used in our work (210 - 488 kHz) provides for a less violent shock wave which reduces the particle velocity. Also, our Au-nanoparticles are between 50 and 100 nm in diameter which further decreases the particle velocity. Localized melting of these Au-nanoparticles is therefore not possible according to equation 2.33-2.34. Instead we attributed the attachment of the particles to ultrasound assisted agglomeration which appears to be frequency dependent for frequencies lower than 326 kHz (See paper 2) [23].

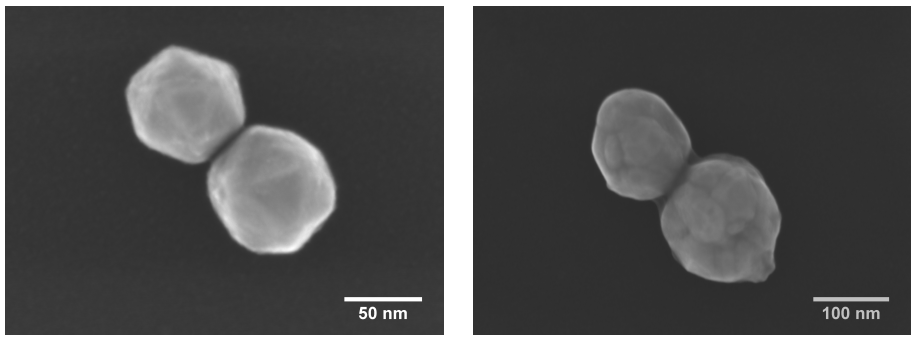

(a) **(b)**

Figure 2.21: Scanning electron microscopy images of Au nanoparticles synthesized sonochemically at 210 kHz (2.21(a)) and 408 kHz (2.21(b)). Necking is only observed for Au nanoparticles at 408 kHz.

The ultrasonic frequency in sonochemical synthesis therefore plays a major role in both the sonochemical generation of radicals and the physical effects determining the dispersion of the particles after they are formed. The impact on both chemical as well as physical effects must therefore be considered when choosing an ultrasonic frequency for a sonochemical synthesis.

Temperature

The collapse temperature of the cavitation bubble is shown to be proportional to the temperature of the bulk solution through equation 2.13. One would therefore assume that the higher the bulk temperature, the higher the yield of primary radicals. However, this is not the case. Increasing the temperature past 30 °C decreases the yield of primary radicals as was shown through single-bubble simulations by Merouani et al. [107]. They explained this by the temperature dependence of the polytropic ratio. When the temperature increases, the vapour pressure of the solution also increases which leads to a higher amount of water vapour in the bubble. Water vapour having a lower polytropic ratio than most common saturation gases will therefore lead to a decrease in the polytropic ratio and consequently also a decrease in the collapse temperature. On the other hand, an increase in the amount of water vapour in the bubbles allows for more radicals to be formed per bubble [107]. An optimal temperature for maximizing radical formation should therefore exist, with the ideal temperature depending on the dissolved gas [107]. Merouani et al. showed through simulations of single bubble systems that the sonochemical radical yield in Ar saturated systems was optimized at a bulk temperature of 30 °C [107].

For multi-bubble systems, the higher solubility of the saturation gas with increasing bulk temperature will also have an effect on the number of cavitation bubbles [108]. From the discussion on dissolved gases, it became clear that a higher gas solubility leads to more cavitation bubbles and a higher radical yield. By increasing the temperature, more cavitation bubbles will therefore form, albeit with a lower collapse temperature. Investigations into the radical formation at different temperatures in real sonochemical systems are somewhat limited. However, Mark et al. [37] measured the ·OH radical yield from H_2O_2 measurements and terephthalate acid dosimetry from 3 °C - 70 °C at 321 kHz, 85 W and using Ar as the saturation gas. They found that the ·OH radical yield decreased monotonically by increasing the temperature. An increase from 3 °C to 20 °C decreased the radical yield to 60 % of the value at 3 °C. They also attribute the decrease in radical yield to a lower polytropic ratio, but also suggest that the compression and rarefaction process is somewhat attenuated due to the higher vapour pressure of the gases inside the cavitation bubble.

On the other hand, there have also been examples in the literature in which no significant differences in radical yields were observed when changing the bulk temperature [21, 118, 119]. In the work of Rochebrochard d'Auzay et al. [118] the yield of I_3^- was unchanged in the temperature range of 15 °C - 34 °C when using an ultrasonic frequency of 365 kHz and an acoustic power of 18.9 W. In our own work, we briefly conducted an assessment of the radical formation at bulk

temperatures of 5 °C and 20 °C in order to validate our other experiments [21]. This was achieved through Weissler dosimetry at 408 kHz with an acoustic power of 53 W under an argon atmosphere. However, we could not find any significant differences between the two temperatures as can be seen in Figure 2.22. A similar result was also found by Raúl Erades de Quevedo [119] who investigated the primary radical formation through Weissler dosimetry and Fricke dosimetry for temperatures between 10 °C and 40 °C. A slight decrease in radical yield was observed close to 40 °C, but no significant differences were observed below that.

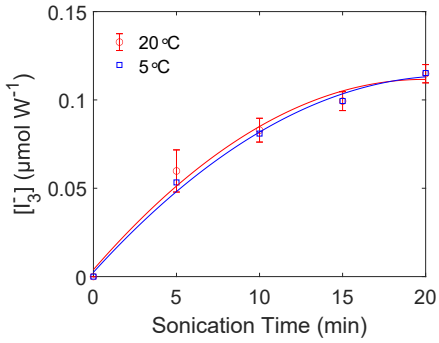

Figure 2.22: Rate of I_3^- formation from ultrasound as a function of sonication time with bulk temperatures of 20 °C (◯) and 5 °C (□). The experiments were performed with an ultrasonic frequency of 408 kHz.

Apart from the apparent influence of bulk temperature on the radical formation, the bulk temperature can also affect the aqueous solution directly by way of heating. Some species in the sonoreactor may react, decompose or evaporate simply due to increased temperatures and not as a result of sonochemical reactions with radicals. For instance, above 110 °C ethylene glycol decomposes to an aldehyde which is capable of reducing metal precursors [120, 121]. Failure to control the temperature during sonication may therefore result in conditions which could have been reached by simply heating the solution on a hot-plate.

High temperature experiments during sonochemical synthesis was explored by Park et al. [11]. They monitored the change in $Fe(acac)_3$ and $Pt(acac)_2$ in an ethylene glycol solution as a function of temperature. The temperature was generated by the 20 kHz horn-type sonifier itself. Successful synthesis of Fe@Pt-nanoparticles only occurred for temperatures above 105 °C. The high temperatures produced by the sonifier therefore appear to cause a polyol synthesis rather than a sonochemical synthesis. Separating the contribution from the temperature and the radical formation towards the nanoparticle formation therefore becomes highly difficult.

Careful control over the temperature through cooling is therefore necessary if the role of sonochemically generated radicals are to be studied.

Acoustic Power

The acoustic power applied during sonochemical synthesis is also of importance to the reduction rate. A higher intensity, or amplitude, for the oscillations leads to a larger ratio between the collapse radius and ambient radius of the bubble [69, 107]. From Equation 2.13, the bubble temperature is therefore increased and the number of radicals is increased.

Another important consequence of the acoustic power is the initiation of cavitation itself. In order for cavitation bubbles to start forming, sufficient energy is required to overcome the molecular forces of the liquid [56, p. 25]. As a result, the liquid properties such as the surface tension and vapour pressure determines the power threshold for cavitation [122]. More cavitation bubbles are therefore formed at higher acoustic powers. This leads to an increase in the number of radicals as well.

Such an increase in radical yield and collapse temperature with increasing acoustic power has also been confirmed experimentally through sonoluminescence measurements and dosimetry experiments [32, 69, 73]. The increase in radical formation at intermediate acoustic powers appears to be quite linear with a less steep slope appearing for higher powers. We also observed such a linear behaviour in our experimental work as shown in Figure 2.23(a). Subtle deviations from linearity at low acoustic powers can be seen when plotting the sonochemical efficiency as a function of power (Figure 2.23(b)). It seems that low acoustic powers exhibit a slight reduction in the sonochemical efficiency compared to intermediate powers where it is fairly constant. This was also observed by Mark et al. [37] and Askakura et al. [32]. At exceedingly high powers, sudden drops in radical yield are reported in the literature [32, 73]. A minimum threshold power for radical formation is also reported which is in agreement with the power required to overcome the molecular forces of the liquid [69, 73]. Assuming linear behaviour at low acoustic powers, our results (Figure 2.23(a)) also confirm this.

The decrease in radical yield for higher acoustic powers can be attributed to the increased interactions between cavitation bubbles [32]. At high acoustic powers the density of cavitation bubbles in the antinodes will increase. As a result, the secondary Bjerknes forces will increase resulting in interactions between individual cavitation bubbles as described in section 2.2.4. Coalescence of cavitation bubbles will therefore be favoured which will effectively quench the radical generation as the bubbles are expelled from the antinodes. The upper power threshold for radical quenching is frequency dependent with lower frequencies displaying a lower

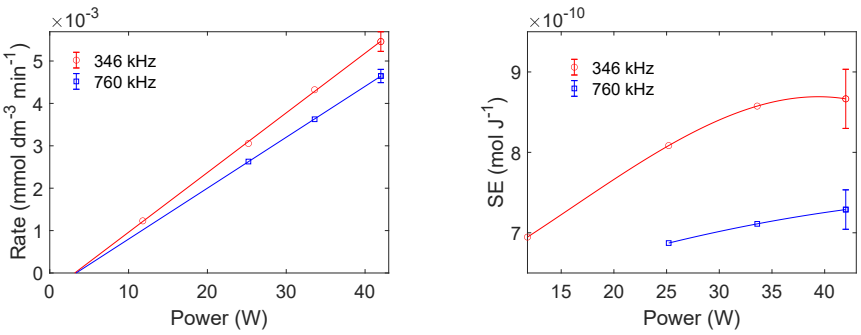

Figure 2.23: Rate of ·OH radical formation measured by H_2O_2-detection (a), and the corresponding sonochemical efficiency (b) as a function of acoustic power at 346 kHz (○) and 760 kHz (□).

threshold [32]. In order to achieve higher radical formation rates, higher frequencies must be applied so that the acoustic power can be further increased without suffering from quenching phenomena. However, as discussed in Section 2.3.3, the frequency range from 200-500 kHz display the optimum sonochemical radical generation. Setting aside the requirement for the highest sonochemical efficiency, the highest overall attainable radical generation should therefore be achieved closer to 500 kHz than 200 kHz due to Bjerknes forces being more dominant at 200 kHz than at 500 kHz.

Systematic investigations of the effect of power on sonochemical syntheses are rather limited in the literature as it appears to be mostly concerned with low frequency (20 kHz) systems [94, 123]. Fuentes-Garcia et al. [94] showed that increasing the acoustic power from 60 W to 210 W at 20 kHz leads to a reduction in gold nanoparticle sizes from 16.2 nm to 12 nm. This is expected as the higher acoustic power leads to higher radical formation rates. Kandjani et al. [123] examined the agglomerate sizes following a change in acoustic power for the sonochemical synthesis of ZnO. They found that the agglomerate size was effectively reduced from $9.5\,\mu m$ at 12 W to $4.25\,\mu m$ at 45 W.

To the best of our knowledge, there is no systematic investigation of the effect of acoustic power for a sonochemical synthesis at higher frequencies. However, results obtained at different acoustic powers in different research papers can still be compared. The acoustic powers in literature varies a lot from tens of watts, to hundreds of watts. In the case of Au-nanoparticles, significantly smaller nanoparticles were acquired at 200 W ($\approx$ 5 nm) [26] compared to 20 W ($\approx$ 15 nm) [1]. Both experiments were conducted at an ultrasonic frequency close to 200 kHz.

Further comparison at 20 kHz also reveals that a low acoustic power of 7 W [1] gave particle sizes of $\approx$ 30 nm while 60 W and 210 W gave 16.2 nm and 12 nm, respectively. In the case of Pt-nanoparticles, the particle sizes obtained in literature are much more monodisperse ranging from 2-6 nm for different powers and frequencies [26–28, 34, 95, 96, 104]. However, no clear trend can be observed when relating power to particle size for Pt-nanoparticles.

The acoustic power has to be higher than the threshold for cavitation which means that acoustic powers above $\approx$ 5 W is needed. It must also be below the onset for sonochemical quenching which is frequency dependent. If fundamental studies on sonochemistry is the target, it is also prudent to stay within the linear region of radical formation with respect to the acoustic power. This would ensure that the effect of any secondary Bjerknes forces does not start to interfere when changing other parameters, and also allow for a fairly constant sonochemical efficiency. If high reduction rates are the purpose of the sonochemical synthesis, high acoustic powers close to the onset of sonochemical quenching should be chosen. Before reaching the onset, however, the power limit of the transducer may also be reached. Exceeding the limit set by the manufacturer may cause it to break down as I have personally experienced. A break down of the transducer is followed by a significant increase in reflected power suggesting that the given resonance frequency is no longer valid.

Radical Scavengers

Even if all ultrasound parameters were optimized to yield maximum radical generation, the generation rate is still on the order of tens of micro molar per minute [26–30]. In addition, most of these radicals are lost to recombination processes due to their short lifetime. Only a fraction of the primary radicals are able to escape through the sonochemical hot-shell where most of the recombination reactions occur [33, 87]. If sonochemistry is to be a viable alternative to traditional chemical reduction methods, those precious few radicals must be utilized for reduction purposes and not wasted on recombination. In order to do so, the surface active properties of a radical scavenger may be utilized.

An efficient radical scavenger is characterized by its excellent surface active properties. As most of the recombination processes take place in the sonochemical hot-shell surrounding the collapsed bubble, it is paramount that the scavenger is present at the bubble solution interface [33, 34]. That way, they are able to collect the primary radicals before they have a chance to recombine. Most radical scavengers therefore consists of a hydrophilic head and a hydrophobic tail. The more hydrophobic the scavenger, the higher its concentration at the bubble solution interface [34]. These scavengers are therefore able to cover the entire cavitation

bubble at much lower concentrations than less hydrophobic scavengers.

Henglein and Kormann [33] demonstrated how the scavenging efficiency is correlated to the hydrophobicity for a range of scavengers including ethanol, methanol, t-butanol, formic acid and glycol. In their work they defined the scavenging efficiency as the scavenger concentration required to reach $50\,\%$ of the H_2O_2 concentration in a scavenger-free system at $300\,\mathrm{kHz}$. Increasing the hydrophobicity by 1 by going from methanol to ethanol was shown to decrease the necessary scavenger concentration by an order of magnitude from $8 \times 10^{-3}\,\mathrm{mol\,dm^{-3}}$ to $8 \times 10^{-4}\,\mathrm{mol\,dm^{-3}}$. We found the exact same trends in our work (See paper IV) which was performed at $346\,\mathrm{kHz}$ [41].

The hydrophobicity of the scavenger has also been shown to be decisive for sonochemical nanoparticle synthesis. Caruso et al. [34] investigated how the scavenger concentration of ethanol, propanol, and pentanol affects the reduction rate of $PtCl_6^{2-}$. They found that a lower scavenger concentration was needed to reach a maximum limiting reduction rate for the more hydrophobic scavengers.

From the present discussion, it may seem that the more hydrophobic scavengers should be used for sonochemical synthesis. However, that is not the case. It is true that the more hydrophobic scavengers are more efficient at scavenging the primary radicals, but the resulting secondary radical must also be able to act as an electron donor or reducing agent.

In order for a hydrocarbon based secondary radical to transfer its electron to another specie, the electron must be located at its α-carbon site [35]. Asumus et al. [35] identified that the shorter the hydrocarbon chain, the more α-radicals are formed. In methanol the percentage of α-radicals was found to be $93.0\,\%$, while for ethanol it was found to be $84.3\,\%$. They attributed this to the probability of hydrogen abstraction. The longer the hydrocarbon chain, the lower the probability of hydrogen abstraction at the α-site. Methanol is therefore the alcohol which provides the highest yield in the transfer of primary radicals to useful secondary radicals. The process of hydrogen abstraction is illustrated for an ethanol molecule in Figure 2.24.

Even though methanol displays a fairly good yield of α-radicals, both ethylene glycol and the formate ion can boast a yield of approximately $100\,\%$ [35]. For the formate ion, there are no other hydrogen atoms to react with than that of the α-carbon. For ethylene glycol, it was shown that hydrogen abstraction from the OH-site was highly unlikely, which necessarily means that the hydrogen abstraction must occur at one of the two equivalent α-sites [35]. The problem with ethylene glycol and formate is that they are not very hydrophobic, which means that

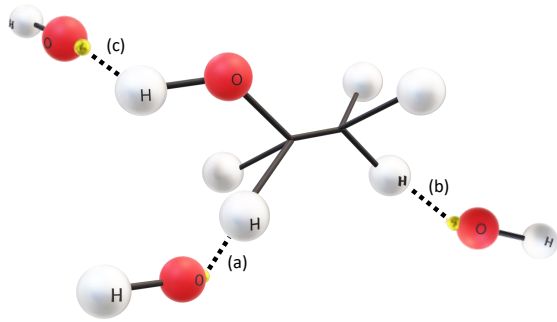

Figure 2.24: Hydrogen abstraction from an ethanol molecule by an ·OH radical. The radical can abstract a hydrogen atom from one of three different sites; the α-carbon site (a), the β-carbon site (b), and the OH-group (c). The abstraction probability is $83.4\,\%$ from the α-site, $13.2\,\%$ from the β-site, and $2.5\,\%$ from the OH-group [35].

a very high concentration is required to completely scavenge all primary radicals. Henglein and Kormann found that in order to reach $50\,\%$ scavenging efficiency a scavenger concentration of $7 \times 10^{-2}\,\mathrm{mol\,dm^{-3}}$ and $2\,\mathrm{mol\,dm^{-3}}$ was required for ethylene glycol and formic acid, respectively [33]. This is several orders of magnitude higher than the alcohols.

So far the benefits of using a radical scavenger has been discussed. However, it does come with some drawbacks as well. Being so closely situated to the cavitation bubble, the scavenger will also be affected by the high temperatures associated with the hot-shell region. The temperatures in the hot-shell can reach around $1900\,\mathrm{K}$ which is comparable to the flame of a bunsen-burner [71]. Scavengers exposed to such high temperatures will be decomposed in a pyrolysis process. The decomposition products are various derivatives of the scavenger. In the case of methanol, the main pyrolysis mechanism is the cleaving of the C-O-bond [82].

$$\mathrm{CH_3OH} \rightarrow \cdot\mathrm{CH_3} + \cdot\mathrm{OH} \tag{2.35}$$

The resulting methyl radical ($\cdot\mathrm{CH_3}$) and hydroxyl radical ($\cdot\mathrm{OH}$) then goes on to react with the excess methanol [82].

$$\cdot\mathrm{OH} + \mathrm{CH_3OH} \rightarrow \cdot\mathrm{CH_2OH} + \mathrm{H_2O} \tag{2.36}$$

$$\cdot CH_3 + CH_3OH \rightarrow \cdot CH_2OH + CH_4 \tag{2.37}$$

The resulting methanol radical($\cdot CH_2OH$) from these reactions is also the result from hydrogen abstraction by primary radicals. However, at higher methanol concentrations the methanol radical can be scavenged by a methyl radical producing methane and formaldehyde [82].

$$\cdot CH_3 + \cdot CH_3OH \rightarrow CH_2O + CH_4 \tag{2.38}$$

The methyl radical can also recombine with itself forming alkanes and alkenes [82].

$$\cdot CH_3 + \cdot CH_3 \rightarrow C_2H_6 \tag{2.39}$$

$$\cdot CH_3 + \cdot CH_3 \rightarrow C_2H_4 + H_2 \tag{2.40}$$

Similar reactions also occur for longer hydrocarbons. Buttner et al. [82] investigated the decomposition products of methanol and found that the decomposition products exhibit a maximum for methanol concentrations between 20 and $40\,\%$.

A decrease in product formation at high scavenger concentrations can be attributed to the collapse temperature. As previously explained, the radical generation increases with increased bubble temperature. The bubble temperature is determined by equation 2.13. When excessive scavenger concentrations are used, the gaseous decomposition products from the scavenger start to enter the cavitation bubble as well. For methanol this means CO, CH_4 an small amounts of C_2H_6 and C_2H_4. The many degrees of freedom displayed by these species results in a low value for the polytropic ratio following equation 2.11. As a result, the collapse temperature of the cavitation bubble decreases when these decomposition products are present in excess. Using too high scavenger concentrations will therefore decrease the radical generation.

Even though the pyrolysis products decrease the temperature of the cavitation bubble, new reducing species are also generated from the pyrolysis as well. In the example of methanol, both methyl radicals and methanol radicals arise as decomposition products. Both these radicals are able to act as reducing agents. However, they are not always able to reduce all precursors. The reduction of Au(III) to Au-nanoparticles, Pd(II) to Pd-nanoparticles, and Pt(IV) to Pt(II) are all known to

proceed through these pyrolytically generated reducing agents [26]. The reduction of Ag(I) to Ag-nanoparticles, and Pt(II) to Pt-nanoparticles, however, only proceed through secondary radicals and not pyrolytically generated radicals [26, 28]. Some sonochemical reactions can therefore be aided by pyrolytic decomposition, while others must rely on secondary radicals only.

2.3.4 Scale Up

In order for nanoparticle synthesis methods to become viable for industrial applications, it must be possible to scale up the reactor volume to facilitate the high throughput requirements put forth by the industry. Challenges to overcome when scaling up a synthesis mostly revolves around achieving the same nanoparticle properties as in laboratory scale measurements. Differing solution volumes and reactor designs are some examples of why different nanoparticle properties are achieved when scaling up a synthesis [16]. We will therefore be looking into how these parameters influence the sonochemical synthesis method.

Increasing the solution volume in sonochemical synthesis either involves an increased diameter of the ultrasonic transducer or an increased liquid height in the reactor. It is often easier to increase the liquid height as the diameter of the ultrasonic transducer is fixed. This is why most of the literature is concerned with investigating the liquid height of the sonoreactor [31, 32]. Son et al. [31] measured the radical yield and the sonoluminescence for liquid heights ranging from 80 to 340 mm (0.75 to 3.2 L). They found that the radical yield was approximately constant for all liquid heights. This was also the case for the acoustic power. This also means that the number of radicals produced was found to increase when increasing the liquid height. They attributed the increased number of radicals at higher liquid heights to the formation of a larger standing wave region as was observed from sonoluminescence images.

Similar observations on the radical yield and acoustic power was made by Asakura et al. [32]. They performed Weissler dosimetry with an ultrasonic frequency of 514 kHz for solution volumes of 25, 50, 100, 150, and 200 mL (1.3 cm to 10.2 cm in liquid height). A constant acoustic power was observed for all frequencies, as well as a fairly constant I_3^- concentration. As a result, the higher solution volume was found to produce more radicals. They also attributed the higher number of radicals at higher solution volumes to the formation of a wider standing wave field region.

Changes in the ultrasonic transducer diameter have been explored by Rochebrochard d'Auzay et al. [118]. In their experiments, plate transducers with diameters of 65 mm and 102 mm were used to measure the radical yield through Weissler dosimetry at 370 kHz. The same solution height (132 mm) was used for both exper-

iments, but the solution volume was 380 mL for the small diameter reactor, and 1000 mL for the large diameter reactor. They found a slightly higher yield of radicals being produced by the lower diameter reactor.

Figure 2.25: Example of two sonoreactors where the left one was increased only in height to facilitate larger scale sonochemical reactions. The diameter of the reactor remained unchanged.

The findings in these works therefore seem to suggest that large scale sonoreactors should be designed as long thin tubes where the liquid height can be increased while maintaining a relatively small diameter for the ultrasonic transducer. However, these experiments are only concerned with the radical formation in these sonochemical reactor configurations. Actual sonochemical synthesis of nanoparticles would also be necessary in order to assess the proposed design of industrial scale reactors. To my knowledge, there are not any mention of this in the literature. It therefore remains relatively unexplored within the field of sonochemistry.

2.4 Electrocatalysis

2.4.1 Introduction to Catalysis

For chemical reactions, a reaction is considered spontaneous if the change in Gibbs energy is negative ($\Delta G < 0$) [124, p. 834]. The reaction is therefore thermodynamically favoured to proceed. However, the rate at which this reaction proceeds can not be predicted from the change in Gibbs energy itself. In order for the reactants to react and form the products, an intermediate species must be formed in a transition state [125, pp. 23–78]. The energy required to form this species is called the activation energy, and it can be high or low dependent on whether formation of the intermediate is facilitated or not [125, p. 36].

To speed up these reactions, the activation energy from reactants to transition state can be reduced by creating an environment in which the transition state becomes more stable [125, p. 3]. This can be achieved by using a catalyst. A catalyst is a species that reduces the activation energy without being consumed itself [125, p. 2]. A catalyst reduces the activation energy by forming an intermediate with the reactants which is more stable than the uncatalyzed intermediate. This can either occur homogeneously in solution as in the formation of a new chemical species, or heterogeneously on the surface of a solid catalyst [125, pp. 5–8]. For a solid catalyst, the reactants adsorb to the surface of the catalyst [125, p. 3]. The relevant bonds in the reactants are then broken as the resulting intermediates are stabilized. Formation of the final products is then facilitated through bond formation between the stabilized intermediates. The final product formed at the catalyst surface can then desorb from the catalyst which completes the process and leaves the catalyst unchanged.

The activation energy (E_a) associated with a reaction is related to the rate constant for the particular reaction (k) and the temperature (T) through the Arrhenius equation [124, p. 626].

$$k = A \exp\left(\frac{-E_\mathrm{a}}{RT}\right) \tag{2.41}$$

A is a constant and R is the gas constant. Plotting the logarithm of k as a function of T^{-1} produces a straight line from which the activation energy can be extracted. We can also infer from this equation that a high rate constant reduces the activation energy.

A high rate constant can be achieved by ensuring that the reactants easily adsorb to the catalyst surface which is characterized by the formation of a stable interme-

diate. However, if the resulting products are too easily adsorbed (or stabilized) on the catalyst surface, no surfaces will be available for further adsorption, and the process is halted. The products must therefore be able to easily desorb from the catalyst surface to make space for additional reactants in order for the catalyst to be efficient [125, p. 4]. A catalytic reaction is therefore typically either limited by the adsorption or desorption, and an effective catalyst should aim towards equal adsorption and desorption rates for the reactants and products, respectively. This is referred to as the Sabatier's principle [125, p. 4]. Following the Arrhenius equation (equation 2.41), the adsorption and desorption steps should also have their own rate constants and activation energies.

What determines whether adsorption or desorption is favoured is the interaction between the reactant and the electrons in the d-orbitals of the catalyst [124]. Many transition metals are therefore commonly used as catalysts due to the availability of these electrons. To further fine-tune the d-orbital interactions with the reactants and the products, alloys of different transition metals can also be developed. When comparing the activity of different catalysts, it is common to present it as a volcano plot [125, p. 383]. In a volcano plot the catalytic activity of each catalyst material is plotted against its corresponding bonding energy. The shape of this plot will take the form of a volcano with the highest activity belonging to the catalyst with a bonding energy that is neither too strong nor too weak (Sabatier's Principle). These plots serve to highlight which materials are suitable as catalysts for a particular reaction and which ones are not. Predicting which materials display the ideal bonding energy for maximum catalytic activity is very complicated. A combination of computer simulation and experimental testing is therefore one of the strategies which is used when developing new catalysts.

2.4.2 Electrochemical Energy Conversion Devices

A special class of chemical reactions is oxidation- and reduction-reactions. These involve changes in oxidation states and transfer of charge as shown below

$$\mathrm{M} \rightleftharpoons \mathrm{M}^{n+} + n\mathrm{e}^{-} \tag{2.42}$$

where the forward reaction is an oxidation, and the reverse reaction is a reduction. Which reactant is reduced and oxidized is determined by the change in Gibbs energy. As described above, the reaction where $\Delta G < 0$ is spontaneous. However, due to the charge transfer associated with these reactions, greater control over the reaction can be achieved as energy can be supplied to the system through electrical devices. The branch of chemistry which deals with how chemical reactions are affected by the flow of charges is called electrochemistry.

Multiple different electrochemical configurations exists, either by design or naturally occurring. The oxidation of iron in contact with acidic water is an example of a naturally occurring (undesired) electrochemical setup

$$2\mathrm{Fe} \rightarrow 2\mathrm{Fe}^{2+} + 4\mathrm{e}^{-} \tag{2.43}$$

$$\mathrm{O}_2 + 4\mathrm{H}^{+} + 4\mathrm{e}^{-} \rightarrow 2\mathrm{H}_2\mathrm{O} \tag{2.44}$$

where iron is oxidized and oxygen is reduced [124, p. 894]. An electrochemical setup made by design, however, typically involves confining the oxidation and reduction at separate places in an electrochemical cell. The reactions typically take place on the surface of a solid conducting material, which is called an electrode [126, p. 105]. The electrode where the oxidation takes place is the anode, and the electrode where the reduction takes place is the cathode [126, pp. 60–61]. The two electrodes are connected with an outer circuit, allowing a pathway for electrons. Ionic transport are ensured through the electrolyte between the two electrode compartments to close the circuit, allowing current to flow through the cell. A potential difference is established between the anode and the cathode where the cathode is located at a higher potential than the anode in a galvanic, spontaneous, cell.

The change in Gibbs energy can be related to the electrode potential (E) as

$$\Delta G = -zFE \tag{2.45}$$

where z is the number of charges and F is Faraday's constant [124, p. 874]. Gibbs energy change is therefore related to the voltage difference between the cathodic and anodic half-reactions. To have a way to compare all possible electrode reactions (half-cell), one of the half-cell reactions are defined as a reference point for potential. This reference potential from which individual cell potentials can be given are defined to be the standard hydrogen electrode (SHE). The electrode potential of the SHE is defined to have an electrode potential (E^0) of 0 V [126, p. 106]. All other electrode reactions can then be compared to the SHE and tabulated, i.e. the standard reduction potentials.

$$2\mathrm{H}^{+} + 2\mathrm{e}^{-} \rightleftharpoons \mathrm{H}_2 \tag{2.46}$$

If electrical work is applied to the cell by an external voltage source connected between the two electrodes, the Gibbs energy is changed. If the voltage applied

is greater than the thermodynamic cell voltage the opposite reaction will proceed instead. The standard reduction potential of oxygen evolution from water is $1.23\,\mathrm{V}$ [110]. Since the standard reduction potential for oxygen is more positive than for hydrogen, water splitting (oxygen evolution and hydrogen evolution) is not spontaneous and requires a voltage higher than $1.23\,\mathrm{V}$ to be applied between the anode and the cathode (at $25\,^{\circ}\mathrm{C}$ and standard conditions) [126, p. 77].

The process of applying a potential to drive an otherwise unfavourable electrochemical reaction is called electrolysis [126, p. 71]. The electrochemical setup used to drive these reactions is therefore called an electrolyzer. Electrolyzers have found their way into several different industries ranging from aluminium plants to hydrogen evolution. In the case of hydrogen evolution, the electrolyzer works by splitting water into hydrogen gas at the cathode, and oxygen gas at the anode [126, p. 77].

$$4\mathrm{H}^{+} + 4\mathrm{e}^{-} \rightarrow 2\mathrm{H}_2 \tag{2.47}$$

$$2\mathrm{H}_2\mathrm{O} \rightarrow 4\mathrm{H}^{+} + 4\mathrm{e}^{-} + \mathrm{O}_2 \tag{2.48}$$

Similarly to other chemical reactions, the kinetics of electrochemical reactions like water electrolysis are not determined by thermodynamics. Applying a voltage of $1.23\,\mathrm{V}$ to a water solution expecting large scale production of hydrogen and oxygen is therefore not realistic as can be seen in Figure 2.26. Differently from regular chemical reactions, though, is that an external energy source is easily available, which can change the rate of reaction by changing the applied voltage. As the transfer of charge is present in the reactions, we need only monitor how fast the charges flow in order to obtain the rate of the reaction. The flow of charge per unit time is electrical current by definition. Measurements of the current therefore give a direct measure of the rate of the reaction. Applying a higher voltage than the thermodynamic cell voltage will therefore increase the rate of the reaction. This is referred to as applying an overvoltage [126, pp. 193–194].

The overvoltage consists of activation overpotentials due to electrode kinetics, concentration overpotential at each electrode and a loss connected to transport of ions in the electrolyte and electrons in electrodes and outer circuit, called ohmic losses or IR loss. Even though the rate of the reactions can be tuned with the applied voltage, the overpotentials should be as low as possible in order to have an effective energy conversion device. The activation overpotential can be reduced by improving the electrode kinetics towards the desired electrode reaction. An essential parameter is the exchange current density, which is an electrode specific

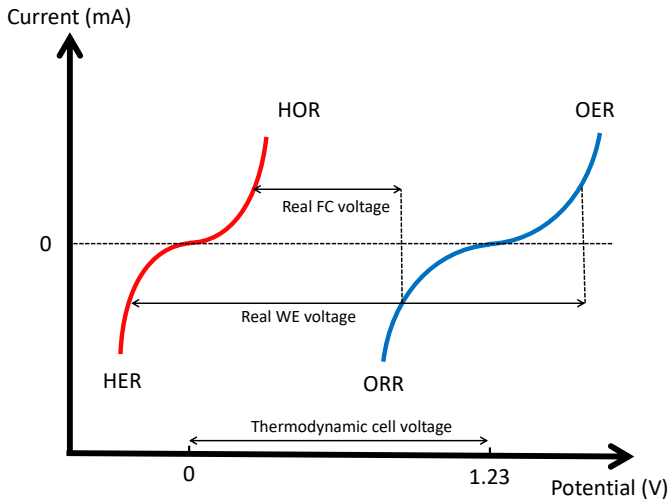

Figure 2.26: Current-voltage graph showing the potential regions where hydrogen evolution (HER) and oxygen evolution (OER) occurs in water electrolysis (WE). The voltage required to produce hydrogen and oxygen in any considerable amounts is indicated. Similarly, the potential regions for the hydrogen oxidation reaction (HOR) and the oxygen reduction reaction (ORR) associated with a fuel cell (FC) are also shown in the same figure. The cell voltage obtained from the fuel cell is also indicated.

parameter that dictates how well-suited the electrode is for transferring electrons [127, 128]. A second important kinetic parameter is the increase in voltage for a certain increase in current, often given in volts per decade and referred to as the tafel slope [127]. The tafel slope for a certain electrode reaction depends on the reaction mechanism. The exchange current density and tafel slope depends on electrode material and can be improved by choosing an electrode material which facilitates the electrochemical reactions better. Once more we have arrived in the world of catalysis.

Electrocatalysts are catalytic materials which enhance electrochemical reactions at the electrodes. Their working principle is similar to chemical catalysts, but an additional requirement to electrocatalysts is that they need to be electrically conductive in order to transfer the charges associated with the reactions. The most commonly used catalysts for water electrolysis are based on noble metals due to their excellent catalytic activity towards hydrogen and oxygen evolution reactions [5, 7, 10, 14]. Platinum for the HER, and iridium for the OER are the two catalysts which have displayed the highest activity [7, 10]. The scarcity of these materials, in particular iridium with an annual production of less than 10 tons, makes

them quite expensive which in turn also makes the resulting electrolyzer expensive [129]. Other cheaper transition metals like nickel and iron have therefore been explored as potential replacements for the noble metals [8, 9].

Another electrochemical energy conversion device which is often mentioned in the same context as water electrolyzers is fuel cells. A fuel cell spontaneously converts chemical energy in a fuel to useful electrical energy. One example is the hydrogen/oxygen fuel cell. These reactions are shown in a current voltage plot in Figure 2.26. Hydrogen is introduced at the anode and oxidized into H^+ in a process known as the hydrogen oxidation reaction (HOR) [125, p. 377].

$$2H_2 \rightarrow 4H^+ + 4e^- \tag{2.49}$$

The electrons can then move through an external circuit and perform work before arriving at the cathode where they reduce oxygen gas into water in a process known as the oxygen reduction reaction (ORR).

$$O_2 + 4e^- + 4H^+ \rightarrow 2H_2O \tag{2.50}$$

In order for this process to proceed, H^+ is transported through a membrane or aqueous electrolyte, connecting the two compartments, ensuring a closed circuit. The most well known proton exchange membrane material is the poly(perfluorosulfonic acid) membrane Nafion^{TM} [14, 125, p. 378].

The maximum cell voltage in a hydrogen/oxygen fuel cell is $1.23\,\mathrm{V}$ at standard conditions and $25\,^\circ\mathrm{C}$, but losses associated with the activation energy of the reactions occurring at both electrodes result in a lower cell voltage [125, p. 381]. This is indicated by the lower cell voltage in Figure 2.26. Electrocatalysts at the electrodes can decrease the losses by way of reducing the activation energy, but some losses are still expected. The same noble metal catalysts used in electrolyzers are also quite efficient towards the reverse reactions in fuel cells as well due to the inherent nature of these metals [12, 95, 130, 131].

Several electrocatalyst designs have been developed to enhance the catalytic activity in water electrolysis and fuel cells [130, 132–134]. Most of these designs are related to increases in the available surface area and intrinsic activity.

Ensuring the catalysts are on the nanoscale greatly contributes to enhanced surface area per gram catalyst. For nanoscale materials, a greater proportion of the atoms are surface atoms, where they can actively facilitate the catalytic reaction with reaction sites. However, decreasing the particle size too much could also have

a negative effect on the inherent catalytic activity. As a nanoparticle approaches $1\,\mathrm{nm}$ a much larger proportion of the surface atoms will be edge or corner atoms. The dangling bonds from these atoms may interact more strongly with the reaction components than the terrace atoms and alter the turn-over frequency at these sites [130]. In the case of Pt-electrocatalysts much work has been conducted on the size effect for different electrochemical reactions [130, 132–134]. A particle size around $3\,\mathrm{nm}$ has been demonstrated to display the maximum mass activity (activity per mass catalyst) towards the ORR [130, 132–134]. Increasing the particle size above $3\,\mathrm{nm}$ increases the specific activity (activity per available surface area), but decreases the mass activity [133]. Great control over the size of the electrocatalyst during large scale synthesis is therefore paramount if more effective electrocatalysts are to be synthesized on an industrial scale.

Another strategy which is essential for achieving high catalytic activity is the use of a catalyst support [135, 136]. The role of the support is to ensure that the individual nanoparticles do not aggregate, which would limit the available surface area. The catalyst support also needs to be highly conductive in order to transfer electrons readily to or from the catalysts. A well dispersed catalyst is therefore desired to optimize the available surface area. The weight percentage of catalyst to support is called the catalyst loading ($\mathrm{wt}\%$)

$$\mathrm{wt}\% = \frac{m_\mathrm{c}}{m_\mathrm{s} + m_\mathrm{c}} \tag{2.51}$$

where m_c is the mass of the catalyst, and m_s is the mass of the support. A loading of $20\,\%$ is common for research purposes, but lower loadings are also used in full scale electrochemical conversion devices [14]. One of the most common catalyst support materials is carbon black. There are many varieties of carbon black, with vulcan carbon (XC-72) perhaps being the most well known [137]. The benefits of carbon black are its high surface area on which the precious catalyst material can be well dispersed, its excellent electrical conductivity, satisfactorily stability in a fuel cell environment, and fairly low cost [137, 138]. Nanostructured supports such as graphene and carbon nano fibers have been attempted as they can provide an even higher electrical conductivity, a larger surface area and improved stability, albeit with a higher production cost [95, 136].

Alloys, bimetallics and core-shell configurations are also possible directions to improve electrocatalytic activity. Introduction of another material can ensure that the active sites on the catalyst have a slightly different d-orbital structure [12]. As a result, the binding of reactants and products could be changed to a more optimal balance closer to the peak of the volcano plot [134]. This would in turn increase

the catalytic activity of the catalyst. For ORR, Stephens et al. [134] showed that Pt/Pd, Pt_3Ni, Pt_5La, and dealloyed PtCu all have a higher catalytic activity than Pt alone [134]. This was found through X-ray photoelectron spectroscopy and density functional theory combined with electrochemical measurements. They attributed this to the slightly stronger OH-binding energy compared to pure Pt.

Chapter 3

Methodology

3.1 Physical Characterization

3.1.1 UV-Visible Spectroscopy

Absorbance and Transmission

Exposing a material to white light will result in the absorption of light of certain wavelengths and the reflection of others. The reflected wavelengths make up the colours we perceive, and so we assign that colour to the material. The reflected wavelengths must therefore necessarily be the complementary colours of the absorbed wavelengths as illustrated in Figure 3.1 [139, pp. 382–383]. This means that if an object appears blue, it will absorb orange. If it appears yellow, it will absorb violet.

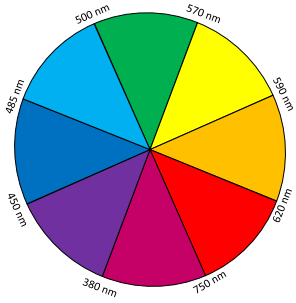

Figure 3.1: Colour circle showing the wavelength ranges of each color. The complementary colours are placed on opposite sides of the circle.

This is also the case for liquid systems containing different ions and complexes. The difference between a liquid and most solid systems is that light is also readily transmitted through the liquid which means that we can measure the intensity of the transmitted light and compare it to the intensity of the incident light. The ratio between transmitted light intensity (I) and incident light (I_0) is called transmittance (T) [139, p. 381].

$$T = \frac{I}{I_0} \tag{3.1}$$

The transmittance can be readily converted to absorbance (A) which is a measure of how much light is absorbed by the solution [139, p. 381].

$$A = \log(1/T) \tag{3.2}$$

The absorbance is proportional to the concentration (c) of photoabsorbing ions and complexes that are in the solution, how much light is absorbed per ion or complex, typically referred to as the molar extinction coefficient (ϵ), and the path length the light has to travel (l). This relation is called Beer-Lambert's law [139, p. 381].

$$A = \epsilon l c \tag{3.3}$$

Absorbance measurements can therefore be used to quantitatively determine the concentration of ions and complexes in solution. There are, however, a limitation to the use of this relation. The proportionality is not valid for high concentrations as interionic effects will start to interfere with the light being transmitted [139, p. 383]. The result will be a saturation of the measured absorbance characterized by a deviation from linearity when plotting absorbance against concentration. A rule of thumb is therefore to ensure that the absorbance is kept below 1. From equation 3.2 an absorbance of 1 corresponds to a transmittance of $10\,\%$ which is well within the detection limit of the spectrophotometer and sufficiently high to avoid interionic effects. An absorbance of 2 for instance will result in a transmittance of $1\,\%$ and we will start seeing more noise in the absorbance spectrum as well as a deviation from linearity in Beer-Lamberts law.

In order to successfully relate the absorbance to the concentration, a value for the molar extinction coefficient must be assigned. Proper estimation of the molar extinction coefficient should be done by performing absorbance measurements over a range of known concentrations as shown in Figure 3.2(a). The slope of the curve resulting from plotting absorbance against concentration (Figure 3.2(b)) equals the

molar extinction coefficient times the path length. It is important to remember that tabulated values for the molar extinction coefficient of a specific ion or complex is given at a specific wavelength, and absorbance measurements should therefore be performed at the same wavelength in order to quantify the concentration.

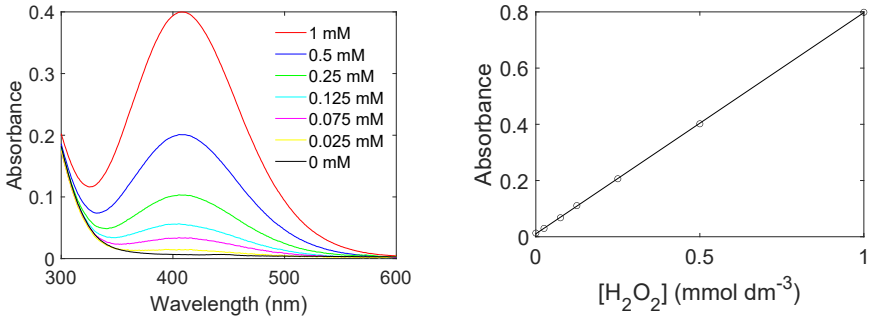

Figure 3.2: UV-Vis absorbance spectra of a H_2O_2-titanyl complex for different concentrations of H_2O_2 (a). The absorbance at the peak (411 nm) for every spectrum is plotted as a function of H_2O_2 concentration (b). The solid line is a linear fit to the datapoints giving a value for $\epsilon = 787\,\mathrm{dm^3\,mol^{-1}\,cm^{-1}}$.

Spectrophotometer

A spectrophotometer is an instrument in which monochromatic light of known intensity is passed through a liquid sample and the resulting light intensity is measured [139, pp. 383–384]. A simple schematic is illustrated in Figure 3.3. The wavelengths typically range from the UV-region (200 nm) to the near infrared region (1000 nm) and is therefore suitable for the quantification of coloured substances in solution. The sample is usually kept in a cuvette with a standard path length of 1 cm [139, p. 384]. Any absorbance from the cuvette itself is eliminated by first performing a blank measurement of the cuvette and the solvent in which the sample is dissolved. It is important to choose the appropriate cuvette material for the wavelength range that is going to be investigated as some materials absorb very efficiently at certain wavelengths [139, p. 384]. Failure to account for this will result in a high absorbance at these wavelengths in the blank measurement which will render this range useless for quantification. Regular glass cuvettes, for example, absorb UV-light, and measurements below 300 nm will be subject to noise [139, p. 384]. Quartz glass or special brands of plastic cuvettes should therefore be used when the UV-range is of interest [139, p. 384].

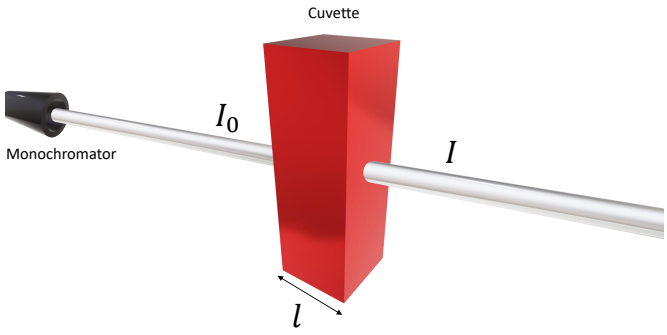

Figure 3.3: Transmission of light through a cuvette of path length l. The light intensity from the monochromator (I_0) is diminished due to absorption in the cuvette resulting in a lower light intensity (I).

Nature of Light Absorption

We have now established that ions/complexes in solution absorb light of certain wavelengths efficiently, while other wavelengths are transmitted quite undisturbed. The question is therefore what makes an ion or complex absorb light at these specific wavelengths. To understand this we must introduce the notion of bonding, non-bonding, and anti-bonding molecular orbitals [139, pp. 387–389].

When atomic orbitals combine to form a molecule the wavefunctions of the atomic orbitals overlap and create constructive and destructive interference. The result of the constructive interference is the stable ground state orbitals referred to as bonding orbitals [140, p. 31]. These are orbitals of lower energies where electrons are distributed in the ground state. For destructive interference, the result is an anti-bonding orbital of higher energy typically marked by a star (*) [140, p. 31]. To move an electron from the bonding orbital to the anti-bonding orbital, an energy equal to the orbital separation must be supplied [140, p. 600]. This energy can be supplied by light of a certain wavelength, as the energy of a photon (E) is inversely proportional to its wavelength (λ).

$$E = \frac{hc}{\lambda} \tag{3.4}$$

Light of the correct wavelength will therefore be absorbed by the specie in order to

excite the electron, and as a result an absorption peak will emerge in the absorbance spectrum.

In addition to the bonding and anti-bonding molecular orbitals, there are non-bonding orbitals [139, pp. 387–389]. These are electrons which are not involved in a chemical bond and are more commonly known as a lone pair. These electrons are also susceptible to excitation to the anti-bonding orbitals and will also result in light absorption. All these transitions are illustrated in Figure 3.4.

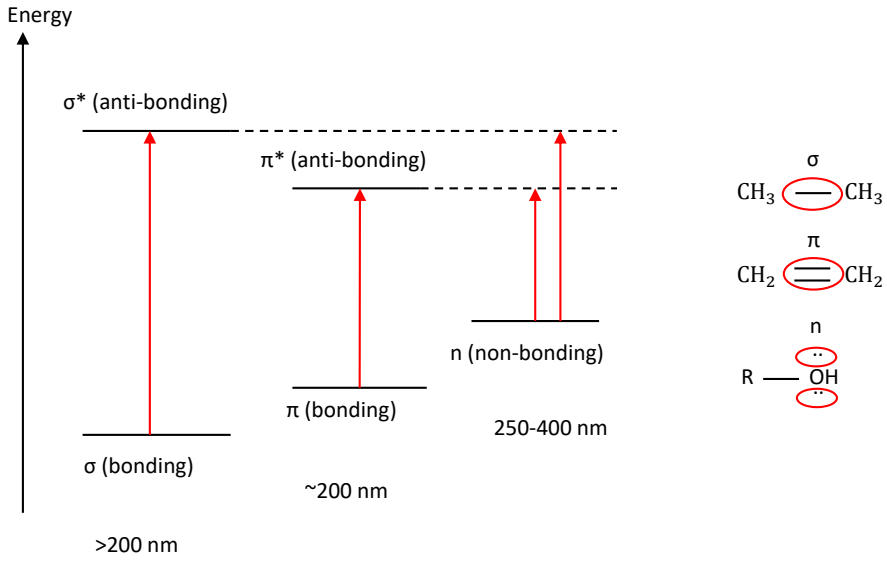

Figure 3.4: Energy diagram showing the relative positions of the σ, σ^*, π, π^* and n orbitals. Approximate excitation wavelengths are shown below each orbital. Examples of σ-, π-, and n-orbitals are shown to the right.

The energy difference separating the bonding and anti-bonding orbitals is greater for the sigma bond than the pi bond, which means that the σ - σ^* transition require very short wavelengths [140, p. 600]. In fact, the wavelength for such transitions are well below the range used in UV-Vis spectroscopy, so these may be ignored. As for the π - π^* transitions, the energy difference is almost within the range of UV-Vis spectroscopy (171 nm, ethene) [140, p. 600]. However, for systems of conjugated π-bonds the electrons are delocalized over multiple π-bonds so that the molecule becomes more stable [140, pp. 600–601]. As such the separation by the π orbitals becomes narrower which means that longer wavelengths may be used to excite electron from π - π^*. For longer conjugated molecules, the electrons

are further delocalized which further decreases the π - π^* energy separation [140, p. 601].

Other important transitions is the n - π^* and n - σ^* transitions [140, p. 602]. As the non-bonding orbitals lie between the bonding and anti-bonding orbitals, these are usually observed at longer wavelengths as well [140, p. 602]. These are more commonly observed in the low wavelength range of the absorption spectrum (<300 nm) [140, p. 602]. Some examples include the n - σ^* transition in ethanol (205 nm) and the n - π^* transition in aldehydes, ketones, carboxylic acids (250 nm - 300 nm) [140, p. 602].

For metal ions in solution, there are a number of factors to consider in order to explain the resulting absorption spectrum. The metal ions will not be freely dissolved as M^{n+} ions. If they were, all d-orbitals would be degenerate and no transition between d-orbitals nor non-bonding orbitals would be possible, and therefore no light absorption would occur [141]. Instead, metal ions form complexes with the solution, any additives, or anions present in the system which creates bonds between the cation and the ligand. These bonds serve two purposes. They introduce the possibility of ligand to metal transitions and, depending on the orientation of the ligand, they can cause a split in the energy levels of the d-orbitals [141]. The two e_g orbitals are oriented along the three axes of the metal ion, and if the ligands orient themselves in an octahedral fashion around the metal ion these orbitals will experience increased repulsion and become less stable [141]. As a result, the e_g orbitals will suffer an increase in energy and an energy difference will arise between the more stable t_{2g} orbitals and the more unstable e_g orbitals [141]. This is illustrated for the octahedral geometry in Figure 3.5

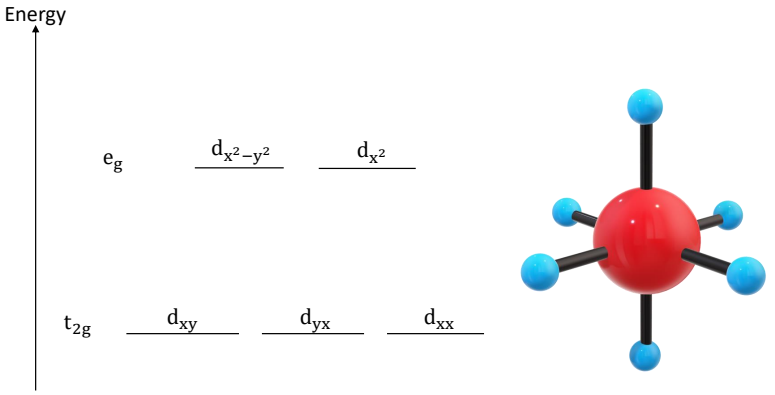

Figure 3.5: Energy diagram showing the relative positions of the e_g and t_{2g} orbitals for an octahedral geometry.

In such a complex there will be several possible transitions in the visible spectrum, most notably, the n - e_g and the t_{2g} - e_g transitions [141]. The n - e_g transition between the ligand and the metal is straight forward and will be characterized by a strong absorbance peak in the near UV-range. The t_{2g} - e_g transition, on the other hand, is more complex. The separation between the t_{2g} - e_g is influenced heavily by the ligand metal interaction, and the t_{2g} - e_g transition itself may also be attenuated due to forbidden transitions related to symmetry and change in spin [141]. As such this transition is characterized by low molar absorptivities. Changing the ligand may therefore shift the absorption spectrum and the measured absorbance.

Localized Surface Plasmon Resonance

Another phenomena which may be observed in UV-Visible spectroscopy is related to the interaction of light with nanoparticles dispersed in solution. Due to the small size of nanoparticles, a photon can cause a collective oscillation of the electron cloud in the metal nanoparticle causing separation of the positive core and the negatively charged electron cloud [142]. This requires energy to be absorbed, and will be reflected in an increased absorbance. The oscillation can be modelled as an oscillating spring, and it will therefore also have a resonance frequency [142]. As the photons are the driving force for the oscillations, resonance can only occur when the frequency (wavelength) of the incident photons match the resonance frequency of the electron oscillations. At this resonance frequency, we observe a maximum in the absorbance spectrum, and the phenomenon is referred to as localized surface plasmon resonance [142]. The resonance frequency is dependent on the dielectric media in which the oscillations occur, the shape of the nanoparticle, and its size [142]. Larger sizes will have a lower resonance frequency which means that light of higher wavelengths will be necessary to achieve resonance. This can be observed in the positive peak shift of the LSPR peak of Ag-nanoparticles in Figure 3.6.

Correspondingly, a smaller nanoparticle will have a higher resonance frequency which means that light of lower wavelengths are needed. As non-polarized light propagates along all directions in the xy-plane, electron oscillations will occur parallel to these electromagnetic waves [142]. The electron oscillations will therefore occur along all dimensions of the nanoparticle which means that the shape of the particle matter [142, 143]. For a spherical shape, there are no differences between the different directions and one strong peak will be seen in the absorption spectrum [143]. For an oblate shape, however, the dimensions have different lengths which will lead to different resonance frequencies depending on the dimension [142, 143]. As a result, two peaks will emerge in the absorption spectrum with the shortest dimension being located at lower wavelengths. This can be observed as an emerging peak in the absorbance spectrum of silver nanoparticles in Figure

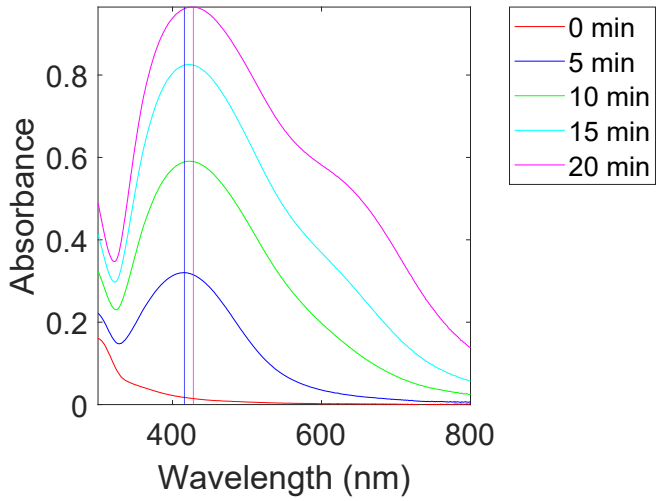

Figure 3.6: UV-Vis spectra of Ag-nanoparticles at different stages of particle growth. Notice a red-shift in the main LSPR peak and the emerging shoulder at higher wavelengths.

3.6. LSPR can therefore be used to obtain information about nanoparticle sizes and shapes. The most common example of LSPR is that of gold nanoparticles [142, 143], but it also happens in other noble metals like silver [144], platinum, palladium and copper [145].

3.1.2 X-ray Diffraction

X-ray diffraction (XRD) is a physical characterization technique in which X-rays are used to obtain crystallographic information about a sample. This occurs through detection of X-rays which are reflected off the material specific atomic planes of the sample at different incident beam angles (θ) [146]. The angle between the incident beam and the detector will therefore be 2θ, and the resulting X-ray diffractograms are typically plotted as a function of the 2θ-angle. An example of an X-ray diffractogram can be seen in Figure 3.7.

The X-ray diffractometer can be designed in several ways with the Bragg-Brentano design being a common configuration [147]. The Bragg-Brentano design uses a stack of closely spaced metal plates referred to as a Soller slits to focus the X-rays on the sample. The diffraction angle in such a design also follows the θ-θ setup where both the X-ray source and the detector move over the specified θ-range while the sample remains fixed horizontally [147]. An image of the Bragg-Brentano setup can be seen in Figure 3.8(a). Parts of the instrumentation necessarily introduces sources of error in the resulting diffractograms. One of these is the Soller

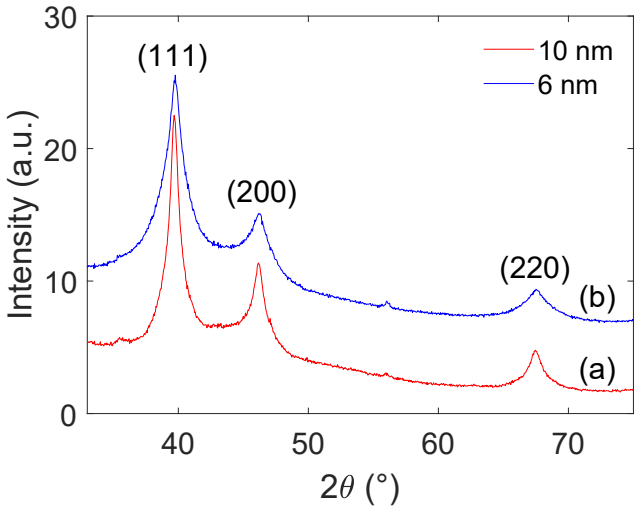

Figure 3.7: X-ray diffractograms showing the characteristic peaks of platinum indicated with their respective miller indices. The crystallite size estimated from the Scherrer equation was found to be 10 nm (a), and 6 nm (b) for the two diffractograms.

slits. As a result of the beam interaction with the Soller slits, instrument aberration will occur, and the flatness of the sample will affect the position of the peaks in the diffractogram. One therefore tries to avoid peaks or valleys in the preparation of XRD samples, as a perfectly flat sample provides for the least error in the peak positioning.

The most common X-ray source used in XRD is CuKα. It has a wavelength of $1.5406\,$Å which is comparable to that of the atomic spacing of crystalline materials. The incident X-ray beam will therefore undergo diffraction when passing through such spacings [146]. At material specific values of 2θ constructive interference between the reflected X-rays will lead to an increased intensity in the diffractogram. This will be seen as peaks in the diffractogram.

Constructive interference occurs when a diffracted X-ray beam has travelled a whole number of wavelengths, $n\lambda$, further than the other diffracted X-ray beam [146]. From the illustration in Figure 3.8(b), the extra distance equals $2d\sin(\theta)$, where d is the interplanar distance between two atomic planes. From these requirements we get Bragg's law.

$$n\lambda = 2d\sin(\theta) \tag{3.5}$$

A crystalline material is therefore needed to produce any peaks at all, however, the sample should also be prepared so that it presents all possible crystal planes. This is achieved by using a powder or a highly polycrystalline material [146]. All crystal planes are needed in the resulting diffractogram if the material is to be identified, as the absence of a characteristic diffraction peak would complicate the analysis.

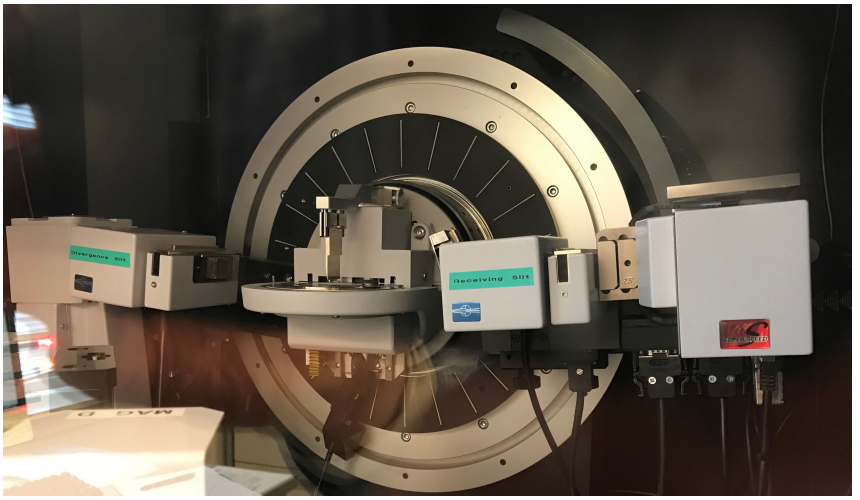

(a)

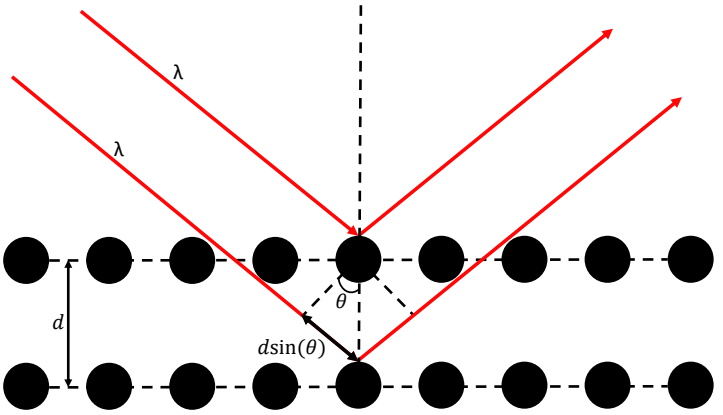

(b)

Figure 3.8: Image of the Bragg Brentano setup in the Bruker D8 A25 DaVinci X-ray Diffractometer (a), and an illustration of how Bragg's law is derived (b).

In addition to the qualitative assessment of the crystal structure of the material,

XRD can also be used to make quantitative estimates of the material composition, average crystallite size, and any lattice distortions in the material [148, 149].

To estimate the average crystallite size, the theory of line broadening must be applied [149]. In the ideal case with an infinite particle size, no defects, monochromatic X-ray radiation, and no geometrical or instrumental aberrations, the peaks of the diffractogram would be delta functions. In reality none of these assumptions apply fully, and they all contribute to a deviation from the perfect delta functions by either shifting the peaks or making them broader. The effect of the instrument and the X-ray beam will be constant for every sample and can therefore easily be accounted for. Material specific properties such as the crystallite size (D) can therefore be estimated by analysing the line broadening through the Scherrer equation [149],

$$D = \frac{K\lambda}{\beta \cos\theta}, \tag{3.6}$$

where K is a constant close to unity depending on the geometry of the particles, and β is the full width at half maximum (FWHM) for the peak being analysed. The effect of the crystallite size on the line broadening can be seen in Figure 3.7. A common value for K is 0.9 which is valid for particles of a cubic shape [149]. Even though using the Scherrer equation provides for an easy assessment of the crystallite size, there are some limitations associated with it. Firstly, the Scherrer equation does not discriminate between crystal directions. High aspect ratio particles such as plates or needles will therefore not be estimated correctly. Secondly, strain in the sample will also contribute to the line broadening which may also introduce some uncertainty in the results. The use of the Scherrer equation can therefore be used to obtain a rough estimate of the particle size, but in order to get more accurate results more sophisticated methods must be used such as Rietveld refinement [149].

Rietveld refinement is a least square method where the diffractogram is fitted to the theoretical space group of the material [149, p. 44]. The method will refine the input parameters such as the lattice parameters, crystallite size, scale factors, and atomic positions until it reaches the smallest possible R-value. This R-value is indicative of how close the fitted curve is to the experimentally obtained curve. From such a refinement, a quantitative phase analysis can also be performed on the sample which provides an indication of the weight percentage of the different phases in the sample. Care must be taken when fitting the multitude of parameters required for a complete analysis, as overfitting of diffractograms can result in a good fit without any basis in reality. This method therefore requires patience and

a systematic approach when fitting the data.

3.1.3 Electron Microscopy

Imaging of nanoscale objects is well outside the capabilities of regular optical microscopes [150, 151]. To overcome this magnification restriction, the electron microscope was developed. An electron microscope utilizes the interactions between a focused electron beam and the sample to form an image of the sample surface [150]. Given that the electron beam is focused to a few nanometers, nanoscale objects are therefore clearly visible.

The primary electrons generated by an electron microscope is sent through a series of electromagnetic lenses in order to focus the beam [150]. Some of these lenses also serve to direct the electron beam. In a scanning electron microscope (SEM), this is utilized in order to get the full image of the sample. The electron beam is scanned in the xy-plane with a set frame rate where the combination of every point forms the final image. Slower scan rates yields a higher resolution image, but it makes navigating the sample more difficult due to the slow frame rate [150]. Faster scan rates are therefore used when navigating the sample, while slower scan rates are used for the actual imaging.

Images from SEM are generated by detection of elastically or inelastically scattered of electrons interacting with the sample [150]. For elastic scattering, the primary electrons are backscattered from interactions with the atomic nuclei. These electrons are therefore called backscattered electrons. Inelastic scattering of the primary electrons occur when the primary electrons collide with the electrons belonging to the sample and transfers some of its energy to them [150]. If the energy is sufficient, these electrons will be excited to become free electrons, and are referred to as secondary electrons.

The primary electrons will not only interact with the surface of the sample, but can also penetrate into the sample depending on their kinetic energy and the density of the material [150]. This is determined by the choice of acceleration voltage used during imaging. The higher the acceleration voltage, the deeper the electrons can penetrate into the sample. However, the signal from the secondary electrons will only be detected from the first 2 nm below the surface which is called the escape depth [150]. This is due to the low kinetic energy of the secondary electrons. The image produced from secondary electrons will therefore mainly represent the surface of the sample. An example of a secondary electron image can be seen in Figure 3.9(a).

Another electron microscopy configuration is when the detector is located below the sample. This is referred to as transmission electron microscopy (TEM). Instead

of focusing the electron beam onto the sample, the optics ensure the electrons strike the sample in parallel beams [150]. Below the sample, the electron beam is then focused onto a detector plate. There are two different ways of positioning the detector. It can either be located directly below the sample which means that only electrons passing through the sample will produce a signal in the detector [150]. The resulting image will then be dark where the sample is, and bright where there is no sample. This is therefore called bright field imaging, and an example of this can be seen in Figure 3.9(b). The detector can also be placed at an angle below the sample [150]. This means that only electrons scattered by interactions with the sample will reach the detector. As a result, the sample will appear bright, while places unoccupied by the sample will be dark. This is called dark field imaging.

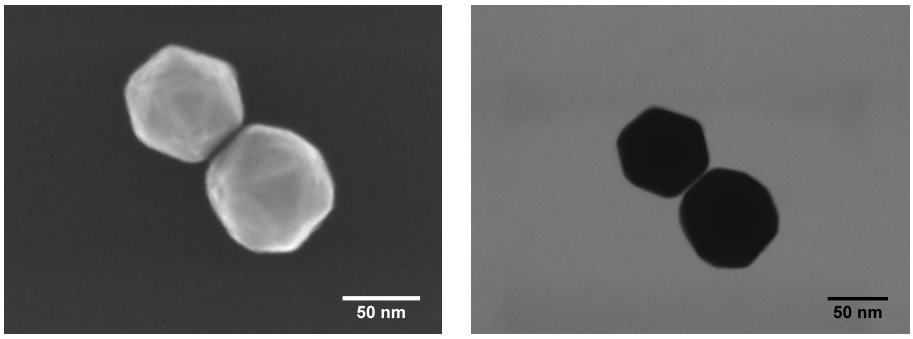

(a) **(b)**

Figure 3.9: Secondary electron image of Au-nanoparticles (a), and the corresponding bright field image (b).

When using TEM-grids with nanometer sized particles, bright field or dark field often provides for a higher resolution than secondary electron imaging. For larger particles where the surface morphology is of interest, secondary electron imaging is typically used.

When preparing samples for either SEM or TEM it is important to make sure the sample is conductive. As electrons are being directed at the sample, they will start to accumulate on the sample surface if the sample is non-conductive [150]. Accumulation of electrons will affect the incident electron beam which will distort the resulting image. This is called charging of the sample. A thin layer of a conductive material may be deposited onto the sample surface to prevent this from happening.

Another type of information which can be obtained from electron microscopy is the chemical composition of the material. This is obtained as a consequence of the

inelastic scattering of primary electrons in which core electrons in the material are excited [150]. When these core electrons relax to their ground state they will emit a photon with a characteristic energy which is material dependent. Several excitations are available for the heavier elements, and will therefore create a fingerprint over a broad range of energies in which the material can be identified. This technique is referred to as energy-dispersive X-ray spectroscopy (EDS or EDX) [150]. Spatial resolution of the elemental composition is also possible when combined with the inherent scanning feature of the scanning electron microscope. The result of this elemental mapping is an EDS map, an example of which can be seen in Figure 3.10(b).

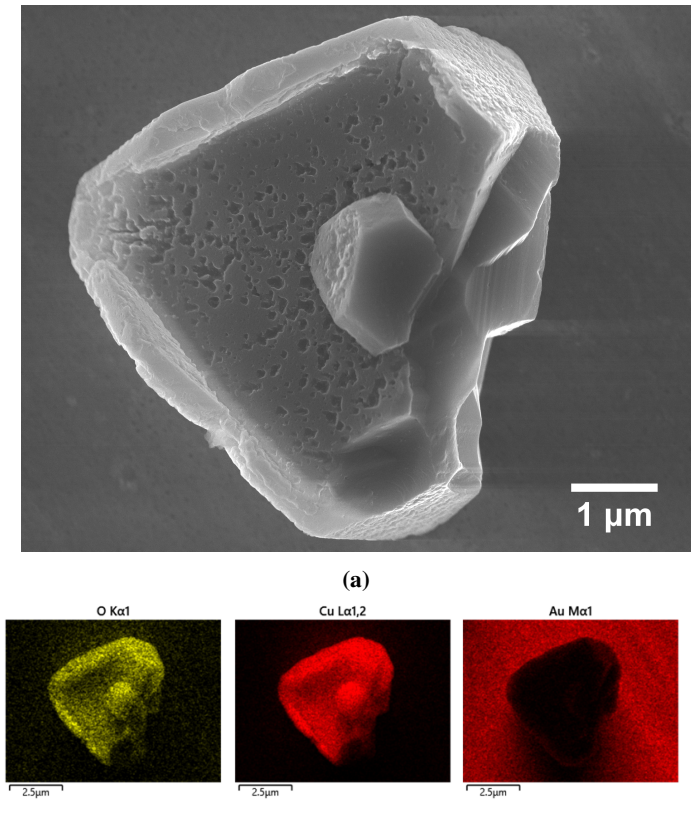

Figure 3.10: Secondary electron image of a Cu_2O particle (a), along with the corresponding EDX maps for oxygen, and copper (b). The EDX map of gold is also shown as the TEM-grid used to support the particles were made of gold.

3.1.4 Dynamic Light Scattering

Dynamic light scattering (DLS) is a method for determining the particle size of sub-micrometer particles by means of light scattering [151]. Particles dispersed in a solution of known viscosity and temperature are subjected to a monochromatic light source and the intensity of the scattered light is measured at a fixed angle with respect to the incident light [151]. Fluctuations in the light intensity is then measured and related to the Brownian motions of the particles which is also related to the particle size through the Stoke-Einstein equation [151].

In a typical setup for DLS a laser is directed towards the sample chamber and is scattered by the particles in the dispersion [151]. The scattered light is then measured at a fixed angle with respect to the incident light by a photodetector. A common scattering angle is 90°, but some instruments also have the opportunity to measure the light intensity at other angles as well [151].

The light intensity is measured over a longer period of time, and during this time the light intensity will fluctuate due to the movement of the particles in the dispersion. These fluctuations can then be Fourier transformed into an autocorrelation function, $g^{(2)}$, showing the light intensity, I, as a function of delay time, τ, after $\tau = 0$ [151].

$$g^{(2)}(\tau) = \frac{\langle I(0) \cdot I(\tau) \rangle}{\langle I \rangle^2} \tag{3.7}$$

As larger particles will be moving slower than smaller particles, the fluctuations in light intensity will also be slower for larger particles [151]. As a result, the autocorrelation function will decay much slower for larger particles as compared to smaller particles.

For a monodisperse system the autocorrelation function, $g^{(1)}$ follows an exponential decay given by

$$g^{(1)}(\tau) = \exp\left(-\Gamma \cdot \tau\right) \tag{3.8}$$

where

$$\Gamma = D \cdot \left(\frac{4\pi n}{\lambda} \sin\frac{\theta}{2}\right)^2 \tag{3.9}$$

In this equation, Γ is the decay constant, D is the diffusion constant of the particles,

n is the refractive index of the dispersion medium, λ is the wavelength of the incident light, and θ is the scattering angle [151]. The diffusion constant of the particles can then be calculated and related to the hydrodynamic radius of the particles (assuming spherical particles) through the Stoke-Einstein equation

$$D = \frac{k_b T}{6\pi\eta r} \tag{3.10}$$

where η is the viscosity of the medium and r is the hydrodynamic radius of the particles [151].

The hydrodynamic radius of the particles encompasses the radius of the particle plus the stationary liquid layer outside the particle surface [151]. As a result, the measured particle size is larger than the actual value and should therefore be treated with caution.

For polydisperse systems, on the other hand, the autocorrelation function will consist of a combination of many different decay constants. In order to obtain some information about the system, this autocorrelation function is fitted to a polynomial of degree m

$$\ln\left(g^{(1)}(\tau)\right) = \sum_{\tau=1}^{\infty} \Gamma_m \frac{-\tau^m}{m!}$$

where Γ_1 and Γ_2 are the two most important values extracted from the fitted polynomial [151]. Γ_1 is the average decay constant for the entire polydisperse system, and Γ_2 is directly related to the degree of polydispersity. By inserting Γ_1 in Equation 3.9 and Equation 3.10, an average particle size of the system can therefore be determined. The degree of polydispersity is typically described by a polydispersity index (PDI) defined as

$$\mathrm{PDI} = \frac{\Gamma_2}{(\Gamma_1)^2} \tag{3.11}$$

where a value higher than 0.1 is an indication of a polydisperse system [151].

In order to obtain reproducible results from dynamic light scattering, the sample preparation is crucial. Firstly, the particles must be dispersed in a liquid with minimal impact on the particle properties. The dispersion must therefore be stable towards agglomeration, and the particles must not be dissolved or chemically altered in any way. Secondly, the particle-particle interactions in the dispersion must be

minimized so that the correct diffusion constant is determined. However, the dispersion must not be too diluted either as the measured signal will be too weak to distinguish from the noise. An ideal dispersion concentration is typically achieved when the instrument detects between $5 \cdot 10^5$ and 10^6 counts per second [151]. As the dispersion concentration corresponding to this interval is sample dependent, no exact concentration can be recommended, but it is typically in the order of $1\,\mathrm{mg/mL}$. Finally, care must be taken as to avoid dust or other contaminations from entering the sample [151]. The presence of impurities will have a major impact on the measured particle sizes, especially if their size is large. This can be avoided to some extent by working in a cleanroom, and by filtering all dispersions with a $3\,\mu\mathrm{m}$. The choice of dispersant, optimizing the sample concentration, and filtering out impurities from the dispersion are therefore very important in order to obtain accurate and reproducible results from DLS-measurements.

3.2 Electrochemical Characterization

Initial testing of electrocatalyst performance is usually performed in three-electrode setups [126, p. 105]. This setup consists of a working electrode (WE) where the electrocatalyst is applied, a counter electrode (CE) to allow flow of charges through the system, and a reference electrode (RE), which marks the reference point for the potential difference applied to the working electrode [126, p. 105]. The potential difference between the WE and the RE is controlled with a potensiostat [152]. The potensiostat controls the potential between the WE and the RE through a feedback loop. If the potential is too low, it increases the current through the CE which results in a higher potential between the WE and RE.

In order to obtain accurate information on the catalytic activity of the electrocatalyst, the area of the working electrode must be precisely defined. This is typically achieved by using a rotating disk electrode (RDE) [153]. The RDE consists of a Teflon sleeve built around a conductive material with a fixed area which makes up the actual WE. This material can be glassy carbon, platinum, nickel or gold depending on the type of experiments being performed. Glassy carbon is typically the material of choice for testing electrocatalysts as it does not produce a strong electrochemical signal in the potential range for most electrochemical characterization. That is not the case for the other metals, which all have characteristic electrochemical behaviour that may interfere with the sample response. The catalyst material is typically applied to the WE as an ink [14]. This is usually performed by simple coating techniques such as drop casting, spin coating, or spray coating. Alternative ways of making electrocatalysts include electrodeposition, chemical vapour deposition, magnetron sputtering, atomic layer deposition and physical vapour deposition. The ink formulation may vary between different research groups,

but there are some key constituents all have in common. The goal of the ink formulation is to make sure the ink is dispersed well, that it is attached to the WE, and that electrochemical reactions are able to proceed once it is applied. In order to do this, the electrocatalyst is typically dispersed in an aqueous solution containing an alcohol [8, 17, 95]. An ionomer is also added to ensure the catalyst sticks to the electrode surface. However, the thickness of the ionomer layer should be kept to a minimum so that it does not affect the catalytic activity of the catalyst or the transport to and from the catalyst [153].

The choice of counter electrode for electrocatalytic testing depends on the nature of the catalyst material itself and which reactions are being investigated. As the counter electrode is not the electrode of interest, its contribution to the detected signal should be minimized. This can be achieved through the use of a CE with a large surface area [152]. It should also be stable towards the potentials applied during testing, and if it is not, the dissolution of the CE should not affect the reactions at the WE. An example of this is using a platinum CE when testing the HER for a nickel electrocatalyst [154]. Moving further into the HER-region on the WE may lead to oxidation of the platinum on the CE resulting in dissolution of Pt-ions. These ions could be reduced to metallic platinum at the WE which would lead to an extreme increase in catalytic activity towards the HER, and an incorrect conclusion [154]. For nickel, one is therefore better off using graphite as the CE.

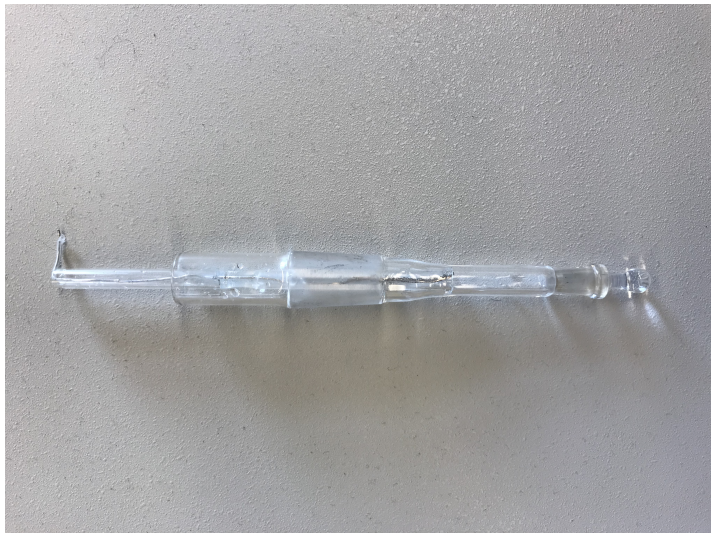

Figure 3.11: Image of a reversible hydrogen electrode (RHE).

As for the reference electrode, the choice mainly depends on what electrolyte is being used. For an acidic solution, the reversible hydrogen electrode (RHE) or

the silver-silver chloride electrode (Ag/AgCl) are two of the most commonly used references [152]. An RHE consists of a platinum wire placed in a separate chamber with ionic contact with the working electrode compartment. One example of the RHE electrode is a Pt-mesh in a glass tube, sealed in one end and placed in a larger glass holder separated from the working electrode compartment with a glass joint. An image of this can be found in Figure 3.11. Approximately half the glass tube is filled with hydrogen gas and the electrolyte has the same pH as in the working electrode compartment.

$$2\mathrm{H}^+ + 2\mathrm{e}^- \rightleftharpoons \mathrm{H}_2 \tag{3.12}$$

As this reaction is dependent on the proton concentration in the electrolyte, the pH of the solution determines the exact reference potential. As for the Ag/AgCl reference, a silver wire is placed inside a separate chamber with AgCl and KCl which is in ionic contact with the electrolyte [152]. AgCl(s) quickly forms at the Ag wire which gives rise to the redox-reaction between Ag and AgCl.

$$\mathrm{AgCl(s)} + \mathrm{e}^- \rightleftharpoons \mathrm{Ag(s)} + \mathrm{Cl}^- \tag{3.13}$$

The electrode potential for this reaction is $\Delta E = 0.207$ V in $3\,\mathrm{mol\,dm^{-3}}$ KCl [126, p. 108]. However, a chloride-based reference electrode should never be used in conjunction with most noble metal catalysts without proper separation from the working electrode compartment. The presence of chlorides significantly impact catalyst performance and durability [155]. A conventional Ag/AgCl reference electrode placed in the working electrode compartment during RDE measurements will continuously leak out chloride ions that may significantly interfere with the catalyst performance as described by Briskeby et al. [156].

Another important aspect of electrochemical characterization is the gas which the electrolyte is saturated with. Care must be taken to ensure the gas is inert towards the electrochemical reactions being tested. Oxygen is not inert within the typical potential range for many electrochemical reactions and will affect the resulting signal [131, 152]. Inert gases like N_2 and Ar are therefore typically used as saturation gases in electrochemical characterization to minimize the amount of dissolved oxygen.

Another aspect of electrochemical testing is related to diffusion. The kinetics of a reaction are often the primary reason for doing electrochemical characterization, so if the reaction is diffusion limited, information about the kinetics are hidden. To ensure that a reaction is kinetically limited, diffusion processes are sped up by ro-

tation of the WE [157]. The rotating disk electrode is connected to a rotator where the rotation speed can be specified. A rotation rate of $1600\,\mathrm{rpm}$ is commonly chosen, however, proper measurements should include several rotation rates.

3.2.1 Linear Sweep Voltammetry

In order to assess the catalytic activity of a catalyst towards an electrochemical reaction, information on how the current is affected by the potential must be examined. From section 2.4.2 a good electrocatalyst was shown to display high currents for low overpotentials (Figure 2.26). For electrode reactions in proton exchange membrane fuel cells and water electrolyzers this is evaluated by examining the overpotential required to reach $10\,\mathrm{mA\,cm^{-2}}$ (Figure 3.12(b)) [7]. In order to obtain current-potential plots from which catalytic activity may be quantified, the current response from the electrochemical setup must be measured for a range of potentials. This can be achieved through linear sweep voltammetry [158]. The potential is swept from the starting potential to the final potential at a fixed scan rate while the current is measured. An example of the scan profile and the resulting voltammogram can be found in Figure 3.12.

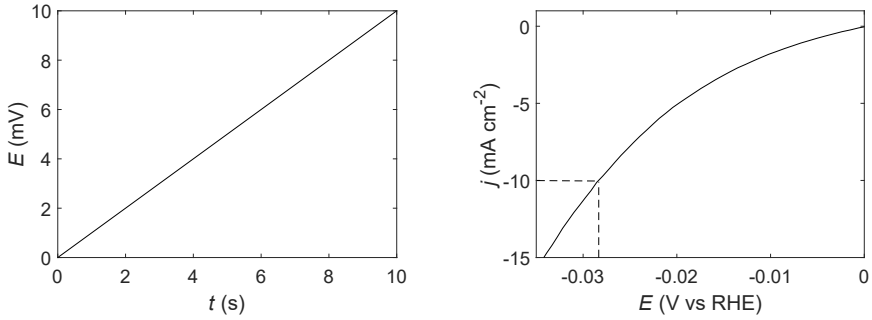

Figure 3.12: Example of a linear sweep voltammetry scan profile at $1\,\mathrm{mV\,s^{-1}}$ (3.12(a)), and the corresponding current response for the hydrogen evolution reaction on a Pt-catalyst (3.12(b)). The overpotential at $10\,\mathrm{mA\,cm^{-2}}$ is indicated by the dashed lines.

Linear sweep voltammetry should be conducted at sufficiently slow scan rates to minimize transient contributions to the current signal. A scan rate of $1\,\mathrm{mV\,s^{-1}}$ is commonly accepted to be a reasonable compromise of scan rate with respect to measurement time and stability of the catalyst/catalyst layer ensuring high degree of reproducibility.

When investigating the catalytic activity using linear sweep voltammetry it is im-

portant to remove contributions from other parts of the electrochemical setup. The solution resistance and the resistance in the external cables are of no interest to the performance of the catalysts, and since they affect the potential associated with the measured current, these should be compensated for [159]. This can be achieved by measuring the series resistance in the system using impedance spectroscopy or current interrupt. The potential associated with the measured current can then be recalculated by subtracting the contribution of this series resistance (R_{s}) from the measured potential (E_0) using Ohm's law.

$$E = E_0 - IR_{\mathrm{s}} \tag{3.14}$$

This is referred to as IR-compensation, and in order to make sure the estimation of the uncompensated series resistance is not overestimated, a common rule of thumb is to multiply the experimentally measured uncompensated resistance with 0.85-0.9 [159] during measurements.

3.2.2 Cyclic Voltammetry

Changes in oxidation states, oxide formation, reduction phenomena, gas evolution and material stripping are all electrochemical processes that are associated with specific material dependent potential regions. A convenient way to monitor these phenomena is to sweep the potential over a larger range while measuring the resulting current. A change in current is associated with the appearance of one of these processes. As the potential at which these processes occurs is material dependent, this technique can be used as a way of identifying the material akin to spectroscopic fingerprints in physical characterization. This electrochemical method is called cyclic voltammetry and it is one of the most important tools in our electrochemical toolbox [152].

Cyclic voltammetry involves sweeping the potential back and forth between two potentials with a constant scan rate [152, 158]. The processes of interest in cyclic voltammetry are transient and does not require quasi steady state conditions like linear sweep voltammetry. Considerably faster scan rates between 5 and $500\,\mathrm{mV\,s^{-1}}$ can therefore be used [158].

The behaviour of the resulting peaks can reveal what type of process is occurring at the electrode surface. For adsorption and desorption processes, sharp symmetrical peaks can be found in the voltammogram [158]. One of the most famous adsorption/desorption peaks are those belonging to hydrogen on a Pt-electrode. Two such peaks arise in the voltammogram. The area under these peaks in the voltammogram is equivalent to how much hydrogen that has been adsorbed or desorbed from the Pt-surface [158]. It can therefore be used to estimate the electrochemically act-

ive surface area (ECSA) of the Pt-surface [160]. In doing so it is also important to disregard the contribution to the current from the electrical double layer and any hydrogen evolution that might be happening moving to lower potentials. The area indicated in Figure 3.13(b) is therefore used to estimate the ECSA of a Pt electrode [160]. This area represents the charge from the hydrogen, and by using literature values for the charge density of hydrogen ($220\,\mu\mathrm{C\,cm^{-2}}$) one can easily calculate the ECSA [160]. The characteristic voltammogram of Pt can be found in Figure 3.13(a).

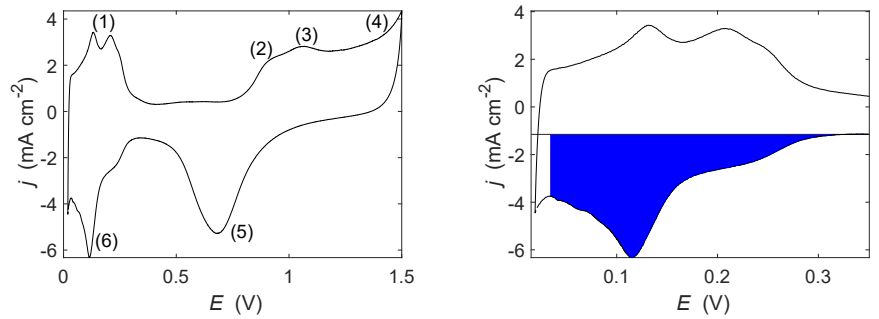

Figure 3.13: Voltammogram of a Pt-electrocatalyst supported on carbon obtained with a scan rate of $50\,\mathrm{mV\,s^{-1}}$ (a), and an illustration of the area used to determine the ECSA from hydrogen adsorption (b). The different surface reactions occuring on Pt are marked. (1) is hydrogen desorption, (2) is the formation of PtOH closely followed by further oxidation into PtO (3). Onset of oxygen evolution then follows (4). On the reverse scan, PtO is reduced back to Pt (5), before underpotential deposition of hydrogen begins (6).

Another common phenomenon found in voltammetry is the appearance of a stripping peak [158]. This is when the electrochemical process removes an existing surface layer from the electrode. This can be recognised as the disappearance of a peak in the voltammogram between two consecutive cycles [158, 161]. A common application of this process is CO-stripping for determination of the surface area of the electrode [161]. CO readily adsorbs to metal surfaces, so by purging the electrolyte with CO prior to electrochemical measurements, one ensures that CO is adsorbed to the metal surface. Cyclic voltammetry is then performed and a large peak belonging to CO-stripping will be observed in the first cycle, whereas on the following cycle, the peak will have disappeared [161]. The difference between the first and second cycle therefore indicates the electrochemical surface area of the catalyst. The position of the CO-stripping peak is also dependent on how strongly it binds to the underlying metal [161]. It can therefore be used to asses the catalytic

activity of the catalyst towards CO-oxidation and reactions involving adsorbed CO as a reaction intermediate.

3.3 Ultrasound Characterization

In order to properly assess the results from a sonochemical synthesis, all sonochemical parameters must be accounted for. This is to ensure that any deviations in results between experiments can be accounted for when drawing a conclusion. The ultrasonic frequency is quite easy to control, as it is directly dictated by the signal generator. The acoustic power, however, is strongly influenced by the impedance mismatch between signal generator and transducer as explained in Section 2.2.2. It must therefore be measured in a separate experiment so it can be accounted for. The sum of all ultrasound parameters also determines the rate of radical generation in the system. One therefore has to measure the rate of radical formation in order to evaluate how the different parameters affect the cavitation process. In this section we will discuss how acoustic power is estimated through calorimetric measurements, and how radical generation from ultrasound is estimated indirectly through dosimetric techniques.

3.3.1 Calorimetry

The acoustic power transferred to a solution determines the maximum bubble size in the final rarefaction cycle (equation 2.13) and the number of cavitation bubbles [69, 107]. It is therefore absolutely essential to the radical generation rate. Failing to account for it when varying other ultrasound parameters will therefore be detrimental to the conclusion. To the inexperienced sonochemist, this is an easy mistake to make as it might be difficult to distinguish between electrical power and acoustic power. As explained in Section 2.2.2, impedance matching between signal generator and transducer determines how much of the electrical signal is converted into mechanical motion. The impedance mismatch is also heavily frequency dependent resulting in larger mismatch for lower frequencies. Failing to account for the mismatch could therefore lead to a conclusion where the frequency is the determining factor, when in reality it is just a difference in acoustic power.

When the acoustic wave propagates through the solution, the energy is lost to cavitation and acoustic streaming [19]. The energy absorbed by the cavitation event is eventually released as a shockwave and a local increase in temperature. However, over multiple ultrasonic cycles, this local heating will start to cause a global heating in the solution as well, which can be detected with a thermocouple [162, 163]. As sonochemists we are mostly concerned with the energy needed to produce the primary radicals. Even though some energy is lost to acoustic streaming and shockwave formation, only the temperature increases can be measured with

the thermocouple. As the temperature increase is mainly caused by the cavitation event, a direct measurement of the acoustic power used to produce radicals is therefore obtained. It should be mentioned that acoustic streaming and shockwave formation also produce some heat due to movements in the solution, but not nearly as much as the bubble collapse [162]. The increase in temperature due to sonication is therefore a reasonable estimate of the acoustic power used to produce radicals in a sonochemical system.

Just like the enthalpy of a chemical reaction can be calculated from calorimetric temperature measurements, so too can the acoustic power (P_a) in sonochemistry [162, 163].

$$P_\mathrm{a} = \rho V C_\mathrm{p} \left(\frac{dT}{dt}\right)_{t=0} \tag{3.15}$$

V is the volume of the solution, ρ is the density of the solution, C_p is the specific heat capacity of the solution at constant pressure, and $\left(\frac{dT}{dt}\right)_{t=0}$ is the initial temperature increase in the solution per unit time. The temperature increase should be linear as can be seen in Figure 3.14. The slope of this curve therefore provides the value for $\left(\frac{dT}{dt}\right)_{t=0}$.

Calorimetric ultrasound measurements are typically conducted in deionized water to avoid the influence of other species, and because its physical and chemical properties are so well known. At $20\,^\circ\mathrm{C}$, the specific heat capacity of water is ($4.186\,\mathrm{J\,g^{-1}\,K^{-1}}$) [164] and the density is $0.998\,\mathrm{kg\,dm^{-3}}$ [54]. The specific heat capacity and density are quite stable between 20 and $30\,^\circ\mathrm{C}$, which means that a dynamic value for these constants is not necessary if the temperature increase is limited to this range. However, a lower acoustic power could be achieved when the solution temperature is higher than room temperature as the surrounding reactor walls (which are still close to room temperature) will absorb some of the heat that is generated. This can be seen in Figure 3.14.

The general procedure for performing calorimetric ultrasound experiments is therefore to limit the temperature increase to relatively short sonication times (1-2 min) [162]. The water should be changed for every measurements in order to return to room temperature and to avoid the buildup of H_2O_2 and other sonolysis products which could affect the specific heat capacity and density. The temperature should also be measured as close to the center as possible to avoid any edge effects from the reactor walls. When reporting the acoustic power, it is also common to report it normalized to the solution volume ($\mathrm{W\,dm^{-3}}$) and/or normalized to the area of the sonotrode/plate ($\mathrm{W\,cm^{-2}}$).

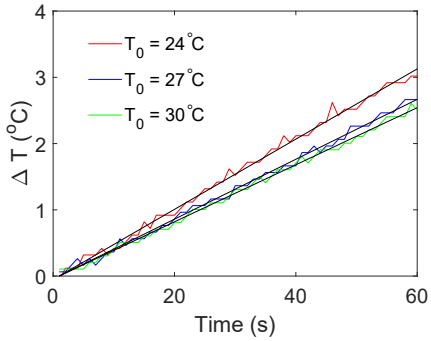

Figure 3.14: Temperature increase as a function of sonication time for three water solutions of 200 mL sonicated at 346 kHz with a load power of 50 W. The starting temperature of each solution was 24 °C (red), 27 °C (blue), and 30 °C (green).

3.3.2 Dosimetry

In order to quantify the sonochemical generation of the short lived radicals in an ultrasonic system, more stable species formed through reactions with the radicals are measured. Such indirect measurements of the radical generation rate is referred to as dosimetry, and there are many different dosimeters available for sonochemical characterization. Through sonolysis of an aqueous system, we would expect [·OH] = [·H], which means that only one of these radicals would have to be measured. As previously explained, the ·H is the most unstable radical of the two, and will recombine into H_2 or recombine with ·OH to form H_2O almost immediately after bubble collapse which means that it is very difficult to indirectly measure the ·H. The ·OH, on the other hand, has a longer lifetime, and will be able to diffuse into the hot-shell surrounding the collapsed bubble and therefore react with species there as well. Dosimeters involving the ·OH are therefore typically used when quantifying the radical formation rate.

Weissler Dosimetry

One of the most common dosimeters for the detection of ·OH is potassium iodide (KI) dosimetry, more commonly known as Weissler dosimetry. This method relies on the oxidation of I^- to $I_3{}^-$ through a series of reaction steps. $I_3{}^-$ has a distinctly yellow colour with a maximum absorbance at 350 nm. It can therefore be quantified by measuring the absorbance using UV-visible spectroscopy (Section 3.1.1). The absorbance (A) can then be related to the concentration (c) of $I_3{}^-$ through Beer-Lambert's law (equation 3.3)

Literature reports varying maximum absorbance wavelengths and ϵ values for $I_3{}^-$

from $26\,000\,\mathrm{mol^{-1}\,dm^{-3}\,cm^{-1}}$ at 350 nm [165] to $26\,300\,\mathrm{mol^{-1}\,dm^{-3}\,cm^{-1}}$ at 355 nm [77].

The oxidation of I^- to $I_3{}^-$ starts with the diffusion of ·OH into the bulk solution where it reacts with I^- forming an iodine atom.

$$I^- + OH \longrightarrow OH^- + I$$

The iodine atom is not stable and will react with I^- and the resulting $I_2{}^-$ will experience a disproportionation reaction

$$I + I^- \longrightarrow I_2{}^-$$

$$2I_2{}^- + \longrightarrow I_2 + 2I^-$$

The molecular iodine will then react with excess I^- and form triiodide $I_3{}^-$

$$I_2 + I^- \longrightarrow I_3{}^-$$

The net reaction for $I_3{}^-$ formation can therefore be expressed as

$$2(\cdot OH) + 3I^- \longrightarrow I_3{}^- + 2OH^- \tag{3.16}$$

which means that the amount of ·OH can be determined from the concentration of $I_3{}^-$ as [·OH] = 2[$I_3{}^-$]. However, the ·OH formed during ultrasonication may also recombine with themselves resulting in hydrogen peroxide following equation 2.19. H_2O_2 could also potentially oxidize the iodide ions to molecular iodine as follows

$$H_2O_2 + 2H^+ + 2I^- \longrightarrow I_2 + 2H_2O \tag{3.17}$$

The oxidation of I^- by H_2O_2 would increase the [$I_3{}^-$] if it were not for the very slow kinetics of this reaction [77]. The generation of H_2O_2 will therefore only slightly increase the [$I_3{}^-$] which means that the total concentration of ·OH can be expressed as

$$[\cdot OH] = 2([I_3{}^-] + [H_2O_2]) \tag{3.18}$$

Only considering the I_3^- formation will therefore result in a lower estimation for the [·OH], but it can still be used as an indication or for comparison purposes. Alternatively, a catalyst can be utilized to facilitate the reaction in Equation 3.17. A molybdate catalyst has been successfully used to enhance the rate of KI oxidation by H_2O_2 [77][166].

It can also be seen from Equation 3.16 that the equilibrium is dependent on the pH of the solution where a higher concentration of I_3^- is expected at lower pH values due to the Le Chatelier principle. Iida et al. [77] showed the pH dependence experimentally by performing Weissler dosimetry at selected pH values between 2 and 9. The expected trend as predicted from Le Chatelier's prinicple was confirmed for pH values below 4 and above 7. However, for pH values between 4 and 7, the concentration of I_3^- was found to be constant. Performing Weissler dosimetry in this pH range is therefore desirable, as slight changes in pH would not affect the I_3^- concentration. The pH of 0.1 $\mathrm{mol\ dm^{-3}}$ KI falls within this range [77], and can therefore be used as is to determine the ·OH formation. For prolonged sonication with a high rate of radical formation, however, an increase in pH could occur as indicated by Equation 3.16. The $[I_3^-]$ as a function of time would therefore be expected to deviate from a linear behaviour yielding a lower $[I_3^-]$ per unit time. Applying a buffer solution in order to keep the pH constant could therefore mitigate the problem. This was done by Gutierrez et al. [165] by using a phosphate buffer to keep the pH at 5.9. Alternatively, the radical generation rate could also be estimated from the time derivative of the $[I_3^-]$ at t = 0 min.

Titanyl Dosimetry

Where the Weissler method relies on the oxidation of an added chemical to estimate the ·OH, the titanyl method is performed in water only [33, 80, 167]. Without any added chemicals to react with, the ·OH will recombine into more stable substances with one of the dominating products being H_2O_2. To detect H_2O_2, a sample is extracted from the ultrasonic reactor and mixed with $TiOSO_4$ which results in the formation of a yellow Ti-complex with a maximum absorbance at $411\ \mathrm{nm}$ [33, 80, 167]. The UV-Vis spectrum of this complex can be seen in Figure 3.2(a). The H_2O_2 concentration can therefore be estimated using Beer-Lambert's law (Equation 3.3) with $\epsilon = 787\ \mathrm{mol^{-1}\ dm^3\ cm^{-1}}$ [23].

Unlike the Weissler method, the titanyl dosimetry method proceeds through zero order kinetics [33, 167]. This is expected as the generation of ·OH radicals is linear with time. The titanyl dosimetry method is a well established method for detecting hydrogen peroxide, even featuring in some of the earliest assessments of sonochemical effects by Alfred Weissler [80]. It is therefore a well established method which has also been utilized more recently as well [33, 167].

Sonochemical Efficiency

Based on the ·OH radical concentration found from dosimetry experiments, and the acoustic power (P_{a}) found from calorimetry experiments, the sonochemical efficiency (SE) is expressed as

$$SE = \frac{[\cdot \mathrm{OH}]V}{P_{\mathrm{a}} \cdot t} \tag{3.19}$$

where V is the volume of the solution, and t is the sonication time [40]. Its purpose is to display the radical yield of ultrasound independent of the applied power. Koda et al. [40] therefore attributed any changes in sonochemical efficiency to changes in frequency. When assessing the radical generation capabilities at a specific ultrasonic frequency, the sonochemical efficiency should therefore be used.

Chapter 4

Two Routes for Sonochemical Synthesis of Platinum Nanoparticles with Narrow Size Distribution

Two Routes for Sonochemical Synthesis of Platinum Nanoparticles with Narrow Size Distribution

Henrik E. Hansen[1,2], Frode Seland[1], Svein Sunde[1], Odne S. Burheim[2], Bruno G. Pollet[2*]

[1]Electrochemistry Group, Department of Materials Science and Engineering, Faculty of Natural Sciences. Norwegian University of Science and Technology (NTNU), NO-7491 Trondheim, Norway

[2]Hydrogen Energy and Sonochemistry Research Group, Department of Energy and Process Engineering, Faculty of Engineering, Norwegian University of Science and Technology (NTNU), NO-7491 Trondheim, Norway

Abstract

A novel sonochemical approach to synthesize platinum (Pt) nanoparticles has been developed to produce smaller, and more monodisperse particles than traditional chemical reduction methods such as the sodium borohydride ($NaBH_4$) reduction method. It was also found that careful experimental manipulation of the ultrasonic conditions such as the ultrasonic frequency (f), the acoustic power (P_a) and the solution volume (V) may be employed to tailor the sonochemical radical yield to the same value for two different ultrasonic systems (20 kHz provided by an ultrasonic probe or sonifier, and 408 kHz by an ultrasonic plate transducer) leading to a similar reduction rate, and as a consequence, to Pt-nanoparticles with similar sizes. The reduction of Pt(IV) was found to be a first order reaction with a rate constant (k) of 0.062 min^{-1} for both ultrasonic systems, and the particle sizes from TEM measurements were found to be (2.2 $\pm$ 0.5) nm and (2.3 $\pm$ 0.4) nm for the 20 kHz and the 408 kHz samples, respectively. In comparison, the chemical reduction method resulted in particle sizes of (3.0 $\pm$ 0.5) nm. It was also found that the sonochemical synthesis at 408 kHz was more efficient than at 20 kHz with an initial sonochemical efficiency of (0.20 $\pm$ 0.04) $\mu mol\ kJ^{-1}$ at 408 kHz and (0.060 $\pm$ 0.004) $\mu mol\ kJ^{-1}$ at 20 kHz. The sonochemical synthesis at 408 kHz also yielded nanoparticles of higher purity. Interestingly, direct sonication into the reaction vessel using the 20 kHz sonication probe produced impurities of Ti, V and Al in the solution, indicating that direct sonication at lower frequencies led to (i) probe material (made of Ti alloy - Ti-6Al-4V) erosion induced by cavitation and (ii) a continuous supply of micro meter sized impurities. It was also observed that the introduction of impurities increased the reduction rate constant of Pt(IV) through heterogeneous nucleation (k = 0.12 min^{-1}) as was demonstrated for the 408 kHz system under controlled addition of Ti/Al/V seed microparticles. Direct sonication using a sonifier should therefore be avoided when high purity catalytic materials are required.

Keywords: power ultrasound; sonochemistry; electrocatalyst; fuel cell; electrolyzer.

Introduction

In the last few years, many research works have been focused on developing new technologies which can replace fossil fuels and other greenhouse gas emitting sources. One such a technology is connected to electrochemical energy conversion where the electrical energy is generated from the oxidation of a fuel (H_2(g) - hydrogen oxidation reaction, HOR), and the reduction of an oxidant (O_2(g) - oxygen reduction reaction, ORR) in the presence of a catalyst to produce water. This device is referred to as a fuel cell. The reverse reactions are also possible, where

H_2(g) and O_2(g) are produced via the hydrogen evolution (HER) and oxygen evolution reactions (OER) at the expense of electrical energy, and this device is called an electrolyzer.

In order for fuel cells and electrolyzers to work efficiently, catalysts present at the anode and cathode must improve the slow kinetics associated with the anode and cathode electrochemical reactions for both fuel cells and electrolyzers [1]. Platinum (Pt), a Platinum Group Metal (PGM), has been proven to be an excellent catalyst for these reactions, and is therefore the material of choice in already available commercial products [2]. Improvements of these technologies therefore lies in either developing low-cost, highly-performing and durable materials with better or similar catalytic activity, or improving the catalytic activity of the Pt-catalysts.

As the overall catalytic activity is closely related to the surface area of the catalyst, synthesis of Pt-nanoparticles with high surface areas has been investigated [2][3]. A common method for such a synthesis is by chemical reduction of Pt-salts (e.g. $PtCl_4$) using for example, $NaBH_4$ [3]. $NaBH_4$ is a strong reducing agent that allows for a simple and fast synthesis procedure, which is ideal for industrial applications. However, the chemical reduction method has limitations, e.g. in controlling the particle size without the addition of additives such as surfactants (e.g. polyvinyl pyrrolidone, PVP) [4]. Moreover, these surfactants must also be removed from the nanoparticles after the synthesis as they are known to block the active sites at the catalyst surface [4], thus adding more complexity to the synthesis procedure. Methods involving co-precipitation [5], microwave irradiation [5], refluxing [5] [6], spray drying pyrolysis [7], and hydrothermal synthesis [5] [8] have also been used successfully to synthesize a range of nanomaterials.

Alternatively, a sonochemical method [5][9][10][11][12][13] can offer an additive-free synthesis with improved control over particle size. This synthesis method employs low-frequency high-power ultrasound (20 kHz - 1 MHz) in order to generate highly reactive radicals (H· and OH·, produced via sonolysis [14]) in the solution, which act as reducing agents (H·) for metal ions (M^{n+}) in the solution. These mechanisms have been described in several works [10][11][15] as follows:

$$H_2O \longrightarrow H\cdot + OH\cdot \tag{1}$$

$$M^{n+} + \text{reducing radicals} \longrightarrow M^0 \tag{2}$$

Such an in situ generation of reducing radicals at room-temperature is a major advantage over traditional methods as it removes the cost of adding expensive

reducing agents, provides an easy way to adjust reduction rates, and reduces the HSE-risks typically associated with powerful reducing agents.

It has been found that the metal nanoparticle sizes depend on the ultrasonic parameters used during the sonochemical synthesis [10][11][15]. Ultrasonic frequency, type of alcohols and surfactants, as well as atmospheric gasses have been shown to contribute to the final nanoparticle size [12]. In the case of atmospheric gasses, Merouani et al. recently simulated free radical production in acoustically driven bubble systems and showed that a low thermal conductivity and high polytropic ratio are favoured in order to achieve a higher radical yield, and therefore smaller particle sizes [16].

Surfactants and alcohols may also be used in order to adjust the final particle size as these act as radical scavengers. Due to the hydrophobic nature of the alcohols and surfactants, they are situated on the bubble/solution interface, and upon bubble collapse they usually are in the most immediate proximity of the radicals generated in the collapse. The alcohols and surfactants (RH) therefore react with these radicals and become secondary radicals (R·). Afterwards, these secondary radicals diffuse into the bulk solution where reactions with the metal ions (M^{n+}) proceed as follows [11][15]:

$$\mathrm{RH} + \mathrm{OH}\cdot\,(\mathrm{H}\cdot\,) \longrightarrow \mathrm{R}\cdot + \mathrm{H_2O}(\mathrm{H_2}) \tag{3}$$

$$\mathrm{M}^{n+} + \text{reducing species}\,(\mathrm{R}\cdot\,, \mathrm{H}\cdot\,, \text{etc.}) \longrightarrow \mathrm{M}^0 \tag{4}$$

The presence of such additives therefore increases the reduction rate constant (k), and decreases the particle size as previously shown in several works [10][11][12]. It has also been found that the role of the surfactant in the sonochemical synthesis is to improve the radical yield, and not to act as steric hindrance as it is for the chemical reduction method.

The effect of ultrasonic frequency (f), however, is one of the main contributors to the final nanoparticle size and is of great interest as it is tuneable (up to 1 MHz). Okitsu et al. [15] showed that the reduction rate exhibited a maximum value around an ultrasonic frequency of 213 kHz. This maximum value resulted from a higher yield of radicals per bubble at lower frequencies, and a higher number of bubbles generated at higher frequencies. Careful considerations of the ultrasonic frequency for a given system can therefore be used to achieve the preferred nanoparticle size.

Using ultrasound to synthesize nanoparticles of specific sizes and shapes can be

an important step when attempting to improve the catalytic activity of catalysts for applications such as fuel cells and electrolyzers. Much research has already been published on sonochemical synthesis of PGMs where the main focus has been on exploring the contributions from the individual ultrasonic parameters on the overall reduction rate and yield. Okitsu et al. [15] also investigated the effect of ultrasonic frequency on the reduction rate and particle size of gold (Au) nanoparticles and found that the highest reduction rate and the smallest nanoparticles were achieved using an ultrasonic frequency of 213 kHz. The same group [11] also investigated the sonochemical synthesis of Ag, Pd, Au, Pt and Rh. Caruso et al. [10] demonstrated that the reduction rate of Pt can be increased by adding alcohols to the solution. Much work has therefore been carried out on the fundamental understanding of how sonochemical reduction occurs for these noble metals, and thus, the next step is to explore its potential for industrial applications. Here, it is important to assess whether the sonochemical route can compete with the well established chemical reduction methods in terms of achieving the target size and shape of the final nanoparticles, obtaining a monodisperse particle system, and the possibility of scaling up the process.

The scope of this study is to assess whether two ultrasonic reactors generating different frequencies (20 kHz and 408 kHz) can result in the same size of Pt-nanoparticles when the radical yield from the sonolysis is tuned to the same value. Taking into account the solution volume (V) and the applied acoustic power (P_{a}), we can therefore determine which sonochemical reactor is more efficient for potential industrial scale production. To quantify the radical yield, the potassium iodide (KI) dosimetry method was used (also known as the Weissler method [17]), while the reduction rate of Pt(IV) was monitored with a colorimetric technique involving UV-Vis spectroscopy. Pt-nanoparticles were also synthesized by the chemical reduction route using $NaBH_4$, and then compared to the sonochemical method. Additionally, the use of seed Ti/V/Al microparticles to enhance the reduction rate of Pt(IV) in the sonochemical method was also explored as a possible solution for scaling up the production of Pt-nanoparticles. The chemical composition and the particle sizes were investigated using X-ray diffraction (XRD), scanning (SEM) and transmission electron microscopy (TEM) and dynamic light scattering (DLS).

Experimental Methods

Synthesis

For the sonochemical synthesis of Pt-nanoparticles, an aqueous solution of 2.0 mmol dm^{-3} $PtCl_4$ (99.9% metal basis) was prepared using a solution of 0.8 mol dm^{-3} $96\,\%$ ethanol. Milli-Q water with a resistivity of $18.2\,\mathrm{M\Omega cm}$ at $25\,^{\circ}\mathrm{C}$ was

used for preparing the ethanol solution. The solution was then stirred with an electromagnetic stirrer for 10 min to ensure a homogeneous solution.

Sonication was performed using a 20 kHz sonicator probe (sonifier) and a 408 kHz plate transducer, both described in detail in Section . For the 20 kHz sonicator, 50 mL of the prepared solution was purged with Ar-gas for 10 min before being sonicated using an on:off cycle of 1s:1s to prevent excessive heating. An Ar-atmosphere was also maintained above the solution. Samples of 4 mL were extracted after 0 min, 5 min, 10 min, 20 min, and 40 min of sonication for the determination of the reduction rate constants. The temperature was maintained at $5\,^{\circ}\mathrm{C}$ by active cooling of the solution. For the 408 kHz plate transducer, 200 mL of the prepared solution was purged with Ar-gas for 10 min before being sonicated continuously for 80 min. An Ar-atmosphere was maintained above the solution throughout the sonication, and the temperature was maintained at $20\,^{\circ}\mathrm{C}$ due to practical limitations. 4 mL samples were extracted after 0 min, 5 min, 10 min, 20 min, 40 min, 60 min, and 80 min of sonication. The sonochemical syntheses were repeated three times for each of the two ultrasonic systems used in this study.

For the chemical reduction of Pt-nanoparticles, a method described by Morales et al. [18] involving sodium borohydride ($NaBH_4$) as the reducing agent was used. 1 mL of 44 mmol dm^{-3} $NaBH_4$ (granular, 10-40 mesh, $98\,\%$) from Sigma Aldrich was added to 50 mL of 2.0 mmol dm^{-3} (99.9% metal basis) $PtCl_4$ prepared in 0.8 mol dm^{-3} $96\,\%$ ethanol. The solution was then stirred with an electromagnetic stirrer for 30 min.

Pt-nanoparticles were then removed from the remaining solution by centrifugation at 12,000 rpm for 15 min, and redispersed in ethanol in preparation for SEM, TEM and XRD measurements. For all other measurements, the original solution was used.

Sonochemical Setup

The experimental setup for the 20 kHz sonicator probe is shown in Figure 1a. It uses a Q700 sonicator system from QSonica with a maximum power output of 700 W along with a probe measuring 19 mm in diameter. The temperature was maintained using a compact recirculating chiller from QSonica in combination with a water bath surrounding the beaker containing the solution. An ultrasonic amplitude of $50\,\%$ was used. The acoustic power of the system was determined calorimetrically [19] and was found to be (42.9 $\pm$ 0.3) W. The ultrasonic probe was immersed directly into the reaction vessel.

The plate transducer used at a frequency of 408 kHz is shown in Figure 1b. This setup differs from the QSonica system in that a plate transducer at the bottom of

the reactor supplies the ultrasonic power, and that the atmosphere inside the reactor is isolated from the external environment. The temperature was maintained using a cooling jacket around the reactor where water was circulated from a cooling bath. An ultrasonic amplitude of $100\,\%$ was employed and the acoustic power was determined calorimetrically and found to be (54 ± 2) W. The ultrasonic plate transducer was directly in contact with the reaction solution.

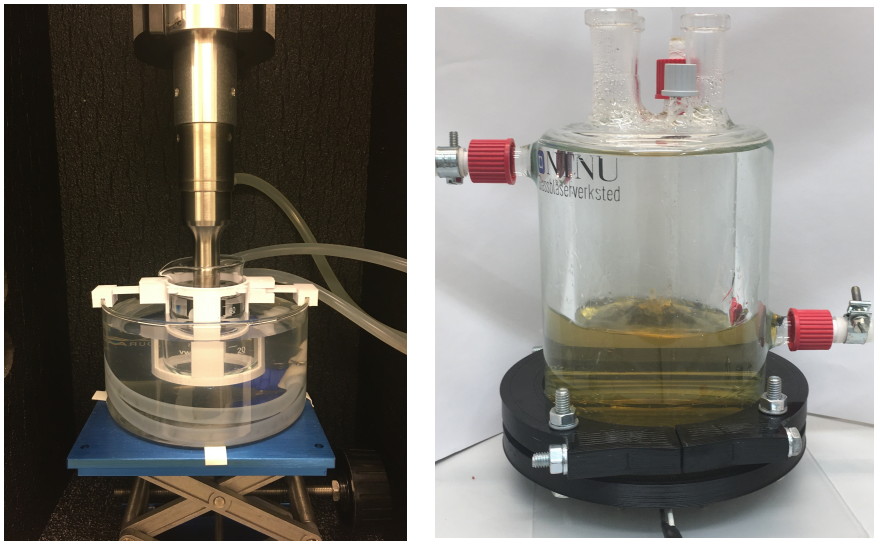

(a) **(b)**

Figure 1: Ultrasonic setup for the QSonica Q700 20 kHz sonicator probe (a), and the 408 kHz plate transducer (b).

Physical Characterizations

In order to observe if exposure to ultrasound affected the $PtCl_4$-solution, samples were extracted at selected time intervals and subjected to UV-Vis spectroscopy using a Thermo Scientific Evolution 220 UV-Vis spectrophotometer. The absorbance of the samples was measured over a wavelength range of 200 nm-800 nm with a scan rate of 100 nm min^{-1}.

Further investigations into the reduction of $PtCl_4$ were also performed using a colorimetric technique based upon potassium iodide (KI). This technique involves mixing a $PtCl_4$-solution and an excess of KI which allows the remaining Pt(IV) in the solution to react with I^--ions forming $PtI_6{}^{2-}$ [20]. Using this technique for the samples extracted at different sonication times allowed us to determine the changes in the Pt(IV)-concentration and therefore also the reduction rate constant

of $PtCl_4$. This was achieved by plotting the concentration of Pt(IV) as obtained by UV-Vis spectroscopy against sonication time, and fitting the resulting curve to an exponential function. Semi-logarithmic plots were also used to easily identify any deviations from the exponential fit. These semi-logarithmic plots were also normalized against the respective initial concentrations of Pt(IV) for both samples. In order to avoid interference from any Pt-nanoparticles formed during the sonication, the original UV-Vis spectra of the samples were subtracted from their respective colorimetric spectrum.

The Pt(II)-concentration was also determined using the same colorimetric technique. However, due to the overlap of the Pt(II) peaks with the rest of the spectrum, the Pt(IV) spectrum had to be subtracted before quantification at 388 nm could be performed. Assuming that the sum of the Pt(IV)- Pt(II)- and Pt(0)-concentration equals the initial concentration of Pt(IV), the yield of Pt-nanoparticles from the sonochemical methods could be determined.

For X-ray diffraction (XRD), measurements were performed using a Bruker D8 A25 DaVinci X-ray Diffractometer with CuKα radiation. The samples were drop cast onto a flat Si wafer and covered with a Kapton film to prevent unwanted exposure to the surrounding environment. The measurements were carried out using a scan rate of $0.044\,^\circ/\mathrm{step}$ for 2θ-angles between 15°-75° and a 0.3° fixed slit for 60 min. The resulting diffractograms were then compared to the COD database using the DIFFRAC.EVA software before undergoing Rietveld refinement using the Topas software.

The sample preparation for dynamic light scattering (DLS) involved diluting the samples in Milli-Q water until the particle count was sufficient (below 2×10^6 cps). The samples were then sonicated in the Elmasonic P ultrasonic bath for 1 min with a frequency of 80 kHz to obtain a homogeneous dispersion. The DLS-measurements were performed in an ISO 7 cleanroom using a Beckmann Coulter N5 submicron particle size analyzer. The cuvettes used for the measurements were cleaned with Milli-Q water filtered through a $0.2\,\mu\mathrm{m}$ particle filter. The particle dispersions were then transferred to the cuvettes using a syringe with a $2.7\,\mu\mathrm{m}$ particle filter. The detector angle was chosen to be 90° for all measurements. Ten measurements were performed for each sample. Using the obtained autocorrelation function, the Beckmann Coulter PCS software calculated the mean particle size, standard deviation and polydispersity index for every measurement.

Sample preparation for scanning (SEM) and transmission electron microscopy (TEM) was performed by dispersing the particles in ethanol ($96\,\%$). The samples were then drop cast onto a Formvar, Copper TEM-grid, before being allowed to dry over night. SEM images were acquired with an APREO SEM using an accel-

eration voltage of 30 kV and an emission current of 0.4 nA, while TEM images were acquired with a JEOL JEM-2100 TEM with an acceleration voltage of 100 kV.

Dosimetry Determination

Measuring the sonochemical formation of radicals (H· and OH·) in an aqueous solution during sonication is challenging due to the radicals' short lifespan. There are several chemical dosimetry methods (e.g. terephthalic acid, Fricke and Weissler methods) for determining the hydrogen peroxide (H_2O_2) or the hydroxyl radical (OH·) formation during sonication. In this study, we used the Weissler dosimetry method, i.e. the sonication of pure aqueous potassium iodide (KI) solution. 0.1 mol dm^{-3} KI solution saturated with Ar-gas for 10 min was sonicated for 20 min, as described by Iida et al. [21], Son et al. [22], and La Rochebrochard d'Auzay et al. [23], to determine OH· radical concentrations. The resulting I_3^- formation was monitored by a Thermo Scientific Evolution 220 UV-Vis spectrophotometer at a wavelength of 350 nm (λ_{max}), using a molar extinction coefficient (ϵ) of 26,000 $dm^3\ mol^{-1}\ cm^{-1}$.

For the Weissler dosimetry, the reaction pathway is the direct oxidation of iodide ions I^- in solution by OH· forming iodine I (Equation 5).

$$OH\cdot + I^- \rightarrow OH^- + I \tag{5}$$

The iodine reacts with I^- to produce I_2^- (Equation 6) which subsequently give rises to I_2 (Equation 7).

$$I + I^- \rightarrow I_2^- \tag{6}$$

$$2\,I_2^- \rightarrow I_2 + 2\,I^- \tag{7}$$

Molecular iodine produced from these reaction pathways reacts with excess I^- to form triiodide ions, I_3^- (Equation 8).

$$I_2 + I^- \rightarrow I_3^- \tag{8}$$

This method also allows the determination of the rate of triiodide anion formation $\nu(I_3^-)$ (mol s^{-1}) and thus the rate of formation of OH·, i.e. assuming that $\nu(I_3^-)$ = ν(OH·). However, in order to assess the sonochemical effects of an ultrasound

system, the sonochemical efficiency (SE) must be calculated as shown by Koda et al.[24]

$$SE = \frac{[\mathrm{I_3}^-] \times V}{P_\mathrm{a} \times t} \tag{9}$$

where V is the volume of the KI-solution, P_a is the acoustic power transferred by the ultrasonic reactor to the solution, and t is the sonication time. As a result, the sonochemical efficiency is given in units of mol J^{-1}. This determination of the sonochemical effects therefore allows for a direct comparison of the results of the two different ultrasonic setups used in this study. The ultrasonic frequency should therefore be the only factor responsible for any differences in the sonochemical efficiency of the two setups.

Acoustic Power Determination

The ultrasonic or acoustic powers were determined calorimetrically using the methods of Margulis et al. [19] and Contamine et al. [25] and using Equation 10:

$$P_\mathrm{a} = mC_\mathrm{p} \left(\frac{dT}{dt}\right)_{t=0} \tag{10}$$

where $(\mathrm{d}T/\mathrm{d}t)_{t=0}$ is the temperature slope of water per unit of sonication time (at t = 0) in K s^{-1}; m is the mass of the water used in g and C_p is the specific heat capacity of water (4.186 J g^{-1} K^{-1}). Here, the calorimetric method consists in measuring the heat dissipated in a volume of water, taking into account the water heat capacity (C_p) in which the acoustic energy is absorbed. This method assumes that all absorbed acoustic energy is transformed into heat. From the calorimetric experiments, the acoustic power, P_a in W mL^{-1} was determined.

Results

Synthesis

To monitor the Pt(IV) concentration throughout the sonication process a colorimetric technique was used (as the method enhances the Pt(IV) peaks in the spectrum). Such a procedure involves adding an excess of KI to the $PtCl_4$-solution which leads to the formation of $PtI_6{}^{-2}$ which has a characteristic peak at 495 nm with a molar extinction coefficient of 9,400 dm^3 mol^{-1} cm^{-1} [20]. The resulting UV-Vis spectra obtained after adding KI can be seen in Figure 2a for the chemically synthesized Pt-nanoparticles, and in Figure 2b and Figure 2c for the sonochemical synthesis at frequencies of 20 kHz and 408 kHz respectively. The spectra also

reveal the appearance of a peak at 388 nm which can be attributed to $PtI_4{}^{-2}$ [20]. This peak is observed to reach a maximum point at intermediate sonication times, which indicates that Pt(IV) is first reduced to Pt(II) before finally being reduced to Pt-nanoparticles during the sonochemical synthesis. This is in good agreement with previous studies on the sonochemical reduction of Pt(IV) [20]. Based on the concentrations of Pt(IV) and Pt(II), as well as the initial concentration of $PtCl_4$, the yield of Pt-nanoparticles was determined to be 65% and 46% for the 20 kHz system and 408 kHz system respectively.

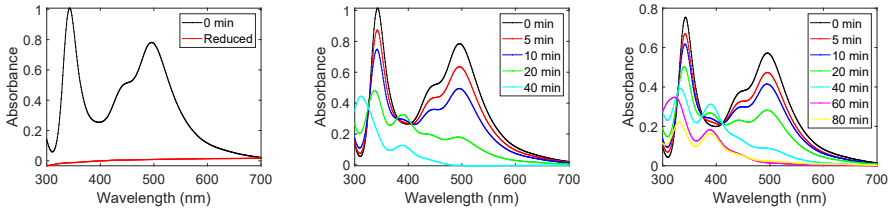

Figure 2: UV-Vis spectra of the $PtCl_4$-solutions after the addition of excess KI for (a) the chemical synthesis, and the sonochemical synthesis at (b) 20 kHz, and (c) 408 kHz. For the sonochemical syntheses, measurements at different sonication times are plotted in the same figure.

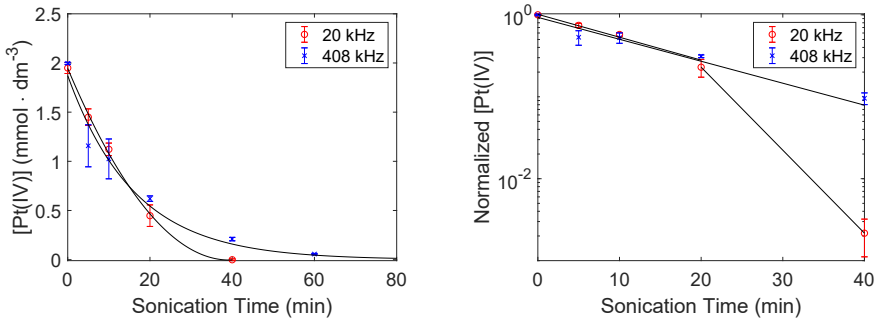

Figure 3: Concentration of Pt(IV) in the solution as a function of sonication time under 20 kHz (○) and 408 kHz (×) (a), and the normalized concentration of Pt(IV) in the solutions plotted on a semi-logarithmic scale (b).

From these UV-Vis spectra, the concentration of Pt(IV) in the solution was calculated and plotted against sonication time as can be seen in Figure 3a. The linear behavior of the semi-logarithmic plots in Figure 3b also reveal that the reduction of

Pt(IV) is a first order reaction. For the first 10 minutes of sonication, no significant differences in the reduction rate constants were observed for the two systems, as k = 0.062 min^{-1} in both cases. However, in the range of 20 min - 80 min, the reduction rate constant in the 20 kHz system (k = 0.23 min^{-1}) was much higher than the one at 408 kHz (k = 0.062 min^{-1}), and the curve started deviating from the exponential fit.

Physical Characterization

X-ray diffractograms for the Pt-nanoparticles are shown in Figure 4. Pt is observed for all samples at $39.8°$, $46.3°$, and $67.6°$, while the 20 kHz sample also display Ti at $38.4°$ and $40.2°$. Rietveld refinement of the diffractogram obtained at 20 kHz revealed that the Pt- and Ti-content was $86\,\%$ and $14\,\%$ respectively. For the other samples, only fcc Pt was found to match the diffractograms. Another interesting observation is that the diffractograms of the sonochemically synthesized particles display much wider peaks compared to those of the chemical reduction. This was also confirmed through Rietveld refinement, where the peak widths were related to the crystallite sizes. The size of the particles synthesized sonochemically with a frequency of 408 kHz was found to be 1.4 nm, at 20 kHz it was found to be 2.7 nm, while the particles synthesized through chemical reduction was found to be 4.1 nm. Thus, the sonochemical synthesis appears to produce nanoparticles of smaller crystallite sizes than the chemical reduction method. A final remark on the diffractograms is the difference in peak heights from one sample to another. This is simply a result of the sample preparation where the higher volume of Pt-nanoparticles produced at 408 kHz was more concentrated upon re-dispersion in ethanol compared to the 20 kHz sample. In addition, the nearly complete reduction of Pt(IV) to Pt-nanoparticles for the chemical reduction also provided the chemical reduction sample with a higher Pt-nanoparticle concentration than the 20 kHz sample, and therefore also higher peaks.

Normal distributions of the agglomerate sizes for the Pt-nanoparticles were obtained from dynamic light scattering, and are shown in Figure 5. From these results, the mean agglomerate size was found to be (143 $\pm$ 85) nm for the chemical reduction, (198 $\pm$ 50) nm for the sonochemical synthesis at 20 kHz, and (255 $\pm$ 105) nm at 408 kHz. The polydispersity of the agglomerates was also found to be significantly smaller for the chemical reduction as compared to the sonochemical synthesis. This suggests that the chemical reduction method leads to smaller agglomerates of more uniform sizes than the sonochemical synthesis.

TEM images for Pt-nanoparticles of all samples are shown in Figure 6a-c. Both samples that were produced sonochemically displayed a structure with small, spherical nanoparticles clearly connected in larger agglomerates. The particles also

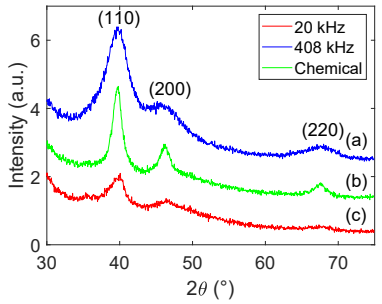

Figure 4: X-ray diffractograms for Pt-nanoparticles synthesized sonochemically with an ultrasonic frequency of 408 kHz (a), chemically using sodium borohydride (b), and sonochemically with an ultrasonic frequency of 20 kHz (c).

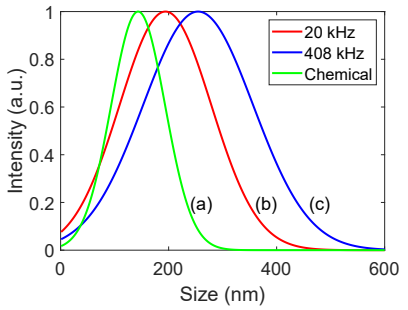

Figure 5: Average agglomerate size distributions for Pt-nanoparticles synthesized chemically using sodium borohydride (a), and sonochemically with ultrasonic frequencies of 20 kHz (b), and 408 kHz (c).

appear to be fairly monodispersed. For the sample which was produced chemically, however, the microstructure shows a larger network consisting of particles of different sizes and shapes with most of the particles being agglomerated. Lone particles were used to determine the average sizes which were found to be (2.2 $\pm$ 0.5) nm for the 20 kHz sample, (2.3 $\pm$ 0.4) nm for the 408 kHz sample, and (3.0 $\pm$ 0.5) nm for the chemical reduction sample. As very few lone particles were found for the chemical reduction sample, the estimated particle size was less certain than for the other samples where lone particles were found in abundance.

EDX analyses revealed that the particles consisted of Pt in all cases. For the 20 kHz samples, micrometer sized particles comprised of Ti, Al, and V were also found distributed among the smaller Pt-nanoparticles (Figure 7a-c). Closer inspection of these micrometer sized impurities showed that Pt particles were supported on the surface as can be seen in Figure 7b and from the elemental maps in Figure 7c.

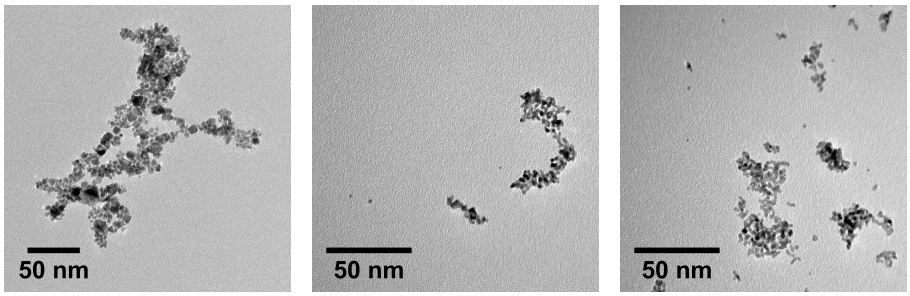

Figure 6: Transmission electron microscopy images of the Pt-nanoparticles synthesized chemically (a), and sonochemically at frequencies of 20 kHz (b), and 408 kHz (c).

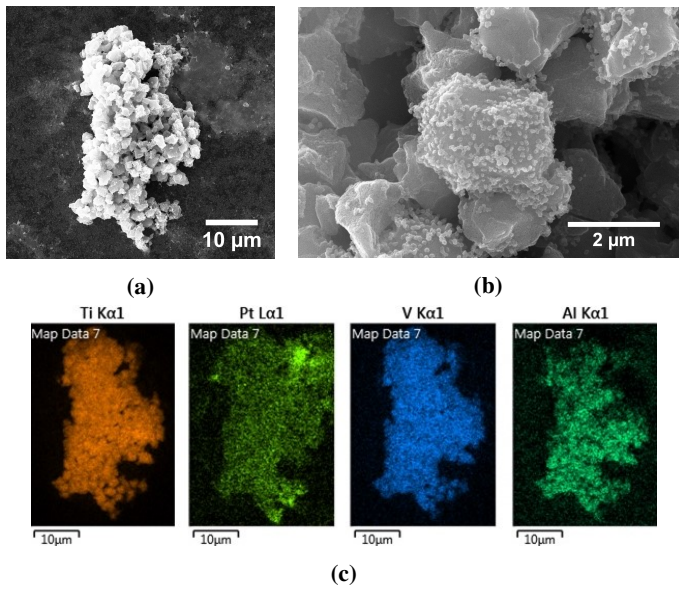

Figure 7: Scanning electron microscopy image of impurities for the 20 kHz sample (a-b), and EDX-maps of the same impurities (c).

Calorimetry and Dosimetry

Measurements of the acoustic power (W) as a function of applied amplitude (%) for the 20 kHz probe sonicator and the 408 kHz plate transducer are shown in Figure 8. Curves fitted to the measured data are also plotted along with error bars for the individual measurements. For the 20 kHz probe sonicator, an amplitude of 50 % was used during the synthesis, and the corresponding acoustic power was

measured to be (42.9 $\pm$ 0.3) W. For the 408 kHz system, an amplitude of 100 % was used during the synthesis, and the corresponding acoustic power was found to be (54 $\pm$ 2) W.

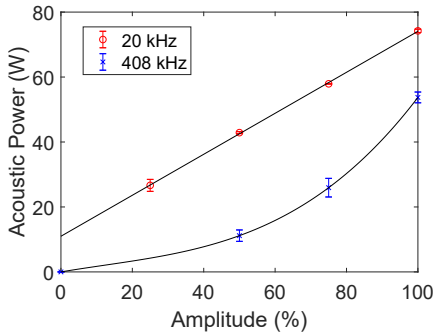

Figure 8: Acoustic power as a function of applied amplitude for the 20 kHz probe sonicator (∘), and for the 408 kHz plate transducer (×). The error bars are equal to the respective standard deviations.

KI dosimetry results from the 20 kHz probe sonicator and the 408 kHz plate transducer are shown in Figure 9a. The 20 kHz probe sonicator displayed an initial oxidation rate of (3.1 $\pm$ 0.3) $\mu\mathrm{mol\ dm^{-3}\ min^{-1}}$ while the 408 kHz plate transducer showed an initial oxidation rate of (2.9 $\pm$ 0.8) $\mu\mathrm{mol\ dm^{-3}\ min^{-1}}$. The results show that the I_3^- concentration is linear with respect to sonication time for the 20 kHz probe sonicator, while for the 408 kHz plate transducer the I_3^- concentration flattens out over time. Consequently, the I_3^- concentration is higher at longer sonication times for the 20 kHz probe sonicator than for the 408 kHz plate transducer even though there is no significant difference before 5 minutes of sonication.

However, when accounting for the volume and the applied acoustic power, the initial sonochemical efficiency was found to be (0.20 $\pm$ 0.04) $\mu\mathrm{molkJ^{-1}}$ at 408 kHz and (0.060 $\pm$ 0.004) $\mu\mathrm{molkJ^{-1}}$ at 20 kHz by using Equation 9. The 408 kHz plate transducer is therefore much more efficient than the 20 kHz probe sonicator as can also be seen in Figure 9b.

Investigations into the effect of bulk temperature, acoustic power, and solution volume on the sonochemical efficiency were also performed. For temperature, no significant differences in sonochemical efficiency were observed between 5 °C and 20 °C for the 408 kHz system. As for the acoustic power, no significant differences in the sonochemical efficiency were found between 43 W and 54 W (corresponding to the acoustic power used for the 20 kHz and 408 kHz ultrasound systems, respectively) for the 408 kHz system, but for much lower acoustic powers (11 W) the sonochemical efficiency improved. For the solution volume, volumes of 200

mL and 50 mL were compared at the same conditions using the 20 kHz probe sonicator, and it was found that increasing the volume leads to a lower sonochemical efficiency. Additional information is provided in Figure S10 and Table S1 in the supporting information.

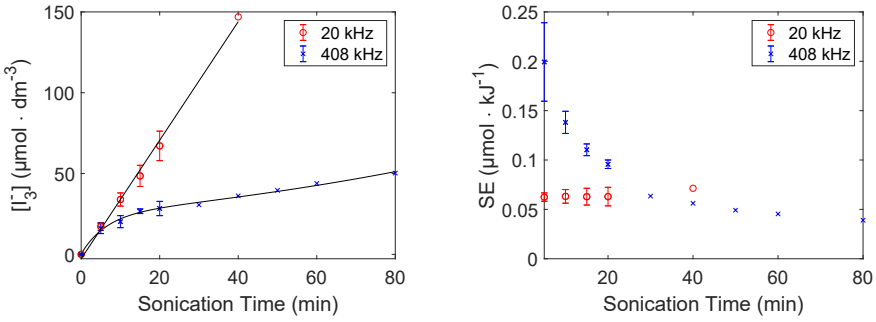

Figure 9: Concentration of I_3^- (a) and sonochemical efficiency (b) plotted against sonication time for the 20 kHz probe sonicator (○), and the 408 kHz plate transducer (×). The error bars are equal to the respective standard deviations.

Discussion

Reduction Rate Constant (k)

The observed increase in the reduction of Pt(IV) after 20 min of sonication using the 20 kHz system can be attributed to the continuous supply of micrometer sized eroded particles. The strong mechanical forces originating from the 20 kHz ultrasonic probe (made of a Ti alloy) is eroding the probe itself leaving large particles (sizes up to 3 µm) comprising of Ti, V, and Al (probe elements) dispersed throughout the solution as was confirmed by EDX. No evidence of such erosion processes were found for the 408 kHz system. The amount of these eroded microparticles increased with increased sonication time, and was also independent on the solution being sonicated as the same phenomenon occurred when sonicating pure water. The presence of impurities, such as these eroded particles, during the synthesis of nanomaterials could lead to heterogeneous nucleation on the surface of these particles due to a significantly reduced nucleation energy required and enhanced reduction kinetics [26]. The gradual introduction of such nucleation sites for the 20 kHz system can therefore explain why the rate constant for Pt(IV)-reduction increases after 20 minutes of sonication. As Pt was confirmed to be present on the surface of the eroded particles through SEM and EDX, this indicates a possible

heterogeneous nucleation process. In order to verify this hypothesis, 200 mL of Milli-Q water was sonicated for 40 minutes with the 20 kHz probe. The resulting water (containing eroded particles) was used to prepare a 200 mL $PtCl_4$ solution which was then sonicated with the 408 kHz system (where no erosion processes occur) in the same manner as before, and the reduction rate was determined colorimetrically (Supporting information Figure S11). From these results it was found that the Pt(IV) concentration decays exponentially, albeit with two times higher rate constant (k = 0.12 min^{-1}) compared to when no nucleation sites were added (k = 0.062 min^{-1}).

In addition, slow degassing of the solution sonicated at 408 kHz could also have affected the reduction rate over the sonication period. Since the dosimetry results of the two systems are similar in the initial stages of sonication, the initial conditions of the two systems appear to offer the same reduction rate, as was intended. However, as sonication proceeds, these conditions are changed especially for the 408 kHz system as can be seen from the deviation from linearity in the dosimetry results (Figure 9a). A similar phenomenon was described by Iida et al. [21] for Ar saturation during sonication and was attributed to the degassing effect caused by ultrasound. As a result, the high collapse temperatures and pressures caused by Ar saturation decrease in turns leading to a lower radical yield and therefore a deviation from linearity. However, the 20 kHz system does not exhibit the same deviation from linearity, indicating that, whatever gas, or composition of gas, the solution is saturated with, is unchanged during the course of sonication. As pulsed sonication was used in a relatively small volume using a lower frequency, one may expect degassing to occur to a much larger extent than for the 408 kHz system. As a result, Ar would be degassed almost immediately leaving behind only water vapour. If all the gases were to be purged away from solution in the first few ultrasonic cycles, a linear behaviour would also be expected as no degassing would take place over an extended period of time.

Comparing the yield of the two sonochemical methods (65% at 20 kHz and 46% at 408 kHz) clearly reveals that more of the precursor was converted to Pt-nanoparticles at 20 kHz when compared to that at 408 kHz. However, due to the different solution volumes used for the two systems (50 mL at 20 kHz and 200 mL at 408 kHz), the yield was not an obvious indication of which system performed better.

The supply of eroded particles to the 20 kHz system might therefore increase the reduction rate over the sonication period, while the degassing of Ar in the 408 kHz system could slightly decrease the reduction rate. This does not seem to affect the final particle sizes in any significant ways as indicated by the TEM results (Figure 6a-c). However, the agglomerate sizes and crystallite sizes as measured by dynamic light scattering and XRD respectively, do seem to differ for the two

ultrasonic systems. Regarding the XRD, the evaluation of the crystallite size for the 20 kHz system might have been influenced by the presence of Ti as it overlaps with the Pt-peak in the diffractogram. As for the agglomerate size, smaller particles tend to form larger agglomerates due to the higher surface free energy associated with the higher specific surface area. It is therefore expected that the Pt-nanoparticles which were produced chemically also display the smallest agglomerate size. However, the significant difference in particle size and standard deviation observed between the particles produced sonochemically could be due to the presence of larger eroded particles in the 20 kHz system during synthesis and/or due to the mechanical effects dominating at lower ultrasonic frequencies. The smaller agglomerates observed at 20 kHz compared to 408 kHz are therefore as expected.

Comparison of Synthesis Methods

The sonochemical method and the chemical reduction method both offer their set of advantages for the production of Pt-nanoparticles. For the chemical reduction method, the most prominent advantage lies in the near instantaneous reduction of Pt(IV) to Pt-nanoparticles. In comparison, the sonochemical method takes around 40 minutes to achieve complete reduction at the conditions used in this work. However, as no attempts were made to optimize the sonochemical processes, there are multiple ultrasonic parameters which can be tuned to achieve faster reduction and in turns making the sonochemical process more efficient [10][11]. The use of additives such as surfactants, seed particles, higher acoustic powers, and optimized ultrasound frequency or other saturation gasses have all been shown to influence the reduction rate [15][11][12]. Even though the reduction rate of the sonochemical method would not be as fast as for the chemical reduction, the large difference that we have observed in our study can definitely be improved upon.

The advantages of the sonochemical method are mainly rooted in the ability to control the reduction rate, and as a consequence, the particle properties such as the size. In this investigation, we have shown that two very different setups operating at two distinct frequencies were able to give the same reduction rate and therefore a similar particle size. Simply by changing some of the ultrasonic conditions, we were able to tune the particle size. The fact that similar results from two completely different ultrasonic reactors can be achieved, also provides the industry with a much higher degree of freedom when it comes to designing the sonochemical reactors and thus, can lead to a more cost effective catalytic material production. In addition, the size and shape of the nanoparticles were found to be very uniform and spherical for the sonochemical method, whereas the chemical reduction method displayed a much wider range of sizes and shapes as is shown in the TEM results. The sonochemical synthesis is therefore very well suited for

applications which requires uniform particle properties. In addition, no use of reducing agents or surfactants, posing HSE risks, were necessary to achieve the desired particle properties as is the case for the chemical reduction.

As for the efficiency of the two ultrasonic setups, it is apparent from the sonochemical efficiency ((0.20 $\pm$ 0.04) μmol kJ^{-1} at 408 kHz and (0.060 $\pm$ 0.004) μmol kJ^{-1} at 20 kHz) that the higher frequency delivers the highest number of nanoparticles per unit energy spent. In addition, by using a 20 kHz sonication probe directly into the reaction vessel, eroded materials (induced by cavitation) are generated and contaminate the sonochemically produced material of interest. The accelerated reduction rate observed when adding such seed microparticles (Ti, V and Al) can also be replicated under more controlled circumstances when turning to higher ultrasonic frequencies. Using direct sonication, especially at low ultrasonic frequencies, for sonochemical synthesis therefore introduces unnecessary complications, which can be avoided by either using higher ultrasonic frequency systems or by separating the ultrasonic probe from the reaction vessel.

Conclusion

The sonochemical approach at two ultrasonic frequencies led to Pt-nanoparticles of similar sizes when the radical yield was tuned to the same initial value. The sonochemical method produced Pt-nanoparticles which were significantly smaller and more monodisperse than the chemical reduction method. The nanoparticles were found to be spherical when using the sonochemical method whereas different shapes were found in the chemical approach. Being able to tune the ultrasonic parameters in order to obtain a specific particle size offers more control over the synthesis without the use of stabilizing agents. This finding is in good agreement with previous works where the nanoparticle size was found to be directly related to the reduction rate, and the radical yield. From an industrial perspective, the higher ultrasonic frequency offers more particles per unit energy and is also free of impurities which is important for electrochemical applications. Direct sonication at lower frequencies (20 kHz) should therefore be avoided if the target catalytic material needs to be of high purity. The gradual introduction of impurities at low frequencies also resulted in complications related to the rate of reduction as the impurities were found to accelerate the reduction of Pt(IV) through heterogeneous nucleation. Controlled addition of such seed Ti, V, and Al microparticles did confirm an increase in reduction rate at higher ultrasonic frequencies as well and could be an important contributor when scaling up the synthesis for industrial purposes.

Bibliography

1. Oldham, K. B., Myland, J. C. & Bond, A. M. *Electrochemical Science and Technology: Fundamentals and Applications* eng (John Wiley & Sons, Ltd, Chichester, UK, 2011).
2. Ren, X. *et al.* Current progress of Pt and Pt-based electrocatalysts used for fuel cells. *Sustainable Energy Fuels* **4,** 15–30 (1 2020).
3. Gama-Lara, S. A. *et al.* Synthesis, Characterization, and Catalytic Activity of Platinum Nanoparticles on Bovine-Bone Powder: A Novel Support. *Journal of Nanomaterials* **2018** (2018).
4. Niu, Z. & Li, Y. Removal and Utilization of Capping Agents in Nanocatalysis. English. *Chemistry Of Materials* **26,** 72–83 (2014).
5. Gholamrezaei, S., Ghiyasiyan-Arani, M., Salavati-Niasari, M. & Moayedi, H. Multidisciplinary methods (co-precipitation, ultrasonic, microwave, reflux and hydrothermal) for synthesis and characterization of CaMn3O6 nanostructures and its photocatalytic water splitting performance. eng. *International journal of hydrogen energy* **44,** 26373–26386 (2019).
6. Ghiyasiyan-Arani, M. & Salavati-Niasari, M. New Nanocomposites Based on Li–Fe–Mn Double Spinel and Carbon Self-Doped Graphitic Carbon Nitrides with Synergistic Effect for Electrochemical Hydrogen Storage Application. eng. *Industrial & engineering chemistry research* **58,** 23057–23067 (2019).
7. Zhang, J. *et al.* Polyimide Encapsulated Lithium-Rich Cathode Material for High Voltage Lithium-Ion Battery. eng. *ACS applied materials & interfaces* **6,** 17965–17973 (2014).

8. Ghiyasiyan-Arani, M. & Salavati-Niasari, M. Strategic design and electrochemical behaviors of Li-ion battery cathode nanocomposite materials based on AlV3O9 with carbon nanostructures. eng. *Composites. Part B, Engineering* **183,** 107734 (2020).
9. Masjedi-Arani, M., Ghiyasiyan-Arani, M., Amiri, O. & Salavati-Niasari, M. CdSnO3-graphene nanocomposites: Ultrasonic synthesis using glucose as capping agent and characterization for electrochemical hydrogen storage. eng. *Ultrasonics sonochemistry* **61,** 104840–104840 (2020).
10. Caruso, R. A., Ashokkumar, M. & Grieser, F. Sonochemical formation of colloidal platinum. eng. *Colloids and Surfaces A: Physicochemical and Engineering Aspects* **169,** 219–225 (2000).
11. Okitsu, K., Bandow, H., Maeda, Y. & Nagata, Y. Sonochemical preparation of ultrafine palladium particles. eng. *Chemistry of Materials (USA)* **8,** 315–317 (1996).
12. Pollet, B. G. The use of ultrasound for the fabrication of fuel cell materials. eng. *International Journal of Hydrogen Energy* **35,** 11986–12004 (2010).
13. Khorasanizadeh, M. H., Ghiyasiyan-Arani, M., Monsef, R., Salavati-Niasari, M. & Moayedi, H. Ultrasound-accelerated synthesis of uniform DyVO4 nanoparticles as high activity visible-light-driven photocatalyst. eng. *Ultrasonics sonochemistry* **59,** 104719–104719 (2019).
14. Pollet, B. G. *Introduction to Ultrasound, Sonochemistry and Sonoelectrochemistry* eng. Cham, 2019.
15. Okitsu, K., Ashokkumar, M. & Grieser, F. Sonochemical synthesis of gold nanoparticles: effects of ultrasound frequency. eng. *The journal of physical chemistry. B* **109,** 20673 (2005).
16. Merouani, S., Hamdaoui, O., Rezgui, Y. & Guemini, M. Sensitivity of free radicals production in acoustically driven bubble to the ultrasonic frequency and nature of dissolved gases. eng. *Ultrasonics - Sonochemistry* **22,** 41–50 (2015).
17. Kimura, T. Standardization of ultrasonic power for sonochemical reaction. eng. *Ultrasonics sonochemistry* **3,** S157–S161 (1996).
18. Escobar Morales, B. *et al.* Synthesis and characterization of colloidal platinum nanoparticles for electrochemical applications. eng. *International journal of hydrogen energy* **35,** 4215–4221 (2010).
19. Margulis, M. & Margulis, I. Calorimetric method for measurement of acoustic power absorbed in a volume of a liquid. eng. *Ultrasonics - Sonochemistry* **10,** 343–345 (2003).

20. Mizukoshi, Y. *et al.* Preparation of platinum nanoparticles by sonochemical reduction of the Pt(IV) ions: role of surfactants. eng. *Ultrasonics sonochemistry* **8,** 1–6 (2001).

21. Iida, Y., Yasui, K., Tuziuti, T. & Sivakumar, M. Sonochemistry and its dosimetry. eng. *Microchemical Journal* **80,** 159–164 (2005).

22. Son, Y., Lim, M., Ashokkumar, M. & Khim, J. Geometric Optimization of Sonoreactors for the Enhancement of Sonochemical Activity. eng. *The Journal of Physical Chemistry C* **115,** 4096–4103 (2011).

23. Rochebrochard D'auzay, S. d. L., Blais, J.-F. & Naffrechoux, E. Comparison of characterization methods in high frequency sonochemical reactors of differing configurations. eng. *Ultrasonics - Sonochemistry* **17,** 547–554 (2010).

24. Koda, S., Kimura, T., Kondo, T. & Mitome, H. A standard method to calibrate sonochemical efficiency of an individual reaction system. eng. *Ultrasonics - Sonochemistry* **10,** 149–156 (2003).

25. Contamine, R. F., Wilhelm, A., Berlan, J. & Delmas, H. Power measurement in sonochemistry. eng. *Ultrasonics - Sonochemistry* **2,** S43–S47 (1995).

26. Thanh, N. T. K., Maclean, N. & Mahiddine, S. Mechanisms of Nucleation and Growth of Nanoparticles in Solution. eng. *Chemical reviews* **114,** 7610–7630 (2014).

Supporting Information

To assess whether the use of different ultrasound conditions like bulk temperature, acoustic power and solution volume has any effect on the sonochemical efficiency, several KI dosimetry experiments where performed as can be seen in Figure S10. The experimental details can be found in Table S1. The results show that by applying the same power and temperature to the 408 kHz system as was used for the 20 kHz system, there are no significant differences in the sonochemical efficiency. Further decreasing the power, however, showed that the sonochemical efficiency increases at low acoustic powers. The results also show that when the solution volume is increased, the sonochemical efficiency is reduced. This means that the difference in sonochemical efficiency between the 20 kHz system and the 408 kHz systems is even larger if both systems are operated at the same conditions.

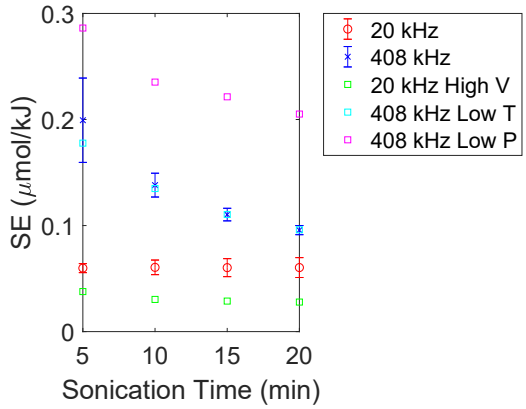

Figure S 10: Sonochemical efficiency as a function of sonication time for different ultrasound conditions listed in Table S1. Measurements performed at the synthesis conditions are only referred to by their frequency, while any modifications are marked as Low P for lower power, High V for higher volume, and Low T for lower temperature compared to the synthesis conditions.

Table S 1: Overview of the different ultrasound parameters which was used in this experiment.

Frequency (kHz)	Gas	Power (W)	Temperature (°C)	Volume (mL)
20	Ar	42.9	5	50
20	Ar	42.9	5	200
408	Ar	54	20	200
408	Ar	42.9	5	200
408	Ar	11.4	20	200

Measurements of the reduction rate of Pt(IV) are shown in Figure 11 and shows the effect of adding the eroded particles from the 20 kHz probe to the 408 kHz system. The rate constant increased from k = 0.062 min^{-1} to k = 0.12 min^{-1} by adding the seed particles to the system.

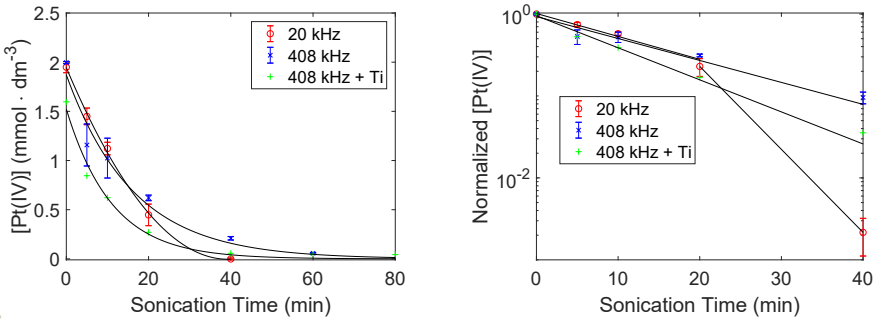

(a) **(b)**

Figure S 11: Concentration of Pt(IV) in the solution as a function of sonication time under 20 kHz (○), 408 kHz (×), and 408 kHz with the addition of Ti seed particles (+) (a), and the normalized concentration of Pt(IV) in the solutions plotted on a semi-logarithmic scale (b).

Chapter 5

Frequency Controlled Agglomeration of Pt-nanoparticles in Sonochemical Synthesis

Frequency Controlled Agglomeration of Pt-Nanoparticles in Sonochemical Synthesis

Henrik E. Hansen[1,2*], Frode Seland[1], Svein Sunde[1], Odne S. Burheim[2], Bruno G. Pollet[2,3]

[1]Electrochemistry Group, Department of Materials Science and Engineering, Faculty of Natural Sciences. Norwegian University of Science and Technology (NTNU), NO-7491 Trondheim, Norway

[2]Hydrogen Energy and Sonochemistry Research Group, Department of Energy and Process Engineering, Faculty of Engineering, Norwegian University of Science and Technology (NTNU), NO-7491 Trondheim, Norway

[3]Green H_2 Lab, Pollet Research Group, Hydrogen Research Institute (HRI), Université Du Québec à Trois-Rivières (UQTR), 3351 Boulevard des Forges, Trois-Rivières, Québec G9A 5H7, Canada

Abstract

Optimizing the surface area of nanoparticles is key to achieving high catalytic activities for electrochemical energy conversion devices. In this work, the frequency range (200 kHz - 500 kHz) for maximum sonochemical radical formation was investigated for the sonochemical synthesis of Pt-nanoparticles to assess whether an optimum frequency exists or if the entire range provides reproducible particle properties. Through physical and electrochemical characterization, it was found that the frequency dependent mechanical effects of ultrasound resulted in smaller, more open agglomerates at lower frequencies with agglomerate sizes of (238 $\pm$ 4) nm at 210 kHz compared to (274 $\pm$ 2) nm at 326 kHz, and electrochemical surface areas of (12.4 $\pm$ 0.9) $\mathrm{m^2 g^{-1}}$ at 210 kHz compared to (3.4 $\pm$ 0.5) $\mathrm{m^2 g^{-1}}$ at 326 kHz. However, the primary particle size (2.1 nm) and the catalytic activity towards hydrogen evolution, (19 $\pm$ 2) mV at $10\,\mathrm{mA\,cm^{-2}}$,remained unchanged over the entire frequency range. Highly reproducible Pt-nanoparticles are therefore easily attainable within a broad range of ultrasonic frequencies for the sonochemical synthesis route.

Keywords: ultrasound; sonochemistry; electrocatalyst; hydrogen; platinum; frequency;

Introduction

The synthesis of nanomaterials with highly reproducible physical properties has been a challenge ever since researchers started to explore their unique capabilities [1][2]. Most synthesis techniques are very sensitive towards changes in the experimental conditions and can yield nanoparticles with very different properties which might not be ideal for the given application it is intended for. In the field of catalysis, precise control over the properties of the catalyst is essential as any changes in the chemical composition, particle size, or surface area might drastically change its catalytic activity. Development of catalysts for electrochemical conversion of hydrogen, e.g., the hydrogen evolution reaction (HER) or the oxygen reduction reaction (ORR), is one of those research areas where reproducible catalysts are highly important as the dominating catalyst materials belong to the Platinum Group Metals (PGM) [3][4]. The high cost of these catalysts inflicted by the price of PGMs makes it even more important to achieve the target properties as any catalytic performance that is not ideal will hinder further commercialization of hydrogen as a possible alternative to fossil fuels [3]. Reducing costs by optimizing the catalytic activity, getting reproducible nanoparticles, and scaling up the catalyst production are therefore paramount if PGMs are to be used in future electrochemical conversion devices for hydrogen [1].

The synthesis of catalysts for electrochemical conversion of hydrogen is predominantly based on the reduction of aqueous solutions of metal salts by a strong reducing agent such as sodium borohydride ($NaBH_4$) [5][6][7][8]. Other methods involve utilizing high temperatures to decompose the solvent into reducing species which will reduce the metal salts in a controlled manner. One of the most common examples of such a synthesis method is the polyol-synthesis [9]. However, to successfully achieve the desired properties, additives such as surfactants or stabilizers must be used [10]. This adds to the total cost of the catalyst by virtue of the price of the additive itself and the effort required to remove the additive post synthesis [10]. Also, the introduction of an additional component in the synthesis makes scaling the production more difficult as careful considerations must be taken into account to ensure reproducibility.

An alternative to the current nanomaterial synthesis methods is the sonochemical synthesis where high power ultrasound is used to reduce metal salts to metal nanoparticles [11][12][13][14][15]. Cavitation bubbles formed in the aqueous medium by ultrasound creates local environments of extreme temperatures and pressures upon collapse, resulting in the splitting of water molecules into hydrogen radicals (H·) and hydroxyl radicals (OH·). By applying a radical scavenger, like ethanol which consists of a polar part (OH-group) and a non-polar part (hydrocarbon chain), it will be situated at the bubble solution interface [16]. When the short-lived radicals are generated inside these bubbles they will be scavenged at the bubble solution interface and turn the scavenger into a reducing radical itself. The resulting radical is referred to as a secondary radical, and it will have a longer lifetime than primary radicals. The secondary radicals will therefore be able to diffuse into the solution, and operate as a continuously generated reducing agent for nanoparticle synthesis [16].

There are mainly two effects of ultrasound which can affect the nanoparticle synthesis; the sonochemical effects arising from radical formation during cavitation, and the mechanical effects caused by the shock wave pressure of the collapsing bubbles. The sonochemical effects are mostly influencing the rate of reduction, while the mechanical effects may affect the agglomeration process. The sonochemical effects of ultrasound have been studied quite extensively and several different groups report an optimum in the sonochemical effects between ultrasonic frequencies of 200 kHz and 500 kHz [14][17][18][19]. At these optimum frequencies the particle size of sonochemically synthesized nanoparticles is expected to reach a minimum due to the increased reduction rate, which have been shown for gold nanoparticles [14] and ruthenium nanoparticles [17]. However, these works have used five frequencies spanning a wide range (20 kHz - 1 MHz) rendering it difficult to pinpoint an exact optimum. Limiting the range of frequencies to the

proposed optimal range for sonochemical radical formation would therefore be beneficial to determine an exact optimum frequency for sonochemical synthesis of nanomaterials. This is especially interesting for platinum (Pt) nanoparticles as its excellent properties as HER- and ORR-catalysts could really benefit from an optimized and robust synthesis method to justify the high cost of Pt. This can be achieved by conducting a thorough investigation of the frequency dependence of the properties of Pt-nanoparticles synthesized sonochemically. To the best of our knowledge, no such investigation has been performed for the sonochemical synthesis of Pt-nanoparticles. As for the mechanical effects, there are two phenomena which can affect the agglomeration process. First is the formation of high velocity microjets which will cause erosion or deagglomeration of the target material. However, microjet formation can only occur when the size of the target material is larger than the collapsing bubble (micro meter size) [20]. The next mechanical effect is the shock waves created by collapsing bubbles. Being multi directional, these are less violent than the microjets, but are also capable of deagglomeration. In addition these shock waves have also been found to aid agglomeration through the facilitation of interparticle collisions as was shown by Suslick et al. [20][21]. The shock waves can therefore lead to both deagglomeration of larger agglomerates and facilitate agglomeration of primary particles. Agglomeration of primary particles on the nano scale is especially interesting in the field of catalysis where available surface area is key to achieving a higher catalytic activity [22]. As shock wave pressures are highly frequency dependent [23], assessing the effect of ultrasonic frequency on primary particle size and agglomeration could therefore provide valuable information on which ultrasonic frequencies to chose to achieve ideal catalyst properties, and which frequency range can be used for high reproducibility.

In this work we want to investigate if any frequency in the proposed optimum range (200 kHz - 500 kHz) for radical formation can be used to synthesize highly reproducible Pt-nanocatalysts. This is achieved by assessing the combined contributions from the sonochemical effects and the mechanical effects of ultrasound. The combined effect of ultrasound on primary particle properties and agglomeration will therefore serve as a measure of how reproducible the sonochemical synthesis of Pt-nanoparticles is. The primary particle properties were evaluated based on measurements of the particle sizes through scanning/transmission electron microscopy (S(T)EM) and X-ray diffraction (XRD), and the catalytic activity towards the HER from electrochemical measurements. As for agglomeration, agglomerate sizes were obtained from dynamic light scattering (DLS), and agglomerate surface area from the electrochemical surface area (ECSA). S(T)EM micrographs were used to get an idea of the shape of the agglomerates.

Experimental

Sonochemical Synthesis Setup

The experimental setup for the sonochemical synthesis is shown in Figure 1. The frequency specific plate transducers (210 kHz, 326 kHz, 408 kHz, and 488 kHz) from Honda Electronics are made from a stainless-steel alloy (SUS304) which is highly corrosion resistant. These transducers were mounted on the bottom of a borosilicate glass reactor being in direct contact with the solution in the inner chamber of the reactor. The issue of eroded particles entering the system due to transducer erosion from micro jet formation has been shown to occur previously [24], but it was only observed at low ultrasonic frequencies (20 kHz) with high acoustic powers (43 W). The lower mechanical effects of ultrasound at higher frequencies ($\geq$ 210 kHz) and lower acoustic powers (11.8 W) are therefore not expected to cause erosion of the transducer. This was also confirmed from the absence of a constant baseline shift in the absorbance spectra (Figure S1). In the outer chamber, water maintained at 20 °C was circulated using a compact recirculating chiller from QSonica to maintain a constant solution temperature throughout the system.

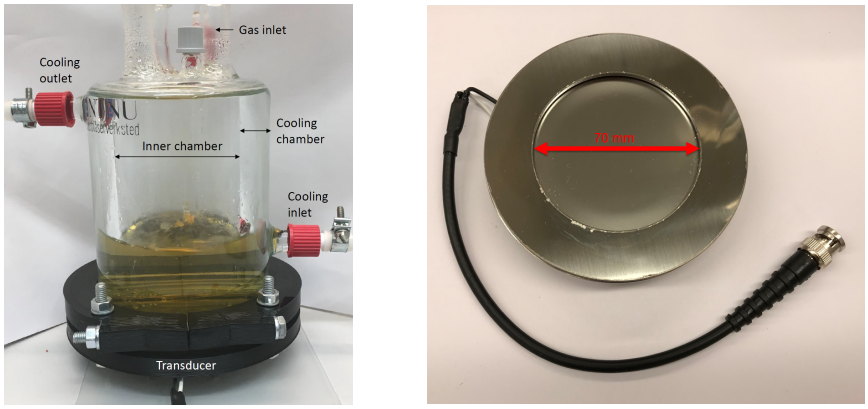

(a) **(b)**

Figure 1: Ultrasound setup used to synthesize Pt-nanoparticles at different ultrasonic frequencies (a), along with one of the ultrasound transducers (b).

Synthesis

Pt-catalysts were synthesized sonochemically using ultrasonic frequencies of 210 kHz, 326 kHz, 408 kHz, and 488 kHz. For each frequency, the acoustic power transmitted to the reactor was measured by calorimetry as described in Section

2.5. All plate transducers were operated at an acoustic power of 11.8 W (which would correspond to 0.307 W cm^{-2} or 0.059 W cm^{-3} for the geometry of our cell.) (Figure S2). The temperature during ultrasonication was maintained at 20 °C throughout the entire experiment. For each synthesis 200 mL of 2 mmol dm^{-3} $PtCl_4$ (99.9 % basis, Alfa Aesar) was prepared in a 0.8 mol dm^{-3} ethanol (96 %, GPR rectapur, VWR) solution where ethanol acts as a radical scavenger. Complete scavenging of the primary radicals by 0.8 mol dm^{-3} ethanol was ensured as shown by a separate dosimetry experiment as described in the supporting information (Figure S3). Prior to ultrasonication, the solution was purged with argon (Ar 5.0) gas for 10 min. Ar-gas was also supplied for the entire duration of the experiment. In order to achieve sufficient amounts of Pt-nanoparticles for further characterization the sonication time was set to 180 min. The Pt-nanoparticles were then extracted from solution by use of an Eppendorf 5810 R centrifuge operated at 12,000 rpm for 15 min. The particles were redispersed in ethanol and water and centrifuged an additional three times. The particles were then dried at room temperature before being ground into a fine powder using a mortar and pestle.

Physical Characterization

The sonochemical synthesis of Pt-nanoparticles is expected to proceed from Pt(IV) to Pt(II) and then to Pt-nanoparticles. Primary radicals (OH· and H·) are scavenged by the scavenger (RH) and will act as reducing agents following the reactions below [25].

$$\mathrm{OH}\cdot(\mathrm{H}\cdot) + \mathrm{RH} \longrightarrow \mathrm{H_2O}(\mathrm{H_2}) + \mathrm{R}\cdot$$

$$\mathrm{Pt(IV)} + 2\mathrm{R}\cdot \longrightarrow \mathrm{Pt(II)} + 2\mathrm{R}$$

$$\mathrm{Pt(II)} + 2\mathrm{R}\cdot \longrightarrow \mathrm{Pt}(0) + 2\mathrm{R}$$

The concentration of Pt(IV) and Pt(II) was therefore measured for all samples as a function of sonication time using UV-visible spectroscopy. A Thermo Scientific Evolution 220 UV-Vis spectrophotometer was used to record the absorbance spectra. To distinguish the absorption peaks of Pt(IV) and Pt(II) a colorimetric technique was applied where an excess of potassium iodide (KI) ($\geq$ 99.0 %, ACS reagent, Sigma Aldrich) was added to the Pt(IV)/Pt(II) solution to form Pt iodide complexes with distinct absorption peaks in the visible spectrum [25]. The resulting PtI_6^{2-} peak at 495 nm (ϵ = 11,170 $\mathrm{dm}^3\mathrm{mol}^{-1}\mathrm{cm}^{-1}$) (Figure S9a) and the

PtI_4^{2-} peak at 388 nm (ϵ = 4,600 $\mathrm{dm^3 mol^{-1} cm^{-1}}$) [26] were related to the concentration of Pt(IV) and Pt(II), respectively through Beer-Lambert's law.To avoid interference from the Pt(IV) peaks in the determination of the Pt(II) concentrations, the contributions of Pt(IV) was subtracted from the spectra. As a result of the uncertainties introduced with this step, the reported Pt(II) concentrations only serve to provide a qualitative assessment of the reduction mechanics of Pt, and is not considered quantitatively. Recording the concentrations of Pt(IV) as a function of sonication time also allowed for the determination of reaction rates at the different ultrasonic frequencies.

To examine the crystal structure, particle size, particle shape, and agglomerate size, XRD, S(T)EM, and DLS were utilized. For XRD and S(T)EM dilute dispersions of the different samples were drop cast onto a flat silicon wafer and a Cu formvar TEM grid from Ted Pella, respectively. The XRD measurements were performed with a Bruker D8 A25 DaVinci X-ray Diffractometer with CuKα radiation. A scan rate of $0.044\,^\circ/\mathrm{step}$ was used for 2θ-angles between 15°-75° with a 0.3° fixed slit for 60 min. From the diffractograms, the mean crystallite sizes, L, were estimated using the Scherrer equation [27]

$$L = \frac{K\lambda}{\beta \cos\theta} \tag{1}$$

where K is the shape factor with a value of 1.333 for spherical particles [27], λ is the wavelength of the incident X-rays, β is the full width at half maximum for the given peak, and θ is the Bragg angle of the given peak.

For S(T)EM measurements a Hitachi High-Tech SU9000 was used in brightfield mode with an acceleration voltage of 30 kV and an emission current of $0.7\,\mu\mathrm{A}$. High angle annular dark field scanning transmission electron microscopy (HAADF-STEM) was also performed on the 210 kHz sample and the 326 kHz sample in order to compare the respective particles in more detail. For these HAADF-STEM measurements, a Jeol JEM ARM200F was used with an acceleration voltage of 200 kV. DLS was performed using a Beckmann Coulter N5 submicron particle size analyzer where samples were diluted to achieve a particle count of approximately 2×10^6 cps [28]. Presence of interfering dust particles was minimized by filtering the dispersions through a $2.7\,\mu\mathrm{m}$ particle filter while working in an ISO 7 cleanroom. Ten consecutive measurements were performed for each sample and using the obtained autocorrelation function, the hydrodynamic diameter of the particle agglomerates was extracted.

Electrochemical Characterization

For electrochemical characterization of the Pt-nanoparticles, catalyst inks were prepared by mixing 10 mg Pt-catalyst with $475\,\mu$L DI-water (Milli-Q, $18.2\,\mathrm{M\Omega\,cm}$), $475\,\mu$L isopropyl alcohol (IPA) (technical, VWR), and $50\,\mu$L Nafion 117 (5 wt$\%$ in mixture of lower aliphatic alcohols and water, Sigma Aldrich). $10\,\mu$L aliquots of the ink were spin coated onto a glassy carbon rotating disc electrode (RDE, Pine Instruments) (area = $0.196\,\mathrm{cm^2}$) at 200 rpm in order to obtain a homogeneous dispersion of the catalyst on the electrode with a Pt loading of 0.5 mg $\mathrm{cm^{-2}}$. The electrochemical measurements were performed in an Ar-saturated solution of 0.5 mol $\mathrm{dm^{-3}}$ H_2SO_4 (95-97$\%$, VWR) with a reversible hydrogen electrode (RHE) as the reference electrode and graphite as the counter electrode. An Ivium-n-stat potensiostat was used to record all data. During the measurements, a rotation rate of 1,600 rpm was used for the RDE. Measures were also taken to cover the solution surface with Ar during the experiments to prevent air from entering the electrolyte. In order to activate the catalysts and obtain a stable voltammogram, the working electrode was cycled 20 times between 0.07 V vs RHE and 1.5 V vs RHE with a scan rate of 50 mV $\mathrm{s^{-1}}$ [29]. The voltammograms obtained during the final cycles were then used to determine the electrochemical surface area, ECSA, of the catalysts assuming a monolayer adsorption of hydrogen, with Q_a = 220 $\mu\mathrm{C\ cm^{-2}}$ [30].

$$\mathrm{ECSA} = \frac{Q_{\mathrm{H}}}{220\,\mu\mathrm{C cm^{-2}}} \tag{2}$$

Linear sweep voltammetry was performed between 0.1 and -0.1 V vs RHE using a scan rate of 1 mV $\mathrm{s^{-1}}$. Due to the high current densities obtained at low potentials, IR-compensation was applied with values chosen as $85\,\%$ of the series resistance obtained from impedance measurements. The overpotential required to reach 10 mA $\mathrm{cm^{-2}}$ (η_{10}) was then recorded for each sample and compared with each other.

Dosimetry and Calorimetry

Prior to the nanoparticle synthesis, the ultrasound reactor and the different ultrasound transducers were subjected to dosimetry experiments and calorimetry experiments in an effort to determine the radical yield and transmitted ultrasonic power. Two different dosimeters were employed; Potassium iodide (Weissler) dosimetry [19][31][32][33], and titanyl sulfate dosimetry ($TiOSO_4$) [34]. For Weissler dosimetry a $0.1\,\mathrm{mol\ dm^{-3}}$ KI solution was oxidized to I_3^- by OH-radicals formed during ultrasonication at the different ultrasonic frequencies [19]. I_3^- having a strong yellow colour (ϵ = 26,000 $\mathrm{dm^3 mol^{-1} cm^{-1}}$) could therefore easily be quantified through UV-visible spectroscopy and Beer Lambert's law. No molybdate

catalyst was used for Weissler dosimetry to avoid the contribution from H_2O_2 as this is already accounted for by titanyl sulfate dosimetry. Instead Weissler dosimetry will indicate the amount of OH radicals that actually escape the cavitation bubbles.

As for titanyl sulfate dosimetry, only DI-water was subjected to ultrasonication. As the radicals being formed have no added species to react with, the radicals recombine themselves, and one of the dominating products is hydrogen peroxide (H_2O_2) due to the combination of two OH-radicals [34]. To detect the H_2O_2 being formed, an excess of $TiOSO_4$ (1.9 % - 2.1 %, Sigma Aldrich) was added to the sample after ultrasonication. The $TiOSO_4$ reacts with H_2O_2 and forms a peroxotitanium (IV) complex with a strong absorption peak at 411 nm [34]. The molar absorption coefficient of this complex was measured in a separate calibration experiment with commercial H_2O_2 to be ϵ = 787 $\mathrm{dm^3 mol^{-1} cm^{-1}}$ (Figure S9b). Similarly to the Weissler method, samples were extracted at various time intervals and measured with UV-visible spectroscopy to determine the [OH·] ([OH·]= 2[H_2O_2]), and therefore the radical generation rate.

For the calorimetric measurements of the ultrasonic power, 200 mL of DI water was sonicated for 2 min at various amplitudes for all frequencies while measuring the temperature increase. Assuming all acoustic energy is transformed to heat the acoustic power can be calculated as [35]

$$P_{\text{acoustic}} = mC_{\text{p}} \left(\frac{dT}{dt} \right)_{t=0} \tag{3}$$

where $(\mathrm{d}T/\mathrm{d}t)_{t=0}$ is the temperature slope of water per unit of sonication time (at t = 0) in K $\mathrm{s^{-1}}$; m is the mass of the water used in g and C_{p} is the specific heat capacity of water (4.186 J $\mathrm{g^{-1}\ K^{-1}}$). All measurements were repeated three times.

Results

The reduction rate constants (k) for the sonochemical reduction of Pt(IV) to Pt(II) obtained at different ultrasonic frequencies are shown in Figure 2a. These values were extracted from the UV-visible absorbance spectra and the Pt(IV) concentration profiles provided in the supporting information (Figure S4 and Figure S5). Application of the lowest ultrasonic frequency (210 kHz) leads to significantly faster Pt reduction compared to the other frequencies. However, at the highest frequency (488 kHz) the reduction rate appears to increase again. The yield of the resulting Pt-nanoparticles are also plotted against applied ultrasonic frequency in Figure 2b, and exhibit the same trend as the reduction rate constants.

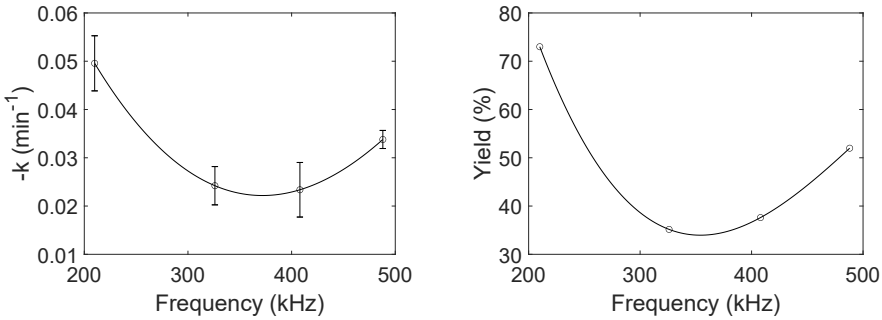

Figure 2: Rate constant (k) for the reduction of Pt(IV) (a), and the yield of Pt-nanoparticles (b) plotted against ultrasonic frequency. The error bars are equal to the respective standard deviations, and the lines through the datapoints are drawn with cubic spline interpolation to guide the eye.

S(T)EM micrographs of all Pt-samples are shown in Figure 3a-d. From these micrographs we can see that the applied ultrasonic frequency during the synthesis does not affect the microstructure of the primary particles nor their size as they all exhibit a spherical shape with a size of (1.9 ± 0.3) nm. This is more apparent from the inset shown in Figure 3b where the primary nanoparticles are more easily resolved compared to the bulky structure of the agglomerate. Even though there are no significant differences in the respective primary particles, the agglomerates formed at 210 kHz appear to be less dense than for the other frequencies. More examples are provided in the supporting information (Figure S6).

HAADF-STEM micrographs of Pt-nanoparticles synthesized using ultrasonic frequencies of 326 kHz and 210 kHz are shown in Figure 3e and Figure 3f, respectively. The way in which agglomeration occurs appear to be somewhat different for the two samples. For the 210 kHz sample, the agglomerates seem to form long strands, whereas for the 326 kHz sample the agglomerates become more clustered together as was also observed for the agglomerates in the S(T)EM images.

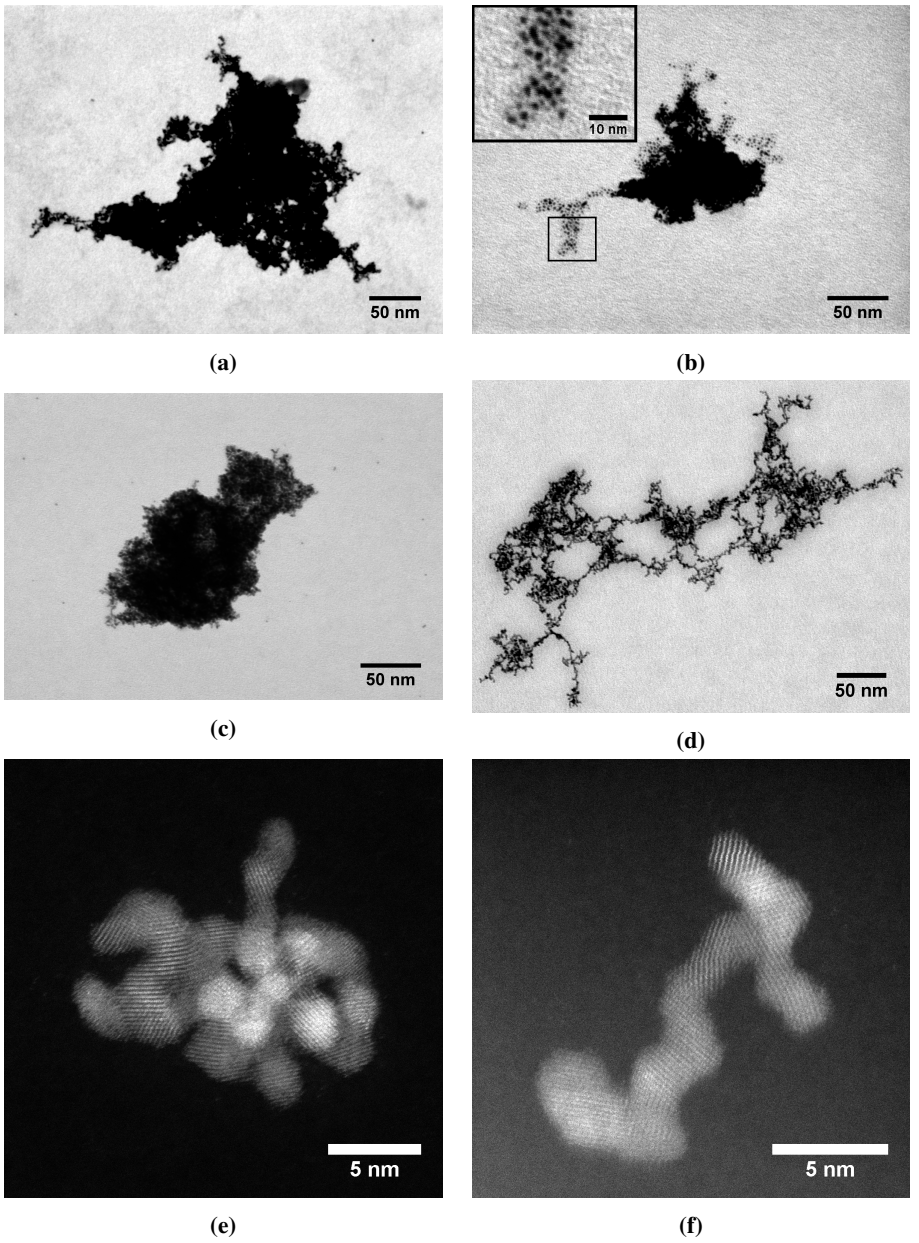

Figure 3: Bright field scanning electron microscopy micrographs of Pt-nanoparticles synthesized at 488 kHz (a), 408 kHz (b), 326 kHz (c), and 210 kHz (d). High angle annular dark field scanning transmission microscopy micrographs were also acquired for Pt-nanoparticles synthesized at 326 kHz (e), and 210 kHz (f). An inset of clearly resolved primary particles have been included for the 408 kHz sample (b).

The X-ray diffractograms of all Pt-samples are plotted together in Figure 4a. These results show that all samples exhibit the same crystal structure of fcc Pt indicated by the peak positions at 40.0° (111), 46.5° (200), and 67.9° (220). Assuming a spherical shape of the crystallites as was observed from the S(T)EM micrographs, the subsequent analysis of the peaks using the Scherrer equation (Equation 1) revealed that all samples displayed an average crystallite size of 2.1 nm which is very similar to the sizes obtained from S(T)EM. Results from dynamic light scattering highlighting the mean agglomerate sizes of the Pt-nanoparticles are shown in Figure 4b. The figure clearly shows that the Pt-nanoparticles synthesized at the lowest ultrasonic frequency of 210 kHz exhibits a smaller agglomerate size compared to the other ultrasonic frequencies where the agglomerates appear to reach a constant value.

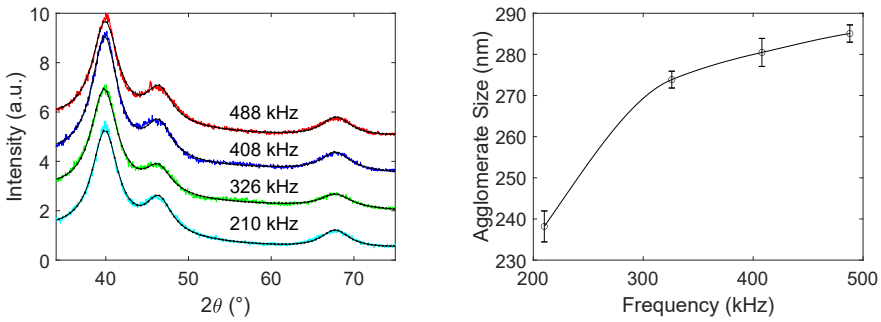

(a) **(b)**

Figure 4: X-ray diffractograms of Pt-nanoparticles synthesized at ultrasonic frequencies of 488 kHz, 408 kHz, 326 kHz, and 210 kHz (a). Average agglomerate sizes of Pt-nanoparticles synthesized at ultrasonic frequencies of 488 kHz, 408 kHz, 326 kHz, and 210 kHz as obtained from dynamic light scattering (b). The line through the datapoints for dynamic light scattering is drawn with cubic spline interpolation to guide the eye.

The cyclic voltammograms (CV) normalized for the geometric surface area, and the corresponding electrochemical surface area for all samples are shown in Figure 5a and Figure 5b, respectively. Significantly higher current densities are observed for the 210 kHz sample compared to all the other samples which also leads to an ECSA nearly three times as high as the other samples. As for the other frequencies, the voltammograms are practically overlapping with each other which is also reflected in their similar electrochemical surface areas.

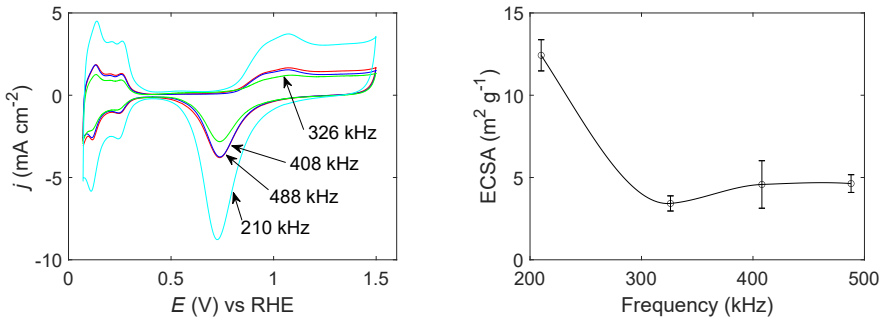

(a) **(b)**

Figure 5: Cyclic voltammograms of Pt nanocatalysts synthesized at different ultrasonic frequencies (a), and the corresponding electrochemical surface area (b). The line through the datapoints is drawn with cubic spline interpolation to guide the eye.

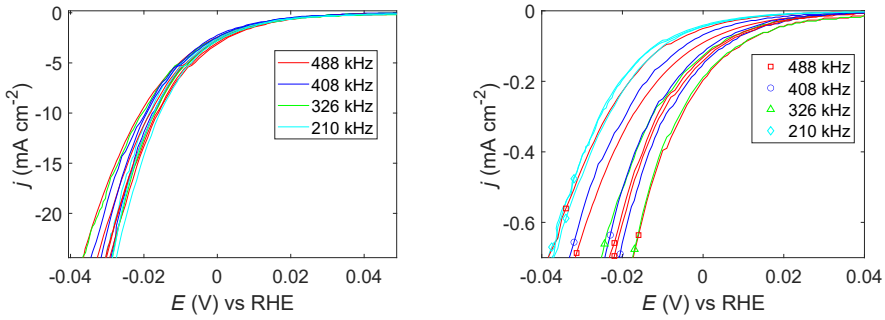

(a) **(b)**

Figure 6: Linear sweep voltammograms of Pt nanocatalysts synthesized at different ultrasonic frequencies with current densities normalized for the geometric surface area (a), and electrochemical surface area (b).

Linear sweep voltammograms normalized for the geometric surface area and the ECSA for all samples are shown in Figure 6a and Figure 6b, respectively. No significant differences were observed between the four samples when the current densities were normalized for the geometric surface area as can be seen from the overlap of the curves and the similar overpotentials at $10\,\mathrm{mA\ cm^{-2}}$ equal to (19 $\pm$ 2) mV. When normalizing the current densities for the ECSA, however, the performance of the 210 kHz catalyst towards hydrogen evolution was worse than the other frequencies. In addition, the 210 kHz catalyst displays a much higher degree of reproducibility compared to the other frequencies as indicated by the

near overlap of the curves at 210 kHz. More variation is observed for the other frequencies, and no significant differences between the 326 kHz, 408 kHz, 488 kHz catalysts can be observed.

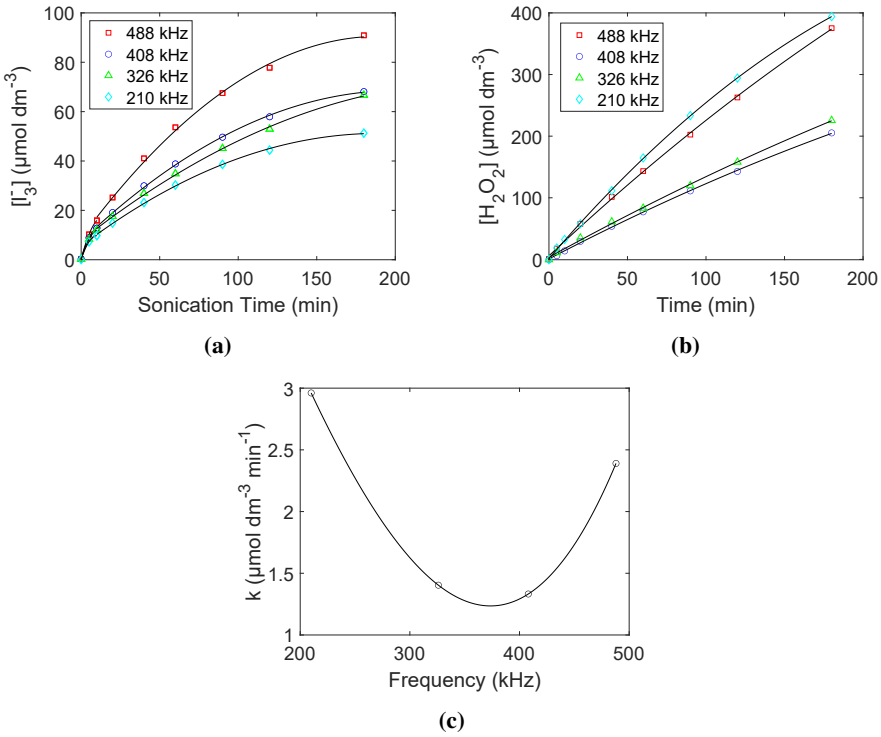

Figure 7: Concentration profiles of I_3^- (a), the concentration profiles of H_2O_2 (b), and the reaction rate of OH· to H_2O_2 (c) for different ultrasonic frequencies. For the concentration profiles (a and b), fitted curves have been included for the respective datapoints. For the rate figure (c), the lines through the datapoints are drawn with cubic spline interpolation to guide the eye.

KI-dosimetry results for the different ultrasonic frequencies are shown in Figure 7a. Concentration profiles were generated from UV-visible absorbance spectra provided in the supporting information (Figure S7). All concentration profiles deviate from linearity after a few minutes of sonication with values starting to flatten out towards the end of the 3 hour sonication period. The final I_3^- concentration for the different systems appear to be lowest at 210 kHz and highest at 488 kHz.

$TiOSO_4$-dosimetry results for the different ultrasonic frequencies are shown in Figure 7b-c, and are also extracted from UV-visible absorbance spectra provided

in the supporting information (Figure S1). The concentration profiles are all approximately linear over the entire ultrasonication period with the exception of the lowest ultrasonic frequency (210 kHz), which flattens out slightly towards the end of the experiment. As for the rate of H_2O_2 formation, the fastest rate is observed at 210 kHz followed by 488 kHz. The 326 kHz and 408 kHz systems both display the slowest rate. This is in contrast to what is observed for KI-dosimetry where the 210 kHz system displayed the lowest I_3^- concentration after 3 h.

For KI-dosimetry, I_3^- is formed in-situ and mostly by reacting with OH-radicals. Any H_2O_2 formed in the process from recombination of OH radicals will therefore not contribute to the I_3^- concentration. The lower concentration of I_3^- observed at 210 kHz may therefore be due to a faster recombination of OH radicals. However, as an interfacial radical scavenger (ethanol) was used in the actual synthesis, radicals are scavenged before they recombine as was also shown with a separate dosimetry experiment (Figure S3). KI-dosimetry is therefore suitable for the detection of OH-radicals when using solution based radical scavengers. The titanyl sulfate dosimeter therefore provides a more accurate estimation of the radical generation rate than KI-dosimetry for this particular synthesis.

Discussion

The agglomeration of Pt-nanoparticles appears to change from diffusion limited growth at lower ultrasonic frequencies to reaction limited growth at higher ultrasonic frequencies due to the frequency dependent mechanical effects of ultrasound. This transition follows from the clear difference in frequency dependence of the agglomerate size (Figure 4b) from dynamic light scattering and the electrochemical surface area (Figure 5b) from electrochemical measurements. Small porous agglomerates with large surface areas are characteristic of diffusion limited growth, while large compact agglomerates are characteristic of reaction limited growth. In addition, it was found from HAADF-STEM and S(T)EM micrographs (Figure 3) that the lower ultrasonic frequency displays a more open, less compact agglomerate structure compared to the other frequencies.

From numerical simulations of agglomerate growth [36, p.29-31] two distinct growth mechanisms can be found; diffusion limited growth and reaction limited growth. For diffusion limited growth, agglomerates will form upon contact between primary particles and therefore result in a more porous agglomerate, while for reaction limited growth the primary particles will have a lower probability for agglomeration and will therefore have time to diffuse into more energetically favourable surface sites. This creates a more compact structure.

Such a change in agglomeration can be attributed to the mechanical effects of ultra-

sound. Previous reports on the agglomeration formation from ultrasound suggests that the shock waves induced by ultrasound allows for high speed collisions of primary particles in such a way that they are fused together [20][21]. Assuming laminar flow of the nanoparticles through the liquid, we can estimate the velocity, v, of the nanoparticles upon collision [21]

$$v = \frac{rP}{6\mu}\left(1 - \exp\left(-\frac{9\mu\Delta t}{2\rho r^2}\right)\right) \tag{4}$$

where P is the shockwave pressure, r is the nanoparticle radius, μ is the viscosity of the liquid medium, ρ is the density of the nanoparticle, and Δt is the time it takes for the particle to collide with another particle. As the Pt-nanoparticle radius was found to be on the scale of 1 nm, the exponential term in Equation 4 becomes negligible, and the collision velocity is given by

$$v \approx \frac{rP}{6\mu} \tag{5}$$

Using the shock wave pressures given by Merouani et al. [23] as an estimate of the pressures exerted on the nanoparticles during bubble collapse and the viscosity of water leads to collision velocities of $23.5\,\mathrm{m\ s^{-1}}$ at 210 kHz, $12.8\,\mathrm{m\ s^{-1}}$ at 326 kHz, $8.2\,\mathrm{m\ s^{-1}}$ at 408 kHz, and $5.9\,\mathrm{m\ s^{-1}}$ at 488 kHz. This is certainly not fast enough for the particles to melt together upon impact [21], but the kinetic energy supplied by the colliding particles could still aid agglomeration. Using the density of Pt ($21.45\,\mathrm{g\ cm^{-3}}$), and assuming spherical particles with a diameter of 1.9 nm, the kinetic energies attained for the different ultrasonic frequencies are estimated to be $0.13\,\mathrm{eV}$ (12.5 kJ $\mathrm{mol^{-1}}$) at 210 kHz, $0.039\,\mathrm{eV}$ (3.8 kJ $\mathrm{mol^{-1}}$) at 326 kHz, $0.016\,\mathrm{eV}$ (1.5 kJ $\mathrm{mol^{-1}}$) at 408 kHz, and $0.008\,\mathrm{eV}$ (0.8 kJ $\mathrm{mol^{-1}}$) at 488 kHz. As such, the lower ultrasonic frequency will provide the highest kinetic energy upon collision and therefore result in the highest probability for agglomeration. However, lower ultrasonic frequencies lead to fewer cavitation events per second due to the slower collapse of cavitation bubbles [23]. And this is only when we consider one cavitation event. As cavitation bubbles form due to the contraction and elongation of sound waves through the medium, the more contractions and elongations happening along the path of the sound wave the more cavitation bubbles will be generated [11]. A higher frequency (and shorter wavelength) will therefore cause more cavitation events.

In summation, the higher number of cavitation events at higher ultrasonic frequencies increases the supply of nanoparticles towards agglomeration, but due to the slower collision velocities, the probability of instantaneous agglomeration is lower

compared to lower frequencies. As a result, more compact agglomerates, which is a characteristic of reaction limited growth, are formed at higher ultrasonic frequencies. Fewer cavitation events occur at lower frequencies resulting in less supply of nanoparticles to the agglomerate. However, the collision velocity is higher allowing agglomeration to occur at sites of lower energy, thus creating a more open agglomerate characteristic for diffusion limited growth. To strengthen this hypothesis molecular dynamics simulations might provide additional insight into particle collisions driven by the collapse of cavitation bubbles.

The impact of heat transfer in the region around the cavitation bubbles were also considered as a possible explanation for the differing agglomeration behaviour, but was not found to be significant. The idea is that metal nanoparticles in the hot spot region are subjected to high temperatures possibly melting and solidifying periodically depending on bubble collapse times (and ultrasonic frequency). However, due to the small size of the nanoparticles, any temperature gradients between the nanoparticles and the surrounding liquid will disappear completely on a much shorter time scale (picosecond scale) than the frequency dependent expansion times of the cavitation bubbles. This can be seen from Figure S8 in the supporting information which was calculated using the work of S. Paterson [37]. If agglomeration due to heat transfer were to be affected by the ultrasonic frequency, the heating and cooling rates of the nanoparticles would have to be at least on the same time scale as the duration of the cavitation events, which is not the case. We can therefore rule out heat transfer as an explanation to why the agglomeration behaviour is frequency dependent. The observed differences in agglomeration behaviour for different frequencies must therefore be due to purely mechanical effects.

For the same range of frequencies (210 - 488 kHz) that displayed a clear change in agglomeration behaviour, no significant differences were observed in the primary particle sizes of Pt-nanoparticles. All results related to the Pt primary particle size were found to be similar and therefore independent on the applied ultrasonic frequency within this range. This includes the crystallite sizes from XRD (2.1 nm) and the primary particle sizes from S(T)EM, (1.9 $\pm$ 0.3) nm. In addition, the overpotential required to reach $10\,\mathrm{mA\ cm^{-2}}$ (geometric surface area) for the HER was the same for all samples (19 $\pm$ 2 mV) as can be seen from Figure 6a. No apparent optimum ultrasonic frequency can therefore be identified within this frequency range. There is, however, a difference in the LSVs when the current is normalized for the ECSA (Figure 6b), but this can be explained by the porosity of the agglomerates. El-Sayed et al. [38] showed that micro-bubbles can be trapped inside the pores of a catalyst effectively blocking the active sites. The porous

agglomerates formed at 210 kHz would therefore be more prone to micro-bubble trapping during hydrogen evolution compared to the compact agglomerates formed at higher frequencies.

Even though previous reports [14][17] have shown a frequency dependence on nanoparticle sizes, their frequencies span the entire sonochemical range from 20 kHz to 1 MHz providing very different synthesis conditions. Although the trends in radical formation rates (Figure 7c) and reduction rates (Figure 2a) for the different frequencies correspond well with these reports, the differences are apparently too small to be reflected in a detectable particle size change. An ideal frequency for producing the smallest Pt-nanoparticles may therefore exist in theory, but for all practical purposes, the entire frequency range between 210 kHz and 488 kHz can be used to obtain Pt-nanoparticles with the same primary particle size when using low acoustic powers (11.8 W).

Combining the sonochemical and mechanical effects of ultrasound therefore reveals that ultrasonic frequencies between 326 kHz and 488 kHz result in Pt nanoparticles with near identical properties in terms of primary particle size and agglomeration behaviour. These frequencies therefore represent a range where high reproducibility can be expected. Going to even lower frequencies (210 kHz) revealed a change in the agglomeration process opening up the possibility of achieving more porous agglomerates, however the particle properties as well as the catalytic activity towards the HER remained the same. For applications where agglomeration is a problem, lower ultrasonic frequencies can therefore be used without changing the primary particle properties.

Conclusion

The frequency range used in this work clearly demonstrates a significant influence of the mechanical effects of ultrasound on the sonochemical synthesis of Pt-nanoparticles. At lower ultrasonic frequencies, the stronger mechanical effects are capable of changing the agglomeration mechanisms of the primary nanoparticles from reaction limited growth to diffusion limited growth resulting in smaller, more porous agglomerates. The lower ultrasonic frequency (210 kHz) also displayed a higher sonochemical effect as was proved by the higher Pt(IV) reduction rate, and higher radical formation rate. However, no significant changes in the primary nanoparticle size or shape could be found for any of the applied frequencies suggesting that the sonochemical synthesis yields highly reproducible Pt-nanoparticles over a very broad frequency range. This reproducibility was also reflected in the almost similar catalytic activity towards hydrogen evolution displayed by all samples. The sonochemical synthesis of monodisperse spherical Pt-nanocatalysts has therefore proven itself to be highly reliable over a broad frequency range (210 kHz - 488

kHz) making it ideal for applications requiring a high degree of reproducibility.

Acknowledgement

We appreciate the support of ENERSENSE for the funding of this reasearch work, grant 68024013. The Research Council of Norway is acknowledged for the support to the Norwegian Micro- and Nano-Fabrication Facility, NorFab, project number 295864. The authors would like to acknowledge support from the Research Council of Norway through the Norwegian Center for Transmission Electron Microscopy, NORTEM (197405/F50), and TEM operator Inger-Emma Nylund for the acquisition of the TEM-images.

Bibliography

1. Sharma, N., Ojha, H., Bharadwaj, A., Pathak, D. P. & Sharma, R. K. Preparation and catalytic applications of nanomaterials: a review. *RSC Adv.* **5,** 53381–53403 (66 2015).
2. Liz-Marzán, L. M., Kagan, C. R. & Millstone, J. E. Reproducibility in Nanocrystal Synthesis? Watch Out for Impurities! *ACS Nano* **14.** PMID: 32575172, 6359–6361 (2020).
3. Ren, X. *et al.* Current progress of Pt and Pt-based electrocatalysts used for fuel cells. *Sustainable Energy Fuels* **4,** 15–30 (1 2020).
4. Ayers, K. E. *et al.* Pathways to ultra-low platinum group metal catalyst loading in proton exchange membrane electrolyzers. *Catalysis Today* **262.** Electrocatalysis, 121–132 (2016).
5. Kolahalam, L. A. *et al.* Review on nanomaterials: Synthesis and applications. *Materials Today: Proceedings* **18.** 2nd International Conference on Applied Sciences and Technology (ICAST-2019): Material Science, 2182–2190 (2019).
6. Faid, A. Y., Oyarce Barnett, A., Seland, F. & Sunde, S. Highly Active Nickel-Based Catalyst for Hydrogen Evolution in Anion Exchange Membrane Electrolysis. *Catalysts* **8** (2018).
7. Krishna, K. S., Sandeep, C. S. S., Philip, R. & Eswaramoorthy, M. Mixing does the magic: a rapid synthesis of high surface area noble metal nanosponges showing broadband nonlinear optical response. *ACS nano* **4,** 2681–2688 (2010).

8. Escobar Morales, B. *et al.* Synthesis and characterization of colloidal platinum nanoparticles for electrochemical applications. *International journal of hydrogen energy* **35,** 4215–4221 (2010).

9. Dong, H., Chen, Y.-C. & Feldmann, C. Polyol synthesis of nanoparticles: status and options regarding metals, oxides, chalcogenides, and non-metal elements. *Green Chem.* **17,** 4107–4132 (8 2015).

10. Niu, Z. & Li, Y. Removal and Utilization of Capping Agents in Nanocatalysis. *Chemistry Of Materials* **26,** 72–83 (2014).

11. Pollet, B. G. The use of ultrasound for the fabrication of fuel cell materials. *International Journal of Hydrogen Energy* **35,** 11986–12004 (2010).

12. Pollet, B. G. *Introduction to Ultrasound, Sonochemistry and Sonoelectrochemistry* Cham, 2019.

13. Okitsu, K., Bandow, H., Maeda, Y. & Nagata, Y. Sonochemical preparation of ultrafine palladium particles. *Chemistry of Materials (USA)* **8,** 315–317 (1996).

14. Okitsu, K., Ashokkumar, M. & Grieser, F. Sonochemical synthesis of gold nanoparticles: effects of ultrasound frequency. *The journal of physical chemistry. B* **109,** 20673 (2005).

15. Okitsu, K. *et al.* Formation of noble metal particles by ultrasonic irradiation. *Ultrasonics Sonochemistry* **3.** Proceedings of the Symposium on the Chemical Effects of Ultrasound in the 1995 International Chemical Congress of Pacific Basin Societies, S249–S251 (1996).

16. Caruso, R. A., Ashokkumar, M. & Grieser, F. Sonochemical formation of colloidal platinum. *Colloids and Surfaces A: Physicochemical and Engineering Aspects* **169,** 219–225 (2000).

17. He, Y., Vinodgopal, K., Ashokkumar, M. & Grieser, F. Sonochemical synthesis of ruthenium nanoparticles. *Research on chemical intermediates* **32,** 709–715 (2006).

18. Beckett, M. A. & Hua, I. Impact of Ultrasonic Frequency on Aqueous Sonoluminescence and Sonochemistry. *The Journal of Physical Chemistry A* **105,** 3796–3802 (2001).

19. Koda, S., Kimura, T., Kondo, T. & Mitome, H. A standard method to calibrate sonochemical efficiency of an individual reaction system. *Ultrasonics - Sonochemistry* **10,** 149–156 (2003).

20. Doktycz, S. J. & Suslick, K. S. Interparticle Collisions Driven by Ultrasound. *Science* **247,** 1067–1069 (1990).

21. Prozorov, T., Prozorov, R. & Suslick, K. S. High Velocity Interparticle Collisions Driven by Ultrasound. *Journal of the American Chemical Society* **126.** PMID: 15506727, 13890–13891 (2004).

22. Bernt, M. *et al.* Current Challenges in Catalyst Development for PEM Water Electrolyzers. *Chemie Ingenieur Technik* **92,** 31–39 (2020).

23. Merouani, S., Hamdaoui, O., Rezgui, Y. & Guemini, M. Sensitivity of free radicals production in acoustically driven bubble to the ultrasonic frequency and nature of dissolved gases. *Ultrasonics - Sonochemistry* **22,** 41–50 (2015).

24. Hansen, H. E., Seland, F., Sunde, S., Burheim, O. S. & Pollet, B. G. Two routes for sonochemical synthesis of platinum nanoparticles with narrow size distribution. *Mater. Adv.* **2,** 1962–1971 (6 2021).

25. Mizukoshi, Y. *et al.* Preparation of platinum nanoparticles by sonochemical reduction of the Pt(IV) ions: role of surfactants. *Ultrasonics sonochemistry* **8,** 1–6 (2001).

26. Mizukoshi, Y., Oshima, R., Maeda, Y. & Nagata, Y. Preparation of Platinum Nanoparticles by Sonochemical Reduction of the Pt(II) Ion. *Langmuir* **15,** 2733–2737 (1999).

27. Patterson, A. L. The Scherrer Formula for X-Ray Particle Size Determination. *Phys. Rev.* **56,** 978–982 (10 Nov. 1939).

28. Coulter, B. *N5 Submicron Particle Size Analyzer, PCS Software Help Manual* 2003.

29. Conway, B. E., Angerstein-Kozlowska, H., Sharp, W. B. A. & Criddle, E. E. Ultrapurification of water for electrochemical and surface chemical work by catalytic pyrodistillation. *Analytical Chemistry* **45,** 1331–1336 (1973).

30. Angerstein-Kozlowska, H., Conway, B. & Sharp, W. The real condition of electrochemically oxidized platinum surfaces: Part I. Resolution of component processes. *Journal of Electroanalytical Chemistry and Interfacial Electrochemistry* **43,** 9–36 (1973).

31. Iida, Y., Yasui, K., Tuziuti, T. & Sivakumar, M. Sonochemistry and its dosimetry. *Microchemical Journal* **80,** 159–164 (2005).

32. Son, Y., Lim, M., Ashokkumar, M. & Khim, J. Geometric Optimization of Sonoreactors for the Enhancement of Sonochemical Activity. *The Journal of Physical Chemistry C* **115,** 4096–4103 (2011).

33. Rochebrochard D'auzay, S. d. L., Blais, J.-F. & Naffrechoux, E. Comparison of characterization methods in high frequency sonochemical reactors of differing configurations. *Ultrasonics - Sonochemistry* **17,** 547–554 (2010).

34. Dalodière, E., Virot, M., Moisy, P. & Nikitenko, S. I. Effect of ultrasonic frequency on H2O2 sonochemical formation rate in aqueous nitric acid solutions in the presence of oxygen. *Ultrasonics Sonochemistry* **29,** 198–204 (2016).

35. Contamine, R. F., Wilhelm, A., Berlan, J. & Delmas, H. Power measurement in sonochemistry. *Ultrasonics - Sonochemistry* **2,** S43–S47 (1995).

36. Paul C. Hiemenz, R. R. *Principles of Colloid and Surface Chemistry* (CRC Press, 1997).

37. Paterson, S. The heating or cooling of a solid sphere in a well-stirred fluid. *Proceedings of the Physical Society* **59,** 50–58 (1947).

38. El-Sayed, H. A., Weiß, A., Olbrich, L. F., Putro, G. P. & Gasteiger, H. A. OER Catalyst Stability Investigation Using RDE Technique: A Stability Measure or an Artifact? *Journal of The Electrochemical Society* **166,** F458–F464 (2019).

Supporting Information

The absorbance spectra for $TiOSO_4$-dosimetry for all ultrasonic frequencies are shown in Figure S1. The peak absorbance at 411 nm is observed to increase over time in line with the expected increase of OH-radicals.

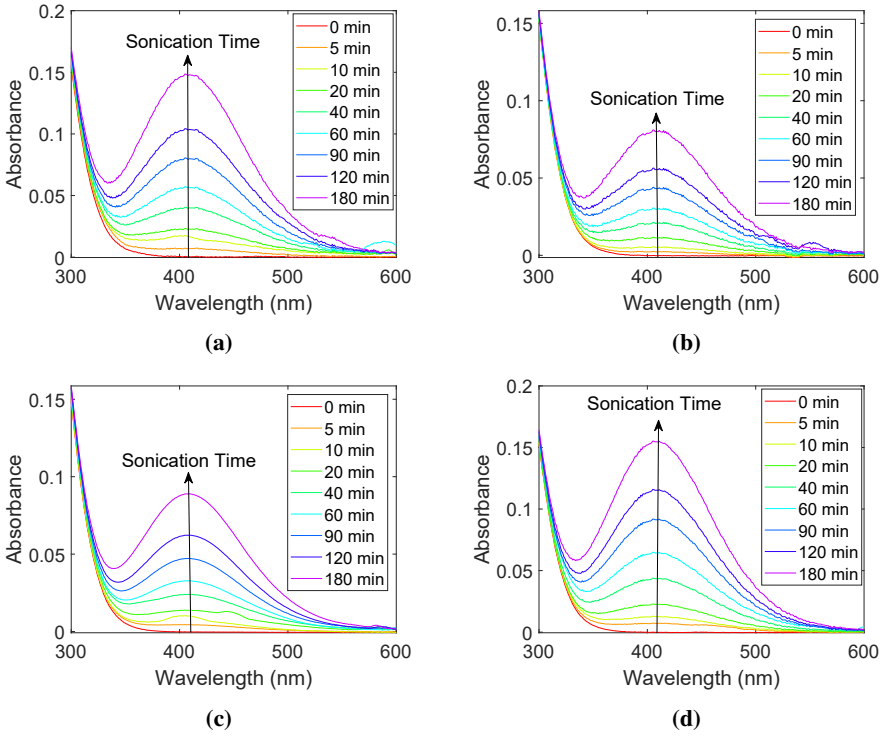

Figure S1: Absorbance spectra of a peroxotitanium (IV) complex plotted at different sonication times at frequencies of 488 kHz (a), 408 kHz (b), 326 kHz (c), and 210 kHz (d).

The ultrasonic power measurements, as calculated from Equation 3, are shown in Figure S2. In order to ensure sufficiently high powers for all frequencies, the maximum power (11.8 W) of the transducer with lowest maximum acoustic power (210 kHz) was chosen for all frequencies meaning amplitudes of 51%, 53%, 73%, and 100% were used at 488 kHz, 408 kHz, 326 kHz, and 210 kHz, respectively.

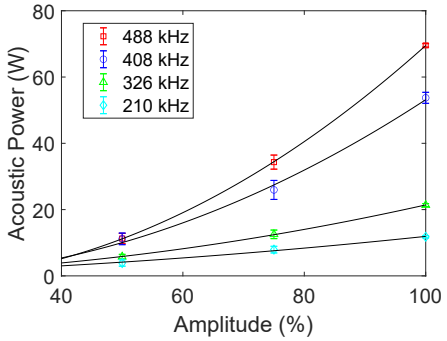

Figure S2: Calorimetric measurements of different ultrasonic frequencies as a function of amplitude.

To ensure that all primary radicals were scavenged by ethanol during the sonochemical synthesis, a separate dosimetry experiment was performed for the frequency which gave the highest radical generation rate (210 kHz) in which pure water was replaced by $0.8\,\mathrm{mol\,dm^{-3}}$ ethanol. The idea being that no H_2O_2 will be observed if ethanol manages to scavenge all primary radicals. This is reflected in the absence of a peak at 411 nm. In addition, the acoustic power was increased to 4 times the value used in the actual synthesis for good measure. The resulting absorbance spectra over a period of 3 hours are shown in Figure S3. The results confirm that no H_2O_2 is produced because all primary radicals are scavenged by ethanol.

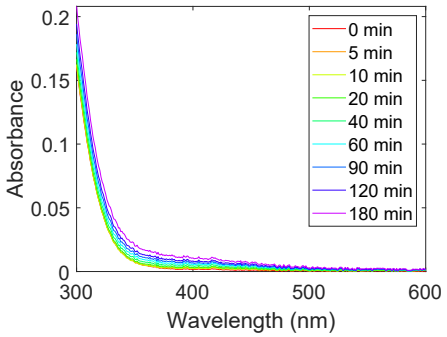

Figure S3: Absorbance spectra of a $0.8\,\mathrm{mol\,dm^{-3}}$ ethanol solution at different sonication times mixed with $TiOSO_4$.

Absorbance spectra of PtI_6^{2-} and PtI_4^{2-} acquired for all Pt-samples at different ultrasonication times (Figure S4). The peak at 495 nm corresponding to PtI_6^{2-}

and the emerging peak at 388 nm corresponding to PtI_4^{2-} can be related to the concentration of Pt(IV) and Pt(II), respectively. These concentrations have been plotted against ultrasonication time for all Pt-samples in Figure S5. The Pt(IV) concentration was found to decrease following an exponential decay. Simultaneously, the Pt(II) concentration was found to increase until it reached a maximum at intermediate ultrasonication times. The following decrease in the Pt(II) concentration is therefore a result of Pt-nanoparticle formation following the reduction of Pt(II) to Pt(0).

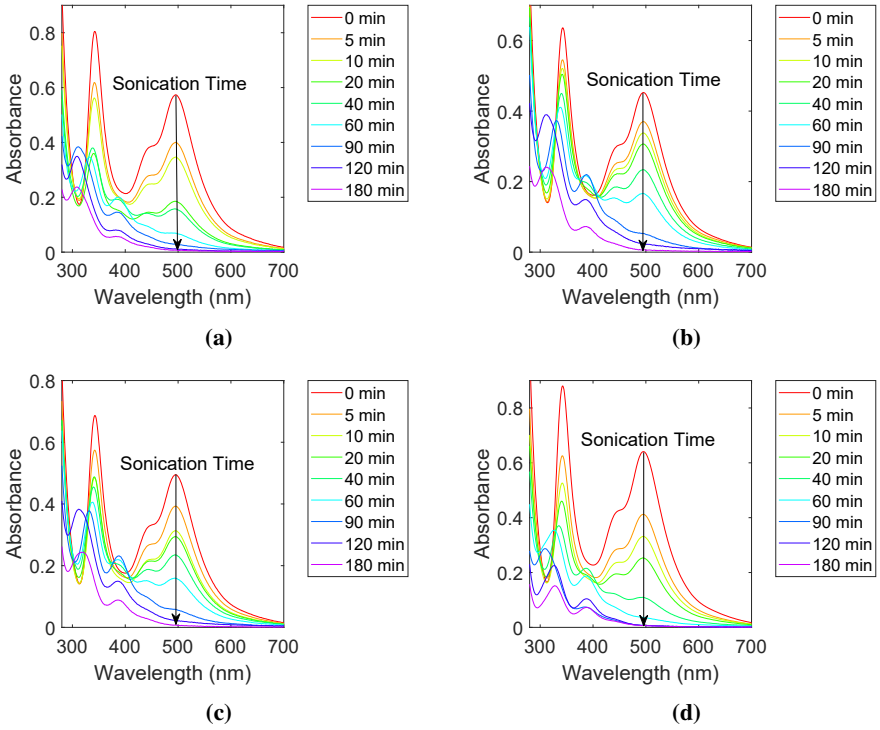

Figure S4: Absorbance spectra of PtI_6^{2-} and PtI_4^{2-} plotted at different sonication times at frequencies of 488 kHz (a), 408 kHz (b), 326 kHz (c), and 210 kHz (d).

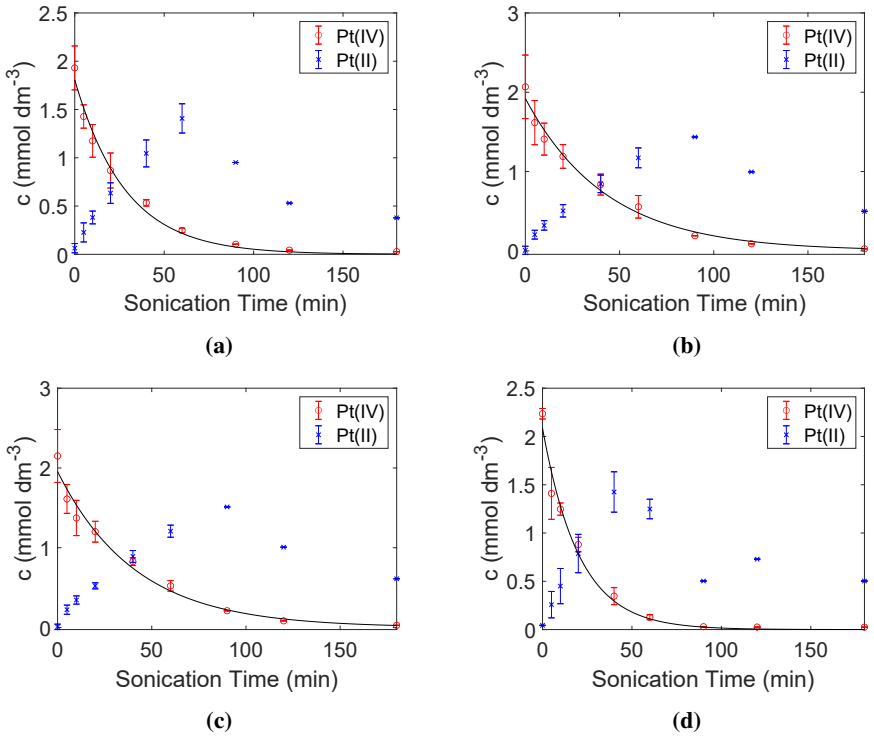

Figure S5: Concentration of Pt(IV) (o) and Pt(II) (x) plotted as a function of sonication time at frequencies of 488 kHz (a), 408 kHz (b), 326 kHz (c), and 210 kHz (d). The error bars are equal to the respective standard deviations.

Additional examples of S(T)EM micrographs of Pt-nanoparticles synthesized at different ultrasonic frequencies are shown in Figure S6.

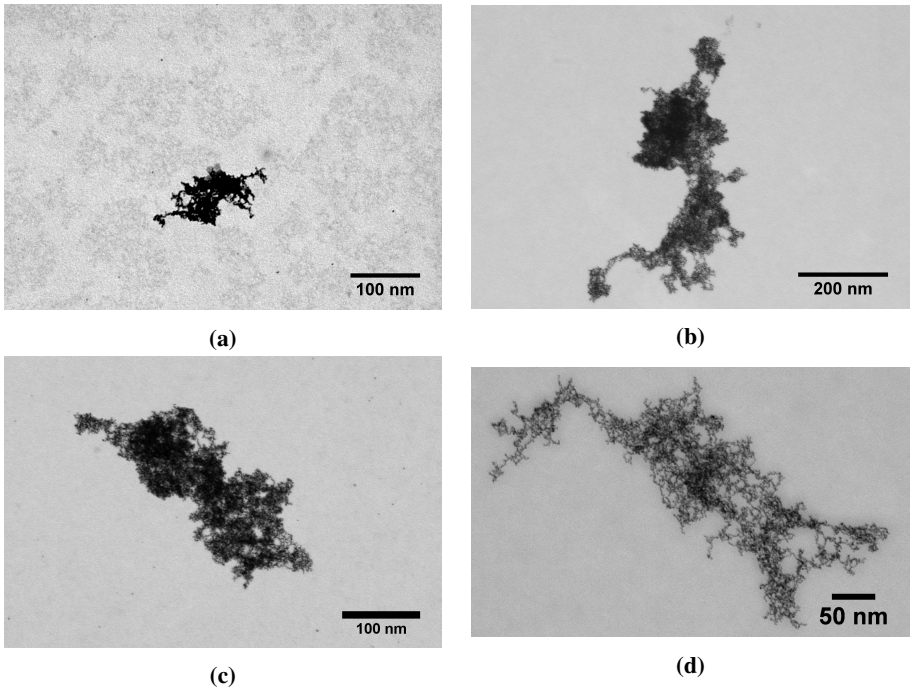

Figure S6: Bright field scanning electron microscopy micrographs of Pt-nanoparticles synthesized at 488 kHz (a), 408 kHz (b), 326 kHz (c), and 210 kHz (d).

The absorbance spectra for KI-dosimetry for all ultrasonic frequencies are shown in Figure S7. The peak absorbance at 350 nm is observed to increase over time in line with the expected increase of OH-radicals.

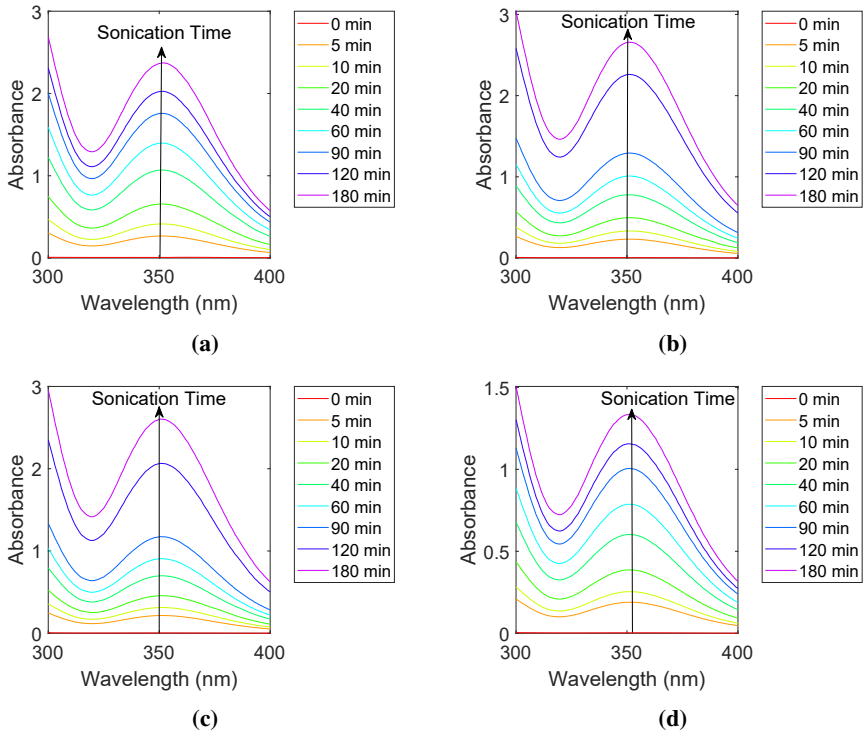

Figure S7: Absorbance spectra of I_3^- plotted at different sonication times at frequencies of 488 kHz (a), 408 kHz (b), 326 kHz (c), and 210 kHz (d).

The temperature profiles from the center of a spherical Pt-nanoparticle to the surface for different cooling times are shown in Figure S8. The temperature of the surrounding liquid is set to 20 °C, and the profiles show a complete cooling of the particle within 1 ps. This estimation assumes that the Pt-nanoparticle is right next to the collapsing bubble, and experience the maximum bubble temperature of 5,000 K.

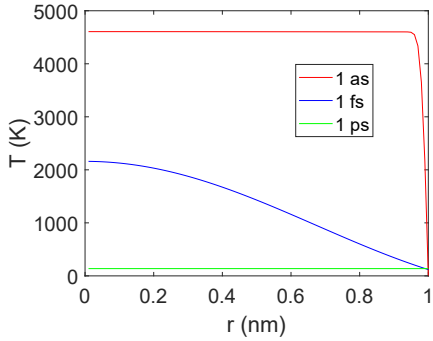

Figure S8: Temperature profiles of a Pt-nanoparticle after being heated by the temperatures generated by a collapsing cavitation bubble as a function of the particle radius. The center of the particle is at x = 0 nm, and the surface is at x = 1 nm. The temperature profiles are also shown for different cooling times (time after the heating was stopped).

Measurements of the molar extinction coefficient at 495 nm for PtI_6^{2-} are shown in Figure S9a. From the slope of this curve, the molar extinction coefficient of PtI_6^{2-} was determined to be ϵ = 11,170 $\mathrm{dm^3 mol^{-1} cm^{-1}}$. Measurements of the molar extinction coefficient at 411 nm for the $TiOSO_4$ complex formed due to interaction with H_2O_2 are shown in Figure S9b. From the slope of this curve, the molar extinction coefficient of this complex was determined to be ϵ = 787 $\mathrm{dm^3 mol^{-1} cm^{-1}}$.

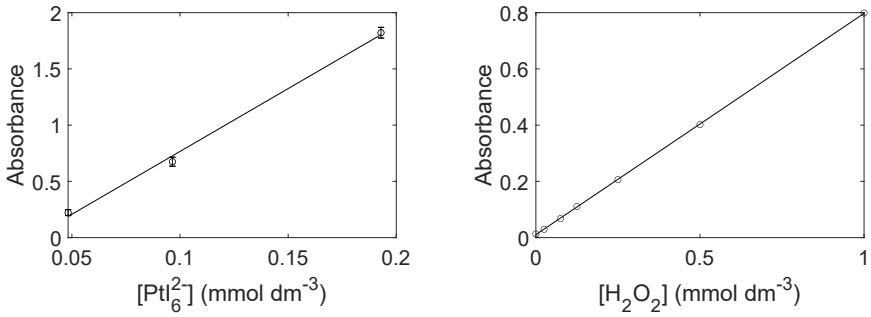

Figure S9: Absorbance of PtI_6^{2-} at a wavelength of 495 nm measured for different known concentrations of Pt(IV) (a), and the absorbance of the $TiOSO_4$ complex at a wavelength of 411 nm measured for different known concentrations of H_2O_2.

Chapter 6

Sonochemical Synthesis of Cu@Pt Bimetallic Nanoparticles

Sonochemical Synthesis of Cu@Pt Bimetallic Nanoparticles

Henrik E. Hansen[1,2*], Daniel Fakhri[1], Frode Seland[1], Svein Sunde[1], Odne S. Burheim[2], Bruno G. Pollet[2,3]

[1]Electrochemistry Group, Department of Materials Science and Engineering, Faculty of Natural Sciences. Norwegian University of Science and Technology (NTNU), NO-7491 Trondheim, Norway

[2]Hydrogen Energy and Sonochemistry Research Group, Department of Energy and Process Engineering, Faculty of Engineering, Norwegian University of Science and Technology (NTNU), NO-7491 Trondheim, Norway

[3]Green Hydrogen Lab, Pollet Research Group, Institute for Hydrogen Research (IHR), Université Du Québec à Trois-Rivières (UQTR), 3351 Boulevard des Forges, Trois-Rivières, Québec G9A 5H7, Canada

Authors to whom correspondence should be addressed:
*henrik.e.hansen@ntnu.no

Abstract

Reducing the amount of noble metals in catalysts for electrochemical conversion devices is paramount if these devices are to be commercialized. Taking advantage of the high degree of particle property control displayed by the sonochemical method, we set out to synthesize Cu@Pt bimetallic nanocatalysts in an effort to improve the mass activity towards the hydrogen evolution reaction. At least 17 times higher mass activity was found for the carbon supported Cu@Pt bimetallic nanocatalyst ($737\,\mathrm{mA\,mg^{-1}}$, $E = -20\,\mathrm{mV}$) compared to carbon supported Pt nanocatalysts prepared with the same ultrasound conditions ($44\,\mathrm{mA\,mg^{-1}}$, $E = -20\,\mathrm{mV}$). The synthesis was found to proceed with the sonochemical formation of Cu and Cu_2O nanoparticles with the addition of $PtCl_4$ leading to galvanic displacement of the Cu-nanoparticles and the formation of a Pt-shell around the Cu-core.

Keywords: ultrasound; sonochemistry; electrocatalyst; hydrogen; platinum; copper; core-shell

Introduction

The sonochemical synthesis method has shown great promise with its ability to easily tune the size of certain noble metal nanoparticles and to achieve narrow nanoparticle size distributions [1–5]. This is achieved through easily adjustable ultrasound parameters such as the ultrasonic frequency and acoustic power which directly control the generation of reducing agents in the form of radicals [4, 6–8]. Such control over nanoparticle properties is essential when developing new nanomaterials for a range of different applications spanning a broad spectrum of fields including the field catalysis.

To develop better catalyst materials, optimizing the surface properties of the catalyst such as the surface area and the particle size is of great importance [9]. Current wet chemical synthesis methods do not offer such ease of control as particle properties are usually adjusted by precise ratios of surfactants and precursors making reproducibility difficult [9, 10]. The sonochemical synthesis method could therefore offer a greater degree of control over these properties thereby paving the way for optimized catalyst materials.

However, many of the best catalyst materials in applications such as water electrolyzers and fuel cells are heavily dependent on noble metals which makes industrial scale production not feasible due to the high cost of these raw materials [11, 12]. The hydrogen evolution reaction is one of those reactions in which noble metals such as platinum have been used extensively. Switching to cheaper catalyst mater-

ials is a possible solution, but the reduction in price is typically also followed by a reduction in performance. Another possible solution is to minimize the amount of noble metals by synthesizing core-shell nanocatalysts with the noble metal making up the shell and a cheaper metal making up the larger core [13, 14]. The noble metal surface properties may therefore be preserved or improved with a reduction in raw material cost.

Several types of core-shell catalysts have been synthesized through various wet-chemical techniques, but one that has received much attention due to its excellent hydrogen evolution and hydrogen oxidation activity is the Cu@Pt bimetallic structure [13–16]. The general approach to this synthesis appears to follow a two-step process in which the Cu core is synthesized in the first step, followed by galvanic displacement of the metallic Cu by a Pt-precursor to make up the shell. One such synthesis was performed by Zhu et al. [13] where they synthesized Cu@Pt bimetallic nanoparticles with a two-step polyol method using ethylene glycol as the reducing agent. Sarkar et al. [14] also synthesized Cu@Pt bimetallic nanoparticles, where they initially formed metallic Cu through reduction of $CuSO_4 \cdot 5\,H_2O$ by $NaBH_4$ before creating the Pt-shell by galvanic displacement using $H_2PtCl_6 \cdot 6\,H_2O$.

The synthesis of core-shell nanoparticles through a sonochemical route, however, is less common and has mostly been performed with probe sonicators taking advantage of the massive temperature increases from acoustic cavitation [17, 18]. Direct sonication with probe sonicators has been shown to cause probe erosion which introduces unpredictable nucleation and growth conditions in turn influencing the particle properties and the purity of the catalyst [19]. Higher frequency plate transducers avoid the problem of erosion all together [19] meaning the high degree of particle control associated with the sonochemical synthesis can be realized. A successful high frequency sonochemical synthesis may therefore offer an easy, reliable way of producing better and cheaper catalyst materials.

In this work we want to determine if the sonochemical synthesis method can be used to synthesize carbon supported Cu@Pt bimetallic nanoparticles, and if the resulting catalyst can challenge a carbon supported Pt-nanocatalyst with respect to its mass activity for hydrogen evolution. Both catalysts were synthesized sonochemically at the same ultrasound conditions to eliminate any effect of the synthesis method. Assessment of the existence of the core-shell structure was performed through physical characterization such as X-ray diffraction and UV-Visible spectroscopy, as well as electrochemical characterization through cyclic voltammetry and linear sweep voltammetry. The hydrogen evolution performance was evaluated based on mass activity at an overpotential of $20\,\mathrm{mV}$.

Experimental

Sonochemical Setup

For all sonochemical experiments a plate transducer ($70\,\mathrm{mm}$ ⌀) with resonance frequency of 346 kHz from Honda Electronics was used to generate the ultrasonic waves. The piezoelectric material making up the transducer is lead zirconate titanate (PZT), while the plate which transfers the ultrasonic waves to the solution is a highly corrosive resistant stainless steel alloy (SUS304). These plate transducers make up the bottom part of the sonochemical reactor. The rest consists of an inner chamber where the solution is sonicated, and an outer chamber where water is circulating to control the temperature. The top part contains several inlets and outlets to maintain proper atmosphere inside the reactor during sonication. The reactor itself is made from borosilicate glass. A detailed figure showing the different parts of the reactor can be found elsewhere [3]. To generate the ultrasonic waves, an AG 1012 RF signal generator was used in conjunction with an impedance matching unit (T1k-7A) both from T&C Power Conversion. If there is a mismatch between the impedance of the incoming electrical signal from the signal generator and the operating impedance of the piezoelectric transducer, the actual acoustic power will be severely reduced. A mismatch in impedance can be detected as a reflected power with the AG 1012 RF signal generator. By adjusting the impedance matching unit appropriately, near zero reflected power can be achieved, which makes the transducer more efficient.

Synthesis

Sonochemical synthesis of Cu@Pt bimetallic nanoparticles supported on XC-72 carbon was performed at $346\,\mathrm{kHz}$ through direct sonication. $2\,\mathrm{mmol\,dm^{-3}}$ of $CuSO_4 \cdot 5\,H_2O$ was prepared in a $200\,\mathrm{mL}$ $0.2\,\mathrm{mol\,dm^{-3}}$ formate/formic acid buffer of pH 5, and sonicated for $6\,\mathrm{h}$. A pH of 5 was chosen as previous radiolytic investigations of Cu(II) reduction showed that the pH range between 2 and 8 yield metallic Cu [20]. The core-shell structure was achieved through galvanic displacement by adding $50\,\mathrm{mL}$ of $0.2\,\mathrm{mmol\,dm^{-3}}$ $PtCl_4$ precursor towards the end of the sonication [14]. Samples taken before the addition of $PtCl_4$ will from now on be referred to as Cu_2O-samples, while samples taken after the addition of $PtCl_4$ will be referred to as Cu@Pt-samples.

The formate ion is an excellent scavenger and a concentration of $0.2\,\mathrm{mol\,dm^{-3}}$ is considered sufficient for radical scavenging without greatly affecting the collapse conditions of the cavitation bubbles [21]. The temperature was maintained at $3\,^{\circ}\mathrm{C}$ with water cooling through the external jacket on the sonochemical reactor. The applied electrical power was kept constant at $50\,\mathrm{W}$, but the effective acous-

tic power was measured to be (38 ± 3) W. To avoid exposure to O_2 and N_2, Ar was supplied to the solution 20 min prior to sonication and throughout the entire synthesis. The resulting particles were extracted from solution using an Eppendorf 5810 R centrifuge operated at 12 000 rpm for 15 min, before being cleaned three times with an ethanol water mixture, and then dried in air over night.

To compare the performance of any Cu@Pt bimetallic catalysts, Pt-nanoparticles supported on XC-72 carbon were also synthesized sonochemically using $0.8\,\mathrm{mol\,dm^{-3}}$ ethanol as a radical scavenger. All other ultrasound parameters were kept the same as described above. These samples will from now on be referred to as Pt-samples.

Characterization

Periodic absorbance measurements were performed throughout the sonication period with an Evolution 220 UV-Visible spectrophotometer. The resulting absorbance spectra were used to assess the development of the metal ions throughout the sonication period. Prior to these measurements, the samples were filtered through a 0.45 µm particle filter from VWR to avoid interference from any precipitates as well as the carbon support.

The resulting Pt-, Cu-, and Cu@Pt-samples were characterized by X-ray diffraction (XRD) in order to determine the crystallographic phases as well as the mean crystallite sizes of these phases. Particles were dispersed in ethanol and drop cast onto flat silicon wafers and dried before being covered by a Kapton film. The measurements were performed with a Bruker D8 A25 DaVinci X-ray Diffractometer with CuKα radiation. A scan rate of $0.044\,^\circ/\mathrm{step}$ was used for 2θ-angles between 30°-75° with a 0.3° fixed slit for 60 min.

Electrochemical characterization was performed in a round bottom electrochemical glass cell with a three electrode configuration. A glassy carbon rotating disk electrode (Pine Instrument) coated with the catalyst ink was used as the working electrode, graphite was used as the counter, and the reversible hydrogen electrode (RHE) was used as the reference electrode. The catalyst ink was prepared by mixing 10 mg catalyst material with 475 µL isopropyl alcohol (technical, VWR), 475 µL ultrapure water (Milli-Q, $18.2\,\mathrm{M\Omega\,cm}$), and 50 µL Nafion 117 (5 wt% in mixture of lower aliphatic alcohols and water, Sigma Aldrich). 10 µL of the catalyst ink was spin coated onto the glassy carbon working electrode with a rotation rate of 200 rpm. As the metal loading on the carbon support was estimated to be 20 wt%, the Pt-loading on the glassy carbon for the Pt-sample amounted to $100\,\mathrm{\mu g\,cm^{-2}}$. For the Cu@Pt-sample, the Pt-loading was even lower with an estimated value of $7.1\,\mathrm{\mu g\,cm^{-2}}$ assuming complete reduction of the $PtCl_4$ precursor.

All measurements were conducted in an Ar-saturated $0.5\,\mathrm{mol\,dm^{-3}}$ H_2SO_4 (95-

97%, VWR) electrolyte. Cyclic voltammetry was performed for potentials between $0.04\,\mathrm{V}$-$1.6\,\mathrm{V}$ vs RHE with a scan rate of $50\,\mathrm{mV\,s^{-1}}$. From the hydrogen under deposition peaks located between $0.04\,\mathrm{V}$-$0.3\,\mathrm{V}$ vs RHE the electrochemical active surface area (ECSA) was estimated using a monolayer coverage value of $220\,\mu\mathrm{C\,cm^{-2}}$ [22]. The activity towards the hydrogen evolution reaction was also investigated through linear sweep voltammetry with a scan rate of $1\,\mathrm{mV\,s^{-1}}$. Mass activities at $-20\,\mathrm{mV}$ vs RHE were compared between the carbon supported Cu@Pt bimetallic nanocatalysts and the carbon supported Pt nanocatalysts.

Transducer Characterization

The ultrasonic plate transducer was subject to rigorous testing before synthesis in an effort to determine its actual acoustic power and radical generation capabilities. To determine the acoustic power, calorimetric measurements were performed in which the temperature increase caused by sonication was measured with the assumption that all acoustic power is transformed into heat [23, 24]. Sonication was performed in $200\,\mathrm{mL}$ of deionized water at room temperature over the course of $1\,\mathrm{min}$. The acoustic power can therefore be calculated as

$$P_{\text{acoustic}} = mC_{\mathrm{p}} \left(\frac{dT}{dt} \right)_{t=0} \tag{1}$$

where $(\mathrm{d}T/\mathrm{d}t)_{t=0}$ is the temperature slope of water per unit of sonication time (at t = 0), m is the mass of the water, and C_{p} is the specific heat capacity of water ($4.186\,\mathrm{J\,g^{-1}\,K^{-1}}$) [23, 24].

As for the radical generation capabilities of the ultrasonic transducer, $TiOSO_4$ dosimetry was used to measure the yield of H_2O_2 generated by sonication [8]. As H_2O_2 is the primary recombination product of the ·OH radicals in pure water systems

$$2\mathrm{OH}\cdot \longrightarrow \mathrm{H_2O_2}$$

we can assume that the yield of ·OH radicals is twice as high as the concentration of H_2O_2. The detection of H_2O_2 was performed spectrophotometrically by measuring the light absorption of a Ti-complex forming when excess $TiOSO_4$ is added to a sonicated sample of water. The $TiOSO_4$ reacts with H_2O_2 to form this yellow Ti-complex which has a molar absorption coefficient of $787\,\mathrm{mol^{-1}\,dm^3\,cm^{-1}}$ at 411 nm in the absorbance spectrum [3]. Sampling from $0\,\mathrm{min}$ to $20\,\mathrm{min}$ was performed in order to obtain the rate of ·OH radical formation for each frequency.

Longer sonication times were not necessary as the ·OH radical formation is expected to follow zero-order kinetics [3].

Results

Absorbance spectra for the Cu(II) species are shown in Figure 1a for different sonication times. The decrease in absorbance with sonication time indicates that the Cu(II) concentration also decreases during sonication signifying a successful reduction by the sonochemically generated radicals. Plotting the absorbance at the peak ($773\,\mathrm{nm}$) as a function of sonication time (Figure 1b) shows that the reduction rate follows first-order kinetics with a rate constant of $k = 0.27\,\mathrm{h}^{-1}$. Such a first-order behaviour is similar to the previously observed sonochemical reduction of Pt(IV) to Pt(II), albeit with a much lower rate constant [3].

After sonicating the Cu-solution for 6 hours, $PtCl_4$ was added to the sonicating solution and the development of the Pt(IV) concentration was measured with UV-Visible spectroscopy for 10 min. To enhance the Pt(IV) peaks, the sample was mixed with an excess of KI to form PtI_6^{2-} ($\lambda_{\max}$ = 495 nm) [25]. The resulting absorbance spectra are shown in Figure 2a. The figure shows a clear decrease in the peak at 495 nm suggesting the successful reduction of Pt(IV) to Pt(II) as indicated by the appearance of a PtI_4^{2-} peak at 388 nm [25].

The absorbance belonging to the Pt(IV) species at 495 nm is also plotted as a function of sonication time in Figure 2b. The Pt(IV) concentration is shown to decrease rapidly to about $50\,\%$ of the starting concentration within the first minute before it experiences a slow increase. Further sonication appears to stabilize the Pt(IV) concentration close to the value obtained after 1 min.

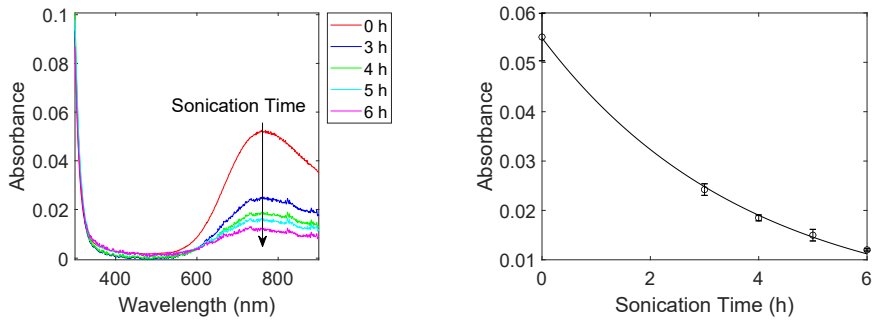

(a) **(b)**

Figure 1: Absorbance spectra of Cu(II) at different sonication times (a), and the absorbance at 773 nm plotted as a function of sonication time (b). The contribution from other interfering species such as the carbon support and the as-formed nanoparticles were removed by filtration.

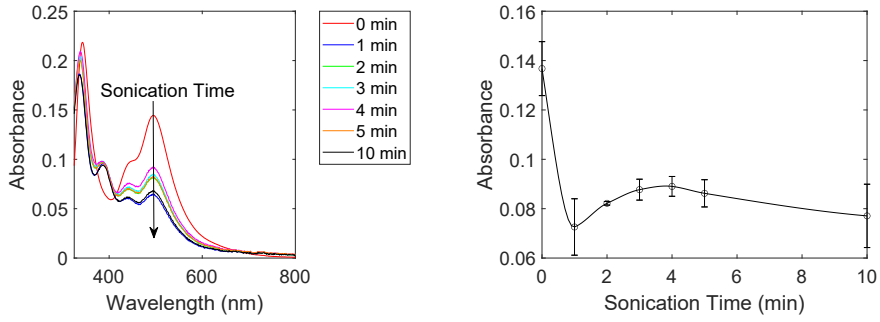

(a) **(b)**

Figure 2: Absorbance spectra of PtI_6^{2-} and PtI_4^{2-} at different sonication times (a) and the absorbance at 495 nm plotted as a function of sonication time (b). The sonication time is measured in minutes after the addition of $PtCl_4$ to the Cu-solution. The contribution from other interfering species such as the carbon support and the as-formed nanoparticles were removed by filtration.

X-ray diffractograms of the resulting particles from the sonochemical synthesis are shown in Figure 3. The Cu@Pt-sample (c) exhibits peaks corresponding to metallic Cu at 2θ angles of $43.3°$ (111), $50.4°$ (200), and $74.1°$ (220). Additional peaks corresponding to Cu_2O are also found at 2θ angles of $29.5°$ (110), $36.4°$ (111), $42.3°$ (200), $61.4°$ (220), and $73.4°$ (311). No clear indication of Pt was found in the diffractogram, but a separate diffractogram of Pt supported on carbon (a) shows that its contribution disappears into the carbon support background. The

Cu_2O-sample (b) only exhibits peaks corresponding to Cu_2O as described above.

Applying the Scherrer equation to the Cu_2O (111) and metallic Cu (111) peaks showed that the crystallite size for the Cu_2O-sample was significantly larger ($84.1\,\mathrm{nm}$) than the Cu@Pt-sample ($35.0\,\mathrm{nm}$). No determination of the crystallite size for the Pt-sample was feasible due to its signal being quenched by the carbon support.

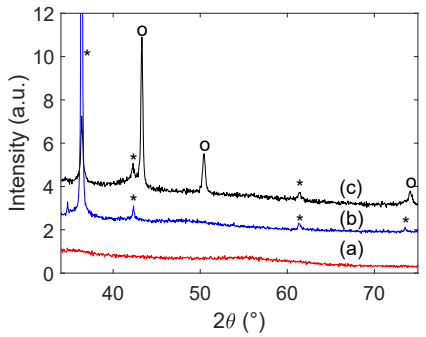

Figure 3: X-ray diffractograms of particles from the sonochemical synthesis. Carbon supported Pt-nanoparticles are shown in red (a), while Cu-samples synthesized before the addition of $PtCl_4$ are shown in blue (b), and Cu-samples synthesized after the addition of $PtCl_4$ are shown in black (c). Peaks corresponding to the Cu_2O phase (*) and the metallic Cu phase (o) are marked in the figure.

The cyclic voltammograms of the Pt-, Cu_2O-, and Cu@Pt-samples are shown in Figure 4. For the Pt-sample (a), the characteristic CV of Pt was observed [13] confirming that Pt was indeed prepared sonochemically. From the hydrogen underpotential deposition peaks, the ECSA was estimated to be $6.2\,\mathrm{m^2\,g^{-1}}$. For the Cu_2O-sample (b), no clear features are observed in the voltammogram at lower potentials. If the particles contained metallic Cu, one would expect to see Cu dissolution represented by a stripping peak around E = 0.6 V for the first cycle in the anodic direction [26]. Towards higher potentials, the Cu_2O-sample displays an increased current, even surpassing that of the Pt-sample. For the Cu@Pt-sample (c), the characteristic voltammogram of Pt can be seen [13], albeit with a smaller current compared to the Pt-sample. This can most likely be attributed to the lower Pt-loading as expected for the Cu@Pt-sample. A voltammogram acquired at $400\,\mathrm{mV\,s^{-1}}$ (Figure S1 from Supplementary Materials) was used to estimate the ECSA of the Cu@Pt-sample in order to enhance the hydrogen underpotential deposition peaks. The resulting ECSA was estimated to be $15.1\,\mathrm{m^2\,g^{-1}}$.

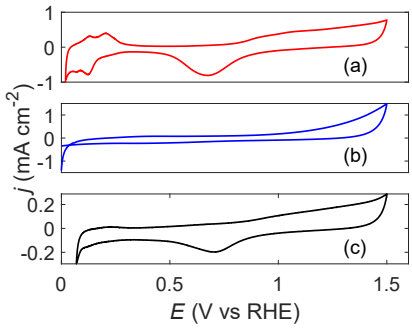

Figure 4: Cyclic voltammograms for sonochemically synthesized carbon supported Pt-nanoparticles (a), and Cu-nanoparticles before (b) and after (c) the addition of $PtCl_4$. All measurements were performed in $0.5\,\mathrm{mol\,dm^{-3}}$ H_2SO_4 with a scan rate of $50\,\mathrm{mV\,s^{-1}}$.

The catalytic activity of the Pt-, Cu_2O-, and Cu@Pt-samples towards the hydrogen evolution reaction (HER) are shown through linear sweep voltammetry (Figure 5). The Pt-sample displays an overpotential of $29.3\,\mathrm{mV}$ at $10\,\mathrm{mA/cm^2_{geo}}$ towards the HER, while the Cu_2O-sample has zero contribution to the HER in the same region. The Cu@Pt-sample has a very similar performance to the Pt-sample with an overpotential of $28.6\,\mathrm{mV}$ at $10\,\mathrm{mA/cm^2_{geo}}$ towards the HER. The mass activity of the Pt-sample at an overpotential of $20\,\mathrm{mV}$ was found to be $44\,\mathrm{mA\,mg^{-1}}$ while the mass activity of the Cu@Pt-sample was found to be $737\,\mathrm{mA\,mg^{-1}}$. This amounts to an approximately 17 times higher mass activity for the Cu@Pt-sample.

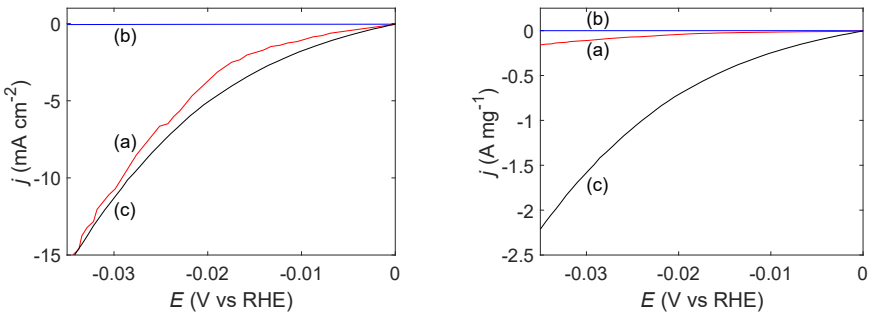

Figure 5: Linear sweep voltammogram acquired over the hydrogen evolution region for sonochemically synthesized carbon supported Pt-nanoparticles (a), and Cu-nanoparticles before (b) and after (c) the addition of $PtCl_4$. Figure a shows the current normalized for the geometric surface area, while Figure b shows the current normalized for the estimated mass of Pt.

Results from dosimetry and calorimetry experiments are shown in Figure 6a and 6b, respectively. The $TiOSO_4$ dosimetry shows an approximately linear increase in the ·OH radical formation. This is also expected as zero-order kinetics has been demonstrated for a similar ultrasound configuration previously [3]. The radical generation rate is estimated to be ($12\,\mu\mathrm{mol\,dm^{-3}\,min^{-1}}$) assuming all ·OH radicals recombine into H_2O_2. The corresponding absorbance spectra are given in the supporting information (Figure S2 from Supplementary Materials). From the calorimetry measurements the acoustic power was estimated using equation 1 to be (38 ± 3) W. The temperature increase in the reactor as a function of sonication time is given in Figure 6b.

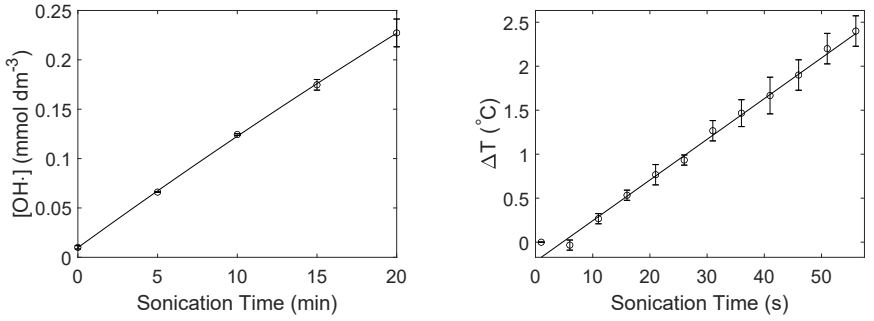

(a) **(b)**

Figure 6: $TiOSO_4$ dosimetry showing the ·OH concentration as a function of sonication time (a). The concentration of the ·OH was estimated from the hydrogen peroxide concentration. Calorimetry measurements of the acoustic power of ultrasound showing the resulting temperature increase in water as a function of sonication time (b).

Discussion

The sonochemical synthesis of Cu@Pt bimetallic nanoparticles appears to be possible by taking advantage of galvanic displacement of Cu by Pt(IV). The characteristic CV of Pt and the enhanced mass activity observed through electrochemical measurements (Figure 4 and Figure 5b, respectively) as well as the existence of metallic Cu as seen from XRD (Figure 3) show that the sample contains both Pt and Cu.

If Pt and Cu were to be separate phases, any metallic Cu would oxidize to Cu_2O upon exposure to air during drying as was observed for the Cu_2O-sample (Figure 3). In addition, we would have seen an increase in the current towards higher potentials in the cyclic voltammogram as was demonstrated by the Cu_2O-sample (Figure 4). The much higher mass activity observed for the Cu@Pt-sample (Figure

5b) is also an indication of a core-shell structure as such low Pt-loadings would not be able to reach such high currents. This was demonstrated by the Pt-sample which reached the same current densities as the Cu@Pt-sample (normalized for geometric surface area) at a much higher Pt-loading (Figure 5a). One can also argue that the presence of Pt(IV)- and Pt(II)-ions in the reaction solution (Figure 2a) after the reaction was completed is an indication of the Cu-sites being fully blocked by a shell of Pt resulting in no further Pt-reduction.

Arguments for the galvanic displacement of Cu by Pt(IV) can be made through careful analysis of the UV-Vis absorbance spectra of Pt (Figure 2a) and the radical generation capabilities of the sonochemical reactor as measured through $TiOSO_4$ dosimetry (Figure 6a). From the Pt UV-Vis absorbance spectra in Figure 2a, the rapid reduction of Pt(IV) to about $50\,\%$ of the starting concentration within the course of 1 min is a clear indication of an assisted reduction. The ·OH radical generation rate was determined to be $12\,\mu\mathrm{mol\,dm^{-3}\,min^{-1}}$ as shown through dosimetry measurements (Figure 6a). If all ·OH radicals generated within this minute was fully scavenged by the formate ions, it would be able to reduce maximum $1.5\,\mu\mathrm{mol}$ Pt(IV) to Pt(II), and only $0.75\,\mu\mathrm{mol}$ Pt(IV) to Pt(0). The amount of Pt(IV) being added to the reactor is $10\,\mu\mathrm{mol}$ which means that if half of this is reduced within the first minute, the sonochemical synthesis must be assisted. With Pt exhibiting a more positive reduction potential than Cu, the galvanic displacement of Cu with Pt(II) and Pt(0) therefore appears to be the dominant reduction mechanism for the added Pt(IV).

The estimated crystallite sizes of the Cu-phases from XRD for the Cu_2O-sample ($84.1\,\mathrm{nm}$) and the Cu@Pt-sample ($35.0\,\mathrm{nm}$) also suggests that the size determining Cu-core has been reduced in size upon adding $PtCl_4$. Such a size reduction would only occur if some of the already formed Cu is galvanically replaced by Pt or Pt(II). Another complementary effect to a size reduction of the Cu@Pt-sample is a size increase for the Cu_2O-sample which would occur upon formation or growth of Cu_2O when the particles are dried in air. Both explanations support the formation of a Cu@Pt bimetallic structure.

The Pt(IV) concentration was also observed to stabilize after the reaction was completed (Figure 2) which could suggest that there are no more Cu-sites available for galvanic displacement. From the X-ray diffractograms (Figure 3) it is shown that metallic Cu still prevails in the sample. The metallic Cu present in the sample must therefore be protected from the Pt(IV) still present in the reactor. This could be due to the formation of a metallic Pt shell around the Cu-particles.

Another argument which can be made for the formation of the Cu@Pt bimetallic structure is the fact that the metallic Cu phase is not present in the X-ray diffracto-

gram of the Cu_2O-sample taken before the addition of $PtCl_4$ as seen in Figure 3. The absence of a covering Pt-shell could allow for the oxidation of metallic Cu to Cu_2O when dried in air, but if the particles are coated with a layer of Pt no such oxidation is possible. Peaks belonging to Cu_2O are still seen in the X-ray diffractogram of the Cu@Pt-samples which might suggest that not all particles are perfectly covered with Pt or that this Cu_2O phase was also formed to some degree during sonication. As was previously discussed, no free Cu sites should be available as this would have ensured further Pt(IV) reduction. Cu_2O may form in situ through the reaction between metallic Cu and hydrogen peroxide which is an expected byproduct of unreacted ·OH during sonication.

$$2\mathrm{Cu} + \mathrm{H_2O_2} \longrightarrow \mathrm{Cu_2O} + \mathrm{H_2O} \tag{2}$$

This reaction is evidently not dominating as metallic Cu prevails throughout the entire 6 hour sonication period, but it can explain why Cu_2O is observed to some degree for the Cu@Pt-sample. The presence of hydrogen peroxide is further strengthened by the slight increase in Pt(IV) concentration after the initial reduction as seen in Figure 2b. When the Pt(IV) is reduced to Pt(II), Pt(II) may be reoxidized by any residual hydrogen peroxide in the reactor. The hydrogen peroxide is then removed through this reaction, and the Pt(IV) concentration eventually stabilizes. The Cu_2O phase observed along with the Cu@Pt bimetallic structure therefore appears to be a byproduct of unreacted ·OH radicals during sonication.

Conclusion

The sonochemical synthesis of carbon supported Cu@Pt bimetallic nanoparticles proved successful with the catalysts achieving at least 17 times higher mass activity compared to carbon supported Pt-nanoparticles prepared in the same manner. The core-shell formation appears to occur through three steps; Cu(II) is reduced to metallic Cu through sonochemical reduction. A Cu_2O phase then appears to some degree due to oxidation of metallic Cu by hydrogen peroxide. When $PtCl_4$ is added, the Pt is galvanically reduced at the metallic Cu surface until all Cu sites are covered with Pt making up the Cu@Pt bimetallic structure.

Acknowledgements

We appreciate the support of ENERSENSE for the funding of this reasearch work, grant 68024013. The Research Council of Norway is acknowledged for the support to the Norwegian Micro- and Nano-Fabrication Facility, NorFab, project number 295864. The Research Council of Norway is also acknowledged for the support to the INTPART project 261620.

Bibliography

1. Okitsu, K. *et al.* Formation of noble metal particles by ultrasonic irradiation. *Ultrasonics Sonochemistry* **3.** Proceedings of the Symposium on the Chemical Effects of Ultrasound in the 1995 International Chemical Congress of Pacific Basin Societies, S249–S251 (1996).
2. Okitsu, K., Ashokkumar, M. & Grieser, F. Sonochemical synthesis of gold nanoparticles: effects of ultrasound frequency. *The journal of physical chemistry. B* **109,** 20673 (2005).
3. Hansen, H. E., Seland, F., Sunde, S., Burheim, O. S. & Pollet, B. G. Frequency controlled agglomeration of Pt-nanoparticles in sonochemical synthesis. *Ultrasonics Sonochemistry* **85,** 105991 (2022).
4. Pollet, B. G. The use of ultrasound for the fabrication of fuel cell materials. *International Journal of Hydrogen Energy* **35,** 11986–12004 (2010).
5. Pollet, B. G. *Introduction to Ultrasound, Sonochemistry and Sonoelectrochemistry* Cham, 2019.
6. Koda, S., Kimura, T., Kondo, T. & Mitome, H. A standard method to calibrate sonochemical efficiency of an individual reaction system. eng. *Ultrasonics - Sonochemistry* **10,** 149–156 (2003).
7. Rochebrochard D'auzay, S. d. L., Blais, J.-F. & Naffrechoux, E. Comparison of characterization methods in high frequency sonochemical reactors of differing configurations. *Ultrasonics - Sonochemistry* **17,** 547–554 (2010).
8. Dalodière, E., Virot, M., Moisy, P. & Nikitenko, S. I. Effect of ultrasonic frequency on H2O2 sonochemical formation rate in aqueous nitric acid solutions in the presence of oxygen. *Ultrasonics Sonochemistry* **29,** 198–204 (2016).

9. Sharma, N., Ojha, H., Bharadwaj, A., Pathak, D. P. & Sharma, R. K. Preparation and catalytic applications of nanomaterials: a review. *RSC Adv.* **5,** 53381–53403 (66 2015).

10. Krishna, K. S., Sandeep, C. S. S., Philip, R. & Eswaramoorthy, M. Mixing does the magic: a rapid synthesis of high surface area noble metal nanosponges showing broadband nonlinear optical response. eng. *ACS nano* **4,** 2681–2688 (2010).

11. Ren, X. *et al.* Current progress of Pt and Pt-based electrocatalysts used for fuel cells. *Sustainable Energy Fuels* **4,** 15–30 (1 2020).

12. Ayers, K. E. *et al.* Pathways to ultra-low platinum group metal catalyst loading in proton exchange membrane electrolyzers. *Catalysis Today* **262.** Electrocatalysis, 121–132 (2016).

13. Zhu, H., Li, X. & Wang, F. Synthesis and characterization of Cu@Pt/C coreshell structured catalysts for proton exchange membrane fuel cell. *International Journal of Hydrogen Energy* **36,** 9151–9154 (2011).

14. Sarkar, A. & Manthiram, A. Synthesis of Pt@Cu CoreShell Nanoparticles by Galvanic Displacement of Cu by Pt4+ Ions and Their Application as Electrocatalysts for Oxygen Reduction Reaction in Fuel Cells. *The Journal of Physical Chemistry C* **114,** 4725–4732 (2010).

15. Stewart, I. E., Ye, S., Chen, Z., Flowers, P. F. & Wiley, B. J. Synthesis of Cu–Ag, Cu–Au, and Cu–Pt Core–Shell Nanowires and Their Use in Transparent Conducting Films. *Chemistry of Materials* **27,** 7788–7794 (2015).

16. Dhavale, V. M., Unni, S. M., Kagalwala, H. N., Pillai, V. K. & Kurungot, S. Ex-situ dispersion of core–shell nanoparticles of Cu–Pt on an in situ modified carbon surface and their enhanced electrocatalytic activities. *Chem. Commun.* **47,** 3951–3953 (13 2011).

17. Lim, I. *et al.* Sonochemical gram-scale synthesis of core–shell PdCo@Pt nanoparticle and investigation of post heat-treatment effect for various gas atmospheres. *Journal of Alloys and Compounds* **879,** 160441 (2021).

18. Anandan, S., Grieser, F. & Ashokkumar, M. Sonochemical Synthesis of Au-Ag CoreShell Bimetallic Nanoparticles. *The Journal of Physical Chemistry C* **112,** 15102–15105 (2008).

19. Hansen, H. E., Seland, F., Sunde, S., Burheim, O. S. & Pollet, B. G. Two routes for sonochemical synthesis of platinum nanoparticles with narrow size distribution. *Mater. Adv.* **2,** 1962–1971 (6 2021).

20. Khatouri, J., Mostafavi, M., Amblard, J. & Belloni, J. Radiation-induced copper aggregates and oligomers. eng. *Chemical physics letters* **191,** 351–356 (1992).

21. Asmus, K.-D., Mockel, H. & Henglein, A. Pulse radiolytic study of the site of OH · radical attack on aliphatic alcohols in aqueous solution. eng. *Journal of physical chemistry (1952)* **77,** 1218–1221 (1973).

22. Angerstein-Kozlowska, H., Conway, B. & Sharp, W. The real condition of electrochemically oxidized platinum surfaces: Part I. Resolution of component processes. *Journal of Electroanalytical Chemistry and Interfacial Electrochemistry* **43,** 9–36 (1973).

23. Margulis, M. & Margulis, I. Calorimetric method for measurement of acoustic power absorbed in a volume of a liquid. eng. *Ultrasonics - Sonochemistry* **10,** 343–345 (2003).

24. Contamine, R. F., Wilhelm, A., Berlan, J. & Delmas, H. Power measurement in sonochemistry. *Ultrasonics - Sonochemistry* **2,** S43–S47 (1995).

25. Mizukoshi, Y. *et al.* Preparation of platinum nanoparticles by sonochemical reduction of the Pt(IV) ions: role of surfactants. *Ultrasonics sonochemistry* **8,** 1–6 (2001).

26. Gatalo, M. *et al.* Comparison of Pt–Cu/C with Benchmark Pt–Co/C: Metal Dissolution and Their Surface Interactions. *ACS Applied Energy Materials* **2,** 3131–3141 (2019).

Supporting Information

Cyclic voltammogram acquired at $400\,\mathrm{mV\,s^{-1}}$ for sonochemically synthesized carbon supported Cu-nanoparticles after the addition of $PtCl_4$ is shown in Figure S1. The characteristic Pt-behaviour confirms the presence of Pt in the Cu@Pt-sample.

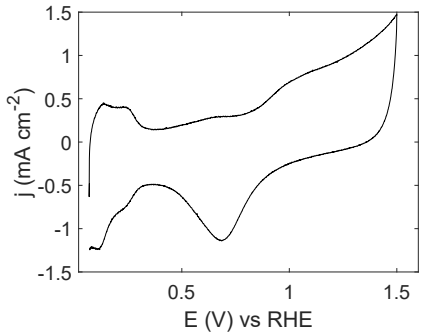

Figure S 1: Cyclic voltammogram for sonochemically synthesized carbon supported Cu-nanoparticles after the addition of $PtCl_4$. Voltammograms were acquired in $0.5\,\mathrm{mol\,dm^{-3}}$ H_2SO_4 with a scan rate of $400\,\mathrm{mV\,s^{-1}}$.

Absorbance spectra showing the development of the Ti-complex formed when $TiOSO_4$ reacts with sonochemically generated H_2O_2 are shown in Figure S2. The constant increase in absorbance suggests a constant generation of ·OH, which in turn form hydrogen peroxide in a pure water solution.

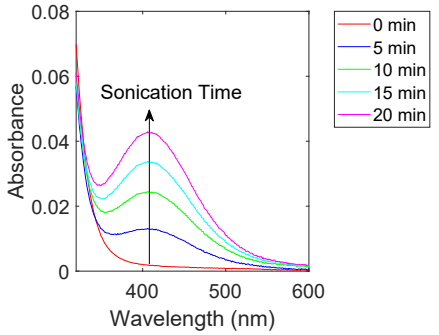

Figure S 2: Absorbance spectra of the Ti complex formed when $TiOSO_4$ reacts with H_2O_2. Spectra were acquired for different sonication times.

Chapter 7

Optimum Scavenger Concentrations for Sonochemical Nanoparticle Synthesis

Optimum Scavenger Concentrations for Sonochemical Nanoparticle Synthesis

Henrik E. Hansen[1,2*], Frode Seland[1], Svein Sunde[1], Odne S. Burheim[2], Bruno G. Pollet[2,3]

[1]Electrochemistry Group, Department of Materials Science and Engineering, Faculty of Natural Sciences. Norwegian University of Science and Technology (NTNU), NO-7491 Trondheim, Norway

[2]Department of Energy and Process Engineering, Faculty of Engineering, Norwegian University of Science and Technology (NTNU), NO-7491 Trondheim, Norway

[3]Green Hydrogen Lab, Institute for Hydrogen Research (IHR), Université Du Québec à Trois-Rivières (UQTR), 3351 Boulevard des Forges, Trois-Rivières, Québec G9A 5H7, Canada

Authors to whom correspondence should be addressed:
*henrik.e.hansen@ntnu.no

Abstract

Maintaining nanoparticle properties when scaling up a chemical synthesis is challenging due to the complex interplay between reducing agents and precursors. A sonochemical synthesis route does not require the addition of reducing agents as they are instead being continuously generated in-situ by ultrasonic cavitation throughout the reactor volume. To optimize the sonochemical synthesis of nanoparticles, understanding the role of radical scavengers is paramount. In this work we demonstrate that optimum scavenger concentrations exist at which the rate of Ag-nanoparticle formation is maximized. Titanyl dosimetry experiments were used in conjunction with Ag-nanoparticle formation rates to determine these optimum scavenger concentrations. It was found that more hydrophobic scavengers require lower optimum concentrations with 1-butanol $<$ 2-propanol $<$ ethanol $<$ methanol $<$ ethylene glycol. However, the optimum concentration is shifted by an order of magnitude towards higher concentrations when pyrolytic decomposition products contribute to the reduction. The reduction rate is also enhanced considerably.

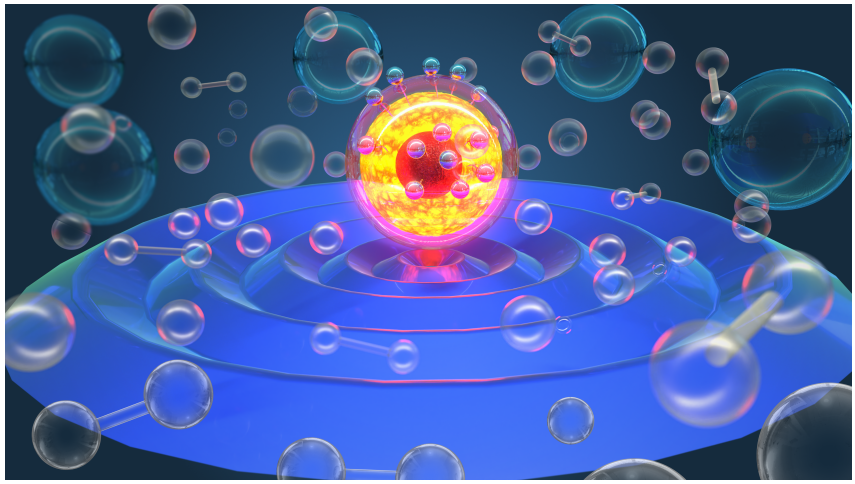

Figure 1: Graphical illustration of the scavenger process in a sonochemical reaction. The central bubble represents the cavitation bubble which achieves extremely high temperatures on collapse. Scavengers are adsorbed on the bubble surface with primary radicals being scavenged by the hydrophobic tail of the scavenger. Incomplete bubble coverage leads to recombination of primary radicals which are illustrated in the surrounding bulk solution.

Continued development of many technological applications require the use of the

unique properties of nanomaterials. The synthesis methods for these materials must therefore ensure that the desired nanoparticle properties are reproducible. Narrow size distributions, good dispersion, ease of changing the nanoparticle properties as well as the possibility of scaling up the synthesis method are therefore desired traits for a well suited synthesis method. Chemical reduction methods by strong reducing agents such as $NaBH_4$ are currently being used for nanoparticle synthesis [1–4]. The addition of a strong reducing agent which reacts very quickly with the precursor makes it difficult to obtain a homogeneous mixture. As such different nucleation and growth conditions arise which can result in poor reproducibility. An alternative synthesis method to chemical reduction is the sonochemical synthesis method which utilizes high power ultrasound to generate reducing agents in-situ.

Sonochemical synthesis of nanoparticles has shown great promise when it comes to tailoring reduction rates and particle sizes [5–12]. This is achieved through adjusting the ultrasonic frequency [7, 13], acoustic power [13], saturation gas [12–15], bulk temperature [13, 14], reactor design [16], and choice of radical scavenger [8, 17–19]. Changes in any of these parameters can influence the size of the resulting nanoparticles as they all affect the generation of radicals, which act as reducing agents [7]. However, the sonochemical method is a very slow process as it is dependent upon in-situ generation of primary radicals which is on the order of 10-20 $\mu mol\,dm^{-3}\,min^{-1}$ depending on the ultrasound parameters [6, 9–12]. If the sonochemical method aims to replace traditional chemical synthesis methods, the utilization of these precious few primary radicals must be optimized. This is ensured by radical scavengers.

The role of a radical scavenger (RH) is to convert the highly unstable primary radicals (·H and ·OH) into more stable reducing secondary radicals (·R) as shown through equation 1 [6]. Less primary radicals are therefore lost to recombination processes (equation 2-4), and can instead be utilized for reductive purposes (equation 5). The choice of a proper scavenger for sonochemical synthesis is very complex as a number of chemical and physical properties must be considered.

$$\cdot OH(\cdot H) + RH \longrightarrow R\cdot + H_2O(H_2) \tag{1}$$

$$\cdot OH + \cdot H \longrightarrow H_2O \tag{2}$$

$$\cdot OH + \cdot OH \longrightarrow H_2O_2 \tag{3}$$

$$\cdot \mathrm{H} + \cdot \mathrm{H} \longrightarrow \mathrm{H_2} \tag{4}$$

$$\mathrm{nR}\cdot + \mathrm{M}^{\mathrm{n}+} \longrightarrow \mathrm{nR}' + \mathrm{M} \tag{5}$$

One such property is the hydrophobicity of the scavenger. To increase the probability of completely scavenging the primary radicals, the radical scavenger should be situated close to the cavitation bubbles [8, 20, 21]. This can be ensured by choosing a hydrophobic scavenger as it will have a higher affinity towards the gas-solution interface presented by the cavitation bubbles. Such a correlation between scavenging efficiency and hydrophobicity of radical scavengers was demonstrated by Henglein and Kormann for various radical scavengers including glycol, methanol, ethanol, and tert-butanol [20].

As the hot-spot surrounding a cavitation bubble will cause the scavenger to decompose, the pyrolytic decomposition products of the scavenger must also be considered as these can directly influence the cavitation bubble or the precursor reduction [10, 22, 23]. Büttner et al. [22] showed that pyrolytic decomposition of methanol leads to the formation of a methyl radical ($\cdot CH_3$) through the pyrolytic cleaving of the C-O bond in methanol. The methyl radical then goes on to form methane, formaldehyde and carbon monoxide through reactions with methanol. Other alcohols, such as ethanol, display similar pyrolytic decomposition reactions as was shown by Gutierrez and Henglein [23]. The introduction of these organic species has been shown to lower the bubble collapse temperature as they evaporate into the cavitation bubbles [17, 22]. Fewer primary radicals are therefore produced [14, 15, 21].

The methyl radical and other pyrolytic decomposition products have also been shown to contribute in the reduction of certain metal precursor like Pt(IV), Pd(II), and Au(III) [6, 10, 11]. For these precursors, the rate of reaction is massively increased compared to processes which relies on secondary radicals only. However, not all precursors appear to react with the methyl radical as both the reduction of Ag(I) and Pt(II) to their respective metal nanoparticles only proceed through reactions with secondary radicals [6, 9, 10, 12].

Even if the scavenging efficiency of the radical scavenger is large, it does not matter if the resulting secondary radical is not able to contribute to the reduction of the metal precursor. For alcohols, hydrogen abstraction from the α-carbon leads to the formation of α-alcohol radicals which has reducing properties [24]. β and higher order alcohol radicals do not have the same reducing properties [24]. Asmus et al. [24] quantified the yield of hydrogen abstraction from the OH-site, α-site, and

higher order sites for different alcohols and found that the shorter hydrocarbon chains lead to higher yields of α-alcohol radicals. Both the formate ion and ethylene glycol was shown to exhibit nearly $100\,\%$ yield of α-radicals, while n-butanol only displayed a yield of $41.0\,\%$.

To achieve faster sonochemical reduction rates, the scavenger must therefore be an efficient primary radical scavenger, and the resulting secondary radical must be able to readily transfer electrons to the metal precursor. Ideally, the pyrolytic decomposition products should also contribute to the reduction before they are converted into volatile gases. However, if they are inactive towards the reduction, their concentration should be minimized. A higher scavenging efficiency will therefore increase sonochemical reduction, while excessive pyrolytic decomposition will decrease the sonochemical reduction. As the scavenging efficiency and pyrolytic decomposition both increase with scavenger concentration, an optimum scavenger concentration for faster sonochemical reduction should therefore exist.

In this work, the optimum scavenger concentrations for methanol, ethanol, 1-butanol, 2-propanol, and ethylene glycol were determined for the sonochemical reduction and formation of Ag-nanoparticles. This was performed through identifying the lowest alcohol concentrations required to reach complete scavenging of primary radicals through absorbance-based detection of H_2O_2. H_2O_2 detection offers useful insight into the degree of scavenging as it will form by recombination of primary radicals in the absence of a scavenger. These results were then compared to the formation rates of Ag-nanoparticles under the same conditions. To determine whether pyrolytic decomposition products affect the optimum scavenger concentration or not, the sonochemical reduction of Pt(IV) to Pt(II) was also assessed for different methanol concentrations. The effect of acoustic power and ultrasonic frequency on the scavenging efficiency was also considered in order to determine the extent to which these must be taken into account when optimizing the scavenger concentrations.

Results

The scavenging efficiency of ·OH radicals for different alcohols and alcohol concentrations are shown in Figure 2. Scavenging efficiency is a measure of how much primary radicals are converted into secondary radicals through scavenging. The alcohol concentration required to reach the scavenging efficiency limit ($90\,\%$) is lower for the more hydrophobic scavengers. These concentrations are approximately $0.3\,\mathrm{mmol\,dm^{-3}}$ for 1-butanol, $1\,\mathrm{mmol\,dm^{-3}}$ for 2-propanol, $10\,\mathrm{mmol\,dm^{-3}}$ for ethanol, $100\,\mathrm{mmol\,dm^{-3}}$ for methanol, and $500\,\mathrm{mmol\,dm^{-3}}$ for ethylene glycol. Absorbance spectra and the corresponding concentration profiles (Figure S1-S5), and H_2O_2 rates as a function of alcohol concentration (Figure S6) for all samples

are provided in the supporting information.

The sonochemical formation rates of Ag-nanoparticles in the presence of different alcohols and alcohol concentrations are shown in Figure 3. The rates are normalized to the maximum formation rate in the methanol series and are corrected for shifts in the localized surface plasmon resonance (LSPR) peak. All alcohols exhibit a maximum rate of Ag-nanoparticle formation. The alcohol concentration required to reach maximum Ag-nanoparticle formation is lower for the more hydrophobic scavengers. These concentrations are approximately $0.3\,\mathrm{mmol\,dm^{-3}}$ for 1-butanol, $1\,\mathrm{mmol\,dm^{-3}}$ for 2-propanol, $10\,\mathrm{mmol\,dm^{-3}}$ for ethanol, $30\,\mathrm{mmol\,dm^{-3}}$ for methanol and $2\,\mathrm{mol\,dm^{-3}}$ for ethylene glycol. The maximum rate for ethylene glycol was found to be 5.4 times higher than the maximum rate for methanol. Absorbance spectra and the corresponding concentration profiles (Figure S7-S11) for all Ag-samples are provided in the supporting information. Ag-nanoparticle formation rates without LSPR peak correction are also provided in the supporting information (Figure S12). Nitrate ions have previously been shown to affect the scavenging of OH radicals [25, 26]. However, the nitrate ions present in $AgNO_3$ in our work have a negligible effect towards the scavenging efficiency as demonstrated in Figure S13 in the supporting information. Representative SEM micrographs of the resulting Ag-nanoparticles are also provided in the supporting information (Figure S14(a)) along with the corresponding EDS-map of Ag (Figure S14(b)).

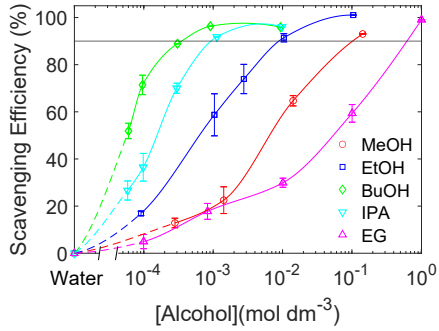

Figure 2: Scavenging efficiency of ·OH radicals as a function of alcohol concentration. Methanol (MeOH) (○), ethanol (EtOH) (□), 1-butanol (BuOH) (◇), 2-propanol (IPA) (▽), and ethylene glycol (EG) (△) were used as radical scavengers. Solid and dotted lines are drawn with spline interpolation to guide the eye. The horizontal line at $90\,\%$ represents the upper detection limit for the scavenging efficiency.

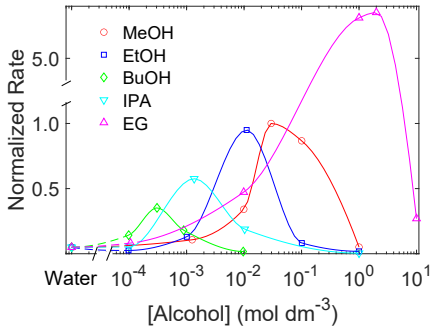

Figure 3: Rate of Ag-nanoparticle formation as a function of alcohol concentration. Methanol (MeOH) (○), ethanol (EtOH) (□), 1-butanol (BuOH) (◇), 2-propanol (IPA) (▽), and ethylene glycol (EG) (△) were used as radical scavengers. The rate of Ag-nanoparticle formation is normalized to the optimum for the methanol series. Solid and dotted lines are drawn with spline interpolation to guide the eye.

Normalized sonochemical formation rates of Ag-nanoparticles and Pt(II) at different methanol concentrations are shown in Figure 4. The methanol concentration required to reach maximum Pt(II) formation ($1\,\mathrm{mol\,dm^{-3}}$) is an order of magnitude higher than what is needed to reach maximum Ag-nanoparticle formation ($30\,\mathrm{mmol\,dm^{-3}}$). Absorbance spectra and the corresponding concentration profiles of Pt(II) (Figure S15), and the non-normalized Pt(II) rates (Figure S16) are provided in the supporting information.

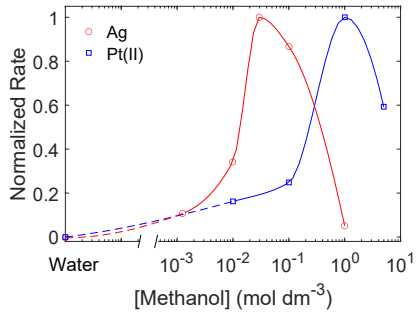

Figure 4: Normalized rate of Ag-nanoparticle formation (○) and Pt(II) formation (□) as a function of methanol concentration. Solid and dotted lines are drawn with spline interpolation to guide the eye.

The effect of acoustic power and ultrasonic frequency on the methanol scavenging efficiency is shown in Figure 5(a) and Figure 5(b), respectively. No significant

differences can be observed between high and low ultrasonic powers, and they both reach the scavenging efficiency limit ($90\,\%$) at the same methanol concentration ($100\,\mathrm{mmol\,dm^{-3}}$). However, when the ultrasonic frequency is increased from 346 kHz to 760 kHz the scavenging efficiency does increase. Complete scavenging of ·OH radicals therefore appears to occur at lower methanol concentrations at 760 kHz ($50\,\mathrm{mmol\,dm^{-3}}$) compared to 346 kHz ($100\,\mathrm{mmol\,dm^{-3}}$). Absorbance spectra and the corresponding concentration profiles for measurements conducted at 30 W (Figure S17) and 760 kHz (Figure S18) are provided in the supporting information.

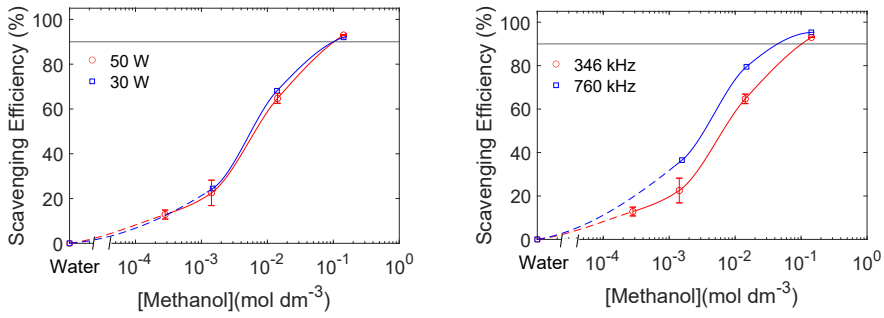

Figure 5: Scavenging efficiency of ·OH radicals as a function of methanol concentration for applied electrical powers of 50 W (○) and 30 W (□) (a), and for applied ultrasonic frequencies of 346 kHz (○) and 760 kHz (□) (b). The power experiments in (a) were acquired at an applied ultrasonic frequency of 346 kHz, while the frequency experiments in (b) were acquired at an applied electrical power of 50 W. Solid and dotted lines are drawn with spline interpolation to guide the eye. The horizontal lines at $90\,\%$ represents the upper detection limit for the scavenging efficiency.

Discussion

The optimal scavenger concentration for sonochemical formation of Ag nanoparticles is achieved for the concentration at which the scavenger exactly covers the cavitation bubble. This is supported by the good agreement between the alcohol concentration required for complete radical scavenging (Figure 2) and maximum Ag-nanoparticle formation rate (Figure 3). At lower alcohol concentrations, primary radicals are lost to recombination due to insufficient bubble coverage. At higher alcohol concentrations pyrolytic decomposition of excess alcohol contributes to a lower formation rate of primary radicals. This is in line with the decrease in Ag-nanoparticle formation rates at low and high alcohol concentrations (Figure 3).

If the cavitation bubble is not completely covered by the scavenger, the primary radicals may recombine in scavenger-deficient areas of the hot-spot [27]. This is consistent with the low scavenging efficiencies observed at low alcohol concentrations (Figure 2). Low scavenging efficiencies means that less secondary radicals are formed. Correspondingly low rates are therefore observed for the Ag-nanoparticle formation (Figure 3) because it proceeds through reactions with secondary radicals [12]. As the alcohol concentration increases, more of the cavitation bubbles are covered by the scavenger and less recombination occurs. This is evident from the high scavenging efficiencies observed at higher scavenger concentrations (Figure 2). As a result, more secondary radicals are generated which increases the Ag-nanoparticle formation rates (Figure 3).

Increasing the scavenger concentration beyond complete bubble coverage does not contribute to more scavenging of primary radicals. However, the excess scavenger will still be subject to the high temperatures that are associated with the hot-spot region [28]. Previous studies on decomposition of alcohols through high frequency ultrasound have shown that alkanes and alkenes are formed as gaseous decomposition products [22, 23]. Accumulation of these compounds in the cavitation bubbles will alter the collapse conditions of the bubbles. This is because the polytropic ratio (γ) is pushed towards lower values when moving from monoatomic Ar (1.66) to polyatomic organic species (1.3-1.2)[17, 21, 29]. A decrease in the polytropic ratio leads to a decrease in the bubble collapse temperature (T)

$$T = T_{\mathrm{bulk}} \left(\frac{R_{\mathrm{max}}}{R_0} \right)^{3(\gamma-1)} \tag{6}$$

where T_{bulk} is the bulk temperature of the solution, R_{max} is the maximum radius of the cavitation bubble and R_0 is the ambient radius of the cavitation bubble [14]. A lower collapse temperature also leads to fewer primary radicals being formed [14]. As a result, the rate of secondary radical formation is also reduced. The slower Ag-nanoparticle formation rate at high alcohol concentrations can therefore be attributed to pyrolytic decomposition of the excess scavenger.

To achieve maximum Ag-nanoparticle formation rates, secondary radical formation must therefore be optimized. Secondary radical formation is maximized when the scavenger concentration is high enough to scavenge all primary radicals, but low enough to limit pyrolytic decomposition of the scavenger. This occurs once the scavenger exactly covers the cavitation bubbles. The observed maximum in Ag-nanoparticle formation rates (Figure 3) does indeed coincide with the concentration where complete bubble coverage is reached (Figure 2). We therefore conclude that maximum Ag-nanoparticle formation rates can be achieved for scavenger con-

centrations at which complete bubble coverage occurs.

Maximum Ag-nanoparticle formation occurring at complete bubble coverage is also supported when comparing the shift in optimum scavenger concentrations between different alcohols (Figure 3). The trend follows the hydrophobicity of the scavengers with the most hydrophobic scavenger (1-butanol) displaying the lowest optimum concentration, and the least hydrophobic scavenger (ethylene glycol) displaying the highest optimum concentration (1-butanol $<$ 2-propanol $<$ ethanol $<$ methanol $<$ ethylene glycol). This is the same trend we observe for the scavenging efficiency experiments (Figure 2). It is also the same trend as Henglein and Kormann [20] observed for their scavenging efficiency experiments which they attributed to the higher degree of bubble coverage displayed by the more hydrophobic scavengers. This further strengthens our finding that the Ag-nanoparticle formation rate is determined by the degree of bubble coverage.

In addition to a shift in optimum scavenger concentration, the relative rates of Ag-nanoparticle formation also appear to be scavenger dependent. The relative rates of Ag-nanoparticle formation for the different scavengers can be related to the conversion efficiency from primary radicals to α-alcohol secondary radicals, where the shorter hydrocarbon chains display higher conversion efficiencies. This is shown from the trends in the normalized rates (Figure 3).

When an alcohol scavenger interacts with a primary radical, the radical may abstract a hydrogen atom from any position in the alcohol [24]. The longer the chain length the lower is the probability of hydrogen abstraction from the α-site which is the only site capable of proper electron transfer to a metal precursor [24]. Abstraction probabilities from the α-site were estimated for methanol ($93.0\,\%$), ethanol ($84.3\,\%$), 2-propanol ($85.5\,\%$), and n-butanol ($41\,\%$) by Asmus et al. [24]. The relative rates we observe for the Ag-nanoparticle formation rates (Figure 3) appear to be consistent with the abstraction probabilities of the linear alcohols.

For ethylene glycol, the relative rate of Ag-nanoparticle formation was observed to be about five times higher than for methanol. It also reached a maximum rate for ethylene glycol concentrations one order of magnitude higher than what is needed for complete bubble coverage (Figure 3). A fast rate of Ag-nanoparticle formation is indeed expected when using ethylene glycol as approximately $100\,\%$ of the secondary radicals are α-alcohol secondary radicals [24]. However, the extremely fast rate and an optimum scavenger concentration which is higher than expected suggests that there are other factors contributing to the reduction process. It is well known that ethylene glycol is used extensively in polyol-reduction methods for synthesizing nanoparticles [30, 31]. This occurs at elevated temperatures where ethylene glycol decomposes into species with reducing capabilities. Excess

ethylene glycol in the hot-spot region could therefore decompose from the high temperatures, but instead of negatively affecting the bubble collapse like the other alcohols, the decomposition products could act as additional reducing agents. This might explain why the relative rate of Ag-nanoparticle formation is so much higher than for methanol, and also why the optimum scavenger concentration is shifted to higher ethylene glycol concentrations.

To assess the extent to which the Ag-nanoparticle formation is aided by pyrolytic decomposition of ethylene glycol, the reduction of Pt(IV) to Pt(II) was monitored for different methanol concentrations (Figure 4). The reduction of Pt(IV) to Pt(II) has also been shown to proceed through pyrolytic decomposition products [10]. This process is driven by the decomposition products from alcohols in general. We observe that the Pt(II) formation rate also displays a maximum for methanol concentrations one order of magnitude higher than the Ag-nanoparticle formation (Figure 4). This is very similar to what we observe for ethylene glycol. The shift in the optimum scavenger concentration for Pt(II) may therefore be attributed to the contribution from the decomposition products towards the reduction. Going beyond complete bubble coverage would therefore increase the number of reducing agents which would lead to further increase in the rate of nanoparticle formation. However, lower collapse temperatures associated with these decomposition products will eventually start to dominate at higher scavenger concentrations leading to lower reduction rates. We therefore conclude that the optimum scavenger concentration is shifted towards higher concentrations when the decomposition products actively participates in the sonochemical reduction.

Thus far we have shown that the scavenger concentration and hydrophobicity determine how much of the bubble area that is covered by the scavenger. If the bubble area is modified through changes in the ultrasound parameters, the bubble coverage might change as well. As a result, we would need to find optimum scavenger concentrations for a given set of ultrasound parameters as well.

An increase in ultrasonic power above 10 W increases the number of cavitation bubbles, but the size of each cavitation bubble remains fairly constant [32]. This leads to a larger total surface area, but the individual bubble area is unchanged. The scavenging efficiency was found to be independent on the ultrasonic power (Figure 5(a)). The bubble coverage is therefore independent on the number of cavitation bubbles.

Increasing the ultrasonic frequency has several effects on the cavitation bubbles. It reduces the size of each bubble, increases the number of cavitation bubbles, reduces the collapse times, decreases the final shock wave pressure, and decreases the collapse temperatures and therefore also the amount of primary radicals gener-

ated per bubble. The scavenging efficiencies of methanol at 346 kHz and 760 kHz (Figure 5(b)) reveals that an increase in frequency increases the bubble coverage for the same methanol concentration. From the power measurements, we know that the bubble coverage is independent of the number of cavitation bubbles. The decrease in the single bubble surface area may affect the bubble coverage through changes in diffusion of the alcohol towards the bubble surface. However, the diffusion process may also be affected by the different collapse times, shock wave pressures and collapse temperatures imposed by the ultrasonic frequency. When optimizing the scavenger concentration, the ultrasonic frequency must therefore be taken into account. An optimum concentration at high ultrasonic frequencies would therefore not be sufficient at lower frequencies which would require a higher scavenger concentration.

Conclusions

For sonochemical reduction of metal precursor to nanoparticles, optimum scavenger concentrations do exist. This depends on the hydrophobicity and pyrolytic decomposition products of the scavenger. More hydrophobic scavengers reduces the optimum scavenger concentration due to their higher affinity towards the bubble solution interface. If the pyrolytic decomposition products of the scavenger are active towards the precursor reduction, the optimum scavenger concentration and the rate of reduction increases. For scavengers without active pyrolytic decomposition products, the optimum scavenger concentration coincides with the scavenger concentration required to reach complete bubble coverage. This is simply determined as the lowest scavenger concentration which yields undetectable amounts of H_2O_2. It was also found that the optimum scavenger concentrations are dependent on the ultrasonic frequency and independent on the ultrasonic power for the acoustic powers and frequencies used in this work.

Methods

Chemicals

Methanol (MeOH) (Acros Organics, $99.8\,\%$ for electronic use), ethanol (EtOH) (VWR, $96\,\%$ GPR RECTAPUR®), 1-butanol (BuOH) (Merck, $\geq 99.5\,\%$ EMSURE® ACS, ISO, Reag. Ph Eur), 2-propanol (IPA) (VWR, $98\,\%$ technical), ethylene glycol (EG) (Sigma Aldrich, $\geq 99.0\,\%$ ReagentPlus®), sodium nitrate ($NaNO_3$) (Merck, EMSURE® ACS, ISO, Reag. Ph Eur), silver nitrate ($AgNO_3$) (Sigma Aldrich, $\geq 99.0\,\%$ ACS reagent), platinum tetrachloride ($PtCl_4$) (Sigma Aldrich, $96\,\%$), titanium(IV) oxysulfate solution ($TiOSO_4$) (Sigma Aldrich, 1.9-2.1 %), and potassium iodide (KI) (Sigma Aldrich, $\geq 99\,\%$ ACS reagent) were used as received from the supplier. Milli-Q water ($18.2\,\mathrm{M\Omega \cdot cm}$) was used for all experiments.

Sonochemical Setup

All sonochemical experiments were performed using Honda Electronics $70\,\mathrm{mm}$ ⌀ stainless steel alloy (SUS304) plates connected to lead zirconate titanate (PZT) piezoelectric transducers (346 kHz and 760 kHz). Temperature control ($3\,^{\circ}\mathrm{C}$) was maintained through water circulation around the reactor. Atmospheric gasses where removed from solution through constant supply of argon (5.0) before and during the sonochemical experiments. An AG 1012 RF signal generator from T&C Power Conversion was used in combination with the plate transducers to generate the ultrasonic waves. Proper transfer of the power from the signal generator to the transducer was ensured through an impedance matching unit (T1k-7A) from T&C Power Conversion. In our previous work, the conversion efficiency from electric power (50 W) to acoustic power (38 ± 3) W was found to be (76 ± 6) % [33]. Detailed schematics of the sonochemical reactor can be found in our previous work [34].

Alcohol Scavenging Efficiency

The scavenging properties of methanol, ethanol, 2-propanol, 1-butanol, and ethylene glycol were determined through titanyl dosimetry. $200\,\mathrm{mL}$ aqueous solutions with scavenger concentrations between $60\,\mu\mathrm{mol\,dm^{-3}}$ and $1\,\mathrm{mol\,dm^{-3}}$ were sonicated for $20\,\mathrm{min}$ at 346 kHz and $50\,\mathrm{W}$ electric power. $500\,\mu\mathrm{L}$ aliquots were taken every 5 minutes and mixed with $500\,\mu\mathrm{L}$ of $0.02\,\mathrm{mol\,dm^{-3}}$ $TiOSO_4$ [18, 26, 35, 36]. The absorbance spectra of these solutions were acquired with a scan rate of $100\,\mathrm{nm\,min^{-1}}$ between $300\,\mathrm{nm}$ and $600\,\mathrm{nm}$ with an Evolution 220 UV-Visible spectrophotometer from Thermo Fisher. The H_2O_2 concentration for all samples was determined from the absorbance peak at $411\,\mathrm{nm}$ (ϵ = $787\,\mathrm{mol^{-1}\,dm^3\,cm^{-1}}$) belonging to the yellow titanium hydrogen peroxide complex [34]. The H_2O_2 formation rates at the given alcohol concentrations were determined from the slopes of the resulting linear concentration profiles. The rates were then converted to scavenging efficiencies (S) by comparing the rate of H_2O_2 production with a scavenger present (r_S) and without a scavenger present (r_0 = $5.5\,\mu\mathrm{mol\,dm^{-3}\,min^{-1}}$).

$$S = \left(1 - \frac{r_\mathrm{S}}{r_0}\right) \times 100\% \tag{7}$$

A lower detection limit for H_2O_2 of $10\,\mu\mathrm{mol\,dm^{-3}}$ after 20 min sonication was used as an indicator of complete scavenging for the different alcohols. This was identified as the H_2O_2 concentration where the absorbance peak at 411 nm was no longer discernible from the background. From equation 7, a scavenging efficiency above $90\,\%$ can therefore be regarded as complete scavenging of the primary rad-

icals. The alcohol concentrations were increased until complete scavenging was achieved. Three replicate experiments were performed for all scavenger concentrations below the scavenging efficiency limit. The standard deviation from these replicates were then used as error bars in the resulting graphs. The scavenging efficiency of methanol was also determined at 760 kHz with a 50 W electric power, and at 346 kHz with a 30 W electric power to assess the effect of ultrasonic frequency and power.

Sonochemical Reduction Rate of Silver Nitrate

The reducing capabilities of the secondary radicals were evaluated in terms of the sonochemical reduction of Ag(I) to Ag-nanoparticles. The Ag(I) reduction was chosen specifically because it has been shown to proceed mainly through reactions with secondary radicals [6, 12]. $200\,\mathrm{mL}$ of $10\,\mathrm{mmol\,dm^{-3}}$ $AgNO_3$ solutions with scavenger concentrations between $100\,\mu\mathrm{mol\,dm^{-3}}$ and $10\,\mathrm{mol\,dm^{-3}}$ were sonicated for $20\,\mathrm{min}$ at 346 kHz and $50\,\mathrm{W}$ electric power. $500\,\mu\mathrm{L}$ aliquots were taken every 5 minutes and mixed with $500\,\mu\mathrm{L}$ of Milli-Q water. The absorbance spectra of these solutions were acquired with a scan rate of $100\,\mathrm{nm\,min^{-1}}$ between $200\,\mathrm{nm}$ and $800\,\mathrm{nm}$ with an Evolution 220 UV-Visible spectrophotometer from Thermo Fisher. Ag-nanoparticle formation rates were estimated from the development of the localized surface plasmon resonance (LSPR) peak in the absorbance spectra which is located between $400\,\mathrm{nm}$ and $500\,\mathrm{nm}$.

As the exact wavelength of the LSPR peak of Ag-nanoparticles is dependent on the Ag-nanoparticle size, nanoparticle growth throughout the sonication period will shift the LSPR peak to higher wavelengths and therefore result in different molar extinction coefficients for the Ag-nanoparticles. In order to compensate for the LSPR peak shift throughout the sonication period and between different samples, the Ag-nanoparticle concentration had to be evaluated with the molar extinction coefficient corresponding to the individual LSPR peak positions. In a work by Paramelle et al. [37] they measured the molar extinction coefficient of citrate capped Ag-nanoparticles for LSPR peak positions between $392.1\,\mathrm{nm}$ and $492.8\,\mathrm{nm}$. They found that the molar extinction coefficient is proportional to the square of the LSPR peak position. From their data we corrected the Ag-nanoparticle absorbance values at every sample interval by matching the observed LSPR peak positions with the corresponding molar extinction coefficients. The calibration curve relating the molar extinction coefficient to the peak wavelength is provided in the supporting information (Figure S19). To estimate the rate of Ag-nanoparticle formation for the different scavengers, the slope of the absorbance profiles at 0 min was used.

Sonochemical Reduction Rate of Platinum Chloride

The reduction of $PtCl_4$ from Pt(IV) to Pt(II) was chosen to investigate the scavenger concentration dependence when pyrolytic decomposition also plays a part in the reduction process. $200\,\mathrm{mL}$ of $1\,\mathrm{mmol\,dm^{-3}}$ $PtCl_4$ solutions with methanol concentrations between $10\,\mathrm{mmol\,dm^{-3}}$ and $5\,\mathrm{mol\,dm^{-3}}$ were sonicated for $20\,\mathrm{min}$ at 346 kHz and $50\,\mathrm{W}$ electric power. $100\,\mu\mathrm{L}$ aliquots were taken every 5 minutes and mixed with $100\,\mu\mathrm{L}$ of KI and $800\,\mu\mathrm{L}$ of Milli-Q water. The resulting PtI_6^{2-} complex (ϵ = $11\,170\,\mathrm{dm^3\,mol^{-1}\,cm^{-1}}$, λ_{max} = $495\,\mathrm{nm}$) and PtI_4^{2-} complex (ϵ = $4600\,\mathrm{dm^3\,mol^{-1}\,cm^{-1}}$, λ_{max} = $388\,\mathrm{nm}$) were determined spectrophotometrically as described in our previous work [34]. The formation rates of Pt(II) for the different methanol concentrations were determined as the slope of the Pt(II) concentration profiles at 0 min.

Acknowledgements

We appreciate the support of ENERSENSE for the funding of this reasearch work, grant 68024013. The Research Council of Norway is also acknowledged for the support to the INTPART project 261620. We would also like to thank Daniel Ø. Fakhri for his efforts in determining the standard deviations in the scavenging efficiencies for the different alcohols and alcohol concentrations. We would also like to acknowledge George Crystal for his work on making and designing the illustration of the sonochemical process for this work.

Bibliography

1. Faid, A. Y., Oyarce Barnett, A., Seland, F. & Sunde, S. Highly Active Nickel-Based Catalyst for Hydrogen Evolution in Anion Exchange Membrane Electrolysis. *Catalysts* **8.** ISSN: 2073-4344 (2018).
2. Krishna, K. S., Sandeep, C. S. S., Philip, R. & Eswaramoorthy, M. Mixing does the magic: a rapid synthesis of high surface area noble metal nanosponges showing broadband nonlinear optical response. *ACS nano* **4,** 2681–2688. ISSN: 19360851 (2010).
3. Kolahalam, L. A. *et al.* Review on nanomaterials: Synthesis and applications. *Materials Today: Proceedings* **18.** 2nd International Conference on Applied Sciences and Technology (ICAST-2019): Material Science, 2182–2190. ISSN: 2214-7853 (2019).
4. Escobar Morales, B. *et al.* Synthesis and characterization of colloidal platinum nanoparticles for electrochemical applications. *International journal of hydrogen energy* **35,** 4215–4221. ISSN: 0360-3199 (2010).
5. Pollet, B. G. The use of ultrasound for the fabrication of fuel cell materials. *International Journal of Hydrogen Energy* **35,** 11986–12004 (2010).
6. Okitsu, K. *et al.* Formation of noble metal particles by ultrasonic irradiation. *Ultrasonics Sonochemistry* **3,** S249–S251 (1996).
7. Okitsu, K., Ashokkumar, M. & Grieser, F. Sonochemical synthesis of gold nanoparticles: effects of ultrasound frequency. *The journal of physical chemistry. B* **109,** 20673 (2005).
8. Caruso, R. A., Ashokkumar, M. & Grieser, F. Sonochemical formation of colloidal platinum. *Colloids and Surfaces A: Physicochemical and Engineering Aspects* **169,** 219–225 (2000).

9. Mizukoshi, Y., Oshima, R., Maeda, Y. & Nagata, Y. Preparation of Platinum Nanoparticles by Sonochemical Reduction of the Pt(II) Ion. *Langmuir* **15,** 2733–2737 (1999).

10. Mizukoshi, Y. *et al.* Preparation of platinum nanoparticles by sonochemical reduction of the Pt(IV) ions: role of surfactants. *Ultrasonics sonochemistry* **8,** 1–6 (2001).

11. Okitsu, K., Bandow, H., Maeda, Y. & Nagata, Y. Sonochemical Preparation of Ultrafine Palladium Particles. *Chemistry of Materials* **8,** 315–317 (1996).

12. Nagata, Y., Watananabe, Y., Fujita, S.-i., Dohmaru, T. & Taniguchi, S. Formation of colloidal silver in water by ultrasonic irradiation. *J. Chem. Soc., Chem. Commun.,* 1620–1622 (21 1992).

13. Mark, G. *et al.* OH-radical formation by ultrasound in aqueous solution – Part II: Terephthalate and Fricke dosimetry and the influence of various conditions on the sonolytic yield. *Ultrasonics Sonochemistry* **5,** 41–52 (1998).

14. Merouani, S., Hamdaoui, O., Rezgui, Y. & Guemini, M. Sensitivity of free radicals production in acoustically driven bubble to the ultrasonic frequency and nature of dissolved gases. *Ultrasonics Sonochemistry* **22,** 41–50 (2015).

15. Merouani, S., Ferkous, H., Hamdaoui, O., Rezgui, Y. & Guemini, M. New interpretation of the effects of argon-saturating gas toward sonochemical reactions. *Ultrasonics Sonochemistry* **23,** 37–45 (2015).

16. Son, Y., Lim, M., Ashokkumar, M. & Khim, J. Geometric Optimization of Sonoreactors for the Enhancement of Sonochemical Activity. *The Journal of Physical Chemistry C* **115,** 4096–4103 (2011).

17. Xiao, R., Diaz-Rivera, D., He, Z. & Weavers, L. K. Using pulsed wave ultrasound to evaluate the suitability of hydroxyl radical scavengers in sonochemical systems. *Ultrasonics Sonochemistry* **20,** 990–996 (2013).

18. Weissler, A. Formation of Hydrogen Peroxide by Ultrasonic Waves: Free Radicals. *Journal of the American Chemical Society* **81,** 1077–1081 (1959).

19. Anbar, M. & Pecht, I. On the Sonochemical Formation of Hydrogen Peroxide in Water. eng. *Journal of physical chemistry (1952)* **68,** 352–355 (1964).

20. Henglein, A. & Kormann, C. Scavenging of OH Radicals Produced in the Sonolysis of Water. *International Journal of Radiation Biology and Related Studies in Physics, Chemistry and Medicine* **48,** 251–258 (1985).

21. Gutiérrez, M., Henglein, A. & Dohrmann, J. K. H atom reactions in the sonolysis of aqueous solutions. eng. *Journal of physical chemistry (1952)* **91,** 6687–6690 (1987).

22. Buettner, J., Gutierrez, M. & Henglein, A. Sonolysis of water-methanol mixtures. *The Journal of Physical Chemistry* **95,** 1528–1530 (1991).

23. Gutierrez, M. & Henglein, A. Sonolytic decomposition of poly(vinylpyrrolidone), ethanol and tetranitromethane in aqueous solution. eng. *Journal of physical chemistry (1952)* **92,** 2978–2981 (1988).

24. Asmus, K.-D., Mockel, H. & Henglein, A. Pulse radiolytic study of the site of OH · radical attack on aliphatic alcohols in aqueous solution. eng. *Journal of physical chemistry (1952)* **77,** 1218–1221 (1973).

25. Nikitenko, S., Venault, L. & Moisy, P. Scavenging of OH radicals produced from H2O sonolysis with nitrate ions. *Ultrasonics Sonochemistry* **11.** 4th Conference on the Applications of Power Ultrasound in Physical and Chemical Processing, 139–142 (2004).

26. Dalodière, E., Virot, M., Moisy, P. & Nikitenko, S. I. Effect of ultrasonic frequency on H2O2 sonochemical formation rate in aqueous nitric acid solutions in the presence of oxygen. *Ultrasonics Sonochemistry* **29,** 198–204 (2016).

27. Peng, K., Tian, S., Zhang, Y., He, Q. & Wang, Q. Penetration of hydroxyl radicals in the aqueous phase surrounding a cavitation bubble. *Ultrasonics Sonochemistry* **91,** 106235 (2022).

28. Suslick, K. S., Hammerton, D. A. & Cline, R. E. Sonochemical hot spot. *Journal of the American Chemical Society* **108,** 5641–5642 (1986).

29. Merouani, S., Hamdaoui, O., Rezgui, Y. & Guemini, M. Computational engineering study of hydrogen production via ultrasonic cavitation in water. *International Journal of Hydrogen Energy* **41,** 832–844 (2016).

30. Skrabalak, S. E., Wiley, B. J., Kim, M., Formo, E. V. & Xia, Y. On the Polyol Synthesis of Silver Nanostructures: Glycolaldehyde as a Reducing Agent. *Nano Letters* **8,** 2077–2081 (2008).

31. Coskun, S., Aksoy, B. & Unalan, H. E. Polyol Synthesis of Silver Nanowires: An Extensive Parametric Study. *Crystal Growth & Design* **11,** 4963–4969 (2011).

32. Brotchie, A., Grieser, F. & Ashokkumar, M. Effect of Power and Frequency on Bubble-Size Distributions in Acoustic Cavitation. *Phys. Rev. Lett.* **102,** 084302 (8 Mar. 2009).

33. Hansen, H. E. *et al.* Sonochemical Synthesis of Cu@Pt Bimetallic Nanoparticles. *Molecules* **27** (2022).

34. Hansen, H. E., Seland, F., Sunde, S., Burheim, O. S. & Pollet, B. G. Frequency controlled agglomeration of Pt-nanoparticles in sonochemical synthesis. *Ultrasonics Sonochemistry* **85,** 105991 (2022).

35. Eisenberg, G. Colorimetric Determination of Hydrogen Peroxide. *Industrial & Engineering Chemistry Analytical Edition* **15,** 327–328 (1943).

36. Matsubara, C. & Takamura, K. A spectrophotometric study of the formation of the peroxotitanium(IV) complex and its application to the determination of beryllium. *Analytica Chimica Acta* **77,** 255–262 (1975).

37. Paramelle, D. *et al.* A rapid method to estimate the concentration of citrate capped silver nanoparticles from UV-visible light spectra. *Analyst* **139,** 4855–4861 (19 2014).

Supporting Information

Titanyl Dosimetry Results

Absorbance spectra showing the development of H_2O_2 for different sonication times along with their corresponding concentration profiles are given in Figure S1, S2, S3, S4, and S5 for methanol, ethanol, 1-butanol, 2-propanol, and ethylene glycol, respectively. Rates of H_2O_2 formation in the presence of different alcohols and alcohol concentrations are shown in Figure S6.

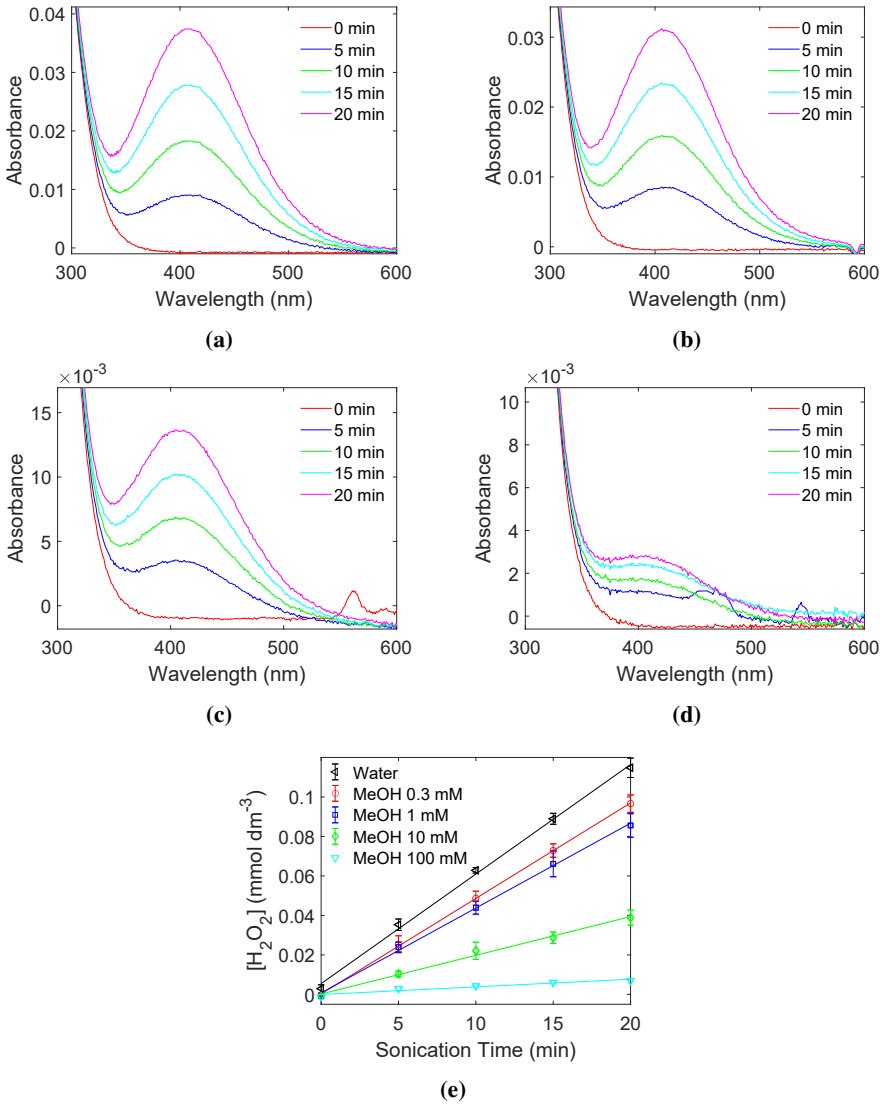

Figure S1: Absorbance spectra of titanium hydrogen peroxide complexes at different sonication times acquired using methanol as the radical scavenger. Initial methanol concentrations of $0.3\,\mathrm{mmol\,dm^{-3}}$ S1(a), $1.0\,\mathrm{mmol\,dm^{-3}}$ S1(b), $10\,\mathrm{mmol\,dm^{-3}}$ S1(c), and $100\,\mathrm{mmol\,dm^{-3}}$ S1(d) were used. The resulting H_2O_2 concentrations for all methanol (MeOH) concentrations are also plotted as a function of sonication time S1(e).

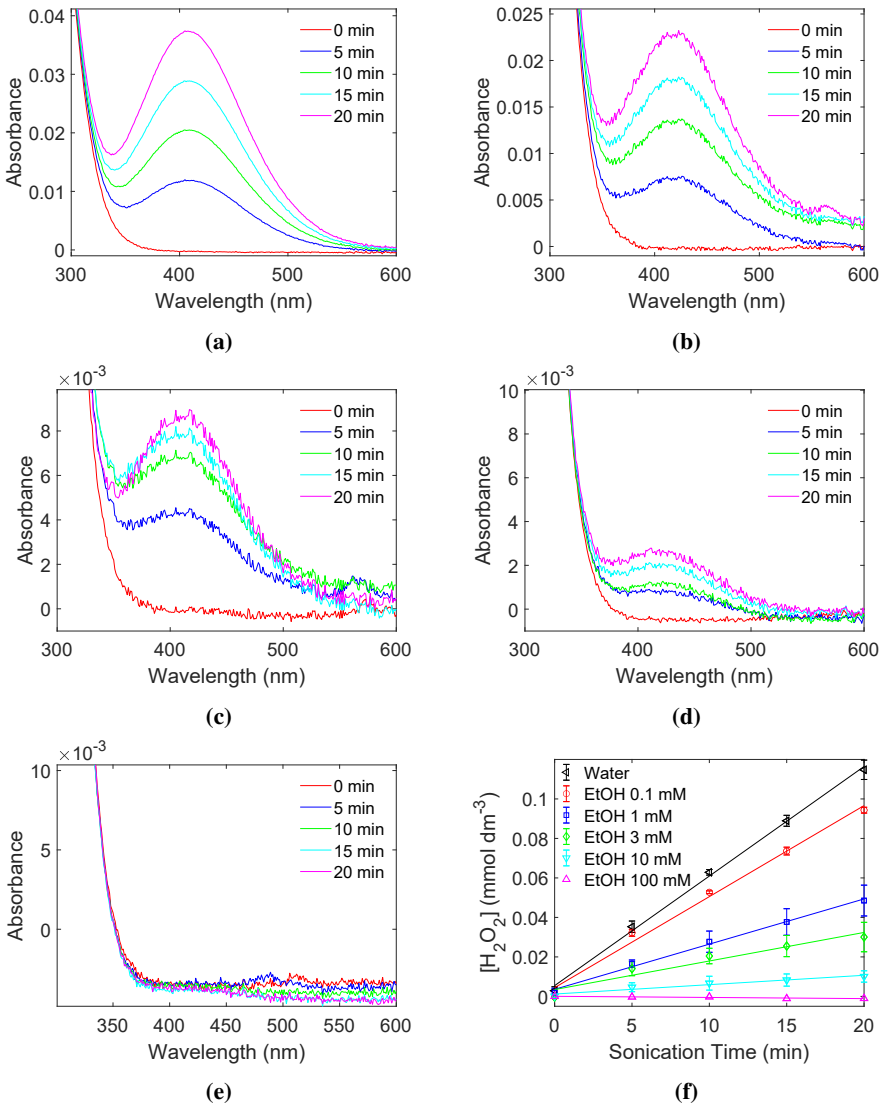

Figure S2: Absorbance spectra of titanium hydrogen peroxide complexes at different sonication times acquired using ethanol as the radical scavenger. Initial ethanol concentrations of $0.1\,\mathrm{mmol\,dm^{-3}}$ S2(a), $1.0\,\mathrm{mmol\,dm^{-3}}$ S2(b), $3.0\,\mathrm{mmol\,dm^{-3}}$ S2(c), $10\,\mathrm{mmol\,dm^{-3}}$ S2(d), and $100\,\mathrm{mmol\,dm^{-3}}$ S2(e) were used. The resulting H_2O_2 concentrations for all ethanol (EtOH) concentrations are also plotted as a function of sonication time S2(f).

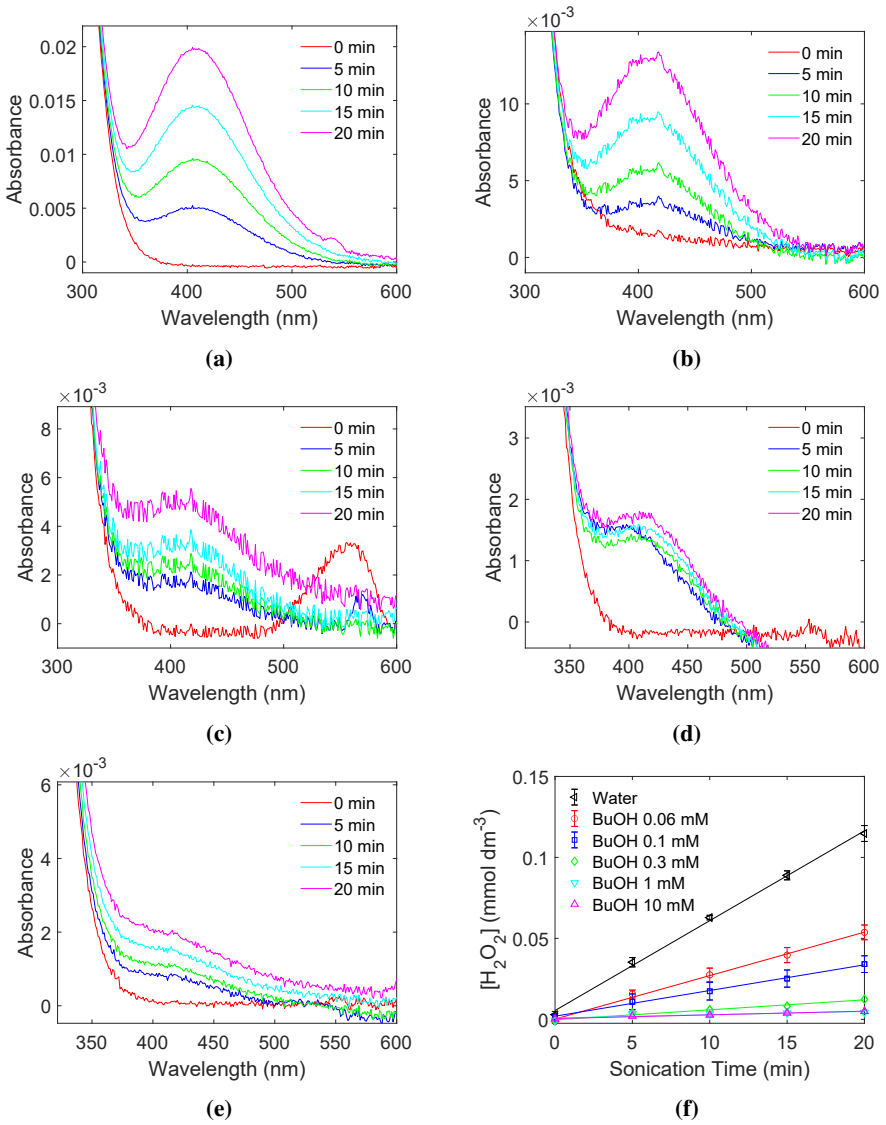

Figure S3: Absorbance spectra of titanium hydrogen peroxide complexes at different sonication times acquired using 1-butanol as the radical scavenger. Initial 1-butanol concentrations of $0.06\,\mathrm{mmol\,dm^{-3}}$ S3(a), $0.1\,\mathrm{mmol\,dm^{-3}}$ S3(b), $0.3\,\mathrm{mmol\,dm^{-3}}$ S3(c), $1.0\,\mathrm{mmol\,dm^{-3}}$ S3(d), and $10\,\mathrm{mmol\,dm^{-3}}$ S3(e) were used. The resulting H_2O_2 concentrations for all 1-butanol (BuOH) concentrations are also plotted as a function of sonication time S3(f).

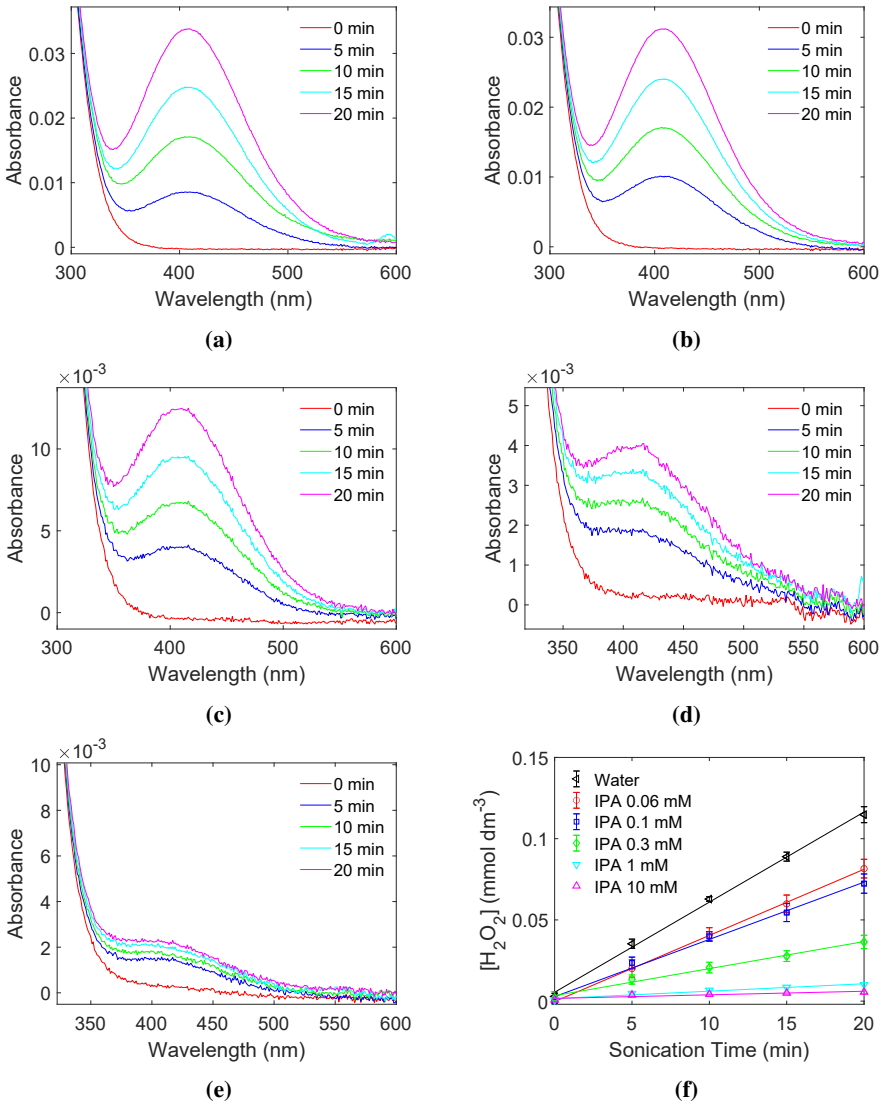

Figure S4: Absorbance spectra of titanium hydrogen peroxide complexes at different sonication times acquired using 2-propanol as the radical scavenger. Initial 2-propanol concentrations of $0.06\,\mathrm{mmol\,dm^{-3}}$ S4(a), $0.1\,\mathrm{mmol\,dm^{-3}}$ S4(b), $0.3\,\mathrm{mmol\,dm^{-3}}$ S4(c), $1.0\,\mathrm{mmol\,dm^{-3}}$ S4(d), and $10\,\mathrm{mmol\,dm^{-3}}$ S4(e) were used. The resulting H_2O_2 concentrations for all 2-propanol (IPA) concentrations are also plotted as a function of sonication time S4(f).

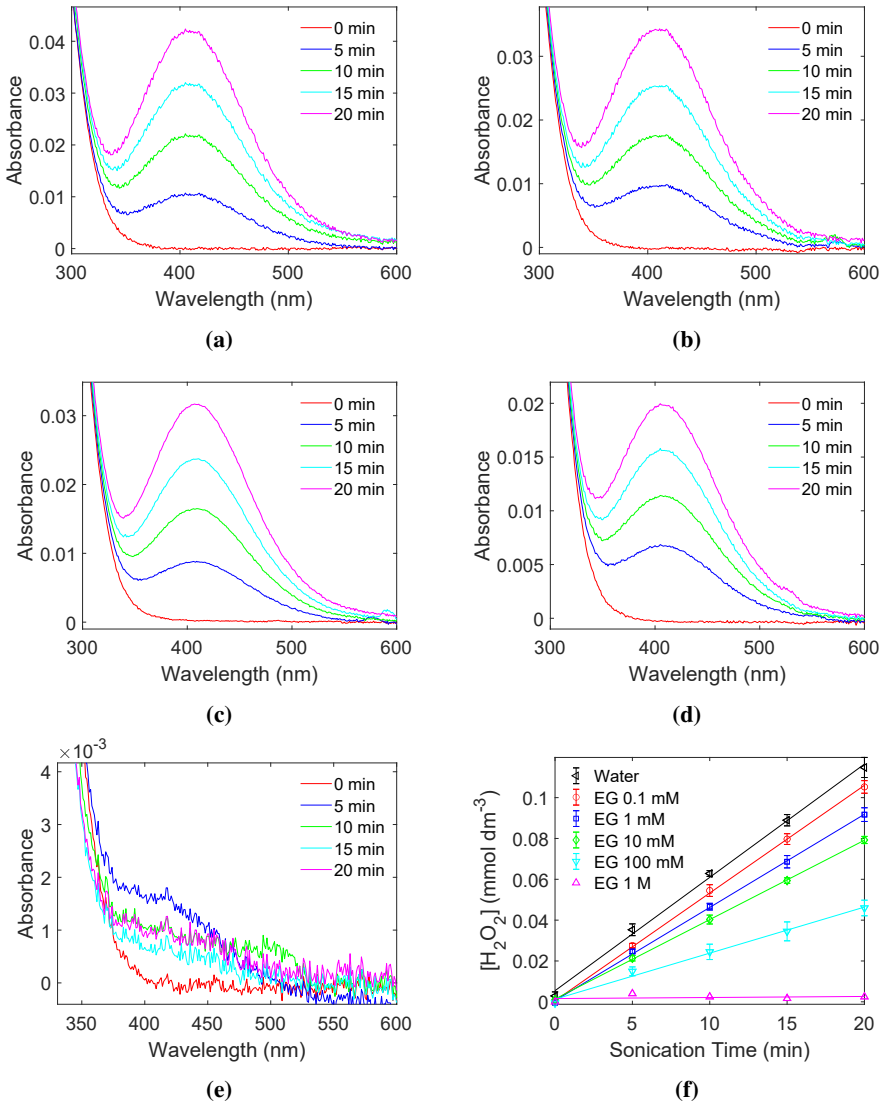

Figure S5: Absorbance spectra of titanium hydrogen peroxide complexes at different sonication times acquired using ethylene glycol as the radical scavenger. Initial ethylene glycol concentrations of $0.1\,\mathrm{mmol\,dm^{-3}}$ S5(a), $1.0\,\mathrm{mmol\,dm^{-3}}$ S5(b), $10\,\mathrm{mmol\,dm^{-3}}$ S5(c), $100\,\mathrm{mmol\,dm^{-3}}$ S5(d), and $1.0\,\mathrm{mol\,dm^{-3}}$ S5(e) were used. The resulting H_2O_2 concentrations for all ethylene glycol (EG) concentrations are also plotted as a function of sonication time S5(f).

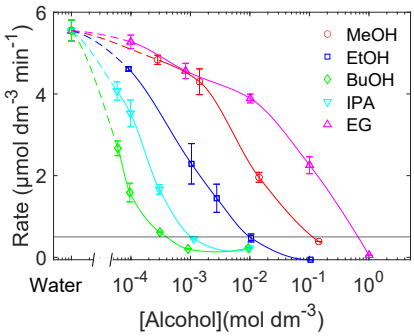

Figure S6: Rate of H_2O_2 formation as a function of alcohol concentration. Methanol (MeOH) (○), ethanol (EtOH) (□), 1-butanol (BuOH) (◇), 2-propanol (IPA) (▽), and ethylene glycol (EG) (△) were used as radical scavengers. Solid lines are drawn with spline interpolation to guide the eye. The horizontal line represents the lower detection limit of H_2O_2.

Silver Nanoparticle Absorbance Spectra

Absorbance spectra showing the development of the Ag plasmon peak for different sonication times along with their corresponding concentration profiles are given in Figure S7, S8, S9, S10, and S11 for methanol, ethanol, 1-butanol, 2-propanol, and ethylene glycol, respectively. The rates of Ag-nanoparticle formation for different alcohols and alcohol concentrations are shown in Figure S12. The absorbance values are not corrected for shifts in the Ag LSPR peak.

We would also like to briefly address the validity of the method used to quantify the rate of Ag-nanoparticle formation. Considering the short sonication time (20 min), the relatively high initial Ag(I) concentration ($1\,\mathrm{mmol\,dm^{-3}}$), the one-electron transfer from Ag(I) to Ag(0), and the fact that formation of primary (and secondary) radicals is linearly dependent on time, we also expect the Ag-nanoparticle formation to behave linearly as well within this short time frame. From the concentration profiles in the supporting information (Figure S7-S11), we observe that the Ag-nanoparticle formation is indeed linear. All concentration profiles appear to be quite linear except for the optimum concentrations for ethylene glycol (where pyrolytic decomposition is significant). Interference from the asymmetric or overlapping peaks therefore appear to not interfere much with the analysis of the results. Certainly not enough to change the clearly different trends observed in Figure S12.

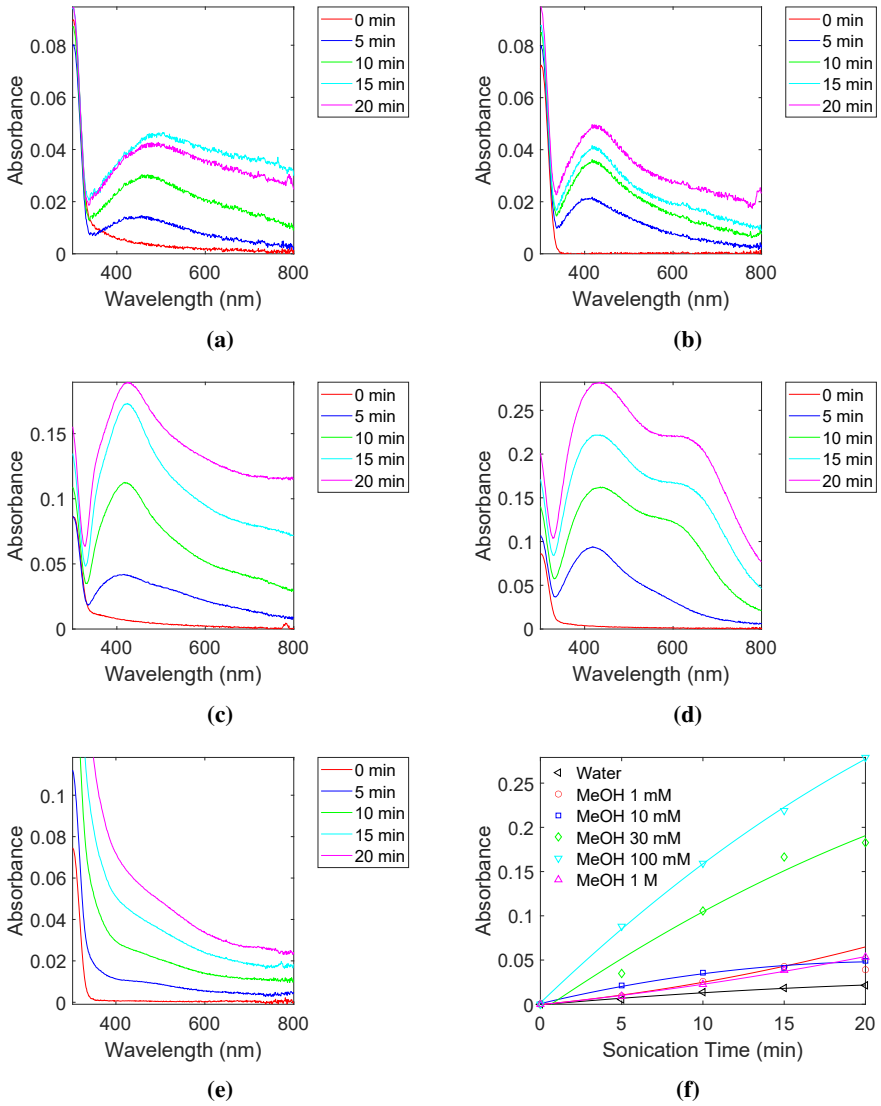

Figure S7: Absorbance spectra of Ag-nanoparticles at different sonication times acquired using methanol as the radical scavenger. Initial methanol concentrations of $1.0\,\mathrm{mmol\,dm^{-3}}$ S7(a), $10\,\mathrm{mmol\,dm^{-3}}$ S7(b), $30\,\mathrm{mmol\,dm^{-3}}$ S7(c), $100\,\mathrm{mmol\,dm^{-3}}$ S7(d), and $1.0\,\mathrm{mol\,dm^{-3}}$ S7(e) were used. The absorbance for all methanol (MeOH) concentrations are also plotted as a function of sonication time S7(f).

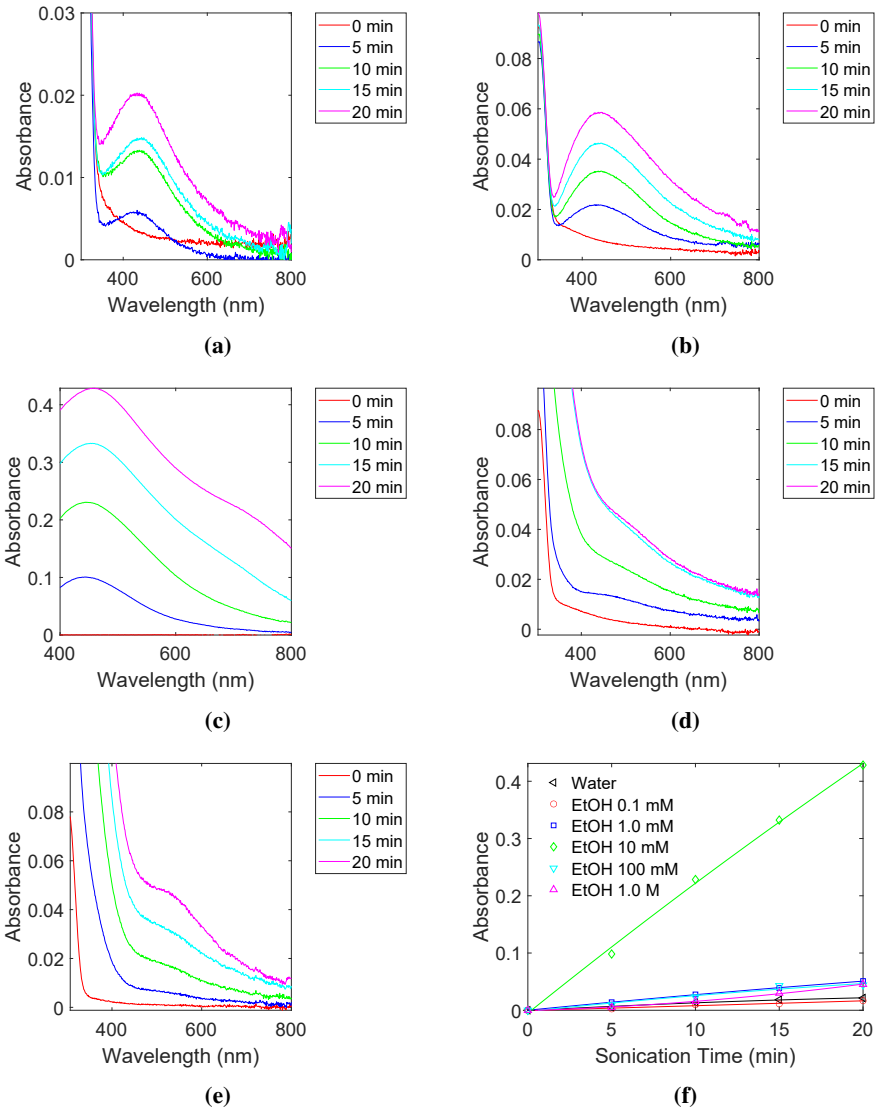

Figure S8: Absorbance spectra of Ag-nanoparticles at different sonication times acquired using ethanol as the radical scavenger. Initial ethanol concentrations of $0.1\,\mathrm{mmol\,dm^{-3}}$ S8(a), $1.0\,\mathrm{mmol\,dm^{-3}}$ S8(b), $10\,\mathrm{mmol\,dm^{-3}}$ S8(c), $100\,\mathrm{mmol\,dm^{-3}}$ S8(d), and $1.0\,\mathrm{mol\,dm^{-3}}$ S8(e) were used. The absorbance for all ethanol (EtOH) concentrations are also plotted as a function of sonication time S8(f).

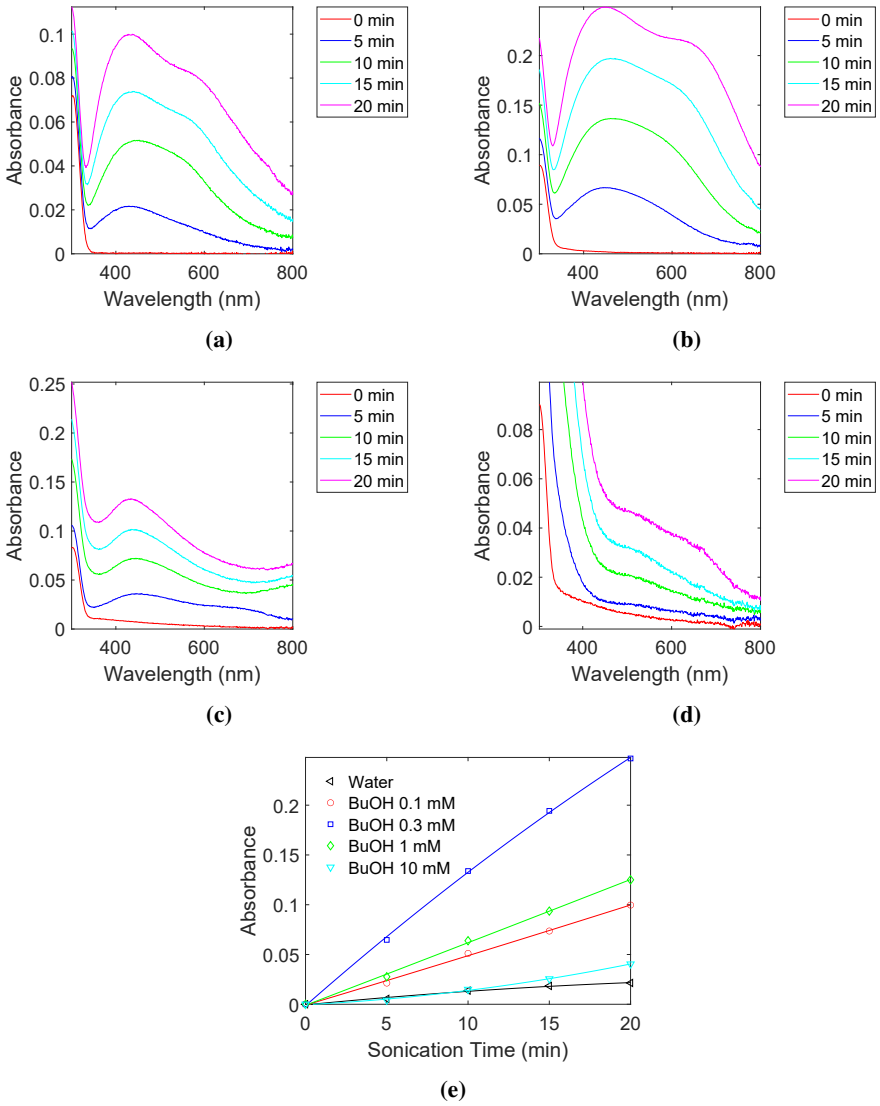

Figure S9: Absorbance spectra of Ag-nanoparticles at different sonication times acquired using 1-butanol as the radical scavenger. Initial 1-butanol concentrations of $0.1\,\mathrm{mmol\,dm^{-3}}$ S9(a), $0.3\,\mathrm{mmol\,dm^{-3}}$ S9(b), $1.0\,\mathrm{mmol\,dm^{-3}}$ S9(c), and $10\,\mathrm{mmol\,dm^{-3}}$ S9(d) were used. The absorbance for all 1-butanol (BuOH) concentrations are also plotted as a function of sonication time S9(e).

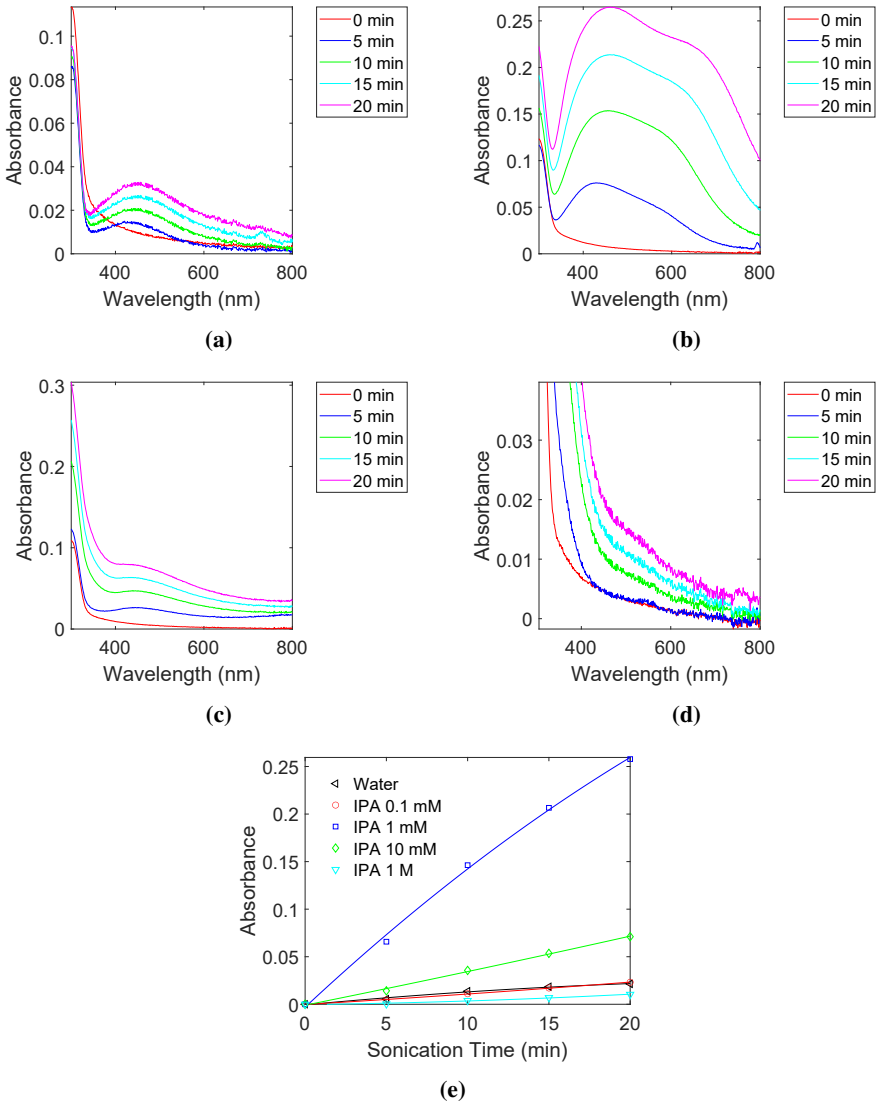

Figure S10: Absorbance spectra of Ag-nanoparticles at different sonication times acquired using 2-propanol as the radical scavenger. 2-propanol concentrations of $0.1\,\mathrm{mmol\,dm^{-3}}$ S10(a), $1.0\,\mathrm{mmol\,dm^{-3}}$ S10(b), $10\,\mathrm{mmol\,dm^{-3}}$ S10(c), and $1.0\,\mathrm{mol\,dm^{-3}}$ S10(d) were used. The absorbance for all 2-propanol (IPA) concentrations are also plotted as a function of sonication time S10(e).

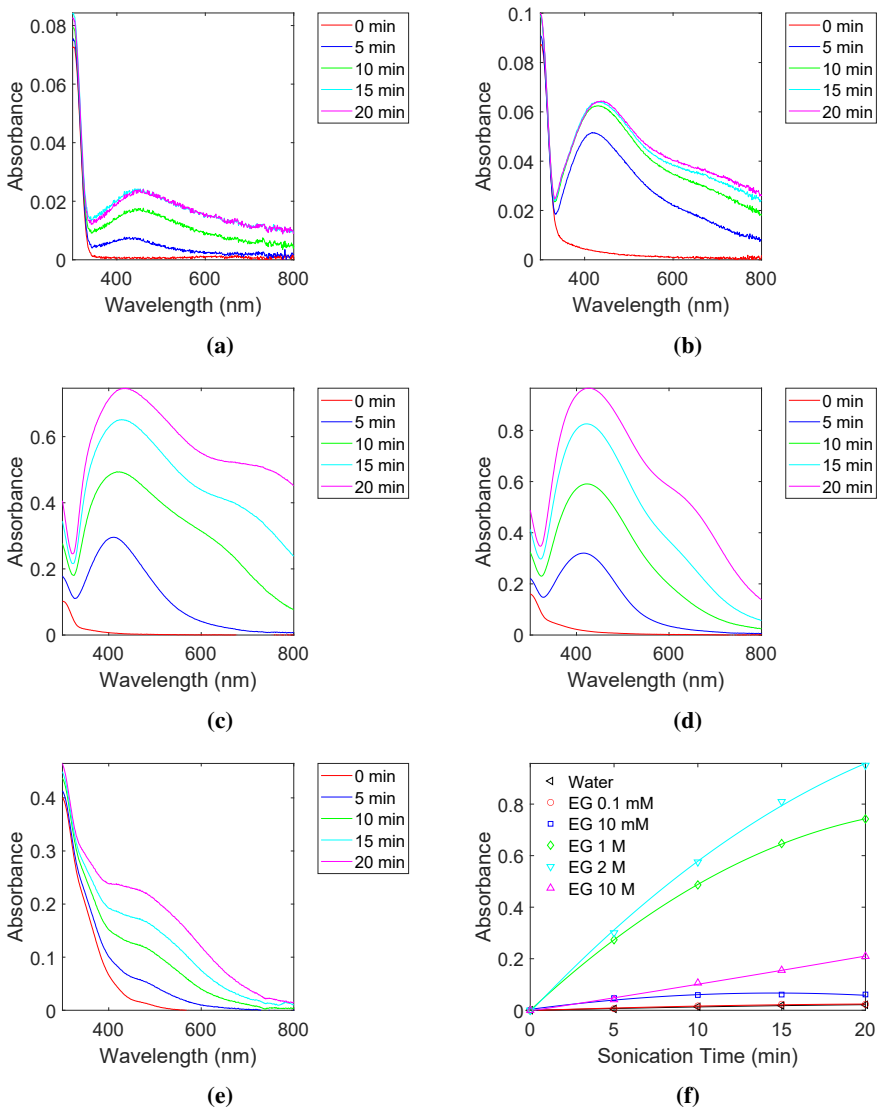

Figure S11: Absorbance spectra of Ag-nanoparticles at different sonication times acquired using ethylene glycol as the radical scavenger. Initial ethylene glycol concentrations of $0.1\,\mathrm{mmol\,dm^{-3}}$ S11(a), $10\,\mathrm{mmol\,dm^{-3}}$ S11(b), $1.0\,\mathrm{mol\,dm^{-3}}$ S11(c), $2.0\,\mathrm{mol\,dm^{-3}}$ S11(d), and $10\,\mathrm{mol\,dm^{-3}}$ S11(e) were used. The absorbance for all ethylene glycol (EG) concentrations are also plotted as a function of sonication time S11(f).

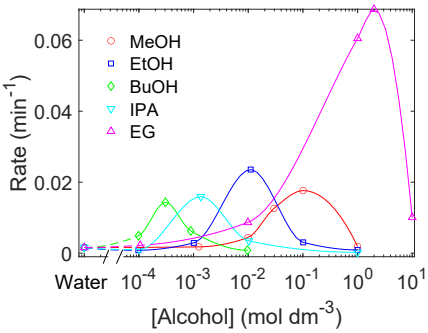

Figure S12: Rate of Ag-nanoparticle formation as a function of alcohol concentration. Methanol (MeOH) (○), ethanol (EtOH) (□), 1-butanol (BuOH) (◇), 2-propanol (IPA) (▽), and ethylene glycol (EG) (△) were used as radical scavengers. The rates of Ag formation are extracted from the slopes of the absorbance profiles and are not corrected for shifts in the localized surface plasmon resonance peaks. Solid lines are drawn with spline interpolation to guide the eye.

Scavenging Efficiency of Nitrate

Concentration profiles of H_2O_2 in water and in $10\,\mathrm{mmol\,dm^{-3}}$ $NaNO_3$ are shown in Figure S13. Both concentration profiles overlap completely showing that the nitrate ions which are present during the Ag synthesis does not contribute to any scavenging of primary radicals.

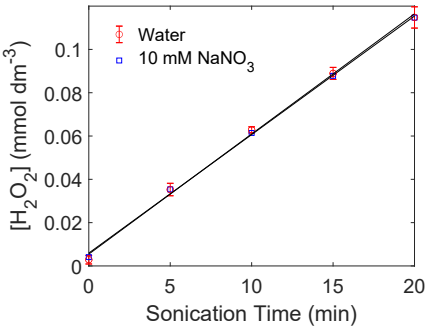

Figure S13: Concentration of H_2O_2 as a function of sonication time in water (○) and in $10\,\mathrm{mmol\,dm^{-3}}$ $NaNO_3$ (□). The solid lines are linear fits to the datapoints.

Electron Microscopy

SEM micrographs of Ag-nanoparticles synthesized with ethylene glycol ($2\,\mathrm{mmol\,dm^{-3}}$) as the scavenger is shown in Figure S14(a). Micrographs were acquired with a Hitachi High-Tech SU9000 scanning (tunneling) electron microscope using an acceleration voltage of 20 kV and a beam current of $10.5\,\mu\mathrm{A}$. An energy-dispersive X-ray spectroscopy (EDS) map of Ag for the same particle is shown in Figure S14(b). EDS was performed with an Oxford Ultim Extreme EDX-system. Both single nanoparticles and agglomerates were observed.

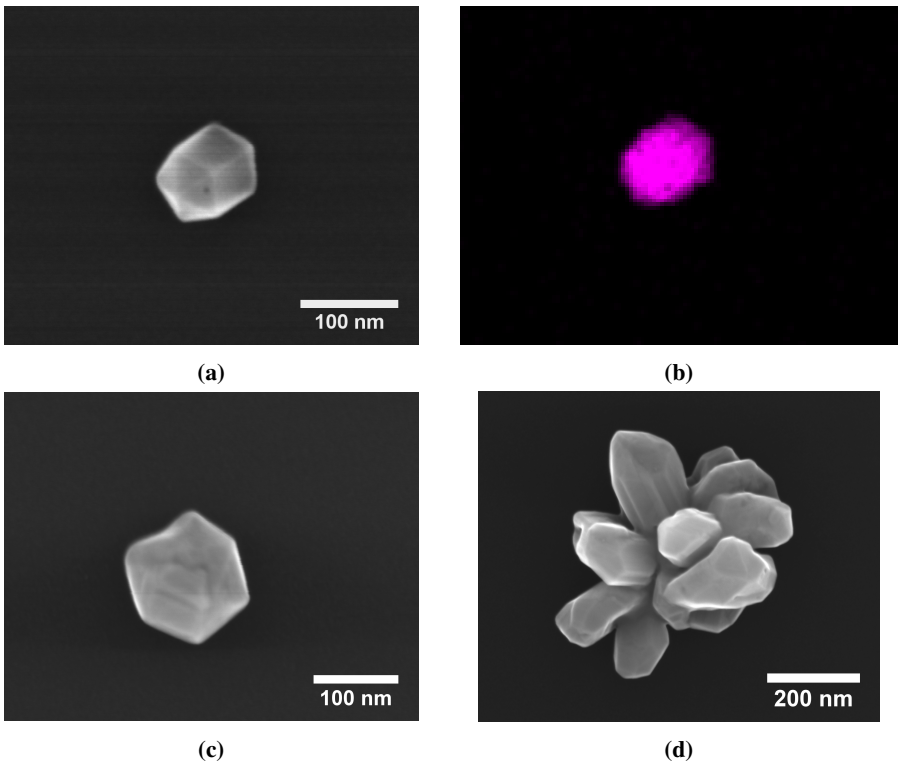

Figure S14: Secondary electron image (S14(a)) and the corresponding EDS map of Ag (S14(b)) synthesized with ethylene glycol as the radical scavenger. Additional images of a single nanoparticle (S14(c)) and an agglomerated particle (S14(d)) are also provided.

Platinum(II)/Platinum(IV) Absorbance Spectra

Absorbance spectra and the corresponding Pt(II) concentration profiles for all methanol concentrations are shown in Figure S15. The rate of Pt(II) formation at different methanol concentrations are given in Figure S16.

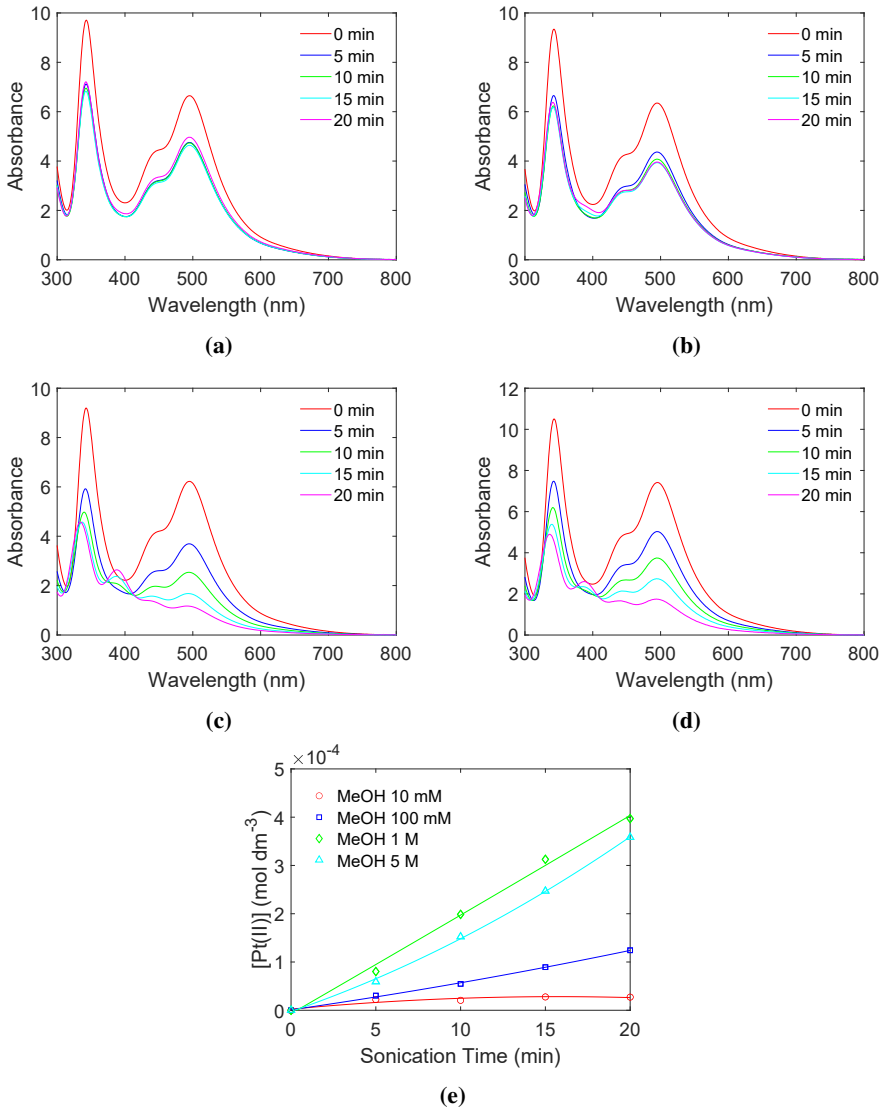

Figure S15: Absorbance spectra of Pt(IV)/Pt(II)-iodide complexes at different sonication times acquired using methanol as the radical scavenger. Initial methanol concentrations of $10\,\mathrm{mmol\,dm^{-3}}$ S15(a), $100\,\mathrm{mmol\,dm^{-3}}$ S15(b), $1.0\,\mathrm{mol\,dm^{-3}}$ S15(c), and $5.0\,\mathrm{mol\,dm^{-3}}$ S15(d) were used. The Pt(II) concentrations for all methanol (MeOH) concentrations are also plotted as a function of sonication time S15(e).

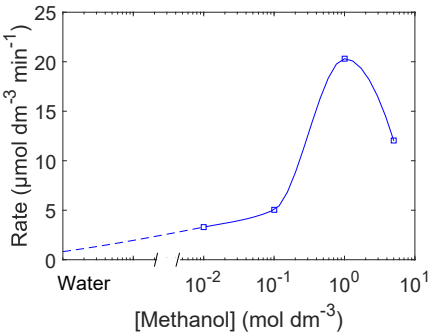

Figure S16: Rate of Pt(II) formation as a function of methanol concentration. The solid lines are drawn with spline interpolation to guide the eye.

Absorbance Spectra at 30 W and 760 kHz

Absorbance spectra of H_2O_2 for different sonication times along with their corresponding concentration profiles are given in Figure S17. The measurements were conducted using an ultrasonic frequency of 346 kHz and an electrical power of 30 W with methanol as the radical scavenger.

Absorbance spectra of H_2O_2 for different sonication times along with their corresponding concentration profiles are given in Figure S18. The measurements were conducted using an ultrasonic frequency of 760 kHz and an electrical power of 50 W with methanol as the radical scavenger.

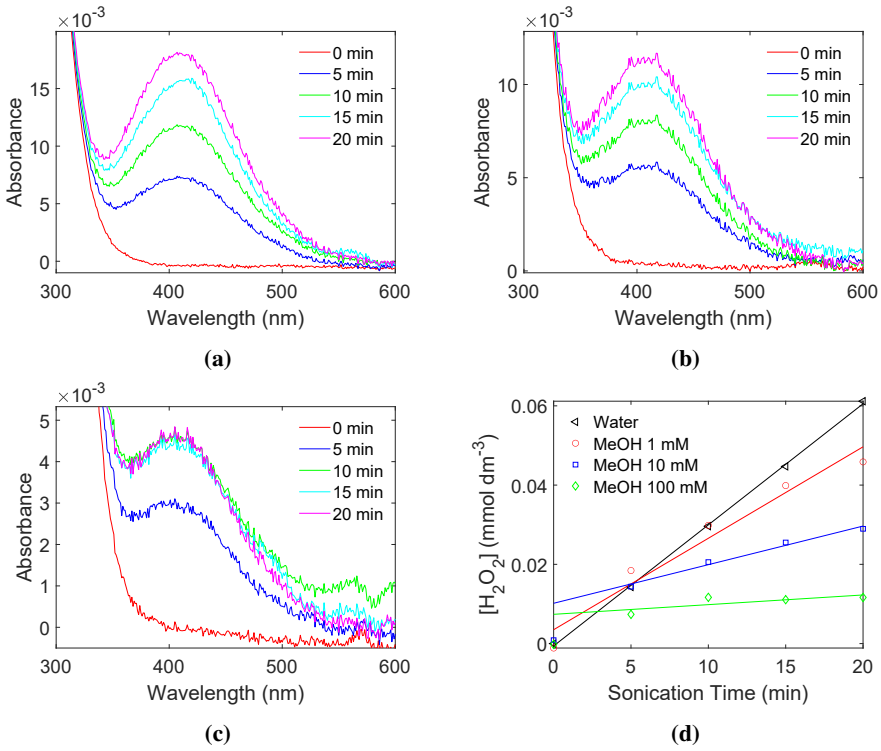

Figure S17: Absorbance spectra of H_2O_2 at different sonication times acquired with an electrical power of 30 W, an ultrasonic frequency of 346 kHz, and methanol as the radical scavenger. Initial methanol concentrations of $1.0\,\mathrm{mmol\,dm^{-3}}$ S17(a), $10\,\mathrm{mmol\,dm^{-3}}$ S17(b), and $100\,\mathrm{mmol\,dm^{-3}}$ S17(c) were used. The resulting H_2O_2 concentrations for all methanol (MeOH) concentrations are also plotted as a function of sonication time S17(d).

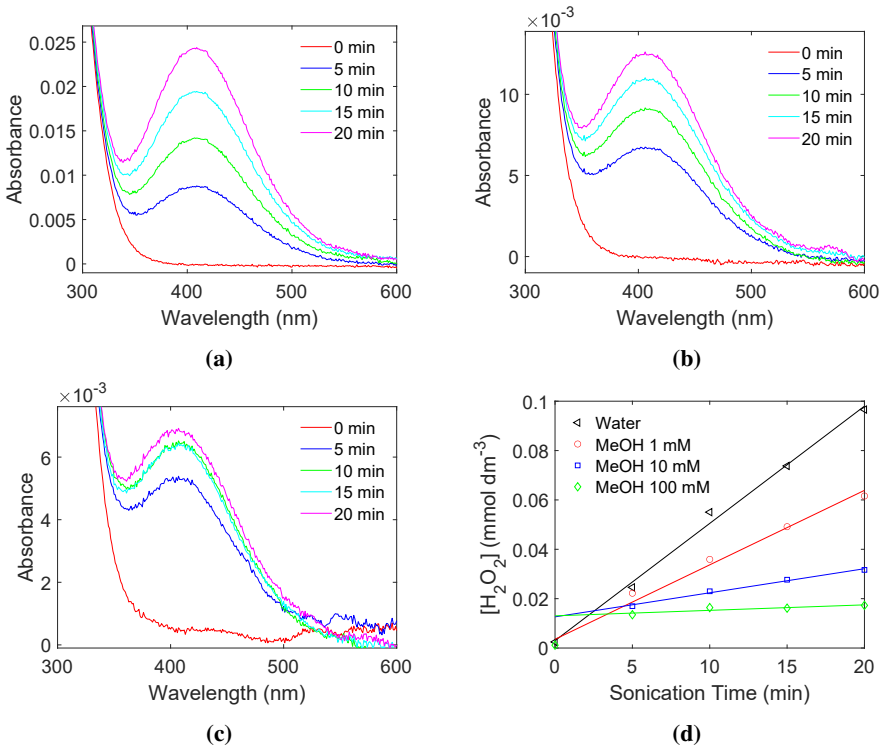

Figure S18: Absorbance spectra of H_2O_2 at different sonication times acquired with an ultrasonic frequency of 760 kHz, an electrical power of 50 W, and methanol as the radical scavenger. Initial methanol concentrations of $1.0\,\mathrm{mmol\,dm^{-3}}$ S18(a), $10\,\mathrm{mmol\,dm^{-3}}$ S18(b), and $100\,\mathrm{mmol\,dm^{-3}}$ S18(c) were used. The resulting H_2O_2 concentrations for all methanol (MeOH) concentrations are also plotted as a function of sonication time S18(d).

Localized Surface Plasmon Resonance Peak Correction

The calibration curve used to correct the absorbance at the LSPR peak for Ag nanoparticles is shown in Figure S19.

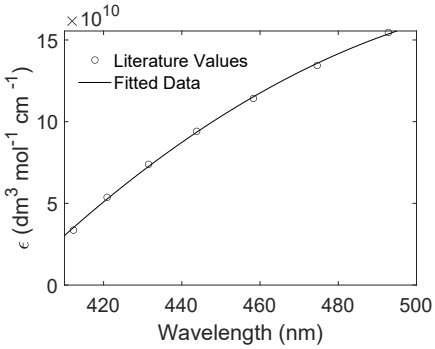

Figure S19: Molar extinction coefficient of Ag-nanoparticles as a function of the localized surface plasmon resonance peak in the absorbance spectrum. Experimental values (○) are obtained from Paramelle et al. [37]. The data were fitted to a 2. order polynomial and is plotted as a solid line.

Chapter 8

Discussion

The most important findings in paper I-IV are concerned with expanding the understanding of the sonochemical synthesis. There are still many unanswered questions about the mechanisms governing the sonochemical synthesis of nanomaterials, and a proper understanding of these are needed if the synthesis method is to be used as a regular nanocatalyst production method for electrochemical energy conversion devices. This thesis work has therefore mainly focused on investigating fundamental aspects of sonochemistry in relation to nanoparticle synthesis. In this chapter the main findings in this thesis and their importance to the sonochemical community are discussed. Furthermore, findings and interpretations made in the earlier parts of the thesis work are revisited and discussed based on more recent discoveries.

8.1 Effect of Radical Scavengers

Considering all findings in this thesis work, the most significant for the sonochemical community, is the work on scavengers [41]. It shows a direct correlation between the bubble coverage by the radical scavenger and the reduction rate of Ag(I). This correlation is also expected to hold true for any sonochemical reduction which is mainly driven by secondary radicals. It can therefore be used to estimate the ideal concentration of the radical scavenger for maximizing the reduction rate. As the choice of radical scavenger and its concentration was shown to have a massive impact on the sonochemical reduction rate, it is highly important to consider when scaling up the sonochemical method beyond laboratory scale. In addition, fundamental studies on sonochemistry involving radical scavengers will also be influenced by this choice. Failing to account for the contribution of the scavenger may therefore yield inaccurate conclusions on a fundamental level too.

As the work on radical scavengers was performed most recently, all our previous publications have not considered the effect of the scavenger concentration. It is therefore appropriate to revisit them with this new piece of information in hand. In paper I [21], two distinct frequencies (20 kHz and 408 kHz) were employed with different acoustic powers so that the radical generation rate became the same in the two different reactors. Both systems used $0.8\,\mathrm{mol\,dm^{-3}}$ ethanol as the radical scavenger and the target was a sonchemical reduction of Pt(IV) to Pt-nanoparticles. Considering the reduction from Pt(IV) to Pt(II) proceeds through the aid of pyrolytic decomposition products, the optimal ethanol concentration is expected to be 10 times higher than the optimal ethanol concentration found in the sonochemical synthesis of Ag-nanoparticles. This amounts to roughly $0.1\,\mathrm{mol\,dm^{-3}}$. As ethanol was used in slight excess of the optimal value for the sonochemical reduction of Pt(IV) to Pt(II), the frequency effect on the bubble coverage demonstrated in paper IV should not apply. The frequency effect is mainly concerned with the bubble coverage by the scavenger, and as the scavenger was used in excess, the cavitation bubbles originating from the two frequencies are therefore expected to be fully covered anyway. The similar reduction rates observed for short sonication times in paper I can therefore be evaluated without great concern of the radical scavenger behaviour.

More interesting, perhaps, is the detailed investigation of the frequency dependent Pt(IV) reduction rates in paper II [23]. This was also performed using $0.8\,\mathrm{mol\,dm^{-3}}$ ethanol as the radical scavenger. Seeing as the ethanol concentration is once again slightly higher than the optimum value, and far above the concentration leading to complete bubble coverage, the differences in the resulting reduction rate does not seem to originate in the choice of scavenger concentration. The conclusions in paper II are therefore unaffected by the choice of radical scavenger concentration.

The use of $0.2\,\mathrm{mmol\,dm^{-3}}$ formate scavenger in paper III is somewhat more significant to the conclusion [13]. This is most certainly too low to achieve complete scavenging as sodium formate is even less hydrophobic than ethylene glycol as shown by Henglein et al. [33]. In paper IV it was shown that a concentration around $1\,\mathrm{mol\,dm^{-3}}$ ethylene glycol was required for complete scavenging. A separate measurement shown in Figure 8.1 also shows that only $60\,\%$ of primary radicals are scavenged at a formate concentration of $0.2\,\mathrm{mol\,dm^{-3}}$. H_2O_2 is therefore expected to accumulate during operation in the sonochemical reduction of Cu(II) in paper III. The proposed explanation for the presence of Cu_2O in paper III involved the reaction between metallic Cu and H_2O_2. This explanation is therefore strengthened by this information. Based on the results by Henglein et al. [33], formate requires around 20 times higher concentration than ethylene glycol for complete scavenging. A concentration of around $20\,\mathrm{mol\,dm^{-3}}$ would therefore be

needed for complete scavenging. That is 100 times more than what was used in paper III! Sodium formate is not very expensive, but if you need $270\,\mathrm{g}$ for $200\,\mathrm{mL}$ the cost will add up.

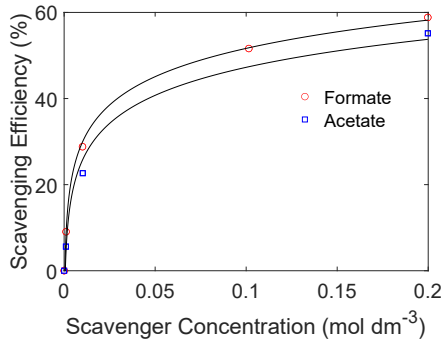

Figure 8.1: Scavenging efficiency for different concentrations of sodium formate and sodium acetate. Meausurements were conducted at 346 kHz with an acoustic power of 38 W.

Our work on sonochemistry before discovering the massive impact of the radical scavenger therefore remains valid through a fortunate choice of ethanol concentration. This choice was initially made based on the work of Caruso et al. [34]. They showed that an ethanol concentration of $0.8\,\mathrm{mol\,dm^{-3}}$ in a 20 kHz system was the lowest concentration of ethanol required before the reduction rate of Pt(IV) stabilized. However, their concentration range only extended to $1\,\mathrm{mol\,dm^{-3}}$ for ethanol. If they had continued to increase the ethanol concentration they would probably have discovered that the reaction rate would have started to decrease. Considering our investigation into the radical concentration spans several orders of magnitude, the higher resolution and more limited range in the work of Caruso et al. [34] provides much needed validation for the stability of the reduction rate. Changes in radical scavenger concentration following evaporation or scavenging throughout sonication may therefore have a negligible effect on the reduction rate. This is under the assumption that a radical scavenger concentration near the optimal concentration is chosen.

A similar fortunate (or maybe deliberate, but not specifically stated) choice of scavenger concentration and target reaction can be found in the fundamental work by Okitsu et al. [1]. Here the frequency effect is explored in the sonochemical reduction of Au(III). They used $20\,\mathrm{mmol\,dm^{-3}}$ of 1-propanol for all frequencies (20 kHz, 213 kHz, 358 kHz, 647 kHz, and 1062 kHz). This concentration is 20 times higher than the optimum concentration for 2-propanol at 346 kHz as demon-

strated in paper IV. In addition, the reduction of Au(III) is also reported to proceed through pyrolytic decomposition products which means that their choice of scavenger concentration is slightly higher than what is expected from 1-propanol. This is very similar to our choice of scavenger concentration in the sonochemical reduction of Pt(IV) which means that the same logic with regards to the frequency effect is valid here as well. The frequency dependence on the reduction rate, and on the resulting particle size can therefore be assumed to be unaffected by their choice of scavenger and its concentration.

8.2 Impedance Mismatch

As described in section 2.2.2, a proper matching of the impedance between the signal generator and the ultrasonic transducer reduces the power which is lost in the signal transfer process. As a result, the acoustic power transferred to the solution will be close to what is supplied by the signal generator. The lack of an impedance matching unit in paper I and II means that the power delivered to the transducer was not optimized as it was in paper III and IV. The increasing impedance following a decrease in frequency therefore means that the lower frequency transducers would necessarily exhibit a lower power output than the higher frequencies. This is a very relevant point concerning the results in paper I, but especially in paper II where the effect of frequency was examined.

When using the Meinhardt signal generator without an impedance matching unit in paper I and II, the delivered acoustic power was visually observed to differ when changing the ultrasonic frequency. This was seen by the ripples in the surface being more violent for higher frequencies when applying the same power from the signal generator. Calorimetric measurements of the acoustic power were therefore introduced as a standard transducer characterization method before using any new transducer. In doing so, a similar acoustic power was delivered to the system at every frequency without having to take impedance matching into account. Of course, this necessarily meant that the acoustic power range was limited to the worst performing transducer which was only able to deliver 11.8 W to the system. A comprehensive study on the acoustic power delivered to each transducer used in paper II can be found in Figure 8.2(a) which is adapted from Figure 2 in the supporting information of paper II. For comparison, the acoustic powers for these frequencies with an impedance matching circuit is shown in Figure 8.2(b). The 488 kHz transducer does not feature in Figure 8.2(b) as it was damaged prior to receiving the impedance matcher.

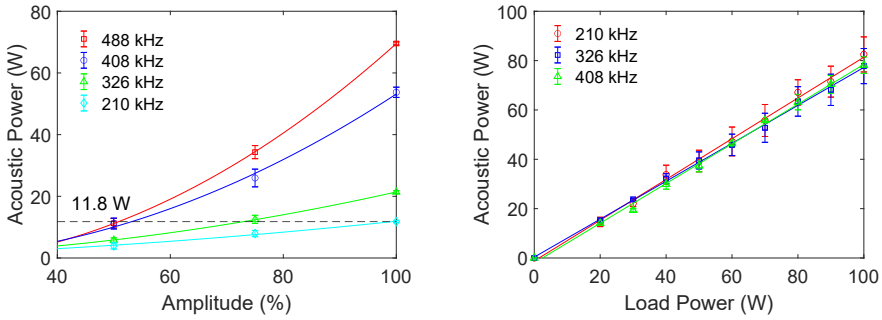

(a) **(b)**

Figure 8.2: Acoustic powers generated by different ultrasonic frequencies as a function of applied power amplitude without impedance matching (8.2(a)) and acoustic powers generated by different ultrasonic frequencies as a function of signal generator load power with impedance matching (8.2(b)).

Not having access to an impedance matching circuit in the first two papers are therefore not of any concern to the conclusions presented in these works as independent acoustic power measurements were performed instead. However, by using an impedance matching circuit you get the added benefit of an expanded power range, greater power efficiency, and less wear and tear on transducers with high impedance differences. Use of impedance matching circuits are very rarely reported in the literature, save for a few exceptions [32, 118]. However, most of the literature is indeed reporting the acoustic power generated by their ultrasonic transducers.

8.3 Direct Sonication and Indirect Sonication

Low frequency horn-type sonifiers have been used for decades to disperse solutions owing to the formation of high power microjets which can break up even the most stubborn agglomerates. However, low frequency, high power ultrasound, is also notorious for causing cavitation damage on the probe material itself as shown in section 2.2.1. Having eroded particles deposited during dispersion of a solution is a cause of contamination which can seriously impact the results depending on the application. In paper I it was shown that nanoparticles are attached to eroded micrometer-sized particles when using a 20 kHz horn-type sonifier in the sonochemical synthesis of Pt-nanoparticles [21]. The effect becomes significant after only 20 min of sonication and can easily be seen in an electron microscope.

Following the findings in paper I, we have recommended that any use of low frequency, high power sonifiers be conducted indirectly as to avoid the inevitable

probe erosion. Indirect sonication has been described in multiple publications [29, 30], and converting an existing direct ultrasound setup to an indirect alternative only requires the design of a new cell. To make sure power is transferred with as little losses in intensity as possible, the distance between the transducer and the bottom of the cell containing the solution should be equal to $\lambda/2$ [29, 30]. For a 20 kHz setup in an aqueous solution the shortest distance is equal to $3.7\,\mathrm{cm}$.

Due to the findings on probe erosion in paper I, combined with the higher sononchemical activity at higher frequencies, all subsequent works were conducted above 200 kHz. The higher frequencies are not sufficient to cause erosion processes, and we therefore opted to use direct sonication in these cases. An indirect sonication cell was also constructed for the high frequency transducers, but due to the much shorter wavelength a precise tuning of the transducer-partition distance to $\lambda/2$ becomes practically impossible, and an application of such a cell would introduce substantial uncertainty in the acoustic power between every experiment. For example, for a 200 kHz transducer, the shortest distance would be $3.7\,\mathrm{mm}$. Misalignment of the cell by just a fraction of a millimeter would therefore significantly alter the transfer of the acoustic waves through the partition.

Indirect sonication is only needed when operating in the low frequency, high power range of ultrasound. Typically, this involves the standard 20 kHz and 40 kHz horn-type sonifiers. Their long half-wavelengths of $3.7\,\mathrm{cm}$ and $1.85\,\mathrm{cm}$, respectively, also makes indirect sonication feasible in practical application.

8.4 Sonochemistry in Electrocatalyst Preparation

In this thesis work, efforts towards electrocatalysis have mostly been concerned with Pt-nanoparticles as hydrogen evolution catalysts. Evaluating sonochemistry as a possible synthesis method for large scale production of hydrogen evolution electrocatalysts is therefore somewhat limited. However, supplementing our own results with those obtained by other sonochemistry groups may allow for a broader overview of the feasibility of sonochemistry towards electrocatalyst synthesis.

In the case of Pt-electrocatalysts, all frequencies between 210 and 488 kHz give identical particle sizes with a narrow size distribution, $(1.9 \pm 0.3)\,\mathrm{nm}$. These are also similar to the ones produced at 20 kHz, $(2.2 \pm 0.5)\,\mathrm{nm}$, and 408 kHz, $(2.3 \pm 0.4)\,\mathrm{nm}$, in paper I, which were synthesized with different volumes, reactors and acoustic powers. Literature values for sonochemically synthesized nanoparticles are also limited to a range between 2-6 nm [26–28, 34, 95, 96, 104]. From these results, it appears that the sonochemical synthesis of Pt-nanoparticles is highly stable yielding small nanoparticles with a very narrow size distribution. This is ideal for electrocatalytic applications as the catalytic activity of Pt-

nanoparticles has been shown to be dependent on the nanoparticle size [132–134]. Incidentally, the ideal particle size for Pt-nanoparticles towards the oxygen reduction reaction is 3 nm [132–134]. In addition to the similar particle sizes observed for sonochemically synthesized Pt-nanoparticles, the catalytic activity towards the hydrogen evolution reaction was also found to be similar as well which further highlights the high degree of reproducibility.

Even though the individual particle properties of sonochemically synthesized Pt-nanoparticles appear to be similar over a wide range of frequencies, the agglomerate characteristics are not. The agglomeration behaviour seems to be frequency dependent, with smaller more open agglomerates forming at low ultrasonic frequencies due to the higher mechanical effect of ultrasound. This was shown in paper II. Somewhere between 210 kHz and 326 kHz, the mechanical effects of ultrasound become less pronounced resulting in similar agglomeration behaviour. Smaller and more open agglomerates are definitely an advantage for increasing the available surface area of non-supported nanoparticles, but it may be harder to control than the equal agglomeration response for the higher frequencies. Some reproducibility could there be sacrificed if small open agglomerates are desired.

However, electrocatalysts are typically supported on a high surface area support in electrochemical applications which means that the agglomeration focus is shifted more towards how well dispersed the particles are on the support. For a regular chemical reduction method, achieving a homogeneous dispersion of catalyst on the support is difficult due to the fast reduction and the inability of achieving a homogeneous distribution of the reducing agent. In the sonochemical method, reducing agents are generated more homogeneously throughout the reactor and acoustic streaming and shockwaves can contribute in directing catalyst nuclei towards an available support site. An example of how sonochemically synthesized Pt-nanoparticles are dispersed on a carbon support is shown in Figure 8.3.

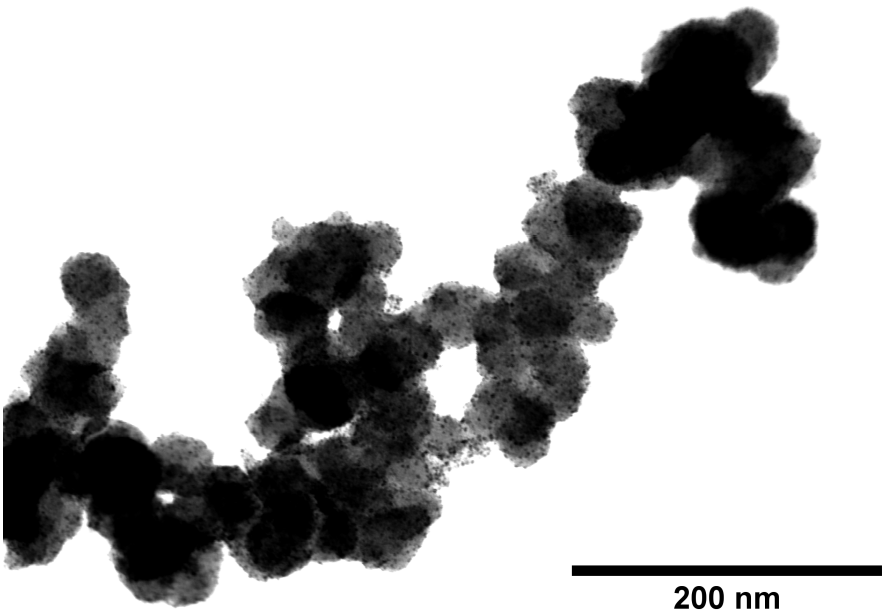

Figure 8.3: Bright field S(T)EM image of Pt-nanoparticles supported on carbon. Pt-nanoparticles were synthesized sonochemially at 346 kHz with an acoustic power of 38 W using $0.5\,\mathrm{mol\,dm^{-3}}$ ethanol.

Sonochemical synthesis of Pt-nanocatalysts for electrochemical energy conversion devices therefore possesses the ability to yield well dispersed, high performance, and highly reproducible Pt-nanoparticles. These are all key characteristics of a well suited synthesis route for electrocatalysts. However, the versatility and scale up potential of the sonochemical synthesis must also be considered before we can recommend it as a catalyst synthesis method.

The sonochemical method has proven to be quite versatile for many of the noble metals. In the case of Au, a wide range of particle sizes are attainable depending on the ultrasound parameters [1]. However, many transition metals which are relevant for developing cheaper electrocatalysts like nickel, iron or copper are either too slow to be viable, or not possible to obtain at all. If future electrocatalyst materials are to be dominated by the more abundant transition metals, sonochemistry will not be able to fill the role as a large scale synthesis method unless these issues are solved. Current state of the art electrolyzers and fuel cells do employ noble metals, and in its current stage sonochemistry must be regarded as a possible contender due the key characteristics discussed above. In addition to the conventional single metal nanocatalysts, we also demonstrated the possibility of making core-shell

nanocatalysts with much improved mass activity in paper 3. The Cu@Pt core-shell nanoparticles displayed an impressive 17 times increase in mass activity over Pt-nanoparticles alone. The sonochemical synthesis therefore offers many different strategies with regards to nanoparticle synthesis, but is not as versatile as chemical reduction.

The second uncertainty with the sonochemical method is scalability. Whether scalibility is a weakness or a strength of the sonochemical method is debatable. On one hand, the formation rate of primary radicals is usually in the order of 10-$20\,\mu\mathrm{mol\,dm^{-3}\,min^{-1}}$ which means that in the ideal case the synthesis of 1 g of Pt-nanoparticles would take about 21 hours in a 200 mL reactor. However, there will be loss of primary radicals during the synthesis, and the yield usually stabilizes well below $100\,\%$ for long sonication times. On the other hand, the sonochemical method generates its reducing agents in-situ which makes it ideal for continuous processes compared to the batch type process of chemical reduction. In addition, increasing the height of the sonochemical reactor has also been shown to yield more primary radicals than lower heights while maintaining the same concentration of radicals [31, 32]. Scaling up the sonochemical method may therefore not suffer from changes in particle properties, which is typical for chemical reduction. Our initial studies on this in paper I led us to believe that sonochemical synthesis of Pt yields similar particle characteristics in widely different reactors. This was performed on a rather small scale (50-200 mL) so it is therefore interesting if similar particle properties are observed for larger volumes as well. We are currently working on how the particle properties of Pt-nanoparticles are affected when the reactor is scaled up, the result of which may help determine if the sonochemical method is viable on a larger scale.

Considering the performance, reproducibility, dispersion, versatility, and scale up potential of the sonochemical method, it may be a better option than chemical reduction for noble metal nanoparticle synthesis. However, fundamental studies related to the electron transfer process between scavengers and metal precursors are needed to solve the issues with using some of the more abundant transition metals in the sonochemical synthesis. Proper large scale studies are also needed to assess if sonochemistry can outperform chemical reduction on an industrial scale. These two aspects should be considered as the two most important research areas to pursue within sonochemical synthesis of electrocatalysts.

Chapter 9

Conclusions and Outlook

For sonochemical reactions driven by secondary radicals, an optimum scavenger concentration exists for achieving the highest reduction rate. The concentration is scavenger dependent and is equivalent to the scavenger concentration required to completely cover the cavitation bubbles. More hydrophobic scavengers therefore require a lower concentration than less hydrophobic scavengers.

For sonochemical reactions driven by pyrolytic decomposition products, the optimum scavenger concentration is found to be approximately one order of magnitude higher than the concentration required for complete bubble coverage. This is attributed to the additional number of pyrolytic decomposition products which can be produced when going beyond complete bubble coverage.

The sonochemical reduction of Ag(I) to Ag-nanoparticles has been shown to proceed through pyrolytic decomposition as well as secondary radicals when ethylene glycol was used as a scavenger. Previously, the sonochemical reduction of Ag(I) to Ag-nanoparticles has been believed to only occur through secondary radicals.

Sonochemical synthesis of Pt-nanoparticles makes for a great synthesis route for achieving highly performing, reproducible electrocatalysts with a high degree of dispersion on carbon supports. This makes them excellent catalysts for electrochemical conversion devices. Some issues must still be solved related to their versatility and scale up processes.

The sonochemical synthesis of Pt, Cu, Cu@Pt, and Ag has been studied in detail, but Au, Ir, Ni and Fe was also investigated during the course of this thesis work. Metallic Ir, Ni and Fe-nanoparticles were not formed to any appreciable extent, the reasons of which are still unclear and would require more research.

Direct sonication of a solution at low ultrasonic frequencies and high acoustic power should be avoided to prevent contamination of the solution by eroded probe material. Indirect sonication should therefore be implemented as a standard operating procedure when dispersing inks for electrochemical characterization purposes.

The electron transfer from scavenger to metal precursor should be explored further in order to explain why some transition metals are more easily reduced than others. Understanding these processes would facilitate establishing favourable synthesis routes through rational choice of scavengers. In addition, a greater focus on scaling up the sonochemical synthesis by use of large scale reactors and high precursor concentrations should be conducted to assess if sonochemistry is to be viable for industrial scale production of nanoparticles. For electrocatalytic purposes, the goal should also be to achieve sufficient amounts of electrocatalysts to be able to conduct full stack fuel cell or electrolyzer performance tests so that their performance can be assessed under real operating conditions.

Bibliography

1. Okitsu, K., Ashokkumar, M. & Grieser, F. Sonochemical synthesis of gold nanoparticles: effects of ultrasound frequency. *The journal of physical chemistry. B* **109,** 20673 (2005).
2. Paris Agreement to the United Nations Framework Convention on Climate Change (Dec. 2015).
3. *Climate Change Indicators: Atmospheric Concentrations of Greenhouse Gases* Accessed: 2023-03-13. `https://www.epa.gov/climate-indicators/climate-change-indicators-atmospheric-concentrations-greenhouse-gases`.
4. *Overview of Greenhouse Gases* Accessed: 2023-03-13. `https://www.epa.gov/ghgemissions/overview-greenhouse-gases`.
5. Terlouw, T., Bauer, C., McKenna, R. & Mazzotti, M. Large-scale hydrogen production via water electrolysis: a techno-economic and environmental assessment. *Energy Environ. Sci.* **15,** 3583–3602 (9 2022).
6. Andersson, J. & Grönkvist, S. Large-scale storage of hydrogen. *International Journal of Hydrogen Energy* **44,** 11901–11919 (2019).
7. Kibsgaard, J. & Chorkendorff, I. Considerations for the scaling-up of water splitting catalysts. eng. *Nature Energy* **4,** 430–433 (2019).
8. Faid, A. Y., Oyarce Barnett, A., Seland, F. & Sunde, S. Highly Active Nickel-Based Catalyst for Hydrogen Evolution in Anion Exchange Membrane Electrolysis. *Catalysts* **8** (2018).
9. Fu, S. *et al.* Ultrafine and highly disordered Ni2Fe1 nanofoams enabled highly efficient oxygen evolution reaction in alkaline electrolyte. *Nano Energy* **44,** 319–326 (2018).

10. Anderson, G., Pivovar, B. & Alia, S. Establishing Performance Baselines for the Oxygen Evolution Reaction in Alkaline Electrolytes. *Journal of The Electrochemical Society* **167,** 044503 (Feb. 2020).

11. Park, A.-H., Shi, W., Jung, J.-U. & Kwon, Y.-U. Mechanism Study of Single-Step Synthesis of Fe(core)@Pt(shell) Nanoparticles by Sonochemistry. *Ultrasonics Sonochemistry* **77,** 105679 (July 2021).

12. Strickler, A. L., Jackson, A. & Jaramillo, T. F. Active and Stable Ir@Pt Core–Shell Catalysts for Electrochemical Oxygen Reduction. *ACS Energy Letters* **2,** 244–249 (2017).

13. Hansen, H. E. *et al.* Sonochemical Synthesis of Cu@Pt Bimetallic Nanoparticles. *Molecules* **27** (2022).

14. Ayers, K. E. *et al.* Pathways to ultra-low platinum group metal catalyst loading in proton exchange membrane electrolyzers. *Catalysis Today* **262.** Electrocatalysis, 121–132 (2016).

15. Kolahalam, L. A. *et al.* Review on nanomaterials: Synthesis and applications. *Materials Today: Proceedings* **18.** 2nd International Conference on Applied Sciences and Technology (ICAST-2019): Material Science, 2182–2190 (2019).

16. Krishna, K. S., Sandeep, C. S. S., Philip, R. & Eswaramoorthy, M. Mixing does the magic: a rapid synthesis of high surface area noble metal nanosponges showing broadband nonlinear optical response. *ACS nano* **4,** 2681–2688 (2010).

17. Escobar Morales, B. *et al.* Synthesis and characterization of colloidal platinum nanoparticles for electrochemical applications. *International journal of hydrogen energy* **35,** 4215–4221 (2010).

18. Niu, Z. & Li, Y. Removal and Utilization of Capping Agents in Nanocatalysis. *Chemistry of Materials* **26,** 72–83 (2014).

19. Ashokkumar, M. The characterization of acoustic cavitation bubbles – An overview. *Ultrasonics Sonochemistry* **18.** European Society of Sonochemistry (ESS12), 864–872 (2011).

20. Pollet, B. G. The use of ultrasound for the fabrication of fuel cell materials. *International Journal of Hydrogen Energy* **35,** 11986–12004 (2010).

21. Hansen, H. E., Seland, F., Sunde, S., Burheim, O. S. & Pollet, B. G. Two routes for sonochemical synthesis of platinum nanoparticles with narrow size distribution. *Mater. Adv.* **2,** 1962–1971 (6 2021).

22. Okitsu, K., Kurisaka, I., Nanzai, B., Takenaka, N. & Bandow, H. Mechanism for sonochemical reduction of Au(III) in aqueous butanol solution under Ar based on the analysis of gaseous and water-soluble products. *Ultrasonics Sonochemistry* **69,** 105241 (2020).

23. Hansen, H. E., Seland, F., Sunde, S., Burheim, O. S. & Pollet, B. G. Frequency controlled agglomeration of Pt-nanoparticles in sonochemical synthesis. *Ultrasonics Sonochemistry* **85,** 105991 (2022).

24. Doktycz, S. & Suslick, K. Interparticle Collision Driven by Ultrasound. *Science* **247,** 1067–1069 (1990).

25. Prozorov, T., Prozorov, R. & Suslick, K. S. High Velocity Interparticle Collisions Driven by Ultrasound. *Journal of the American Chemical Society* **126,** 13890–13891 (2004).

26. Okitsu, K. *et al.* Formation of noble metal particles by ultrasonic irradiation. *Ultrasonics Sonochemistry* **3,** S249–S251 (1996).

27. Mizukoshi, Y., Oshima, R., Maeda, Y. & Nagata, Y. Preparation of Platinum Nanoparticles by Sonochemical Reduction of the Pt(II) Ion. *Langmuir* **15,** 2733–2737 (1999).

28. Mizukoshi, Y. *et al.* Preparation of platinum nanoparticles by sonochemical reduction of the Pt(IV) ions: role of surfactants. *Ultrasonics sonochemistry* **8,** 1–6 (2001).

29. Okitsu, K., Bandow, H., Maeda, Y. & Nagata, Y. Sonochemical Preparation of Ultrafine Palladium Particles. *Chemistry of Materials* **8,** 315–317 (1996).

30. Nagata, Y., Watananabe, Y., Fujita, S.-i., Dohmaru, T. & Taniguchi, S. Formation of colloidal silver in water by ultrasonic irradiation. *J. Chem. Soc., Chem. Commun.,* 1620–1622 (21 1992).

31. Son, Y., Lim, M., Ashokkumar, M. & Khim, J. Geometric Optimization of Sonoreactors for the Enhancement of Sonochemical Activity. *The Journal of Physical Chemistry C* **115,** 4096–4103 (2011).

32. Asakura, Y. & Yasuda, K. Frequency and power dependence of the sonochemical reaction. *Ultrasonics Sonochemistry* **81,** 105858 (2021).

33. Henglein, A. & Kormann, C. Scavenging of OH Radicals Produced in the Sonolysis of Water. *International Journal of Radiation Biology and Related Studies in Physics, Chemistry and Medicine* **48,** 251–258 (1985).

34. Caruso, R. A., Ashokkumar, M. & Grieser, F. Sonochemical formation of colloidal platinum. *Colloids and Surfaces A: Physicochemical and Engineering Aspects* **169,** 219–225 (2000).

35. Asmus, K.-D., Mockel, H. & Henglein, A. Pulse radiolytic study of the site of OH · radical attack on aliphatic alcohols in aqueous solution. eng. *Journal of physical chemistry (1952)* **77,** 1218–1221 (1973).

36. Merouani, S., Hamdaoui, O., Rezgui, Y. & Guemini, M. Sensitivity of free radicals production in acoustically driven bubble to the ultrasonic frequency and nature of dissolved gases. *Ultrasonics Sonochemistry* **22,** 41–50 (2015).

37. Mark, G. *et al.* OH-radical formation by ultrasound in aqueous solution – Part II: Terephthalate and Fricke dosimetry and the influence of various conditions on the sonolytic yield. *Ultrasonics Sonochemistry* **5,** 41–52 (1998).

38. He, Y., Vinodgopal, K., Ashokkumar, M. & Grieser, F. Sonochemical synthesis of ruthenium nanoparticles. *Research on chemical intermediates* **32,** 709–715 (2006).

39. Beckett, M. A. & Hua, I. Impact of Ultrasonic Frequency on Aqueous Sonoluminescence and Sonochemistry. *The Journal of Physical Chemistry A* **105,** 3796–3802 (2001).

40. Koda, S., Kimura, T., Kondo, T. & Mitome, H. A standard method to calibrate sonochemical efficiency of an individual reaction system. *Ultrasonics - Sonochemistry* **10,** 149–156 (2003).

41. Hansen, H., Seland, F., Sunde, S., Burheim, O. & Pollet, B. Optimum scavenger concentrations for sonochemical nanoparticle synthesis. *Scientific Reports* **13** (Apr. 2023).

42. McGillem, C. D. telegraph. eng. *Encyclopedia Britannica.* Accessed 20 March 2023. `https://www.britannica.com/technology/telegraph` (2022).

43. Wolfe, J. *How does a guitar work?* eng. Accessed 20 March 2023. `https://www.phys.unsw.edu.au/music/guitar/guitarintro.html`.

44. Pierce, A. D. in *Acoustics: An Introduction to Its Physical Principles and Applications* (Springer International Publishing, 2019).

45. Cros, A. & Arellano Castro, R. F. Experimental study on the resonance frequencies of a cantilevered plate in air flow. *Journal of Sound and Vibration* **363,** 240–246 (2016).

46. Atkins, P. *Atkins' physical chemistry* eng. Oxford, 2010.

47. *Liquids - speed of sound* `https://www.engineeringtoolbox.com/sound-speed-liquids-d_715.html`.

48. Michaud, M., Leong, T., Swiergon, P., Juliano, P. & Knoerzer, K. Design parameters of stainless steel plates for maximizing high frequency ultrasound wave transmission. *Ultrasonics Sonochemistry* **26,** 56–63 (2015).

49. *Viscosity - Absolute (Dynamic) vs. Kinematic* Accessed 20 March 2023. https://www.engineering-toolbox.com/dynamic-absolute-kinematic-viscosity-d_412.html.

50. *Liquids - Densities* Accessed 20 March 2023. https://www.engineering%20toolbox.com/liquids-densities-d_743.html.

51. Dukhin, A. S. & Goetz, P. J. in *Characterization of Liquids, Nano- and Microparticulates, and Porous Bodies Using Ultrasound* (eds Dukhin, A. S. & Goetz, P. J.) 91–125 (Elsevier, 2010).

52. *Gasses - Densities* Accessed 20 March 2023. https://www.engineering%20toolbox.com/gas-density-d_158.html.

53. *Solids and Metals - Speed of Sound* Accessed 20 March 2023. https://www.engineering%20toolbox.com/sound-speed-solids-d_713.html.

54. *Solids - Densities* Accessed 20 March 2023. https://www.engineering%20toolbox.com/density-solids-d_1265.html.

55. Britannica, T. E. o. E. standing wave. eng. *Encyclopedia Britannica.* Accessed 20 March 2023. https://www.britannica.com/science/standing-wave-physics (2023).

56. Pollet, B. *Power Ultrasound in Electrochemistry: From Versatile Laboratory Tool to Engineering Solution* 1–344 (Jan. 2012).

57. Richards, W. T. & Loomis, A. L. The Chemical Effects of High Frequency Sound Waves I. A Preliminary Survey. *Journal of the American Chemical Society* **49,** 3086–3100 (1927).

58. Peters, A., Lantermann, U. & el Moctar, O. Numerical prediction of cavitation erosion on a ship propeller in model- and full-scale. *Wear* **408-409,** 1–12 (2018).

59. Nad, M. Ultrasonic horn design for ultrasonic machining technologies. *Applied and Computational Mechanics* **4** (June 2010).

60. Fuchs, F. in *Power Ultrasonics* (eds Gallego-Juárez, J. A. & Graff, K. F.) 577–609 (Woodhead Publishing, Oxford, 2015).

61. Davari, P., Ghasemi, N. & Zare, F. *Power converters design and analysis for high power piezoelectric ultrasonic transducers* in (Aug. 2014).

62. Friel, R. in *Power Ultrasonics* (eds Gallego-Juárez, J. A. & Graff, K. F.) 313–335 (Woodhead Publishing, Oxford, 2015).

63. in. *Handbook of Plastics Joining (Second Edition)* (ed Troughton, M. J.) Second Edition, 15–35 (William Andrew Publishing, Boston, 2009).

64. Rathod, V. T. A Review of Acoustic Impedance Matching Techniques for Piezoelectric Sensors and Transducers. *Sensors* **20** (2020).

65. Svilainis, L. & Dumbrava, V. Evaluation of the ultrasonic transducer electrical matching performance. *Ultragarsas* **62,** 1392–2114 (Jan. 2007).

66. Garcia-Rodriguez, M. *et al.* Low cost matching network for ultrasonic transducers. *Physics Procedia* **3.** International Congress on Ultrasonics, Santiago de Chile, January 2009, 1025–1031 (2010).

67. Sapozhnikov, O. in *Power Ultrasonics* (eds Gallego-Juárez, J. A. & Graff, K. F.) 9–35 (Woodhead Publishing, Oxford, 2015).

68. Yasui, K. in *Theoretical and Experimental Sonochemistry Involving Inorganic Systems* (ed Ashokkumar, M.) 1–29 (Springer Netherlands, Dordrecht, 2011).

69. Kanthale, P., Ashokkumar, M. & Grieser, F. Sonoluminescence, sonochemistry (H2O2 yield) and bubble dynamics: Frequency and power effects. *Ultrasonics Sonochemistry* **15,** 143–150 (2008).

70. Merouani, S., Ferkous, H., Hamdaoui, O., Rezgui, Y. & Guemini, M. New interpretation of the effects of argon-saturating gas toward sonochemical reactions. *Ultrasonics Sonochemistry* **23,** 37–45 (2015).

71. Suslick, K. S., Hammerton, D. A. & Cline, R. E. Sonochemical hot spot. *Journal of the American Chemical Society* **108,** 5641–5642 (1986).

72. Castro, L. & Hoyos, M. Determination of the Secondary Bjerknes Force in Acoustic Resonators on Ground and in Microgravity Conditions. *Microgravity Science and Technology* **28** (Apr. 2016).

73. Hatanaka, S.-I., Yasui, K., Tuziuti, T., Kozuka, T. & Mitome, H. Quenching mechanism of multibubble sonoluminescence at excessive sound pressure. eng. *JAPANESE JOURNAL OF APPLIED PHYSICS PART 1-REGULAR PAPERS BRIEF COMMUNICATIONS & REVIEW PAPERS* **40,** 3856–3860 (2001).

74. Gielen, B. *et al.* Influence of dissolved gases on sonochemistry and sonoluminescence in a flow reactor. *Ultrasonics Sonochemistry* **31,** 463–472 (2016).

75. Henglein, A. & Gutierrez, M. Chemical effects of continuous and pulsed ultrasound: a comparative study of polymer degradation and iodide oxidation. *The Journal of Physical Chemistry* **94,** 5169–5172 (1990).

76. Hujjatul Islam, M., Paul, M. T., Burheim, O. S. & Pollet, B. G. Recent developments in the sonoelectrochemical synthesis of nanomaterials. *Ultrasonics Sonochemistry* **59,** 104711 (2019).

77. Iida, Y., Yasui, K., Tuziuti, T. & Sivakumar, M. Sonochemistry and its dosimetry. *Microchemical Journal* **80,** 159–164 (2005).

78. G.F.S. The physical and biological effects of high-frequency sound-waves of great intensity: R. W. Wood and A. L. Loomis. (Phil. Mag., Sept., 1927). *Journal of the Franklin Institute* **205,** 151–153 (1928).

79. Alexander, P. & Fox, M. The role of free radicals in the degradation of high polymers by ultrasonics and by high-speed stirring. *Journal of Polymer Science* **12,** 533–541 (1954).

80. Weissler, A. Formation of Hydrogen Peroxide by Ultrasonic Waves: Free Radicals. *Journal of the American Chemical Society* **81,** 1077–1081 (1959).

81. Anbar, M. & Pecht, I. On the Sonochemical Formation of Hydrogen Peroxide in Water. eng. *Journal of physical chemistry (1952)* **68,** 352–355 (1964).

82. Buettner, J., Gutierrez, M. & Henglein, A. Sonolysis of water-methanol mixtures. *The Journal of Physical Chemistry* **95,** 1528–1530 (1991).

83. Gutiérrez, M., Henglein, A. & Fischer, C.-H. Hot Spot Kinetics of the Sonolysis of Aqueous Acetate Solutions. *International Journal of Radiation Biology and Related Studies in Physics, Chemistry and Medicine* **50,** 313–321 (1986).

84. Hart, E. J. & Henglein, A. Sonolysis of formic acid-water mixtures. *International Journal of Radiation Applications and Instrumentation. Part C. Radiation Physics and Chemistry* **32,** 11–13 (1988).

85. Hart, E. J. & Henglein, A. Free radical and free atom reactions in the sonolysis of aqueous iodide and formate solutions. *The Journal of Physical Chemistry* **89,** 4342–4347 (1985).

86. Mead, E. L., Sutherland, R. G. & Verrall, R. E. The effect of ultrasound on water in the presence of dissolved gases. *Canadian Journal of Chemistry* **54,** 1114–1120 (1976).

87. Gutierrez, M., Henglein, A. & Ibanez, F. Radical scavenging in the sonolysis of aqueous solutions of iodide, bromide, and azide. *The Journal of Physical Chemistry* **95,** 6044–6047 (1991).

88. Gutierrez, M. & Henglein, A. Sonolytic decomposition of poly(vinylpyrrolidone), ethanol and tetranitromethane in aqueous solution. eng. *Journal of physical chemistry (1952)* **92,** 2978–2981 (1988).

89. Suslick, K. The Site of Sonochemical Reactions. *IEEE Transactions on Ultrasonics, Ferroelectrics, and Frequency Control* **33,** 143–147 (1986).

90. Kumar, P. S. S. *et al.* Sonochemical synthesis and characterization of gold ruthenium bimetallic nanoparticles. *Colloids and Surfaces A: Physicochemical and Engineering Aspects* **356,** 140–144 (2010).

91. Brotchie, A., Grieser, F. & Ashokkumar, M. Effect of Power and Frequency on Bubble-Size Distributions in Acoustic Cavitation. *Phys. Rev. Lett.* **102,** 084302 (8 Mar. 2009).

92. Finlayson-Pitts, B. J. & Pitts, J. N. in *Chemistry of the Upper and Lower Atmosphere* (eds Finlayson-Pitts, B. J. & Pitts, J. N.) 179–263 (Academic Press, San Diego, 2000).

93. Armstrong, D. *et al.* Standard Electrode Potentials Involving Radicals in Aqueous Solution: Inorganic Radicals. *BioInorganic Reaction Mechanisms* **9** (Aug. 2013).

94. Fuentes-García, J. *et al.* Effect of ultrasonic irradiation power on sonochemical synthesis of gold nanoparticles. *Ultrasonics Sonochemistry* **70,** 105274 (2021).

95. Ruiz-Camacho, B., Palafox-Segoviano, J., Pérez-Díaz, P. & Medina-Ramírez, A. Synthesis of supported Pt nanoparticles by sonication for ORR: Effect of the graphene oxide-carbon composite. *International Journal of Hydrogen Energy* **46.** XIX Mexican Hydrogen Society Congress Special Issue, 26027–26039 (2021).

96. Fujimoto, T., Terauchi, S.-y., Umehara, H., Kojima, I. & Henderson, W. Sonochemical Preparation of Single-Dispersion Metal Nanoparticles from Metal Salts. *Chemistry of Materials* **13,** 1057–1060 (2001).

97. Lee, E., Park, A.-H., Park, H.-U. & Kwon, Y.-U. Facile sonochemical synthesis of amorphous NiFe-(oxy)hydroxide nanoparticles as superior electrocatalysts for oxygen evolution reaction. *Ultrasonics Sonochemistry* **40,** 552–557 (2018).

98. Kristl, M., Dojer, B., Gyergyek, S. & Kristl, J. Synthesis of nickel and cobalt sulfide nanoparticles using a low cost sonochemical method. *Heliyon* **3,** e00273 (2017).

99. Shafi, K. V. P. M. *et al.* Sonochemical Preparation of Nanosized Amorphous NiFe2O4 Particles. *The Journal of Physical Chemistry B* **101,** 6409–6414 (1997).

100. Goswami, P., Choudhury, H. & Chakma, S. Sonochemical Synthesis of Cobalt Ferrite Nanoparticles. *International Journal of Chemical Engineering* **2013,** 1–6 (Jan. 2013).

101. Lv, W. *et al.* Sonochemical synthesis of cobalt aluminate nanoparticles under various preparation parameters. *Ultrasonics Sonochemistry* **17,** 793–801 (2010).

102. Yang, G.-W. & Li, H. Sonochemical synthesis of highly monodispersed and size controllable Ag nanoparticles in ethanol solution. *Materials Letters* **62,** 2189–2191 (2008).

103. Paramelle, D. *et al.* A rapid method to estimate the concentration of citrate capped silver nanoparticles from UV-visible light spectra. *Analyst* **139,** 4855–4861 (19 2014).

104. Chave, T., Navarro, N., Nitsche, S. & Nikitenko, S. Mechanism of PtIV Sonochemical Reduction in Formic Acid Media and Pure Water. *Chemistry (Weinheim an der Bergstrasse, Germany)* **18,** 3879–85 (Mar. 2012).

105. Wongpisutpaisan, N., Charoonsuk, P., Vittayakorn, N. & Pecharapa, W. Sonochemical Synthesis and Characterization of Copper Oxide Nanoparticles. *Energy Procedia* **9.** 9th Eco-Energy and Materials Science and Engineering Symposium, 404–409 (2011).

106. Bhosale, M. A. & Bhanage, B. M. A simple approach for sonochemical synthesis of Cu2O nanoparticles with high catalytic properties. *Advanced Powder Technology* **27,** 238–244 (2016).

107. Merouani, S., Hamdaoui, O., Rezgui, Y. & Guemini, M. Computational engineering study of hydrogen production via ultrasonic cavitation in water. *International Journal of Hydrogen Energy* **41,** 832–844 (2016).

108. Okitsu, K. *et al.* Acoustic Multibubble Cavitation in Water: A New Aspect of the Effect of a Rare Gas Atmosphere on Bubble Temperature and Its Relevance to Sonochemistry. *The Journal of Physical Chemistry B* **110,** 20081–20084 (2006).

109. Hua, I. & Hoffmann, M. R. Optimization of Ultrasonic Irradiation as an Advanced Oxidation Technology. *Environmental Science & Technology* **31,** 2237–2243 (1997).

110. Aylward, G. & Findlay, T. *SI Chemical Data* 1998.

111. Merouani, S., Hamdaoui, O. & Al-Zahrani, S. M. Toward understanding the mechanism of pure CO2-quenching sonochemical processes. *Journal of Chemical Technology & Biotechnology* **95,** 553–566 (2020).

112. Brems, S. *et al.* The Influence of Dissolved Carbon Dioxide on Cavitation Intensity in Ultrasound Cleaning Systems. *Japanese Journal of Applied Physics* **52,** 066602 (June 2013).

113. Torres, R. A., Pétrier, C., Combet, E., Carrier, M. & Pulgarin, C. Ultrasonic cavitation applied to the treatment of bisphenol A. Effect of sonochemical parameters and analysis of BPA by-products. *Ultrasonics Sonochemistry* **15,** 605–611 (2008).

114. Merouani, S., Hamdaoui, O., Rezgui, Y. & Guemini, M. Effects of ultrasound frequency and acoustic amplitude on the size of sonochemically active bubbles – Theoretical study. *Ultrasonics Sonochemistry* **20,** 815–819 (2013).

115. McNamara, W. B., Didenko, Y. T. & Suslick, K. S. Pressure during Sonoluminescence. *The Journal of Physical Chemistry B* **107,** 7303–7306 (2003).

116. Morosini, V., Chave, T., Virot, M., Moisy, P. & Nikitenko, S. I. Sonochemical water splitting in the presence of powdered metal oxides. *Ultrasonics Sonochemistry* **29,** 512–516 (2016).

117. Geng, J., Jiang, L. & Zhu, J. Crystal formation and growth mechanism of inorganic nanomaterials in sonochemical syntheses. *Science China Chemistry* **55** (Nov. 2012).

118. De La Rochebrochard d'Auzay, S., Blais, J.-F. & Naffrechoux, E. Comparison of characterization methods in high frequency sonochemical reactors of differing configurations. *Ultrasonics Sonochemistry* **17,** 547–554 (2010).

119. Erades de Quevedo, R. *Analysis of the effect of saturation gas, solution temperature and concentration on OH radical formation by ultrasonic irradiation for hydrogen production optimization* eng. 2019.

120. Coskun, S., Aksoy, B. & Unalan, H. E. Polyol Synthesis of Silver Nanowires: An Extensive Parametric Study. *Crystal Growth & Design* **11,** 4963–4969 (2011).

121. Skrabalak, S. E., Wiley, B. J., Kim, M., Formo, E. V. & Xia, Y. On the Polyol Synthesis of Silver Nanostructures: Glycolaldehyde as a Reducing Agent. *Nano Letters* **8,** 2077–2081 (2008).

122. Awad, S. B. & Awad, N. F. in *Particle Adhesion and Removal* 201–241 (John Wiley & Sons, Ltd, 2015).

123. Kandjani, A. E., Tabriz, M. F. & Pourabbas, B. Sonochemical synthesis of ZnO nanoparticles: The effect of temperature and sonication power. *Materials Research Bulletin* **43,** 645–654 (2008).

124. Petrucci, R. H., Herring, F. G., Madura, J. D. & Bissonnette, C. *General Chemistry: Principles and Modern Applications* (Pearson, 2011).

125. Chorkendorff, I. *Concepts of modern catalysis and kinetics* eng. Weinheim, 2017.

126. Oldham, K. B., Myland, J. C. & Bond, A. M. *Electrochemical Science and Technology: Fundamentals and Applications* eng (John Wiley & Sons, Ltd, Chichester, UK, 2011).

127. Shinagawa, T., Garcia-Esparza, A. & Takanabe, K. Insight on Tafel slopes from a microkinetic analysis of aqueous electrocatalysis for energy conversion. *Scientific reports* **5,** 13801 (Sept. 2015).

128. Conway, B. & Jerkiewicz, G. Relation of energies and coverages of underpotential and overpotential deposited H at Pt and other metals to the 'volcano curve' for cathodic H2 evolution kinetics. *Electrochimica Acta* **45,** 4075–4083. ISSN: 0013-4686 (2000).

129. Minke, C., Suermann, M., Bensmann, B. & Hanke-Rauschenbach, R. Is iridium demand a potential bottleneck in the realization of large-scale PEM water electrolysis? *International Journal of Hydrogen Energy* **46,** 23581–23590. ISSN: 0360-3199 (2021).

130. Shao, M., Chang, Q., Dodelet, J.-P. & Chenitz, R. Recent Advances in Electrocatalysts for Oxygen Reduction Reaction. *Chemical Reviews* **116,** 3594–3657 (2016).

131. Kulkarni, A., Siahrostami, S., Patel, A. & Nørskov, J. K. Understanding Catalytic Activity Trends in the Oxygen Reduction Reaction. *Chemical Reviews* **118,** 2302–2312 (2018).

132. Gasteiger, H. A., Kocha, S. S., Sompalli, B. & Wagner, F. T. Activity benchmarks and requirements for Pt, Pt-alloy, and non-Pt oxygen reduction catalysts for PEMFCs. *Applied Catalysis B: Environmental* **56.** Fuel processing and PEM Fuel Cells: advanced cata;ysts, adsorbents and electrocatalysts, 9–35 (2005).

133. Shinozaki, K., Morimoto, Y., Pivovar, B. S. & Kocha, S. S. Re-examination of the Pt Particle Size Effect on the Oxygen Reduction Reaction for Ultrathin Uniform Pt/C Catalyst Layers without Influence from Nafion. *Electrochimica Acta* **213,** 783–790 (2016).

134. Stephens, I. E. L., Bondarenko, A. S., Grønbjerg, U., Rossmeisl, J. & Chorkendorff, I. Understanding the electrocatalysis of oxygen reduction on platinum and its alloys. *Energy Environ. Sci.* **5,** 6744–6762 (5 2012).

135. Oh, H.-S. *et al.* Electrochemical Catalyst–Support Effects and Their Stabilizing Role for IrOx Nanoparticle Catalysts during the Oxygen Evolution Reaction. *Journal of the American Chemical Society* **138,** 12552–12563 (2016).

136. Seselj, N., Engelbrekt, C. & Zhang, J. Graphene-supported platinum catalysts for fuel cells. *Science Bulletin* **60,** 864–876 (2015).

137. Pérez-Rodríguez, S., Pastor, E. & Lázaro, M. Electrochemical behavior of the carbon black Vulcan XC-72R: Influence of the surface chemistry. *International Journal of Hydrogen Energy* **43,** 7911–7922. ISSN: 0360-3199 (2018).

138. Muthuswamy, N. *et al.* Towards a highly-efficient fuel-cell catalyst: optimization of Pt particle size, supports and surface-oxygen group concentration. *Phys. Chem. Chem. Phys.* **15,** 3803–3813 (11 2013).

139. Harris, D. C. *Quantitative chemical analysis* eng. New York, 2007.

140. Solomons, T. W. G. *Organic chemistry* eng. Singapore, 2014.

141. Crichton, R. R. in *Biological Inorganic Chemistry (Second Edition)* (ed Crichton, R. R.) Second Edition, 21–34 (Elsevier, Oxford, 2012).

142. Amendola, V., Pilot, R., Frasconi, M., Maragò, O. M. & Iatì, M. A. Surface plasmon resonance in gold nanoparticles: a review. *Journal of Physics: Condensed Matter* **29,** 203002 (Mar. 2017).

143. Poletti, A., Fracasso, G., Conti, G., Pilot, R. & Amendola, V. Laser generated gold nanocorals with broadband plasmon absorption for photothermal applications. *Nanoscale* **7,** 13702–13714 (32 2015).

144. Ider, M., Abderrafi, K., Eddahbi, A., Ouaskit, S. & Kassiba, A. Silver Metallic Nanoparticles with Surface Plasmon Resonance: Synthesis and Characterizations. *Journal of Cluster Science* **28** (May 2017).

145. Bárta, J., Pospíšil, M. & Čuba, V. Photo and radiation-induced preparation of nanocrystalline copper and cuprous oxide catalysts. *Journal of Radioanalytical and Nuclear Chemistry - J RADIOANAL NUCL CHEM* **286,** 611–618 (Dec. 2010).

146. Callister, W. D. *Materials science and engineering* eng. Hoboken, N.J, 2015.

147. ARL, T. *Introduction to Powder/Polycrystalline Diffraction* eng. 1999.

148. Hubbard, C. R. & Snyder, R. L. RIR - Measurement and Use in Quantitative XRD. eng. *Powder Diffraction* **3** (1988).

149. Will, G. *Powder Diffraction: The Rietveld Method and the Two Stage Method to Determine and Refine Crystal Structures from Powder Diffraction Data* eng (Springer Berlin Heidelberg, Berlin, Heidelberg, 2006).

150. Egerton, R. *Physical Principles of Electron Microscopy: An Introduction to TEM, SEM, and AEM* eng (Springer US, Boston, MA, 2005).

151. Merkus, H. G. *Particle Size Measurements : Fundamentals, Practice, Quality* eng. Dordrecht, 2009.

152. Elgrishi, N. *et al.* A Practical Beginner's Guide to Cyclic Voltammetry. *Journal of Chemical Education* **95,** 197–206 (2018).

153. Schmidt, T. J. *et al.* Characterization of High-Surface-Area Electrocatalysts Using a Rotating Disk Electrode Configuration. *Journal of The Electrochemical Society* **145,** 2354 (July 1998).

154. Chen, R. *et al.* Use of Platinum as the Counter Electrode to Study the Activity of Nonprecious Metal Catalysts for the Hydrogen Evolution Reaction. *ACS Energy Letters* **2,** 1070–1075 (2017).

155. Ofstad, A. B. *et al.* Assessment of Platinum Dissolution from a Pt/C Fuel Cell Catalyst: An Electrochemical Quartz Crystal Microbalance Study. *Journal of The Electrochemical Society* **157,** B621 (Mar. 2010).

156. Briskeby, S. T., Tsypkin, M., Tunold, R. & Sunde, S. Stability of carbon nanofibre-supported platinum catalysts in the presence of chloride under controlled mass-transfer conditions. *Journal of Power Sources* **251,** 1–7. ISSN: 0378-7753 (2014).

157. PLETCHER, D., GREFF, R., PEAT, R., PETER, L. & ROBINSON, J. in *Instrumental Methods in Electrochemistry* (eds PLETCHER, D., GREFF, R., PEAT, R., PETER, L. & ROBINSON, J.) 113–148 (Woodhead Publishing, 2010).

158. PLETCHER, D., GREFF, R., PEAT, R., PETER, L. & ROBINSON, J. in *Instrumental Methods in Electrochemistry* (eds PLETCHER, D., GREFF, R., PEAT, R., PETER, L. & ROBINSON, J.) 178–228 (Woodhead Publishing, 2010).

159. PLETCHER, D., GREFF, R., PEAT, R., PETER, L. & ROBINSON, J. in *Instrumental Methods in Electrochemistry* (eds PLETCHER, D., GREFF, R., PEAT, R., PETER, L. & ROBINSON, J.) 356–387 (Woodhead Publishing, 2010).

160. Angerstein-Kozlowska, H., Conway, B. & Sharp, W. The real condition of electrochemically oxidized platinum surfaces: Part I. Resolution of component processes. *Journal of Electroanalytical Chemistry and Interfacial Electrochemistry* **43,** 9–36 (1973).

161. Ciapina, E. G., Santos, S. F. & Gonzalez, E. R. Electrochemical CO stripping on nanosized Pt surfaces in acid media: A review on the issue of peak multiplicity. *Journal of Electroanalytical Chemistry* **815,** 47–60 (2018).

162. Margulis, M. & Margulis, I. Calorimetric method for measurement of acoustic power absorbed in a volume of a liquid. eng. *Ultrasonics - Sonochemistry* **10,** 343–345 (2003).

163. Contamine, R. F., Wilhelm, A., Berlan, J. & Delmas, H. Power measurement in sonochemistry. *Ultrasonics - Sonochemistry* **2,** S43–S47 (1995).

164. *Water - Specific Heat vs. Temperature* Accessed 20 March 2023. `https://www.engineeringtoolbox.com/specific-heat-capacity-water-d_660.html`.

165. Gutierrez, M., Henglein, A. & Ibanez, F. Radical scavenging in the sonolysis of aqueous solutions of iodide, bromide, and azide. *The Journal of Physical Chemistry* **95,** 6044–6047 (1991).

166. Allen, A. O., Hochanadel, C. J., Ghormley, J. A. & Davis, T. W. Decomposition of Water and Aqueous Solutions under Mixed Fast Neutron and γ-Radiation. *The Journal of Physical Chemistry* **56,** 575–586 (1952).

167. Dalodière, E., Virot, M., Moisy, P. & Nikitenko, S. I. Effect of ultrasonic frequency on H2O2 sonochemical formation rate in aqueous nitric acid solutions in the presence of oxygen. *Ultrasonics Sonochemistry* **29,** 198–204 (2016).

Nomenclature

Roman Letters

A	Amplitude	1
A	Pre-exponential factor	1
A	Acoustic factor	1
A	Absorbance	1
A	Area	cm^2
C	Capacitance	F
C_P	Specific heat at constant pressure	$\mathrm{J\,g^{-1}\,K^{-1}}$
C_V	Specific heat at constant volume	$\mathrm{J\,g^{-1}\,K^{-1}}$
c	Concentration	$\mathrm{mol\,dm^{-3}}$
c	Speed of light	$\mathrm{m\,s^{-1}}$
D	Diffusion constant	$\mathrm{m^2\,s^{-1}}$
D	Crysallite size	nm
d	Distance between cavitation bubbles	m
d	Interplanar distance	nm
E	Photon Energy	J
E	Electrode potential	V
E_a	Activation energy	$\mathrm{J\,mol^{-1}}$
F	Faraday's constant	$\mathrm{C\,mol^{-1}}$
F_p	Primary Bjerknes force	N
F_s	Secondary Bjerknes force	N
f	Frequency	Hz
f	Degrees of freedom	1
G	Gibbs energy	J
$g^{(1)}$	Autocorrelation function for monodisperse systems	1
$g^{(2)}$	General autocorrelation function	1
h	Planck's constant	$\mathrm{m^2\,kg\,s^{-1}}$
I	Transmitted light intensity	$\mathrm{W\,m^{-2}}$
I	Current	A
I_0	Incident light intensity	$\mathrm{W\,m^{-2}}$
j	Current density	$\mathrm{A\,cm^{-2}}$
j_0	Exchange current density	$\mathrm{A\,cm^{-2}}$
K	Geometric constant in X-ray diffraction	1
K_s	Stiffness coefficient	$\mathrm{kg\,m^{-1}\,s^{-2}}$
k	Stiffness	$\mathrm{kg\,s^{-2}}$
k	Rate constant	$\mathrm{min^{-1}}$
k_b	Boltzmann's constant	$\mathrm{J\,K^{-1}}$

L	Heat of fusion	$\mathrm{J\,kg^{-1}}$
L	Inductance	H
l	Pathlength of light	cm
l	Thickness of partition	m
m	Mass	kg
n	Refractive index	1
P	Pressure	Pa
P_0	Bubble pressure before collapse	Pa
P_a	Acoustic power	W
R	Universal gas constant	$\mathrm{J\,mol^{-1}\,K^{-1}}$
R	Degree of reflection	$\%$
R	Charge transfer resistance	Ω
R_s	Series resistance	Ω
r	Bubble radius	m
r	Particle radius	m
r	Hydrodynamic radius	nm
r_0	Initial bubble radius	m
SE	Sonochemical efficiency	$\mathrm{mol\,J^{-1}}$
T	Temperature	K
T	Transmittance	1
T_0	Temperature before bubble collapse	K
T_b	Bulk temperature of solution	°C
T_m	Melting temperature	°C
V	Bubble volume	$\mathrm{m^3}$
V_0	Initial bubble volume	$\mathrm{m^3}$
v	Wave velocity	$\mathrm{m\,s^{-1}}$
z	Number of electrons	1
v_c	Collision velocity threshold	$\mathrm{m\,s^{-1}}$
Z_S	Impedance of the electrical signal	Ω
Z_L	Impedance of the transducer	Ω

Greek Letters

α	Sound attenuation coefficient	m^{-1}
β	full width at half maximum	1
Γ	Decay constant	min^{-1}
γ	Polytropic ratio	1
ϵ	Molar extinction coefficient	$\mathrm{dm}^3\,\mathrm{mol}^{-1}\,\mathrm{cm}^{-1}$
η	Viscosity	$\mathrm{kg\,m}^{-1}\,\mathrm{s}^{-1}$
θ	Diffraction angle	$^\circ$
θ	Scattering angle	$^\circ$
λ	Wavelength	nm
μ	Viscosity	$\mathrm{kg\,m}^{-1}\,\mathrm{s}^{-1}$
ν	Scan rate	$\mathrm{mV\,s}^{-1}$
ρ	Density	$\mathrm{kg\,m}^{-3}$
τ	Delay time	min
φ	Phase shift	$^\circ$
ω_r	Angular resonance frequency	Hz

Abbreviations

BuOH	Butanol
CE	Counter electrode
CV	Cyclic voltammetry
DLS	Dynamic light scattering
ECSA	Electrochemically active surface area
EDS	Energy-dispersive X-ray spectroscopy
EDX	Energy-dispersive X-ray spectroscopy
EG	Ethylene glycol
EtOH	Ethanol
HER	Hydrogen evolution reaction
HOR	Hydrogen oxidation reaction
IPA	Isopropyl alcohol
LSPR	Localized surface plasmon resonance
LSV	Linear sweep voltammetry
MeOH	Methanol
OER	Oxygen evolution reaction
ORR	Oxygen reduction reaction

PDI	Polydispersity index
PEG	Polyethylene glycol monostearate
PEMFC	Proton exhange membrane fuel cell
PGM	Platinum group metal
PVP	Polyvinylpyrrolidone
PZT	Lead zirconate titanate
RDE	Rotating disk electrode
RE	Reference electrode
RH	Radical scavenger
RHE	Reversible hydrogen electrode
SDS	Sodium dodecylsulfate
SEM	Scanning electron microscopy
SHE	Standard hydrogen electrode
S(T)EM	Scanning (transmission) electron microscopy
TEM	Transmission electron microscopy
Tween20	Polyoxyethylenesorbitan monolaurate
UV-vis	Ultraviolet-visible spectroscopy
WE	Working electrode
XRD	X-ray diffraction

ISBN 978-82-326-7132-8 (printed ver.)
ISBN 978-82-326-7131-1 (electronic ver.)
ISSN 1503-8181 (printed ver.)
ISSN 2703-8084 (online ver.)

NTNU

Norwegian University of
Science and Technology